ARTIFICIAL INTELLIGENCE APPLIED TO SPEED SENSORLESS INDUCTION MOTOR DRIVES

Shady Mostafa Gadoue

B.Sc., M.Sc.

A thesis submitted for the degree of

Doctor of Philosophy

January, 2009

School of Electrical, Electronic and

Computer Engineering

Newcastle University

United Kingdom

ABSTRACT

During the last two decades there has been considerable development of sensorless vector controlled induction motor drives for high performance industrial applications. Such control strategies reduce the drive's cost, size and maintenance requirements while increasing the system's reliability and robustness. Parameter sensitivity, high computational effort and instability at low and zero speed can be the main shortcomings of sensorless control. Sensorless drives have been successfully applied for medium and high speed operation, but low and zero speed operation is still a critical problem. Much recent research effort is focused on extending the operating region of sensorless drives near zero stator frequency.

Several strategies have been proposed for rotor speed estimation in sensorless induction motor drives based on the machine fundamental excitation model. Among these techniques Model Reference Adaptive Systems (MRAS) schemes are the most common strategies employed due to their relative simplicity and low computational effort. Rotor flux-MRAS is the most popular MRAS strategy and significant attempts have been made to improve the performance of this scheme at low speed. Artificial Intelligence (AI) techniques have attracted much attention in the past few years as powerful tools to solve many control problems. Common AI strategies include neural networks, fuzzy logic and genetic algorithms.

The main purpose of this work is to show that AI can be used to improve the sensorless performance of the well-established MRAS observers in the critical low and zero speed region of operation. This thesis proposes various novel methods based on AI combined with MRAS observers. These methods have been implemented via simulation but also on an experimental drive based around a commercial induction machine.

Detailed simulations and experimental tests are carried out to investigate the performance of the proposed schemes when compared to the conventional rotor flux-MRAS. Various schemes are implemented and tested in real time using a 7.5 kW induction machine and a dSPACE DS1103 controller board. The results presented for these new schemes show the great improvement in the performance of the MRAS observer in both open loop and sensorless modes of operation at low and zero speed.

ACKNOWLEDGMENTS

I would like to express my thanks to everyone that makes the development of this work possible. Sincere gratitude goes out to my supervisors: Dr Damian Giaouris and Prof John Finch for their continuous support, guidance and encouragement throughout the research. I would like also to thank them not only for the professional supervision but also for their genuine friendship.

I am also grateful to all my friends and colleagues in the Power Electronics, Drives and Machines research group at Newcastle University for their friendly discussions. Very special thanks go out to Mr Andrew Smith for his appreciated assistance during the development of the experimental stage of this work.

I would like also to gratefully acknowledge The Ministry of Higher Education, Arab Republic of Egypt for the financial support of this research project.

I wish to express my deepest appreciation to my family, my father and my mother, for their continuous support they provided me through my entire life.

Finally I would like to thank God that gives me the power and the patience to complete this work.

TABLE OF CONTENTS

PRINCIPAL NOMENCLATURE

B	Friction coefficient
$\bar{i}_r$	Space phasor of the rotor current
i_{ra}, i_{rb}, i_{rc}	Rotor currents in rotor phases
$i_{r\alpha}, i_{r\beta}$	Components of the rotor current vector in the rotor reference frame
$\bar{i}_s$	Space phasor of the stator current
i_{sA}, i_{sB}, i_{sC}	Stator currents in stator phases
i_{sD}, i_{sQ}	Components of the stator current vector in the stator reference frame
i_{sd}, i_{sq}	Components of the stator current vector in the synchronous reference frame
J	Rotor inertia
K_T	Torque constant
L_m	Mutual inductance
L_s, L_{ls}	Stator self and leakage inductances
L_r, L_{lr}	Rotor self and leakage inductances
p	Differential operator
P	Number of pole pairs
R_s, R_r	Stator and rotor resistances
t	Time
T	Sampling time
T_e	Electromagnetic torque
T_l	Load torque
T_r	Rotor time constant
$\bar{v}_r$	Space phasor of the rotor voltage

v_{ra}, v_{rb}, v_{rc}	Rotor voltages in rotor phases
$\bar{v}_s$	Space phasor of the stator voltage
v_{sA}, v_{sB}, v_{sC}	Stator voltages in stator phases
v_{sD}, v_{sQ}	Components of the stator voltage vector in the stator reference frame
v_{sd}, v_{sq}	Components of the stator voltage vector in the synchronous reference frame
x, y	Axes of the general reference frame
α	Momentum constant
ε_ω	Speed tuning signal
θ_e	Rotor flux angle
θ_r	Rotor angle
θ_{sl}	Slip angle
η	Learning rate
σ	Leakage coefficient
$\bar{\psi}_r$	Space phasor of the rotor flux linkage
$\psi_{ra}, \psi_{rb}, \psi_{rc}$	Rotor flux linkages in rotor phases
ψ_{rd}, ψ_{rq}	Components of the rotor flux linkage vector
$\bar{\psi}_s$	Space phasor of the stator flux linkage
$\psi_{sA}, \psi_{sB}, \psi_{sC}$	Stator flux linkages in stator phases
ψ_{sD}, ψ_{sQ}	Components of the stator flux linkage vector in the stator reference frame
ω_e	Angular synchronous speed
ω_r	Angular rotor speed
ω_{rm}	Mechanical angular rotor speed
ω_{sl}	Angular slip speed

Superscripts

*	Command
^	Estimated quantity

$\Im$	Complex conjugate
e	Excitation frame
g	General reference frame
r	Rotor reference frame
s	Stator reference frame

List of Acronyms

AC	Alternating Current
ADC	Analogue to Digital Converter
AI	Artificial Intelligence
CM	Current Model
DAC	Digital to Analogue Converter
DC	Direct Current
DSP	Digital Signal Processor
DTC	Direct Torque Control
EKF	Extended Kalman Filter
ELO	Extended Luenberger Observer
EMF	Electro-motive Force
FL	Fuzzy Logic
FLC	Fuzzy Logic Control
GA	Genetic Algorithm
HPF	High Pass Filter
IM	Induction Motor
LPF	Low-Pass Filters
MMF	Magneto-motive Force
MRAC	Model Reference Adaptive Control
MRAS	Model Reference Adaptive Systems
MSE	Mean-Squared Error
NN	Neural Network
OLS	Ordinary Least-Squares
PCLPF	Programmable Cascaded Low Pass Filter

PI	Proportional-Integral
PMSM	Permanent Magnet Synchronous Motor
PWM	Pulse Width Modulation
RFO	Rotor Flux Oriented
RTI	Real Time Interface
RTW	Real Time Workshop
SA	Simulated Annealing
SM	Sliding Mode
SMC	Sliding Mode Control
SVM	Space Vector Modulation
UKF	Unscented Kalman Filter
V/f	Volts/Hertz
VM	Voltage Model
VSC	Variable Structure Control
WNN	Wavelet Neural Network

CHAPTER 1

INTRODUCTION AND SCOPE OF THE THESIS

1.1 Introduction

Recently, controlled AC drives have been extensively employed in various high performance industrial applications. This has been conventionally achieved by using DC drives with their simple control structure. AC machines are generally inexpensive, compact and robust with low maintenance requirements compared to DC machines but require complex control [1, 2]. However, recent advances in power electronics, control techniques and signal processing have led to significant developments in AC drives. Induction Motors (IMs) and Permanent Magnet Synchronous Motors (PMSMs) are increasingly replacing traditional DC motors in a wide range of applications where a fast dynamic response is required. The majority of the AC drives used in industry are those employing squirrel-cage IMs. This motor is characterised by a simple and rugged structure, low cost, high efficiency and high reliability [2].

Variable speed IM drives can be generally classified into low performance and high performance controlled drives. Scalar control is used for low performance drives where only the magnitude and frequency of the stator voltage or current is regulated. The most common scalar control technique is the constant Volts/Hertz (V/f) control in which the magnitude of the stator voltage is adjusted in proportion to the demand stator frequency

in order to keep the stator flux constant [3]. The basic idea of this method is to control the speed of the rotating magnetic field by changing the supply frequency.

V/f IM drives offer moderate dynamic performance and are therefore used in applications where high speed precision is not required such as fans, pumps and simple elevators [4]. When high performance dynamic operation is required, these control techniques become unsatisfactory.

High performance IM drives can be implemented either by vector control or Direct Torque Control (DTC) strategies [2]. In these types of control, the instantaneous values of the motor torque and the magnetic field are regulated in the steady state and in transient operating conditions. The proper application of these control techniques allows the IM to achieve similar dynamic performance to that of a separately excited DC motor. The rapid evolution of high speed power electronic converters, digital signal processors and inexpensive, powerful microcontrollers allow the spread of these control strategies in many industrial applications. The block diagram of a closed loop IM drive is shown in Fig. 1.1.

One of the more recent developments in the control of IM drives is the elimination of the speed sensor mounted on the motor shaft. This technology is usually referred to as "sensorless control" where the motor speed is estimated rather than measured. However, the drive will still usually need current and perhaps voltage sensors to achieve the control task [2].

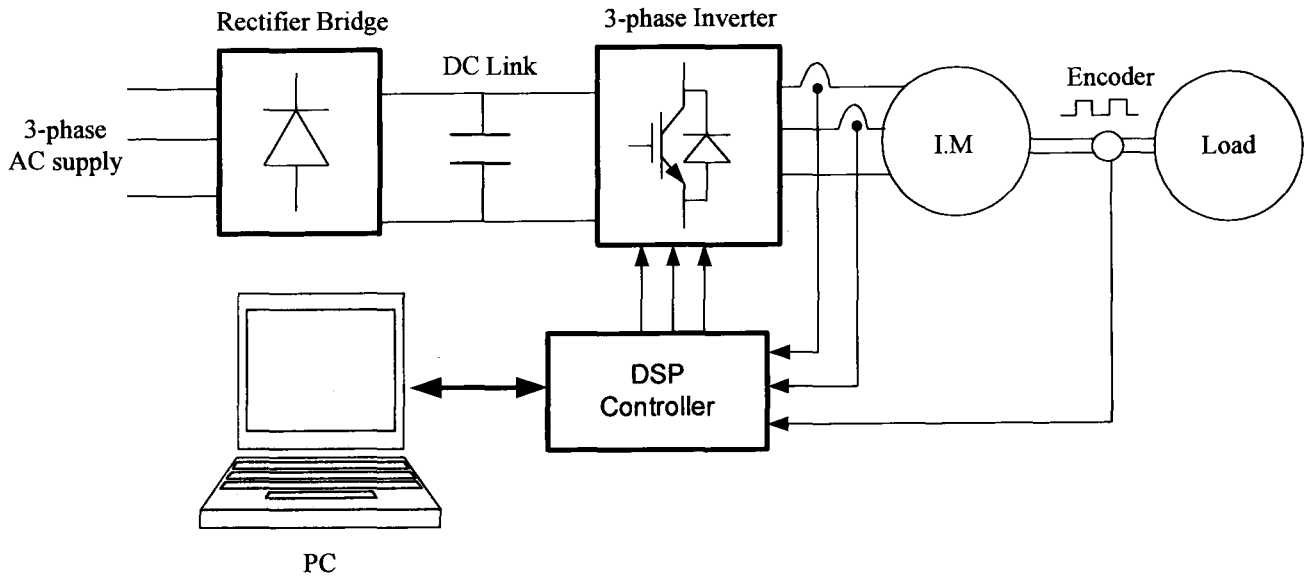

Fig. 1.1 Block diagram of a closed loop induction motor drive

1.2 Sensorless Control of Induction Motor Drives

Sensorless vector controlled IM drives are being vigorously developed for high performance industrial drive systems. Such control reduces the drive's cost, size and maintenance requirements while increasing the system's reliability, robustness and noise immunity [1, 3]. Moreover, using a speed sensor in a hostile environment is not practical. Parameter sensitivity, high computational effort and instability at low and zero speed can be the main shortcomings of sensorless control [5].

Sensorless drives have been successfully applied in medium and high speed regions, but low and zero speed operation is still a critical problem specially for sensorless IM drives [1]. In fact, some applications such as cranes, traction drives and presses are required to maintain the desired torque down to zero speed [6]. Much recent research effort is focused on extending the operating region of sensorless drives near zero stator frequency [5, 7].

Several strategies have been proposed for rotor speed estimation in sensorless IM drives [1, 2]. In general, these methods fall into two main categories: fundamental excitation and spectral analysis techniques [1, 8]. A broad classification of methodologies applied to speed sensorless AC drives is shown in Fig. 1.2. The two main techniques used for sensorless control are described in the following sections.

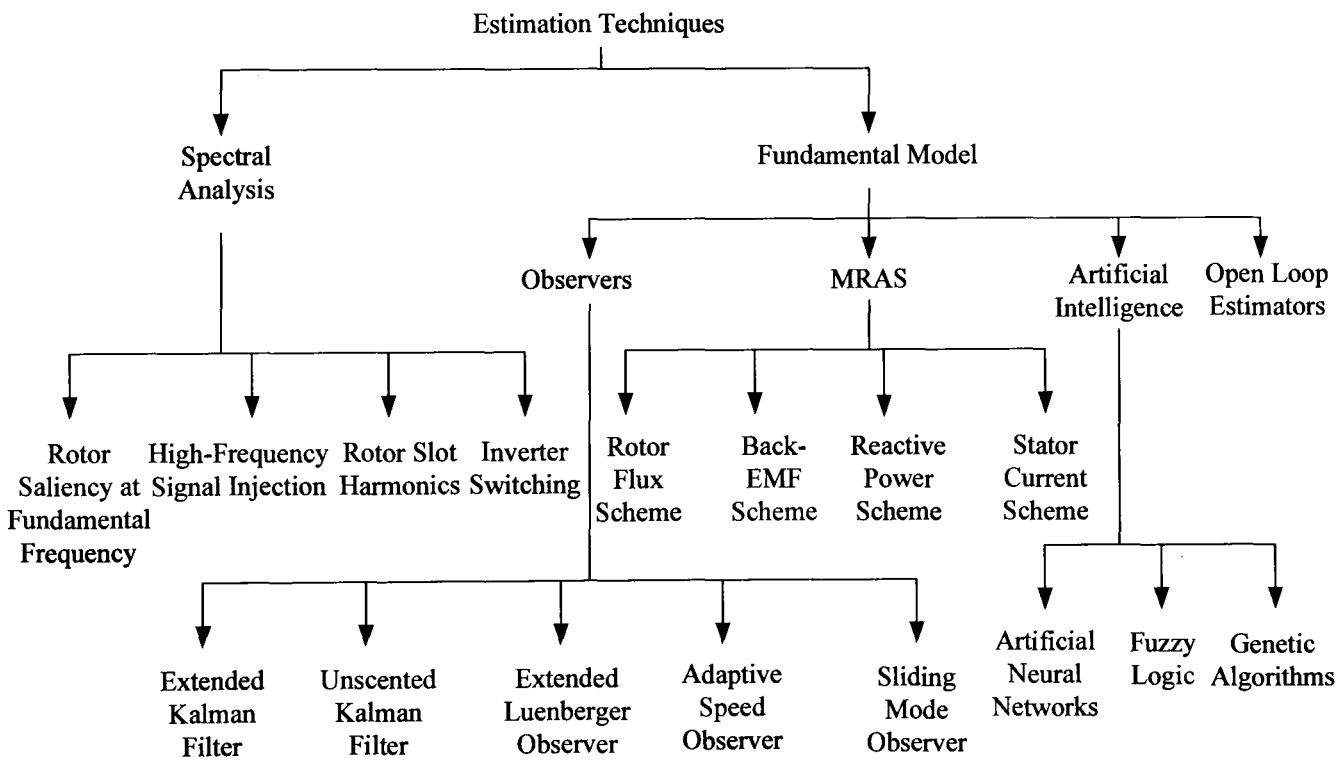

Fig. 1.2 Classification of speed estimation techniques for sensorless control

1.2.1 Spectral Analysis Strategies

These algorithms benefit from a rotor position-dependence feature present in many AC motors to extract the rotor speed or position information. The estimation strategy is based on saliency introduced by special geometrical effects which are naturally present in PMSM [1]. However, this technique can be inappropriate for machines with cylindrical rotor design such as IM. Therefore non model-based strategies for sensorless IM drives can use other specific effects such as slot harmonics, magnetic saturation and transients caused by inverter switching to exploit the machine anisotropic properties [1, 9]. Magnetic saturation in IM can be introduced by injecting a high frequency signal into the machine stator windings [1, 3].

Using these techniques shows low parameter dependency with an improved low and zero speed performance if signal injection techniques are used [3]. However, rotor saliency- based schemes with fundamental excitation is machine specific and may not be suitable for standard machines because it requires special rotor design [1]. High-frequency signal injection techniques are highly complicated and their design is not general since it needs to match the properties of the specific machine drive [9]. Furthermore, these methods may introduce audible noise and torque ripple to the motor [8]. Therefore the focus of this research is on model-based techniques that can be applied to any type of machine [1].

1.2.2 Fundamental Model-Based Strategies

These strategies make use of the instantaneous values of stator voltages and currents to estimate flux linkage and motor speed from the machine fundamental model. These methods usually utilize a *d-q* model to describe the machine equations by assuming sinusoidal flux distribution and neglecting space harmonics [1]. These schemes usually work well above 2% of the base speed [1]. A block diagram of a model-based sensorless AC drive is shown in Fig. 1.3.

The main problems associated with the low speed operation of model-based sensorless drives are related to machine parameter sensitivity, stator voltage and current acquisition, inverter nonlinearity and flux pure integration problems [1, 5]. Since all model-based estimation techniques rely on rotor induced voltages, which are very small

and even vanish at zero stator frequency, these techniques usually fail at or around zero speed due to lost observability [1, 5, 9].

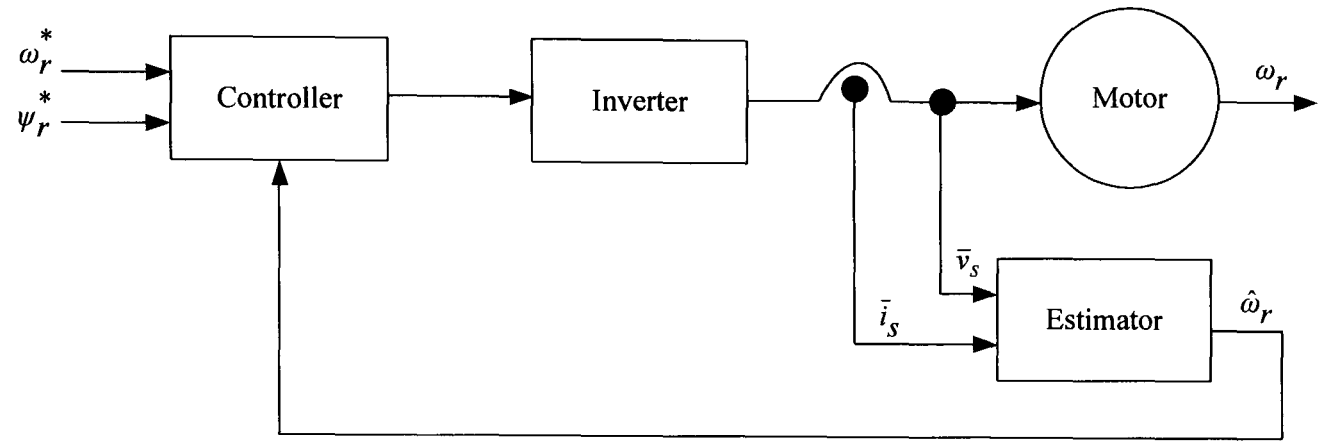

Fig. 1.3 Block diagram of a model based sensorless AC drive

Fundamental model-based estimation strategies can be generally grouped into open loop estimators, observer-based schemes, Model Reference Adaptive Systems (MRAS) and Artificial Intelligence (AI) based methods. MRAS observers are well-established sensorless techniques that have attracted much attention due to their simplicity and direct physical interpretation. However, improving the performance of these schemes at very low speed remains challenging.

Recently various AI-based techniques have been successfully applied to electric drives. In general increased robustness against parameter variations and improved performance are expected when these methods are employed [10], which encourages the application of these techniques to improve sensorless control.

1.3 Artificial Intelligence for Electric Drives

AI techniques have gained much interest over the past few years. These strategies consist of expert systems, artificial Neural Networks (NNs), Fuzzy Logic (FL), fuzzy-neural networks and Genetic Algorithms (GAs) [10, 11]. The main idea of AI is to mimic natural human intelligence in the form of a computer program to tackle problems that are hard to solve by traditional methods. While expert systems and FL are rule-based techniques emulating the behaviour of human experience, NNs directly mimic the human brain with capability of generalization and learning [11]. The GA is a stochastic search technique that mimics the mechanism of natural selection. GA is considered as an

evolutionary computing technique, which is a rapidly emerging area of AI. It has been recognized as an effective and powerful technique to solve optimization and search problems.

Compared to classical control strategies, AI techniques eliminate the need for mathematical models which are often complicated and rely on several assumptions with some parameters that may be difficult to measure [10]. Therefore, more robustness with respect to parameter variation is expected when using such schemes [10]. Moreover, due to their adaptive capabilities these techniques may lead to improved performance when combined with conventional methods. Several books have been published in the area of AI applications in power systems and electric drives [10, 12-14]. Various AI-based schemes used for control applications have been studied by the author and presented previously [15, 16]. A detailed comparison of different AI applications in the control of IM drives from this present work has been recently published by the author [17]. Broadly, AI techniques have found widespread applications in the field of variable speed drives in the following areas [10, 18]:

- Replacement of conventional speed, position and current controllers [19-22]
- Tuning of conventional PI controllers [15, 23]
- Improving the performance of conventional controllers [16, 24, 25]
- Parameter and state estimation of DC and AC machines [10, 18, 26-30]
- Fault detection and condition monitoring [31]
- Efficiency optimization for AC drives [32]
- Machine design optimization [33, 34]

1.4 Scope and Novelty of the Thesis

The research reported in this thesis investigates the operation of speed sensorless vector controlled IM drive using MRAS speed observer. Particular attention is given to the low and zero speed regions of operation where the performance of the conventional observer usually deteriorates. An experimental evaluation of the performance of the conventional rotor flux-based MRAS scheme at very low and zero speed has been presented by the author in [35]. Despite considerable research effort, it is still problematic for MRAS-based sensorless schemes to provide a satisfactory response in this region of operation. Therefore the main intent of this work is to develop new hybrid

AI-MRAS schemes that are capable of achieving better performance at and around zero stator frequency. The main motivation is to exploit the effectiveness of AI techniques to overcome the problems associated with the classical methods. This research presents entirely new applications of AI in MRAS-based speed sensorless IM drives.

Conventionally, a simple fixed gain linear PI controller is employed to generate the estimated rotor speed in rotor flux-MRAS. Not much interest has been devoted to considering other types of adaptation mechanisms to minimize the speed tuning signal. An attempt to fill in this research gap is described by proposing alternative adaptation schemes using FL and Sliding Mode (SM) strategies. Results of such schemes have been published by the author [36]. To solve the problems of rotor flux-MRAS, a novel scheme is proposed employing a NN rotor flux observer which serves as a reference model for the MRAS observer. Promising results at low stator frequency are obtained from this scheme and have also been published by the author [37, 38]. Finally, another new approach to produce improved low speed performance is presented using a NN-based stator current-MRAS observer considering different rotor flux estimators. Operations at low speed and at regeneration have been studied and the test results have again been reported [39].

Various novel methods based on AI are implemented and their superiority at zero and low speed regions is proven through numerous and rigorous tests. All the proposed schemes have been simulated and experimentally validated based on 7.5 kW IM and a dSPACE DS1103 controller board.

1.5 Publications

The results of the research presented in this thesis are principally based on number of published/submitted articles to international conferences and journals. A list of these publications is given below:

- S. M. Gadoue, D. Giaouris, and J. W. Finch, "Sensorless Control of Induction Motor Drives at Very Low and Zero Speed Using Neural Network Flux Observers," *IEEE Transactions on Industrial Electronics*, Submitted.

- S. M. Gadoue, D. Giaouris, and J. W. Finch, "Artificial intelligence-based speed control of DTC induction motor drives—A comparative study," *Electric Power Systems Research*, vol. 79, no. 1, pp. 210-219, January 2009.

- S. M. Gadoue, D. Giaouris, and J. W. Finch, "Performance Evaluation of a Sensorless Induction Motor Drive at Very Low and Zero Speed Using a MRAS Speed Observer," in *Proc. The third IEEE International Conference on Industrial and Information Systems, (ICIIS),* India, 2008.

- S. M. Gadoue, D. Giaouris, and J. W. Finch, "A Neural Network Based Stator Current MRAS Observer for Speed Sensorless Induction Motor Drives," in *Proc. IEEE International Symposium on Industrial Electronics, (ISIE),* Cambridge, UK, 2008, pp. 650-655.

- S. M. Gadoue, D. Giaouris, and J. W. Finch, "A new fuzzy logic based adaptation mechanism for MRAS sensorless vector control induction motor drives," in *Proc. 4th IET Conference on Power Electronics, Machines and Drives, (PEMD)*, York, UK, 2008, pp. 179-183.

- S. M. Gadoue, D. Giaouris, and J. W. Finch, "Genetic Algorithm Optimized PI and Fuzzy Sliding Mode Speed Control for DTC Drives," in *Proc. World Congress on Engineering, (WCE)*, London, UK, 2007, pp. 475-480.

- S. M. Gadoue, D. Giaouris, and J. W. Finch, "Low speed operation improvement of MRAS sensorless vector control induction motor drive using neural network flux observers," in *Proc. 32nd Annual Conference on IEEE Industrial Electronics, (IECON)*, Paris, France, 2006, pp. 1212-1217.

- S. M. Gadoue, D. Giaouris, and J. W. Finch, "Tuning of PI speed controller in DTC of induction motor based on genetic algorithms and fuzzy logic schemes," in *Proc. 5th International Conference on Technology and Automation, (ICTA),* Thessaloniki, Greece, 2005, pp. 85-90.

1.6 Layout of the Thesis

The main body of the thesis is organized into eight chapters. In chapter one an introduction to speed sensorless IM drives is given and different AI applications in electric drives are highlighted. Chapter two provides a literature review on speed observers employed for sensorless control. More emphasis is given to applications of MRAS speed estimators and AI-based strategies. Chapter three covers induction machine modelling, vector control strategy and speed estimation using the conventional rotor flux-MRAS. In chapter four, a detailed description of the experimental setup used in the project is given. Chapter five describes two novel adaptation mechanisms for rotor flux-based MRAS observer based on FL and SM strategies. The two methods are compared to the conventional PI controller and all schemes are validated through simulation and experimental tests. Chapter six presents a new rotor flux-based MRAS scheme using NN flux observer. A brief introduction to NN is given followed by a detailed description of its application for rotor flux estimation compared to conventional observers. The capability of the proposed scheme to produce an improved performance is illustrated and verified through a detailed experimental comparison with the classical MRAS observer. Chapter seven describes a new approach for speed estimation based on a stator current-MRAS scheme. The stator current observer equations are derived and represented by a linear NN. Various rotor flux observers required for the stator current estimation are tested and compared based on simulations and experimental tests. Chapter eight gives conclusions and suggestions for future work.

CHAPTER 2

MODEL REFERENCE ADAPTIVE SYSTEMS AND ARTIFICIAL INTELLIGENCE FOR SENSORLESS CONTROL-A LITERATURE REVIEW

2.1 Introduction

Sensorless control techniques for IM drives have been widely investigated over the last two decades. The great advantages offered by sensorless control including compactness and robustness make it attractive for many industrial applications specially those operating in hostile environments. Among several strategies proposed for sensorless IM drives, MRAS are the most popular schemes employed due to their simple implementation and smaller computational effort. However, these schemes usually fail to provide a satisfactory response at low stator frequency. Much research interest has been devoted to improve the performance of MRAS-based sensorless schemes in this region of operation.

In recent years, AI techniques, particularly artificial NNs, have received much attention as potential tools to solve system identification problems. In addition, these techniques can be combined with conventional strategies to obtain an improved

performance. As a result, various AI-based schemes have been introduced for sensorless control applications.

This chapter provides a comprehensive review of different model-based strategies employed for sensorless control of IM drives with particular focus given to MRAS and AI techniques. Problems affecting low speed operation of MRAS schemes are discussed and different methods employed in the literature to tackle these problems are illustrated.

2.2 Model-Based Sensorless Strategies

Many different methodologies have been developed for rotor speed estimation of IM using the machine fundamental model. In these strategies, monitored stator voltages and currents are used to extract the rotor speed information from the machine equations. Speed estimators can be implemented either in open loop or closed loop [2, 9]. The difference between the two types is the absence of a correction term in the open loop estimator [2].

Open-loop estimators are based directly on the machine dynamic model and do not employ any forms of feedback. Pure integration problems and voltage measurement noise represent two main deficiencies that can affect the estimation accuracy of these schemes especially at low speed [40]. In addition, open loop estimators are generally sensitive to parameter variations which significantly affects their performance in both transient and steady state [2, 9]. By contrast closed loop estimators, usually referred to as observers [2], use an error signal between measured and estimated quantities to adjust their response [1, 2]. This can lead to considerably improved dynamics and enhanced robustness [9].

According to the plant's form of representation, observers can be classified into deterministic and stochastic. Luenberger and Kalman observers are the most commonly employed non-linear estimators. While the extended Luenberger observer (ELO) can be applied to nonlinear, time–varying deterministic system, the extended Kalman filter (EKF) is applied to nonlinear, time-varying stochastic systems [2]. Adaptive observers have been also proposed for flux and speed estimation [41]. In both ELO and EKF observers, the rotor speed is treated as a state variable which differs from the full-order adaptive state observer where the speed is considered as a parameter [2]. The advantage of ELO and EKF is that they can combine parameter and state estimation [42].

The EKF has been extensively applied to rotor speed estimation of sensorless IM drives [43-46]. The algorithm is based on a mathematical model representing the machine dynamics taking into account plant and measurement noise. The EKF has the advantages of considering modelling errors and inaccuracy as well as measurement errors in addition to accurate speed estimation over a wide speed range but not at zero-speed [2]. The problems associated with the EKF are the intensive computational effort, the lack of design and tuning criteria, the instability due to linearization and the dependency on the machine model accuracy [1, 47]. Moreover, biasing problem may take place due to the mismatch between assumed stochastic noise characteristics and real noise in addition to improper adjustment of covariance matrices [1, 2, 47]. Noise covariance matrices are usually tuned experimentally by a trial and error method which may not lead to an optimal performance. As a result optimization of the EKF has been the subject of recent researches to obtain the best performance of the filter [45, 46]. Shi *et al.* [45] proposed a GA to optimize the noise covariance and weight matrices of the EKF to ensure accurate speed estimation. Recent research proposed the Simulated Annealing (SA) algorithm for EKF optimization [46].

Akin *et al.* [47] proposed another form of Kalman filter: The unscented Kalman filter (UKF) which eliminates derivation and Jacobian matrices calculation while avoiding linearization [47]. However low speed tests, where measurement noise dominates, were not reported [1].

The ELO has been applied for joint rotor flux and rotor speed estimation for deterministic systems where noise is not taken into account [42]. Compared to EKF, its design is relatively flexible with less computational effort and it has the capability of producing unbiased estimates [2]. However, the ELO has weak observability characteristics for joint rotor flux and speed estimation in the low and zero speed region of operation [2]. Therefore other types of deterministic observers, such as those based on SM, have been developed.

Sliding Mode Control (SMC) is known for its capability to cope with bounded disturbance as well as model imprecision. It is also said to be insensitive to parameter variations and external disturbances and can provide fast dynamic response [8, 24, 48] which make it ideal for the robust nonlinear control of IM drives [49]. Mathematical basics, design procedures and applications of SMC in electric drives have been described

in details by Utkin [49]. SM observers have been proposed to solve the problem of speed estimation in IM drives [8, 24, 48, 50]. Reported tests include ±100 rpm, ±1500rpm (±5% and ±100% of rated speed) trapezoid speed command and ±900 rpm speed reversal [8]. Furthermore, a SM flux observer has been also employed as an adaptive model with MRAS [51]. Acceleration from 100-350 rpm and deceleration from 350-100 rpm were used to test the proposed scheme but no zero speed tests were shown.

Owing to their inherent simplicity and effectiveness, MRAS schemes [7, 28, 51-54] have received great attention for sensorless control applications [1, 7, 55]. Armstrong *et al.* [56] provided a detailed comparison between rotor flux-based MRAS and EKF speed observers. Less computational complexity was shown for MRAS with a ratio of 1:20 compared to the EKF [1]. For that reason particular interest has been shown in the literature to the study of these schemes when applied to sensorless IM drives.

2.3 MRAS for Sensorless Control

Adaptive control may be defined as a control system that "*can modify its behaviour in response to changes in the dynamics of the process and the character of the disturbances*" [57]. Adaptive control can be realized by different strategies such as: gain scheduling, model reference adaptive control, self-tuning regulators and dual control [57]. Model Reference Adaptive Control (MRAC) is one of the most attractive adaptive control techniques used for motor control and state estimation applications. A block diagram of the MRAC system is shown in Fig. 2.1.

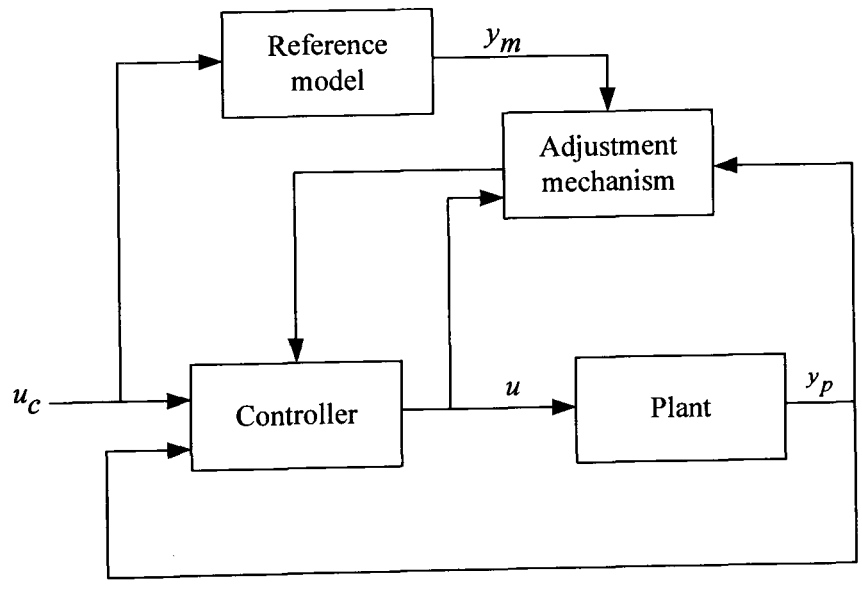

Fig.2.1 Block diagram of MRAC

Originally, MRAC was proposed to solve control problems where the desired performance specifications are given by a reference model that provides the ideal response of the plant to a given command. The error between the reference model output y_m and plant output y_p is driven to zero by a proper alteration mechanism that adjusts the controller parameters. Based on the same mechanism the MRAC approach can be also applied to parameter and state estimation.

MRAS schemes have been commonly employed for sensorless control applications. Depending on the output states that form the error function various MRAS observers have been introduced in the literature based on rotor flux, back EMF and reactive power [2, 53, 54]. Rotor flux MRAS, principally developed by Schauder [53], is the most established MRAS strategy and much effort has aimed at improving its performance. This scheme suffers from machine parameter sensitivity (specially stator resistance), flux pure integration problems which may cause dc drift and initial condition problems [2], stator voltage and current acquisition problems and inverter nonlinearity [1, 5]. These problems may limit the observer's performance at low and zero speed [54]. Applied to a vector control IM drive, a good performance above 2 Hz stator frequency has been reported by Schauder [1, 9, 53]. Speed reversal through zero could be possible providing fast transient is applied. However operation at zero speed for longer period is not satisfactory due to incorrect flux estimation [2, 3].

To avoid the problems associated with rotor flux schemes, Peng and Fukao [54] proposed a MRAS scheme based on the back EMF vector. This scheme avoids using a pure integration in the reference model and hence has neither drift nor initial conditions problems. However, the reference model is still sensitive to stator resistance variation and may have stability problems at low stator frequency [7]. In addition, it shows low noise immunity due to stator current differentiation and poor dynamic performance at low stator frequency [55].

Another MRAS technique based on instantaneous reactive power has been proposed in [54] offering robustness against stator resistance variation while avoiding pure integration [2]. However, this scheme exhibits an unstable nature at some operating conditions when passing through the regenerating mode [7, 58, 59]. Moreover, back EMF and reactive power quantities vanish at low and zero speed [55].

Wu *et al.* [58] provided a detailed study and comparison between back EMF and reactive power based-MRAS speed observers. In this study a verification of the instability features of reactive power based-MRAS scheme was reported.

As a result a rotor flux-based MRAS observer was found to be the most effective solution compared to other MRAS schemes. This scheme also provides an estimation of the rotor flux angle that can be used for direct field orientation [55]. Different methods reported in the literature to improve rotor flux-MRAS performance are reviewed in the next sections.

2.3.1 Parameter Sensitivity

Since the speed estimation is based on the machine model it is highly sensitive to machine parameter variations. During drive operation motor parameters change continuously due to temperature, frequency and magnetic saturation. Stator and rotor resistances change with temperature and frequency, mutual inductance changes with magnetic saturation and the leakage inductances can change with the operating current.

Temperature variation depends on the machine power losses. The stator and rotor copper losses are affected when the motor is operating with variable load whereas the core loss variation depends on the machine flux level. Development of a thermal model describing the machine thermal behaviour or implementation of a temperature sensor to detect resistance variation is not precise. This is partly due to the existence of fans used for cooling that have nonlinear characteristics between cooling flow rate and machine speed. Furthermore the motor thermal time constant itself changes with speed and is decreased as the speed increases [60].

Stator resistance variation with temperature, which can be up to 50% [1, 9], is a very serious problem at low speed [61]. Since the fundamental component of the stator voltage becomes very low, the stator resistance drop becomes comparable to the applied voltage [3]. Hence continuous adaptation of the stator resistance is required to maintain stable operation at low speed [62]. On the other hand incorrect rotor resistance affects the steady state speed estimation accuracy [60, 61]. The effect of machine parameter variation on the performance of MRAS observer has been studied in many works [56, 61]. Armstrong *et al.* [56] provided a detailed study of the performance of the rotor flux-

based MRAS observer with 20%-200% variations in the machine parameters at 95.5 rpm.

Various schemes have been proposed for combined rotor speed and stator resistance identification using MRAS [7, 59, 62-64]. Zhen and Xu [63] used a mutual MRAS scheme with interchangeable reference and adaptive models. This scheme was used for rotor speed and stator resistance estimation in a position sensorless vector control IM drive. A reference model is defined which does not employ a pure integration, is free from the stator leakage inductance variations but depends on the stator resistance. Speed estimation stops briefly when the reference speed does not change and the estimated speed becomes stable. The two observers then switch their functions for stator resistance estimation to take place based on another adaptation mechanism. To allow accurate rotor speed and stator resistance estimation an online adaptation of the rotor time constant is incorporated. Speed commands of 75 rpm and ±1200rpm have been used to test the proposed scheme. However, the two estimation algorithms are not concurrent and the drive has no speed information during stator resistance identification [64].

To avoid these problems Vasic and Vukosavic [62, 64] introduced a simultaneous estimation of rotor speed and stator resistance based on a parallel MRAS observer. In this scheme conventional Voltage Model (VM) and Current Model (CM) flux observers are used as reference and adaptive models respectively for rotor speed estimation as in [53]. The two observers switch roles for stator resistance identification. Using Popov's hyperstability theory two adaptation mechanisms are deduced for simultaneous estimation of rotor speed and stator resistance. Unlike [63], this scheme does not require a steady state condition to estimate the stator resistance and can be activated during transients. Successful estimation was obtained when the scheme was tested at reference speeds of 0.5, 1 and 4Hz with ±20% detuning in the stator resistance. Additionally, operation at zero speed for a short time was realized with accurate estimation of stator resistance. It was also shown that incorrect rotor time constant has a negligible effect on stator resistance identification but significantly affects rotor speed estimation.

Another approach was employed in [59] for rotor speed and stator resistance estimation applied to vector control IM drive. In this scheme, the q-axis rotor flux in the synchronous reference frame is used as a tuning signal for rotor speed estimation. A simple PI controller is used to drive the q-axis rotor flux component to zero in order to

obtain the rotor speed. Another adaptation algorithm for stator resistance identification is defined based on the *d*-axis rotor flux error between CM and VM. The scheme is tested at speed commands of 20 rpm, 50 rpm and ±1200rpm speed reversal. Further tests are shown for reference speed changes from 8-80 rpm and then back to 8 rpm at 50% rated load with 30% detuning in the rotor time constant. This detuning may cause steady state error in the estimated speed but was claimed to keep the system stability unaffected.

Rashed and Stronach [7] proposed a new stable MRAS rotor speed and stator resistance estimator. The adaptation algorithm for the rotor speed estimation is the sum of cross product modulus and dot product of estimated rotor flux and error in estimated back EMF vectors. Another adaptation algorithm for stator resistance identification is derived based on the error in the air gap active power. Estimator gains are designed based on Routh-Hurwitz criteria to ensure stability at different operating modes including low speed. A frequency injection technique is applied to observe the motor speed at zero speed operation. To examine the sensorless drive performance in the regenerating mode, the scheme was tested with ±5 rad/s and 3 to -2 rad/s speed reversals at 50% rated load. It was shown that rotor speed exhibits some oscillations but the drive is stable. Another ±20 rad/s speed reversal test at no load was performed showing satisfactory steady state performance but not during transients.

2.3.2 Pure Integration Problems

Pure integration for flux represents a crucial difficulty that may cause dc drift and initial condition problems [2, 5, 65]. Low-Pass Filters (LPFs) with low cut-off frequency, typically 1-3 Hz [1, 3], have been proposed to replace the pure integrator [3, 6, 28]. However, a LPF behaves like an integrator only at frequencies higher than the filter cut-off frequency as shown in Fig. 2.2 [1, 3]. Therefore, using a LPF introduces phase and gain errors and delays the estimated speed relative to the actual, which may affect the dynamic performance of the drive [51, 66]. In addition this may lead to inaccurate speed estimation below the filter cut-off frequency [2, 3].

To overcome this problem Karanayil *et al.* [66] introduced a Programmable Cascaded LPF (PCLPF) to replace the pure integration by small time constant cascaded filters to attenuate the dc offset decay time. In [67] another technique is used where the rotor flux is estimated by defining a modified integrator having the same frequency response as the

pure integrator at steady state. Gao *et al.* [68] proposed a nonlinear feedback integrator for drift and dc offset compensation used for VM flux observer. This modified VM is incorporated into a rotor flux-based MRAS structure as in [53] and the proposed scheme is tested when applied to a vector control IM drive. Tests at 5 rpm and 900 rpm at no-load and 50% load have been carried out to examine the proposed scheme at open loop. Extensive testing has been performed for the sensorless mode of operation including speed transient from 9rpm to 900 rpm at no-load and 25% load, ±6rpm and ±9rpm speed reversal at 10% and 85% load respectively. Disturbance rejection performance for 80% and 75% load at 9rpm and -9rpm respectively was also investigated. The scheme shows satisfactory performance down to around 0.2 Hz including regeneration but becomes unstable below this frequency. It was claimed that the estimated speed contains a steady state error of about 5 rpm which can be improved by incorporating an online stator resistance identification scheme.

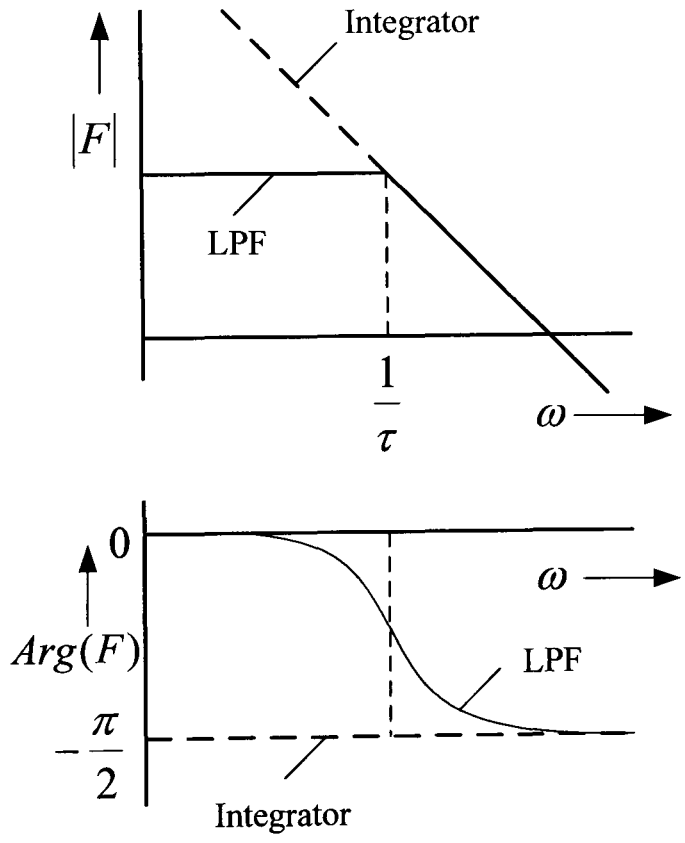

Fig. 2.2 Bode diagram for approximation of ideal integration by a LPF

Further research [65, 69] has tried to entirely replace the VM by other flux observers which may reduce the scheme's simplicity. Both schemes employed the same MRAS structure as in [53] based on PI minimization of the cross product of flux estimates. In

[65] a state observer with current error feedback is used to generate the reference values for the rotor flux in a MRAS observer. Experimental tests have been conducted at 1000, 50 and 25 rpm at no-load, ±200rpm speed reversal and load torque application with 50% mismatch in the rotor resistance. Better performance was obtained using the new scheme compared to the conventional MRAS. Lascu *et al.* used a similar approach in [69] for classical DTC and space vector modulation (SVM) DTC. In this modified MRAS scheme, the reference model employs a full-order stator and rotor flux observer containing both VM and CM with an adaptive model based on the CM. Hence the speed observer employs the CM twice: in the reference model (expressed in the rotor flux oriented reference frame) and in the adaptive model (expressed in the stator reference frame). The limit of this scheme was claimed to be 30 rpm. However, measured speed is not shown for this test and no zero speed tests were reported for this scheme [52].

Another modification to the classical MRAS presented in [53] was applied in [55] using a closed loop flux observer (MRAS-CLFO) that employed a coupling controller between the two flux estimates, VM and CM. Using the closed-loop topology provides the VM open loop integration with the necessary feedback and hence no LPF is required in the VM [52]. However, as frequency approaches zero the cross product between flux estimates also approaches zero and the speed estimation is lost. Therefore, a machine mechanical model was used to compensate for this effect but this may increase the observer's complexity and requires accurate values for the mechanical parameters.

2.3.3 Stator Voltage Acquisition and Inverter Nonlinearity

Stator voltage measurement comes up due to sensorless control. The stator voltage signal is crucial for model based strategies. The most accurate stator voltage acquisition is that measured across the machine terminals. However, this cannot be used easily since it requires a very high sampling rate [5]. Low pass filtering the PWM voltage waveform may solve the problem at medium and high speed but not at low speed, where the effects of filter gain and phase error cause the performance to deteriorate. Another nonlinear filtering method known as the synchronous integrator technique can aid a solution [70]. This technique is based on integrating the PWM voltage signal and resetting at the end of the PWM period. This provides the actual volts-seconds applied to the machine terminals over the PWM period. Using this technique should give better measurement including all

inverter nonlinearities [70]. However it is not desirable to employ voltage sensors for industrial applications [8]. Another possible alternative is to use the reference voltages, available in the control unit, since they are harmonic free. However, at low speed these reference voltages deviate substantially from the actual machine voltages due to inverter nonlinearities and dead time effects. Therefore, Holtz and Quan [71] have modelled the inverter nonlinearities including voltage drops across the switches and the threshold voltage. As a consequence, better acquisition of the stator voltage is obtained from the reference voltage of the PWM inverter at very low speed.

2.4 Artificial Intelligence for Sensorless Control

In recent years, AI techniques have been advocated for different electric drives applications. In the next sections different applications of AI in sensorless control of IM are highlighted. Emphasis is given to the most commonly employed AI strategies, NN and FL techniques.

2.4.1 Applications of Artificial Neural Networks

Artificial NNs have been recognized as a potential solution for many real world problems. Compared to conventional programming, they have the capability of solving problems that do not have algorithmic solution. Therefore they are found to be suitable to tackle problems that suit human reasoning, such as pattern recognition. NNs have been introduced to solve many problems related to prediction, classification, control and identification. A latest comprehensive review of NN applications in the field of power electronics and motor drives is covered in [11]. One of the major advantages of NNs is their ability to learn from experience to improve their performance and to adapt to changes in the environment [10]. In addition they show good capability in dealing with incomplete information or noisy data. NNs are frequently used as universal function approximators to represent these functions with weighted sums of nonlinear terms. This is useful when representing some systems which do not have an accurate mathematical model [10]. In the last few years, NNs have found widespread applications in sensorless control of IM drives.

NN assisted MRAS schemes are discussed in the literature [2, 28, 52, 72]. Its basic idea is to replace the adaptive model of the classical MRAS by an online trained NN as a

state estimator. This strategy avoids using a mathematical adaptive model and the adaptation mechanism is integrated into the network tuning law [2]. However, since these proposed schemes have similar structure to that proposed by Schauder in [53], they would be affected by machine parameter variation and pure integration problems.

Ben-Brahim *et al.* [28, 73] proposed a two-layer linear NN to represent the conventional adaptive CM using a simple forward Euler integration method. In this representation the rotor speed is proportional to one of the NN weights. The reference model is the conventional VM but the pure integrator is replaced by a LPF with a low cut-off frequency. The rotor flux is estimated based on the two models and the error between the two estimates is used for online tuning of the network weights using a backpropagation algorithm. Hence the rotor speed information can be obtained. The NN adaptive model is working in the simulation mode where the delayed estimated flux components from the adaptive model are fed-back to the NN. The proposed observer's performance is verified experimentally without mentioning its low and zero-speed behaviour, no information about the lowest speed limit was given [52].

In [74] a EKF is proposed to adjust the NN weights of the scheme described in [28]. This has the advantage of using a variable learning rate which is constant in the backpropagation algorithm, leading to fast convergence. A ±500rpm speed reversal test at no-load is shown for the proposed scheme. However, the EKF algorithm requires higher computational burden compared to backpropagation.

An evolution to the scheme proposed in [28] has been presented in [52, 72] where an Adaptive linear NN (ADALINE) is employed in the adaptive model using a modified Euler integration to represent the CM. The neural network adaptive model is employed in the prediction mode and not in the simulation mode as in [28, 73]. In the prediction mode the delayed estimated flux components from the reference model, not the adaptive model, are fed-back to the NN. The same reference model described in [28, 73] has been employed. The training of the NN is performed online using Ordinary Least-Squares (OLS) algorithm. Since the problem to be solved is linear, Cirrincione and Pucci [52] claimed that using this linear least-square algorithm is more suitable to estimate the rotor speed compared to the backpropagation algorithm used in [28]. Using the OLS algorithm avoids problems of backpropagation such as initialization, convergence and local minimal problems. Therefore the new speed observer scheme is characterized by fast

convergence and low speed estimation error in both transient and steady-state. Furthermore it showed better performance in low and zero speed operation compared to the backpropagation scheme described in [28]. The proposed scheme is tested with ±50 rad/s and ±10 rad/s speed reversals and the lowest speed shown was 5 rad/s. Zero speed no-load test for 60 s time interval shows a more stable response than [28].

Kim et al [75] proposed another NN-based speed observer where the speed is an output quantity and not integrated into the NN weights as in [28, 52]. In this approach a conventional rotor flux-based MRAS scheme with voltage reference model and current adaptive model is used to estimate the rotor flux. The error between the two estimates is used to adjust the weights of a three-layer NN speed observer using an online backpropagation algorithm. The proposed neural observer is partially recurrent and consists of three inputs: the reference flux magnitude, the estimated flux magnitude and a delay term of the observed rotor speed. The hidden layer consists of five neurons with sigmoid activation functions and the single neuron output layer generates the estimated value of the rotor speed. The scheme is verified experimentally and has shown satisfactory performance at low-speed operation with a step speed command of 10 rpm. Further tests at 1000 rpm, ±500 rpm speed reversal at no-load and disturbance rejection at 500 rpm are also shown. However, pure integration and parameter sensitivity problems associated with this type of MRAS scheme are not discussed. In addition the speed observer performance at zero-speed operation is not mentioned.

Neural networks have been also combined with MRAS for online stator and rotor resistance estimation for speed sensorless indirect vector control IM drive [76]. An MRAS scheme based on rotor flux is used to track the rotor resistance variation online. In this scheme the flux VM is used as a reference model whereas a two layer NN mimics the adaptive CM as in [28]. To avoid pure integration in the reference model, a three-stage PCLPF is used for rotor flux synthesizer from the VM. A backpropagation training algorithm is used online to adjust the NN weights which contain the rotor time constant information. However, precise knowledge of stator resistance is required for accurate rotor resistance estimation. Therefore another stator current-based MRAS scheme has been employed for stator resistance identification [76]. In this scheme the reference model comprises the measured stator current components. A recurrent NN stator current observer is used as an adaptive model where the stator resistance is one of the NN

weights. A backpropagation learning algorithm is used to train the NN online to update the value of the stator resistance. A conventional CM is used for rotor flux estimation. With accurate stator and rotor resistance estimation, rotor speed identification could be realized using machine state equations. The proposed scheme was tested at 1000 rpm, ±1000 rpm and ±150 rpm speed reversal and satisfactory performance at low speed has been reported.

Campbell and Sumner [60] described a sensorless IM drive using a recurrent NN to detect the thermal variations of the stator resistance at different operating conditions. This is performed based on machine current, estimated speed and an additional feed-back path representing the past estimated value of the stator resistance. In this scheme the motor speed is estimated based on rotor flux-based MRAS strategy. The training signals are generated from the real drive when the motor is running at different speeds with various load torque such that the stator resistance variation can be obtained. A small DC voltage is used each time to measure the stator resistance when the machine is brought back to standstill. The training of the NN has been performed off-line using a backpropagation algorithm. Rotor resistance is also updated assuming the same percentage change as the stator resistance. Operation at low and zero speed has been investigated by testing the proposed scheme for load disturbance rejection at 100 rpm, deceleration to rest at rated load and finally zero speed operation at rated load. Better low speed operation was achieved when this NN open loop model is combined with the MRAS observer.

A linear NN has also been presented as an adaptive filter used for signal integration to eliminate the offset in the flux integration for the VM flux observer [72, 77]. Since just one weight is updated online the proposed algorithm is characterised by simple structure and low computational burden. The NN algorithm has been tested experimentally on a scalar and vector control IM drive.

Vas [10] discussed in details NN applications in open loop speed estimation of IM drives. An 8-9-7-1 multilayer feedforward NN is proposed as a speed observer with present and delayed stator voltage and current components as inputs and rotor speed as output. The proposed neural speed observer was successfully tested to estimate the speed of a supply-fed unloaded machine during run-up with less than 3×10^{-3} estimation error. The same network has been reported to correctly estimate rotor speed at different loads.

Another 8-12-10-4 network was proposed for the simultaneous estimation of rotor speed, electromagnetic torque and *d-q* stator flux components in the stator reference frame with the same inputs as the previous network. The neural observer was tested for an unloaded supply-fed induction motor during run-up and satisfactory results have been obtained even in the presence of machine parameter variation. Moreover, a three-layer feedforward NN with 16 neurons in the hidden layer was presented to estimate the rotor speed in a speed-sensorless rotor flux oriented IM drive from the present and past samples of stator voltage and current. Reference stator voltage, available in the control unit, was used instead of the actual voltage. The number of neurons in the hidden layer is chosen by trial and error. The activation functions in the hidden and output layers are tan-sigmoid and linear respectively. The training data of the network was obtained by running the vector drive with a random command speed signal with a speed sensor used to provide the target values for the network training. The trained NN was tested in a vector drive subjected to different speed references including low speed and reversal commands at various loads and satisfactory response was obtained.

Heredia *et al.* [4] used a 2-10-2 three-layer feedforward NN for speed and torque estimation for open loop V/f controlled IM drive using stator current and Volt/Hz ratio as inputs. A test with 1000 rpm and a constant load seen during training has been carried out. Further tests with speed change and loads not seen during training were shown and good estimation accuracy was obtained in all the tests.

Wavelet NN (WNN) was proposed as a new approach for rotor speed estimation in IM drives [78]. WNN combines the features of time-frequency localization property of wavelets and learning capability of NN. This can improve the performance of NN by increasing the convergence speed in addition to avoiding local minima. In [78], a three-layer WNN was trained to identify the nonlinear relationship between rotor speed and stator current. The network training was performed using supervised backpropagation and the speed identifier was simulated in a DTC IM drive. However, no experimental tests were shown for this scheme.

Neural networks can also be applied for stator and rotor flux estimation in IM drives. Two multilayer NN architectures have been proposed in [10]. The first network estimates the rotor flux modulus and position from present and past samples of stator voltage and current. The other NN generates the same outputs from present and past samples of stator

current and rotor speed to mimic the classical CM flux observer. Simoes and Bose [26] employed a three layer NN with 20 neurons in the hidden layer for rotor flux and electric torque estimation. The inputs to the network are the *d-q* components of the stator flux and stator current. Training data are obtained by simulating the drive system and the training is performed off-line using backpropagation algorithm. Nevertheless, oscillatory performance was obtained from the NN observer compared to conventional mathematical model estimators [10]. However, if stator flux and current are known rotor flux and electric torque can be obtained directly from machine equations without using a NN [10]. Another 5-8-8-2 multilayer feedforward NN has been proposed to estimate the stator flux from stator voltage, current and speed signals [27]. The drawback of this technique is the requirement of flux and speed sensors to achieve proper training of the network.

2.4.2 Applications of Fuzzy Logic

Fuzzy Logic Control (FLC) is achieved by converting the linguistic control strategy of human experience and knowledge into an automatic control strategy. Therefore no mathematical model of the controlled system is needed. FLC has been found to be excellent in dealing with systems that are imprecise, non-linear, or time-varying and with uncertain or unknown parameter and structure variation. FL is a well-established technique used in many industrial control applications. Unlike NN strategy, few attempts have been made to apply FL for sensorless control.

Lopez *et al.* [40] described a scheme where a FL system is proposed to perform an intelligent mixing between an Open Loop (OL) and a Steady-State (SS) estimator by proper weighting the output of each one according to the motor operating condition. A high weight is assigned to the OL estimator during transients and to the SS estimator in the steady state. The final estimated speed is obtained by averaging these weighted speed values. Another application of FL was described in [40] to improve the performance of OL estimators. This is performed by using an adaptive filter with a variable cut-off frequency selected by a FLC depending on the operating condition. During transients the FLC selects a high cut-off frequency to decrease the effect of the filter delay. In the steady state, where the delay effect is not important, lower values of cut-off frequency are selected to eliminate the ripple in the estimated speed. Simulation and experimental

results are shown for a step response to rated speed and for a load torque step with moderate performance shown.

A fuzzy self-tuning identifier was proposed to solve speed estimation problems for vector control IM drive [79]. The scheme has a similar structure as the rotor flux-based MRAS observer in [28, 53] with a VM as a reference model. A fuzzy self-tuning identifier integrating a three-layer network is employed for the adaptive model. The backpropagation algorithm is used online to minimize the error between reference and estimated rotor flux by adjusting the fuzzy identifier membership functions. Hence the output of the fuzzy model is forced to follow the desired reference and an estimate of the rotor speed can be obtained. The scheme was tested for a step speed command of 500 rpm and for a command change from 500rpm to 900 rpm and back to 500 rpm. However no results are shown for speed estimation performance at low speed.

Lian and Hung [80] proposed a fuzzy observer for rotor flux and rotor speed estimation for IM. Observer gains were obtained by solving a set of linear matrix inequalities. Tests with a sinusoidal reference speed were shown. However, parameter variation and low speed problems were not mentioned.

2.5 Conclusion

This chapter has provided a detailed review of different model based techniques applied to speed sensorless IM drives with most emphasis given to MRAS and AI strategies. Different problems affecting the low speed operation of MRAS observers have been illustrated. Various methods employed in the literature to improve the rotor flux-based scheme's performance have been carefully reviewed. Different applications of NN and FL techniques for sensorless control have been also highlighted. It appears that, despite much attempt and progress, operation at very low speed for MRAS-based sensorless IM drives is still challenging and needs more investigation.

CHAPTER 3

MODEL REFERENCE ADAPTIVE SYSTEMS FOR VECTOR CONTROL INDUCTION MOTOR DRIVE

3.1 Introduction

Induction motors are the workhorse for industrial applications due to their ruggedness, simplicity and low cost. IM drives have replaced DC drives in many high performance applications due to the advances in control strategies such as vector and direct torque control. Fast development of power electronics and microprocessors has provided an economic way for implementation of these control techniques. Therefore an accurate model that well represents the induction machine is required to allow proper design of the control and observer system. This chapter first presents the mathematical model of the induction machine using space vector and two-axis theory. This model is then used to understand the dynamic performance of the machine using vector control. Finally, rotor speed estimation using a MRAS strategy is investigated using the induction machine model to formulate the rotor flux based speed observer.

This chapter is divided into three parts. The first part presents the dynamic modelling of the induction machine using space vector theory and state space representation. The second part investigates the dynamic behaviour of the IM under rotor field orientation.

The final part is concerned with modelling of rotor flux MRAS observer for speed sensorless IM drives.

3.2 Dynamic Modelling of the Induction Machine

The IM equivalent circuit is used to calculate the machine quantities such as stator current, motor torque and power factor under steady state operating conditions and running from a balanced sinusoidal supply. However, this equivalent circuit cannot be used for transient analysis or when the motor is fed from a non sinusoidal supply which is the case with converter fed machines. To allow the analysis of the transient and the steady state performance of the machine when supplied from any type of supply, a dynamic model of the machine will be defined based on space vector theory [2]. This is related to the two-axis theory of electric machines. In this analysis, the three phase variables are described by an equivalent two phase representation which simplifies the machine equations.

In a three phase induction machine, the space vector of the stator current in the stationary reference frame fixed to stator can be defined as [2]:

$$\bar{i}_s = \frac{2}{3}(i_{sA} + a i_{sB} + a^2 i_{sC}) \tag{3.1}$$

where:

$$a = e^{j\frac{2\pi}{3}} = -\frac{1}{2} + j\frac{\sqrt{3}}{2}$$
$$a^2 = e^{j\frac{4\pi}{3}} = -\frac{1}{2} - j\frac{\sqrt{3}}{2} \tag{3.2}$$

In (3.1), i_{sA}, i_{sB} and i_{sC} are the three phase currents that flow in three phase windings displaced by 120^0 from each other and producing sinusoidal distributed magneto-motive force (mmf). Resolving the stator current space vector in (3.1) into its real and imaginary parts yields the two axis components of the stator current vector in the stator reference frame as shown in Fig. 3.1 [2].

$$i_{sD} = \frac{2}{3} i_{sA} - \frac{1}{3} i_{sB} - \frac{1}{3} i_{sC}$$
$$i_{sQ} = \frac{1}{\sqrt{3}} i_{sB} - \frac{1}{\sqrt{3}} i_{sC} \tag{3.3}$$

i_{sD} and i_{sQ} are the actual currents that flow in the two-phase stator windings sD and sQ which are quadrature in space [2]. The stator current space vector can be written in polar and rectangular form as:

$$\bar{i}_s = |\bar{i}_s| e^{j\alpha_s} = i_{sD} + j i_{sQ} \tag{3.4}$$

In a matrix form such a transformation from three phase to two phase can be written as:

$$\begin{bmatrix} i_{sD} \\ i_{sQ} \end{bmatrix} = \frac{2}{3} \begin{bmatrix} 1 & -\frac{1}{2} & -\frac{1}{2} \\ 0 & \frac{\sqrt{3}}{2} & -\frac{\sqrt{3}}{2} \end{bmatrix} \begin{bmatrix} i_{sA} \\ i_{sB} \\ i_{sC} \end{bmatrix} \tag{3.5}$$

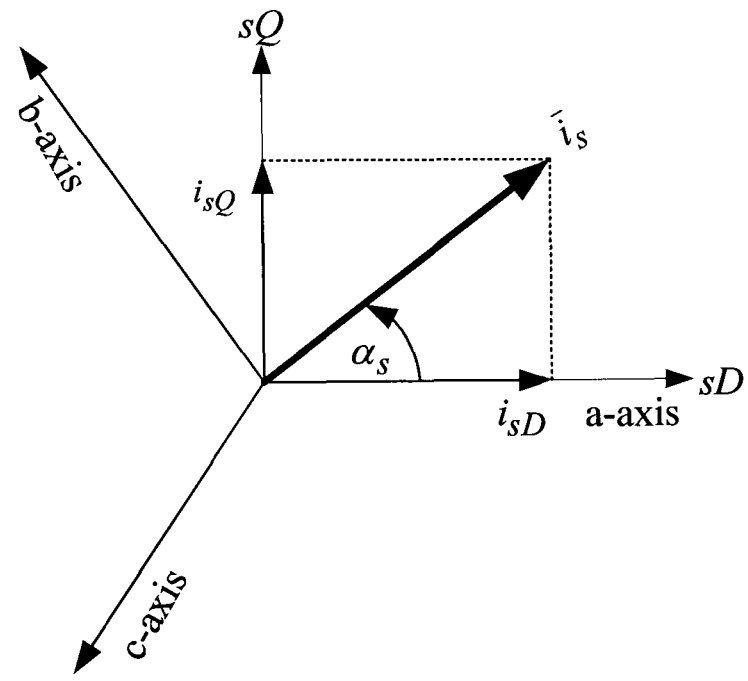

Fig. 3.1 Stator current space vector and its two-axes components

The transformation from two phase quantities into three phase quantities can be written as:

$$\begin{aligned} i_{sA} &= i_{sD} \\ i_{sB} &= -\frac{1}{2} i_{sD} + \frac{\sqrt{3}}{2} i_{sQ} \\ i_{sC} &= -\frac{1}{2} i_{sD} - \frac{\sqrt{3}}{2} i_{sQ} \end{aligned} \tag{3.6}$$

This transformation can be expressed in a matrix form as:

$$\begin{bmatrix} i_{sA} \\ i_{sB} \\ i_{sC} \end{bmatrix} = \begin{bmatrix} 1 & 0 \\ -\frac{1}{2} & \frac{\sqrt{3}}{2} \\ -\frac{1}{2} & -\frac{\sqrt{3}}{2} \end{bmatrix} \begin{bmatrix} i_{sD} \\ i_{sQ} \end{bmatrix} \tag{3.7}$$

For vector control implementation, a transformation between stator (*D-Q*) and excitation (*d-q*) frames is required as shown in Fig. 3.2 where θ_e is the rotor flux position. The stator coordinates are fixed to stator and therefore are stationary while the excitation (synchronous) frame coordinates rotates synchronously with the stator magnetic field.

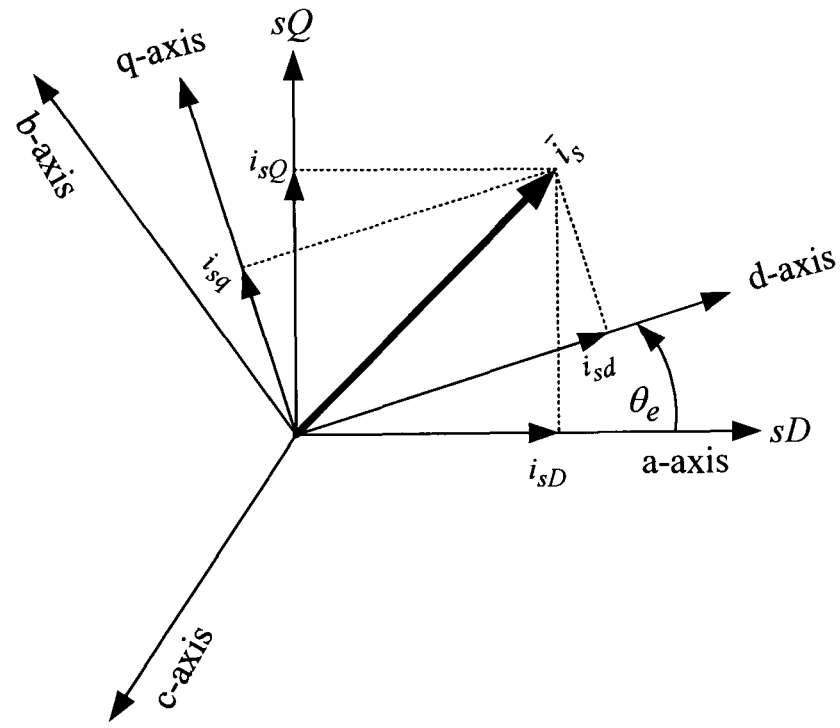

Fig. 3.2 Transformation between stationary and synchronous frames

The transformation from the stator frame to the synchronous frame is given by [2]:

$$\bar{i}_s^e = i_{sd} + j\, i_{sq} = \bar{i}_s^s\, e^{-j\theta_e} = (i_{sD} + j\, i_{sQ}) e^{-j\theta_e} \tag{3.8}$$

The superscripts *s* and *e* stand for the stator and excitation reference frames while the subscript *s* stands for the stator quantities. The transformation defined in (3.8) can be written in matrix form as:

$$\begin{bmatrix} i_{sd} \\ i_{sq} \end{bmatrix} = \begin{bmatrix} \cos\theta_e & \sin\theta_e \\ -\sin\theta_e & \cos\theta_e \end{bmatrix} \begin{bmatrix} i_{sD} \\ i_{sQ} \end{bmatrix} \tag{3.9}$$

while the transformation from synchronous frame to stator frame is given by:

$$\bar{i}_s^s = i_{sD} + j\,i_{sQ} = \bar{i}_s^e\, e^{j\theta_e} = (i_{sd} + j\,i_{sq})\, e^{j\theta_e} \tag{3.10}$$

In matrix form:

$$\begin{bmatrix} i_{sD} \\ i_{sQ} \end{bmatrix} = \begin{bmatrix} \cos\theta_e & -\sin\theta_e \\ \sin\theta_e & \cos\theta_e \end{bmatrix} \begin{bmatrix} i_{sd} \\ i_{sq} \end{bmatrix} \tag{3.11}$$

Similarly, the stator voltage and flux space vectors expressed at the stator reference frame are:

$$\begin{aligned} \bar{v}_s &= \frac{2}{3}(v_{sA} + a v_{sB} + a^2 v_{sC}) \\ &= v_{sD} + j v_{sQ} \end{aligned} \tag{3.12}$$

$$\begin{aligned} \bar{\psi}_s &= \frac{2}{3}(\psi_{sA} + a\psi_{sB} + a^2 \psi_{sC}) \\ &= \psi_{sD} + j\psi_{sQ} \end{aligned} \tag{3.13}$$

In a similar manner to the definition of the stator current space vector expressed in the stator reference frame, the space vector of the rotor current in a reference frame fixed to rotor, shown in Fig. 3.3, can be expressed as:

$$\begin{aligned} \bar{i}_r &= \frac{2}{3}(i_{ra} + a i_{rb} + a^2 i_{rc}) \\ \bar{i}_r &= |\bar{i}_r| e^{j\alpha_r} = i_{r\alpha} + j i_{r\beta} \end{aligned} \tag{3.14}$$

$i_{r\alpha}$ and $i_{r\beta}$ are the actual currents that flow in the two-phase rotor windings $r\alpha$ and $r\beta$ which are quadrature in space and θ_r is the rotor position [2].

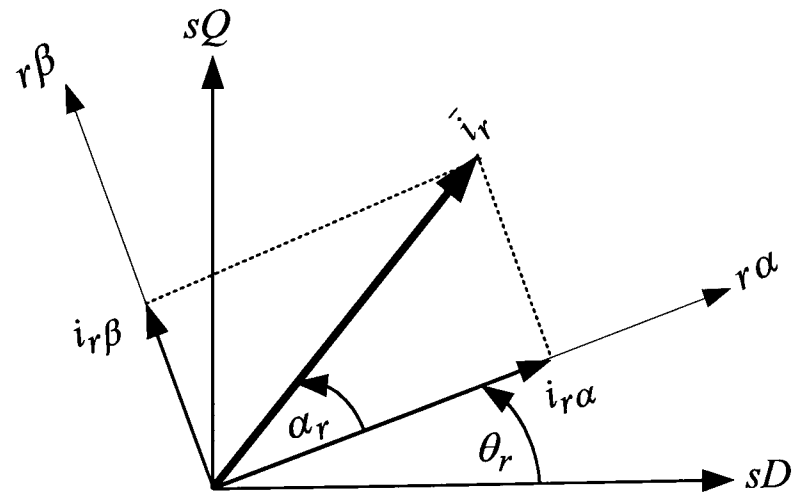

Fig. 3.3 Rotor current space vector and its two-axes components

A set of differential equations based on Faraday's and Kirchoff's laws is used to describe the induction machine mathematical model. Detailed mathematical modelling of the induction machine is given in Appendix A. Using space vector notation the stator and rotor voltage equations can be written as:

$$\bar{v}_s^s = R_s \bar{i}_s^s + \frac{d\bar{\psi}_s^s}{dt} \tag{3.15}$$

$$\bar{v}_r^r = R_r \bar{i}_r^r + \frac{d\bar{\psi}_r^r}{dt} \tag{3.16}$$

The superscripts s and r stand for the stator and rotor reference frames while the subscripts s and r stand for the stator and rotor quantities.

Equations (3.15) and (3.16) can be written in d-q coordinates established in the stator reference frame as:

$$\begin{aligned} v_{sD} &= R_s i_{sD} + \frac{d\psi_{sD}}{dt} \\ v_{sQ} &= R_s i_{sQ} + \frac{d\psi_{sQ}}{dt} \\ v_{rd} &= R_r i_{rd} + \frac{d\psi_{rd}}{dt} + \omega_r \psi_{rq} \\ v_{rq} &= R_r i_{rq} + \frac{d\psi_{rq}}{dt} - \omega_r \psi_{rd} \end{aligned} \tag{3.17}$$

where the stator and rotor flux linkages are given by:

$$\begin{aligned} \psi_{sD} &= L_s i_{sD} + L_m i_{rd} \\ \psi_{sQ} &= L_s i_{sQ} + L_m i_{rq} \\ \psi_{rd} &= L_m i_{sD} + L_r i_{rd} \\ \psi_{rq} &= L_m i_{sQ} + L_r i_{rq} \end{aligned} \tag{3.18}$$

The voltage equations of the induction machine in the stator reference frame can be written in terms of stator and rotor current space vectors as:

$$\bar{v}_s^s = (R_s + L_s p)\bar{i}_s^s + L_m p \bar{i}_r^s \tag{3.19}$$

$$\bar{v}_r^s = (R_r + L_r p)\bar{i}_r^s + L_m p \bar{i}_s^s - j\omega_r \left(L_m \bar{i}_s^s + L_r \bar{i}_r^s\right) \tag{3.20}$$

where p is the differential operator.

In matrix form using space vector notation these equations can be written as:

$$\begin{bmatrix} \bar{v}_s^s \\ \bar{v}_r^s \end{bmatrix} = \begin{bmatrix} R_s + L_s p & L_m p \\ (p - j\omega_r)L_m & R_r + (p - j\omega_r)L_r \end{bmatrix} \begin{bmatrix} \bar{i}_s^s \\ \bar{i}_r^s \end{bmatrix} \tag{3.21}$$

A convenient way to solve estimation and control problems using computer simulation is to use a state space model. In this representation, shown in Fig. 3.4, the machine dynamic model is described by a set of first order differential equations.

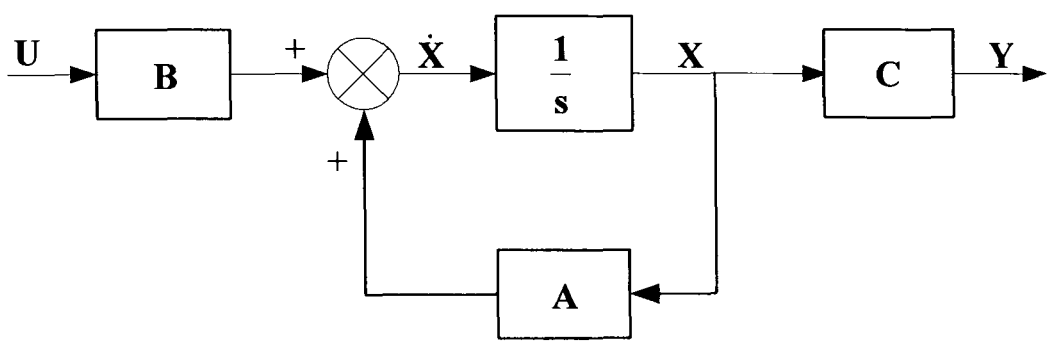

Fig. 3.4 State space model

By writing the stator and rotor voltage equations in terms of stator current and rotor flux space vectors, a state space representation of the induction machine can be obtained. For a squirrel-cage IM, these equations can be written as:

$$\bar{v}_s^s = R_s \bar{i}_s^s + \sigma L_s p \bar{i}_s^s + \frac{L_m}{L_r} p \bar{\psi}_r^s \tag{3.22}$$

$$0 = \frac{1}{T_r}\left(\bar{\psi}_r^s - L_m \bar{i}_s^s\right) + p\bar{\psi}_r^s - j\omega_r \bar{\psi}_r^s \tag{3.23}$$

where σ is the leakage coefficient given by:

$$\sigma = 1 - \frac{L_m^2}{L_s L_r} \tag{3.24}$$

and T_r is the rotor time constant given by:

$$T_r = \frac{L_r}{R_r} \tag{3.25}$$

The state space representation of the IM in the stator reference frame with the stator currents and the rotor flux linkages components as state variables can be written as:

$$\begin{bmatrix} pi_{sD} \\ pi_{sQ} \\ p\psi_{rd} \\ p\psi_{rq} \end{bmatrix} = \begin{bmatrix} -a_1 & 0 & a_2 & a_3\omega_r \\ 0 & -a_1 & -a_3\omega_r & a_2 \\ \frac{L_m}{T_r} & 0 & -\frac{1}{T_r} & -\omega_r \\ 0 & \frac{L_m}{T_r} & \omega_r & -\frac{1}{T_r} \end{bmatrix} \begin{bmatrix} i_{sD} \\ i_{sQ} \\ \psi_{rd} \\ \psi_{rq} \end{bmatrix} + \begin{bmatrix} \frac{1}{\sigma L_s} & 0 \\ 0 & \frac{1}{\sigma L_s} \\ 0 & 0 \\ 0 & 0 \end{bmatrix} \begin{bmatrix} v_{sD} \\ v_{sQ} \end{bmatrix} \tag{3.26}$$

where:

$$\begin{aligned} a_1 &= \frac{R_s}{\sigma L_s} + \frac{1-\sigma}{\sigma T_r} \\ a_2 &= \frac{L_m}{\sigma L_s L_r T_r} \\ a_3 &= \frac{L_m}{\sigma L_s L_r} \end{aligned} \tag{3.27}$$

The machine model can be written using the standard state space notation as:

$$\begin{aligned} \dot{\mathbf{X}}(t) &= \mathbf{A}\mathbf{X}(t) + \mathbf{B}\mathbf{U}(t) \\ \mathbf{Y}(t) &= \mathbf{C}\mathbf{X}(t) \end{aligned} \tag{3.28}$$

where:

$$\begin{aligned} \mathbf{X}(t) &= \begin{bmatrix} i_{sD} & i_{sQ} & \psi_{rd} & \psi_{rq} \end{bmatrix}^T \\ \mathbf{U}(t) &= \begin{bmatrix} v_{sD} & v_{sQ} \end{bmatrix}^T \\ \mathbf{Y}(t) &= \begin{bmatrix} i_{sD} & i_{sQ} \end{bmatrix}^T \end{aligned}$$

$$\mathbf{A} = \begin{bmatrix} -a_1 & 0 & a_2 & a_3\omega_r \\ 0 & -a_1 & -a_3\omega_r & a_2 \\ \frac{L_m}{T_r} & 0 & -\frac{1}{T_r} & -\omega_r \\ 0 & \frac{L_m}{T_r} & \omega_r & -\frac{1}{T_r} \end{bmatrix} \quad \mathbf{B} = \begin{bmatrix} \frac{1}{\sigma L_s} & 0 \\ 0 & \frac{1}{\sigma L_s} \\ 0 & 0 \\ 0 & 0 \end{bmatrix} \quad \mathbf{C} = \begin{bmatrix} 1 & 0 & 0 & 0 \\ 0 & 1 & 0 & 0 \end{bmatrix} \tag{3.29}$$

As shown in Appendix A, the electromagnetic torque for a machine with P pole pairs is given by:

$$T_e = \frac{3}{2} P \frac{L_m}{L_r} (\psi_{rd} i_{sQ} - \psi_{rq} i_{sD}) \tag{3.30}$$

3.3 Principles of Vector Control

The main objective of vector control is to make the dynamic performance of the induction machine similar to that of a separately excited DC machine. This can be achieved by orienting the synchronous frame axes so that the *d*-axis is aligned with the rotor flux space vector as shown in Fig. 3.5. Therefore this control technique is also referred to as Rotor Flux Oriented (RFO) control.

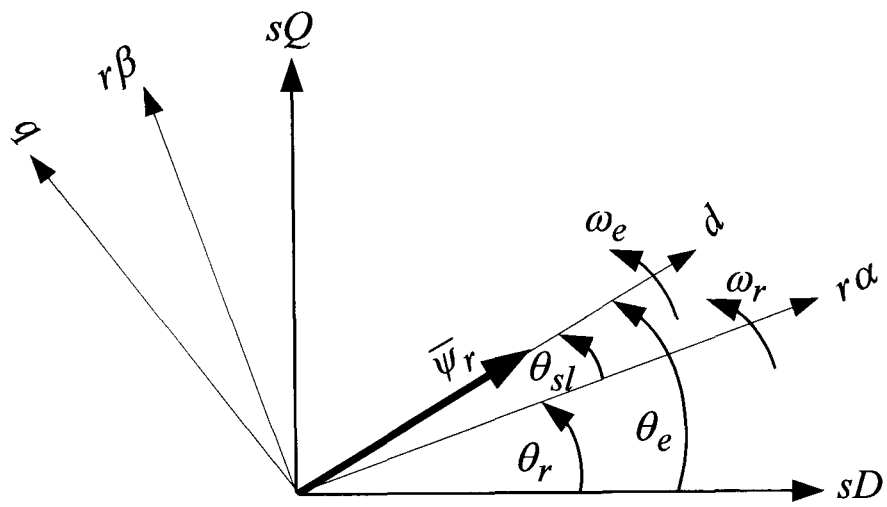

Fig. 3.5 Principle of rotor flux orientation

The main concept of vector control can be explained by considering the mathematical model of the squirrel-cage IM in *d-q* coordinates expressed in the synchronous reference frame:

$$\begin{aligned} v_{sd} &= R_s i_{sd} + p\psi_{sd} - \omega_e \psi_{sq} \\ v_{sq} &= R_s i_{sq} + p\psi_{sq} + \omega_e \psi_{sd} \\ 0 &= R_r i_{rd} + p\psi_{rd} - \omega_{sl} \psi_{rq} \\ 0 &= R_r i_{rq} + p\psi_{rq} + \omega_{sl} \psi_{rd} \end{aligned} \tag{3.31}$$

where the rotor flux components are given by:

$$\psi_{rd} = L_m i_{sd} + L_r i_{rd} \tag{3.32}$$

$$\psi_{rq} = L_m i_{sq} + L_r i_{rq} \tag{3.33}$$

Under the rotor flux orientation conditions, the rotor flux is aligned on the *d*-axis of the synchronous frame, and the rotor flux components can be written as:

$$\overline{\psi}_r = \psi_{rd}$$
$$\psi_{rq} = 0 \quad p\psi_{rq} = 0 \tag{3.34}$$

Substituting (3.34) into the rotor voltage equations of (3.31) and (3.33) yields:

$$R_r i_{rd} + p\psi_{rd} = 0 \tag{3.35}$$

$$R_r i_{rq} + \omega_{sl}\psi_{rd} = 0 \tag{3.36}$$

$$L_m i_{sq} + L_r i_{rq} = 0 \tag{3.37}$$

From (3.37):

$$i_{rq} = -\frac{L_m}{L_r} i_{sq} \tag{3.38}$$

Substituting (3.38) into (3.36) yields the expression for the slip frequency command:

$$\omega_{sl} = \frac{L_m}{T_r \psi_{rd}} i_{sq} \tag{3.39}$$

From (3.35):

$$i_{rd} = -\frac{1}{R_r} p\psi_{rd} \tag{3.40}$$

Substituting (3.40) into (3.32) yields the rotor flux dynamics:

$$T_r p\psi_{rd} + \psi_{rd} = L_m i_{sd} \tag{3.41}$$

Under steady state conditions:

$$p\psi_{rd} = 0 \tag{3.42}$$

Substituting (3.42) into (3.40) and (3.41) yields:

$$i_{rd} = 0 \tag{3.43}$$

$$\psi_{rd} = L_m i_{sd} \tag{3.44}$$

From which the slip angular frequency ω_{sl} in (3.39) can be written as:

$$\omega_{sl} = \omega_e - \omega_r = \frac{1}{T_r}\frac{i_{sq}}{i_{sd}} \tag{3.45}$$

The slip frequency can be also calculated from the reference values of the stator current components represented in the rotor flux oriented reference frame as follow [2]:

$$\omega_{sl} = \frac{1}{T_r}\frac{i_{sq}^*}{i_{sd}^*} \tag{3.46}$$

The rotor flux position θ_e can be written as:

$$\theta_e = \theta_r + \int \frac{1}{T_r} \frac{i_{sq}^*}{i_{sd}^*} dt \tag{3.47}$$

Under field orientation conditions, substituting (3.34) into (3.30) yields the electromagnetic torque equation which become analogous to that of a DC machine and can be written as:

$$T_e = \frac{3}{2} P \frac{L_m}{L_r} \psi_{rd} i_{sq} \tag{3.48}$$

This can be written as:

$$T_e = K_T \psi_{rd} i_{sq} \tag{3.49}$$

where K_T is the torque constant given by:

$$K_T = \frac{3}{2} P \frac{L_m}{L_r} \tag{3.50}$$

Equations (3.44) and (3.49) are similar to that of a separately excited DC machine where i_{sd} and i_{sq} are analogous to the field and armature current respectively. Control of IM is performed in the synchronous frame so that the sinusoidal variables appear as DC quantities in the steady state. Flux and torque control is achieved by separately controlling the d-axis and q-axis components of the stator current space vector in the synchronous frame respectively. Usually the rotor flux is kept constant by a constant i_{sd} command and the torque is controlled directly by adjusting the i_{sq} command yielding fast dynamic response of the drive.

Implementation of vector control requires the accurate knowledge of the rotor flux angle θ_e. This angle represents the position of rotor flux space vector with respect to the D-axis of the stationary reference frame. The method of detection of this angle yields two types of vector control: direct and indirect method.

Direct field orientation relies on the direct measurement of the rotor flux position. Traditionally, this was performed by fixing flux sensors in the air gap such as search coils or Hall-effect sensors. Currently, flux observers are used extensively for this purpose where the rotor flux position is estimated from monitored stator current and voltage as shown in Fig. 3.6(a).

On the other hand, in the indirect field orientation, the machine mathematical model is used for slip calculation, based on (3.46), which when added to the rotor position

yields the rotor flux angle as shown in Fig. 3.6(b). Indirect technique is commonly used because it is simple and does not require flux sensors or flux observers. However, it is highly sensitive to rotor time constant variation which may deteriorate the drive performance. The block diagram of indirect vector control IM drive is shown in Fig. 3.7.

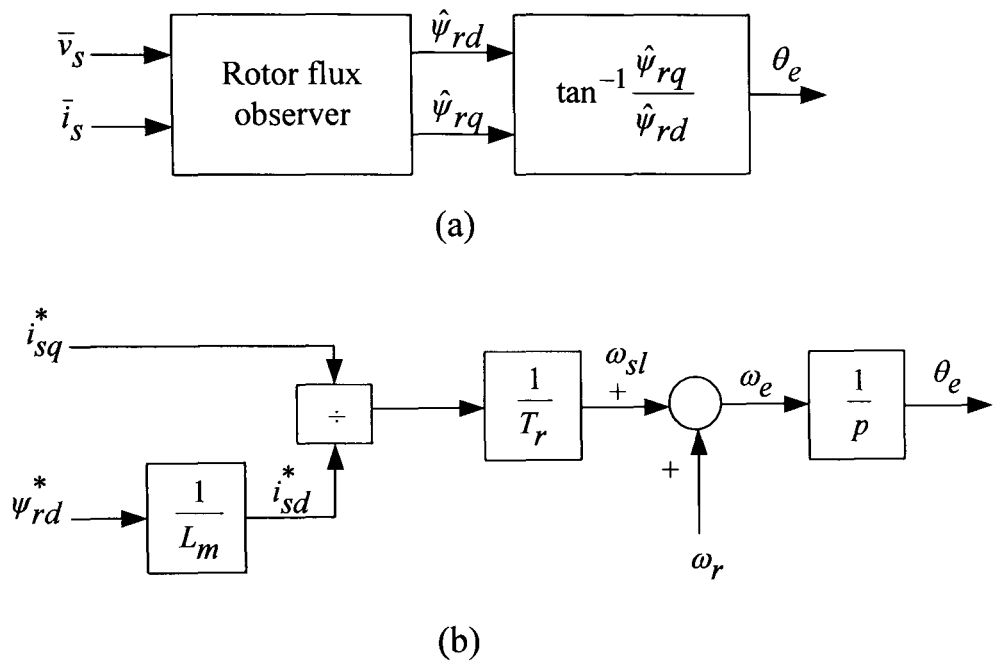

Fig. 3.6 Types of rotor flux orientation schemes (a) Direct method (b) Indirect method

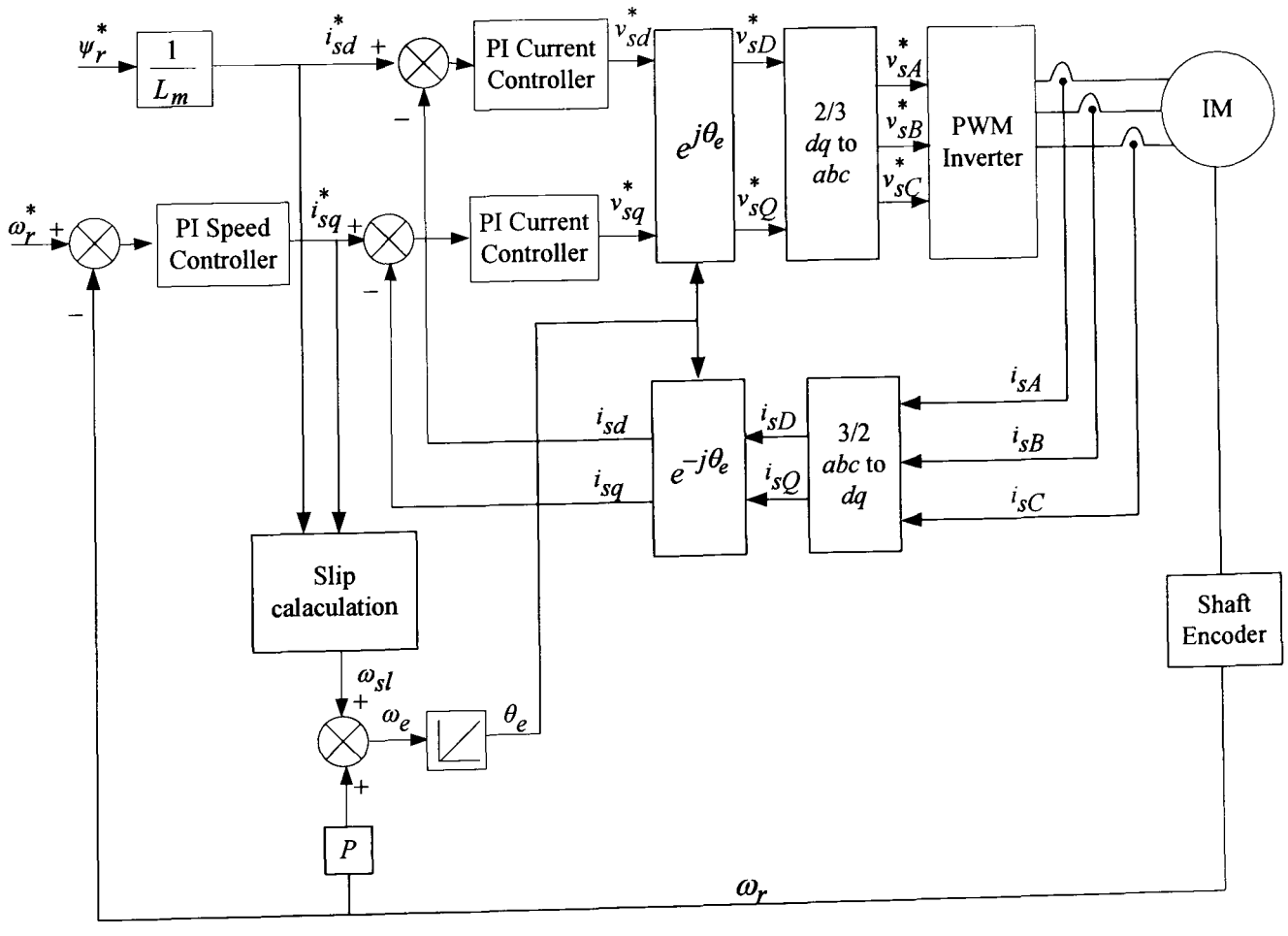

Fig. 3.7 Block diagram of indirect vector control IM drive

3.4 Model Reference Adaptive System for Induction Motor

The model reference adaptive system is one of the most successful adaptive control techniques applied to motor control and parameter estimation. Fig. 3.8 shows a classical MRAS observer structure used for parameter identification which consists of a reference model, an adaptive model, and an adaptation mechanism. The basic concept of MRAS is the presence of a reference model which determines the desired states θ_R and an adaptive (adjustable) model which generates the estimated values of the states $\hat{\theta}_A$. The error between these states is fed to an adaptation mechanism to generate an estimated value of the parameter λ which is used to adjust the adaptive model. This process continues till the error ε between the two outputs tends to zero [2]. Modelling a MRAS observer for speed estimation of IM is demonstrated in the following sections.

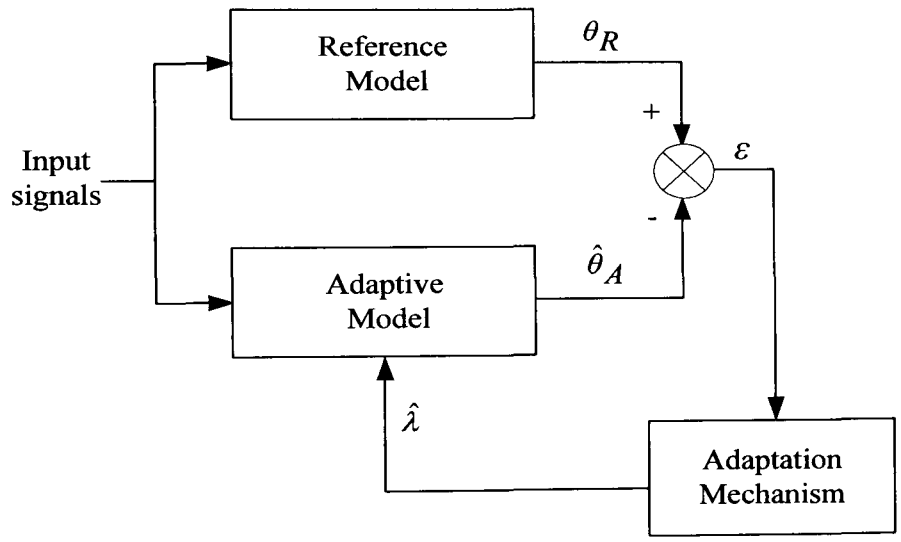

Fig. 3.8 Basic configuration of a MRAS observer

3.4.1 Rotor Flux MRAS Modelling for Speed Estimation

The design of a MRAS estimator for speed estimation of IM drives requires the definition of two models having similar outputs. One model, termed the reference model, should be independent of the rotor speed while the other, the adaptive model, is speed dependent. In the following section a MRAS observer based on rotor flux is derived using the *d-q* model of the induction machine.

The stator voltage equations of the induction machine (3.22) can be written in *d-q* coordinates established in the stator reference frame as:

$$v_{sD} = R_s i_{sD} + \sigma L_s p i_{sD} + \frac{L_m}{L_r} p\psi_{rd}$$
$$v_{sQ} = R_s i_{sQ} + \sigma L_s p i_{sQ} + \frac{L_m}{L_r} p\psi_{rq} \tag{3.51}$$

Similarly, the rotor voltage equations (3.23) can be written in the same coordinates as:

$$0 = \frac{1}{T_r}\psi_{rd} - \frac{L_m}{T_r} i_{sD} + p\psi_{rd} + \omega_r \psi_{rq}$$
$$0 = \frac{1}{T_r}\psi_{rq} - \frac{L_m}{T_r} i_{sQ} + p\psi_{rq} - \omega_r \psi_{rd} \tag{3.52}$$

Rotor flux components in the stationary reference frame are the common outputs from equations (3.51) and (3.52). Moreover, (3.51) is free from a rotor speed term while (3.52) has speed dependent terms. Therefore these equations can be used to setup a model reference adaptive system with rotor flux as output state and rotor speed as adopted parameter.

The reference model can be formulated by rearranging (3.51) to generate the reference value of the rotor flux components. This is usually expressed by the VM that represents the stator voltage equations. These rotor flux components are obtained from the monitored stator voltage and current components and can be written using *d-q* representation as [2, 53]:

$$p\psi_{rd} = \frac{L_r}{L_m}\left(v_{sD} - R_s i_{sD} - \sigma L_s p i_{sD}\right)$$
$$p\psi_{rq} = \frac{L_r}{L_m}\left(v_{sQ} - R_s i_{sQ} - \sigma L_s p i_{sQ}\right) \tag{3.53}$$

An adaptive model generating estimate values of the rotor flux based on the rotor speed information can be established by rearranging equation (3.52). This is usually represented by the CM that describes the rotor voltage equation. Estimated rotor flux components are expressed in terms of stator current components and the estimated rotor speed and are given by [2, 53]:

$$p\hat{\psi}_{rd} = \frac{L_m}{T_r} i_{sD} - \frac{1}{T_r}\hat{\psi}_{rd} - \hat{\omega}_r \hat{\psi}_{rq}$$
$$p\hat{\psi}_{rq} = \frac{L_m}{T_r} i_{sQ} - \frac{1}{T_r}\hat{\psi}_{rq} + \hat{\omega}_r \hat{\psi}_{rd} \tag{3.54}$$

Equations (3.53) and (3.54) form the classical rotor flux MRAS speed observer described in [53] that can be applied to an IM as shown in Fig. 3.9. An adaptation

scheme generates the value of the estimated speed used so as to minimize the error between the reference and estimated fluxes. Design of this adaptation mechanism will be explained in detail in the following section.

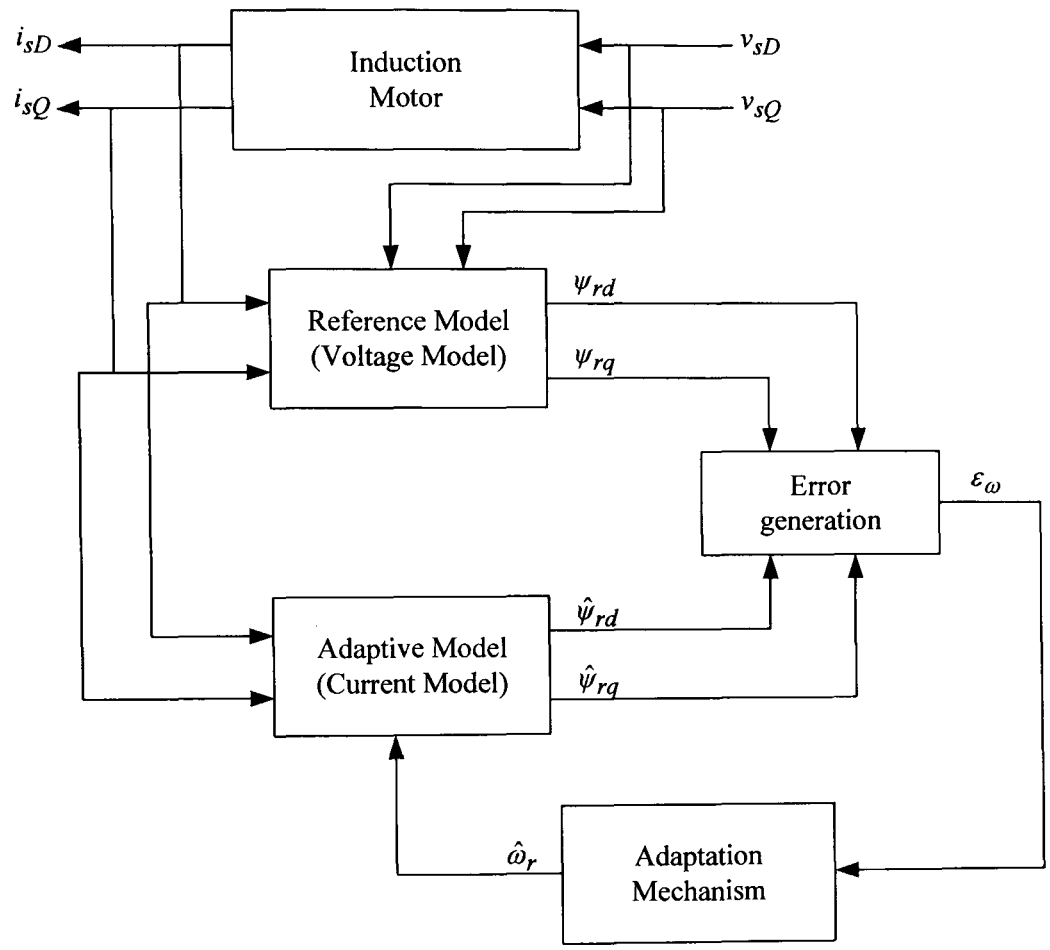

Fig. 3.9 Rotor flux-MRAS speed observer for IM

Due to the presence of speed dependent cross coupling components in the *d-q* axis flux loops in (3.54), CM implementation using a stationary reference frame representation as in (3.54) may lead to stability problems [81]. To eliminate this mutual coupling, an implementation in the rotor reference frame can be used [68, 81]. In the rotor reference frame, the rotor flux space vector can be written as:

$$\bar{\psi}_r^r = L_m \bar{i}_s^r + L_r \bar{i}_r^r \tag{3.55}$$

Using the rotor voltage equation in the rotor reference frame from (3.16) with zero rotor voltage for a squirrel-cage machine gives:

$$p\bar{\psi}_r^r = -R_r \bar{i}_r^r \tag{3.56}$$

Substituting (3.56) into (3.55) yields:

$$\bar{\psi}_r^r = L_m \bar{i}_s^r - T_r p\bar{\psi}_r^r \tag{3.57}$$

Rearranging (3.57) yields the expression for the rotor flux space vector in the rotor reference frame:

$$\bar{\psi}_r^r = \frac{L_m}{1+T_r p}\bar{i}_s^r \tag{3.58}$$

Equation (3.58) is used to implement the CM in the rotor reference frame which, different from (3.54), yields real eigenvalues at $-1/T_r$. Stator reference frame implementation of the CM using rotor frame representation is shown in Fig. 3.10. The stator current space vector is transformed from the stator to rotor reference frame using the following transformation as described in Appendix A:

$$\bar{i}_s^r = \bar{i}_s^s e^{-j\theta_r} \tag{3.59}$$

The rotor flux in the stator reference frame is obtained by transforming the rotor flux space vector in the rotor reference frame back to the stator reference frame:

$$\bar{\psi}_r^s = \bar{\psi}_r^r e^{j\theta_r} \tag{3.60}$$

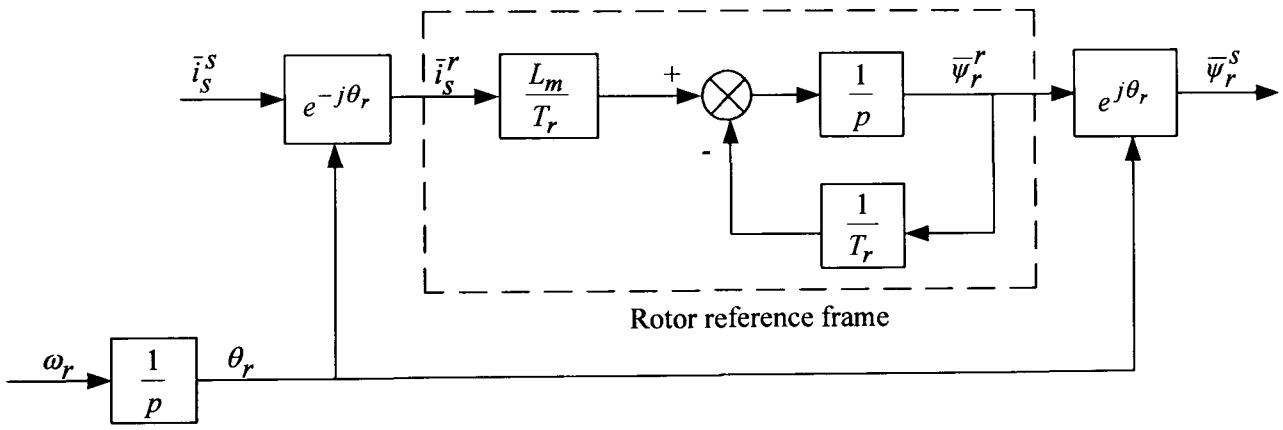

Fig. 3.10 CM implementation using rotor reference frame representation

3.4.2 Design of Adaptation Mechanism for MRAS Observer

One of the main approaches employed to design MRAS observers is based on the hyperstability theory. This technique allows the stability analysis of feedback systems that can be represented by a feedforward and feedback blocks as shown in Fig. 3.11 [2]. The input to the linear feedforward subsystem is $\mathbf{U}$ and its output is ε. The output of the nonlinear feedback subsystem is $\mathbf{W}$ and $\mathbf{U} = -\mathbf{W}$. The adaptation mechanism is designed based on Popov's hyperstability theory where the transfer function matrix of the linear feedforward subsystem is strictly positive real and the nonlinear feedback

subsystem satisfies Popov's integral inequality $\int_0^t \varepsilon^T \mathbf{W}\, dt \geq -\gamma_o^2$ where γ_o^2 is a positive constant [53, 82]. Detailed description of hyperstability theory is complicated and is beyond the scope of this work. More details can be found in Landau [83] where procedures of MRAS design using hyperstability approach is demonstrated.

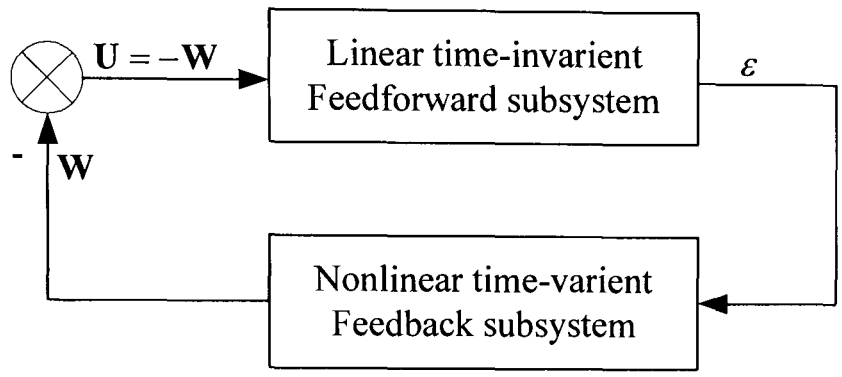

Fig. 3.11 Equivalent of a nonlinear feedback system

Design of the adaptation mechanism for MRAS using this concept will ensure overall stability and convergence of the estimated speed to the desired value with suitable dynamics [53]. For the derivation of the adaptation mechanism it is valid to initially consider the rotor speed as constant parameter of the reference model [53]. To transform the MRAS observer into an equivalent feedforward and feedback subsystems consider the state error equation of the system. This can be obtained by subtracting the outputs of reference and adaptive models.

$$\begin{aligned} \varepsilon_d &= \psi_{rd} - \hat{\psi}_{rd} \\ \varepsilon_q &= \psi_{rq} - \hat{\psi}_{rq} \end{aligned} \tag{3.61}$$

Defining an error vector ε:

$$\varepsilon = \begin{bmatrix} \varepsilon_d & \varepsilon_q \end{bmatrix}^T \tag{3.62}$$

Differentiating (3.61) and substituting from (3.54) gives:

$$\begin{aligned} p\varepsilon_d &= -\frac{1}{T_r}\varepsilon_d - \omega_r \varepsilon_q - (\omega_r - \hat{\omega}_r)\hat{\psi}_{rq} \\ p\varepsilon_q &= -\frac{1}{T_r}\varepsilon_q + \omega_r \varepsilon_d + (\omega_r - \hat{\omega}_r)\hat{\psi}_{rd} \end{aligned} \tag{3.63}$$

These equations can be written in standard matrix form as:

$$\begin{bmatrix} p\varepsilon_d \\ p\varepsilon_q \end{bmatrix} = \begin{bmatrix} -\frac{1}{T_r} & -\omega_r \\ \omega_r & -\frac{1}{T_r} \end{bmatrix} \begin{bmatrix} \varepsilon_d \\ \varepsilon_q \end{bmatrix} + \begin{bmatrix} -\hat{\psi}_{rq} \\ \hat{\psi}_{rd} \end{bmatrix} (\omega_r - \hat{\omega}_r) \tag{3.64}$$

Equation (3.64) is similar to the nonlinear feedback system shown in Fig. 3.11 and can be written as:

$$p\varepsilon = \mathbf{A}\varepsilon - \mathbf{W} \tag{3.65}$$

where:

$$\mathbf{A} = \begin{bmatrix} -\frac{1}{T_r} & -\omega_r \\ \omega_r & -\frac{1}{T_r} \end{bmatrix} \quad \mathbf{W} = \begin{bmatrix} \hat{\psi}_{rq} \\ -\hat{\psi}_{rd} \end{bmatrix} (\omega_r - \hat{\omega}_r) \tag{3.66}$$

MRAS representation in the general form of a nonlinear feedback system is shown in Fig. 3.12. It can be shown that the feedforward transfer function matrix of the linear subsystem is strictly positive real [53].

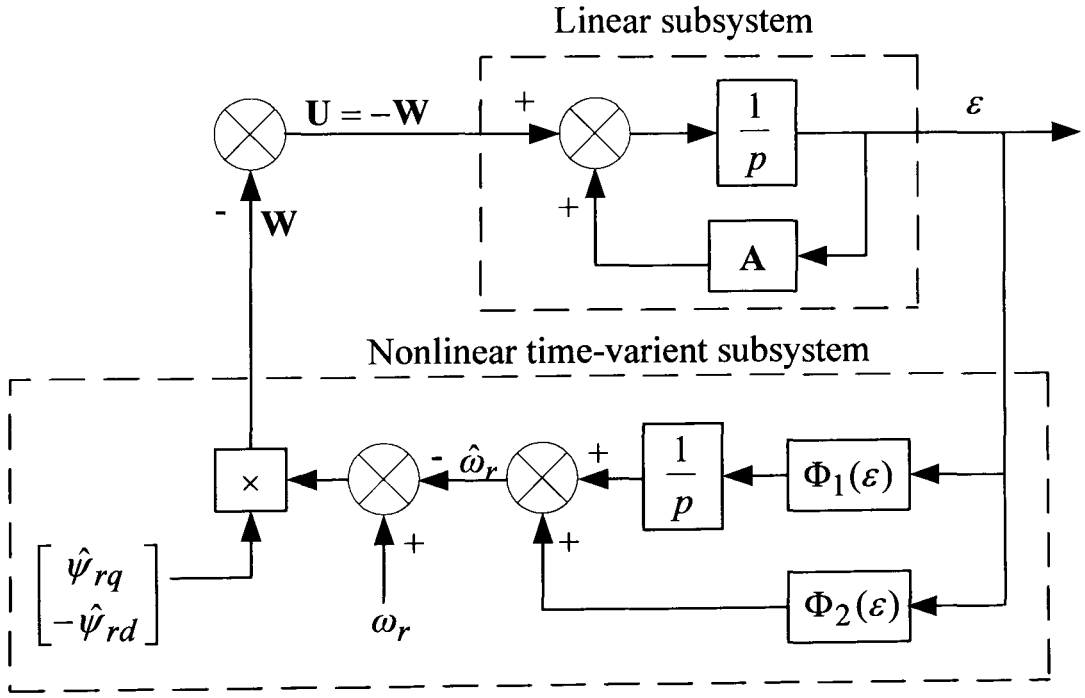

Fig. 3.12 Representation of MRAS as a nonlinear feedback system

Defining an adaptation law as follow [53]:

$$\hat{\omega}_r = \Phi_2(\varepsilon) + \int_0^t \Phi_1(\varepsilon)\, d\tau \tag{3.67}$$

To satisfy Popov's integral inequality:

$$\int_0^t \varepsilon^T \mathbf{W}\, dt \geq -\gamma_o^2 \tag{3.68}$$

Substituting from (3.62), (3.66) and (3.67) into (3.68) yields the following inequality:

$$\int_0^t (\varepsilon_d \hat{\psi}_{rq} - \varepsilon_q \hat{\psi}_{rd})(\omega_r - \Phi_2(\varepsilon) - \int_0^t \Phi_1(\varepsilon)\, d\tau) dt \geq -\gamma_o^2 \tag{3.69}$$

This inequality can be satisfied using the following functions [53]:

$$\begin{aligned} \Phi_1(\varepsilon) &= k_2(\varepsilon_q \hat{\psi}_{rd} - \varepsilon_d \hat{\psi}_{rq}) = K_i(\psi_{rq} \hat{\psi}_{rd} - \psi_{rd} \hat{\psi}_{rq}) \\ \Phi_2(\varepsilon) &= k_1(\varepsilon_q \hat{\psi}_{rd} - \varepsilon_d \hat{\psi}_{rq}) = K_p(\psi_{rq} \hat{\psi}_{rd} - \psi_{rd} \hat{\psi}_{rq}) \end{aligned} \tag{3.70}$$

where $\Phi_2(\varepsilon)$ and $\Phi_1(\varepsilon)$ are the proportional and integral parts of the adaptation law respectively. Defining the speed tuning signal ε_ω as the cross product between reference and adaptive model output vectors which can be written as:

$$\varepsilon_\omega = \psi_{rq} \hat{\psi}_{rd} - \psi_{rd} \hat{\psi}_{rq} \tag{3.71}$$

This speed tuning signal is minimized by a PI controller which generates the estimated value of the rotor speed as shown in Fig. 3.13. Estimated rotor speed can be expressed as:

$$\hat{\omega}_r = (K_p + \frac{K_i}{p})\, \varepsilon_\omega \tag{3.72}$$

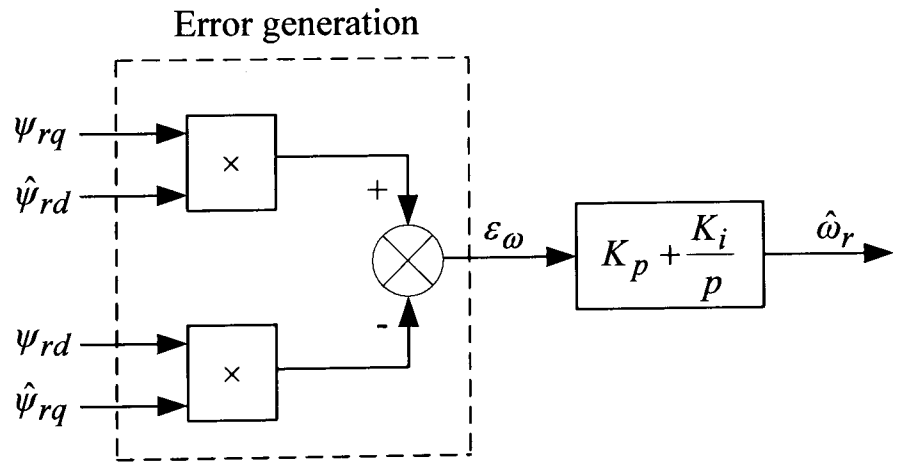

Fig. 3.13 Adaptation mechanism for MRAS observer

3.5 Conclusion

This chapter has presented the induction machine dynamic modelling using space vector theory. Transformations from three phase to two phase and between different reference frames have been discussed. Accordingly, a two-axis state space representation of the IM in the stator frame has been also developed. The machine equations, expressed

in the synchronous frame, have been then used to explain the principles of vector control strategy. Rotor speed estimation of the IM using MRAS approach has been presented. Reference and adaptive models that form the rotor flux-MRAS observer have been defined based on machine equations. Finally, the design of an appropriate adaptation mechanism using hyperstability criterion has been demonstrated.

CHAPTER 4

THE EXPERIMENTAL SYSTEM

4.1 Introduction

To allow practical testing of the schemes developed in this project an implementation in real time is required. An experimental platform based on a 7.5 kW induction machine and dSPACE DS1103 controller board is used to validate the proposed schemes. This experimental setup should allow the analysis of both open loop and sensorless modes of operation. The test rig, which has been developed in another work [84], consists mainly of an induction machine, AC drive, DC machine, DC drive, microprocessor-based control system and various interface circuits. The architecture of the experimental system is shown in Fig. 4.1. The main components of the experimental system are described in details in the following sections.

4.2 The Induction Machine

A 7.5 kW, 415 V, 50 Hz, 4-pole delta connected three phase squirrel-cage induction machine, manufactured by Brook Hansen, is used as the tested machine. To obtain the equivalent circuit parameters of the machine a set of tests has been carried out as

described in [85]. These tests consist of DC, no-load and locked rotor tests. The DC test is used to calculate the stator resistance value, while the no-load test is used to calculate the magnetizing inductance and the core and mechanical losses. Finally the locked rotor test is used to calculate the stator and rotor leakage inductances and the rotor resistance. The parameters for the delta connected machine obtained from these tests are given in Table 4.1.

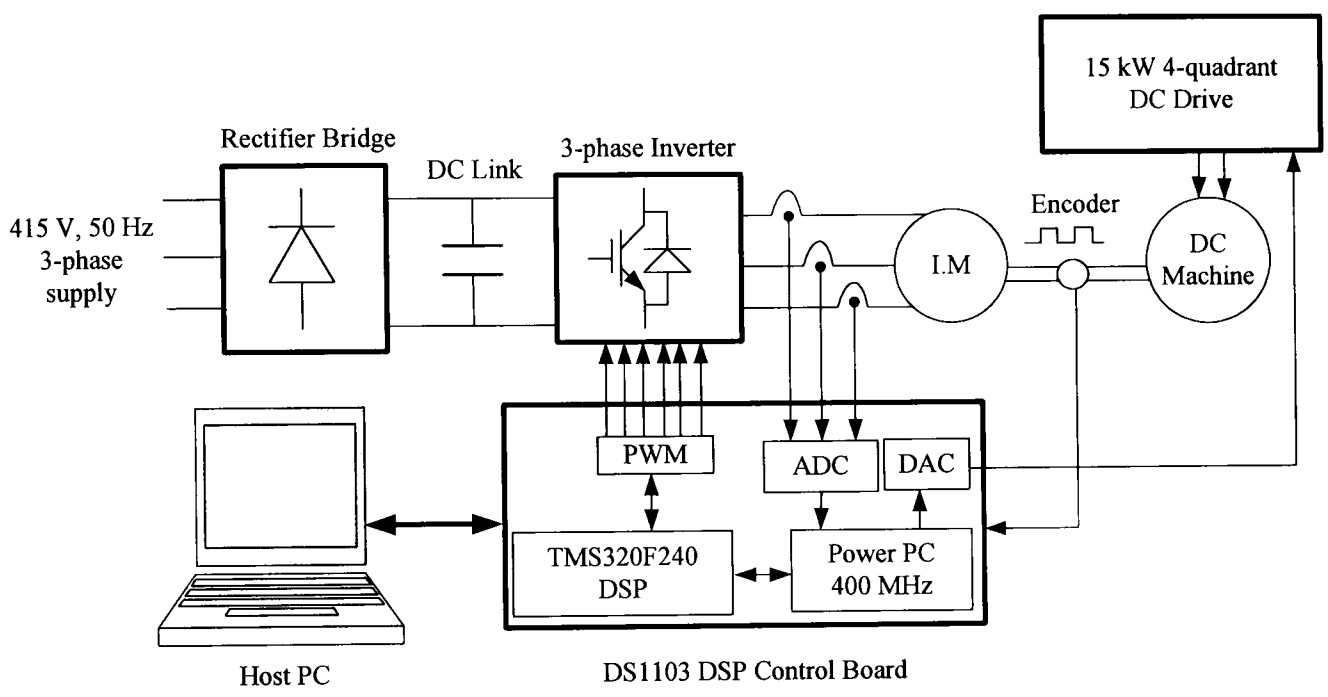

Fig. 4.1 Experimental system architecture

Table 4.1

Equivalent circuit parameters for the delta connected machine

Machine parameter	**Value**
R_s	2.33 Ω
R_r	2.11 Ω
L_{ls}	13.54 mH
L_{lr}	13.54 mH
L_m	309.67 mH

The parameters for the delta connected machine can be transformed into star equivalent parameters using the delta-star conversion $z_{star} = \frac{z_{delta}}{3}$. The star equivalent parameters for the induction machine are given in Table 4.2.

Table 4.2

Star Equivalent parameters

Machine parameter	**Value**
R_s	0.7767 Ω
R_r	0.703 Ω
L_{ls}	4.51 mH
L_{lr}	4.51 mH
L_m	103.22 mH

These parameters are converted to their equivalent dynamic two-axis model using appendix equation (A.32) [70]. The *d-q* axis parameters of the induction machine are given in Table 4.3.

Table 4.3

Two-axis model parameters

Machine parameter	**Value**
R_s	0.7767 Ω
R_r	0.703 Ω
L_s	107.73 mH
L_r	107.73 mH
L_m	103.22 mH

4.3 The AC Drive

The AC drive power electronics consists mainly of a rectifier, DC link circuit and an inverter. The rectifier is a Semikron SKD51/14 50A 3-phase diode bridge which consists of six uncontrolled diodes. The rectifier output voltage is smoothed through a 0.75 mH, 40 A choke, placed on the AC side, and DC link capacitors consisting of two 4700 μF, 400V capacitors connected in series. Two balancing resistors of 22 kΩ each are connected across the capacitors to ensure voltage sharing. To limit the inrush current when the system is first switched on, a 56Ω-50W aluminium housed wire wound resistor is used. A relay is placed in parallel with the inrush resistor to provide a short circuit path when the capacitor is charged to prevent power loss in the resistor during normal operation. A system is provided to prevent excessive increase in the DC link voltage when the motor is braking. This is achieved by using a SKAI100 DC link brake chopper

that switches on a resistor to dissipate the regeneration power and reduce the capacitor charge and hence decrease the DC link voltage. The DC link circuit is shown in Fig. 4.2.

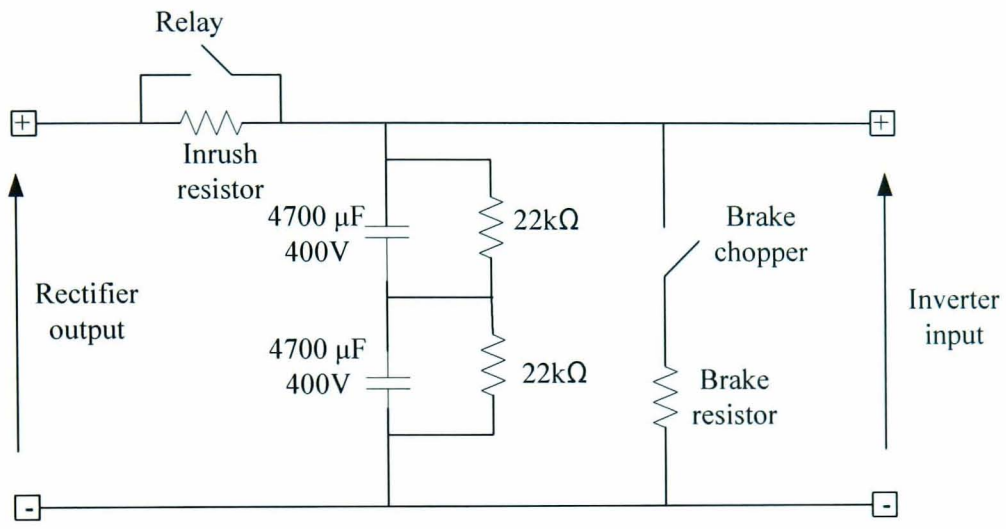

Fig. 4.2 DC link circuit

The drive inverter uses Semikron SKM50GB123D 1200V, 50A half bridge IGBT power modules. The switching pattern of the IGBT's is supplied through a Semikron SKHI22B dual gate driver. Tasks achieved by the gate driver include isolation between power and control circuits, short circuit protection, error outputs and programmable dead time generation. The inverter outputs are connected to the induction machine through current sensors. A photograph of the experimental hardware is shown in Fig. 4.3.

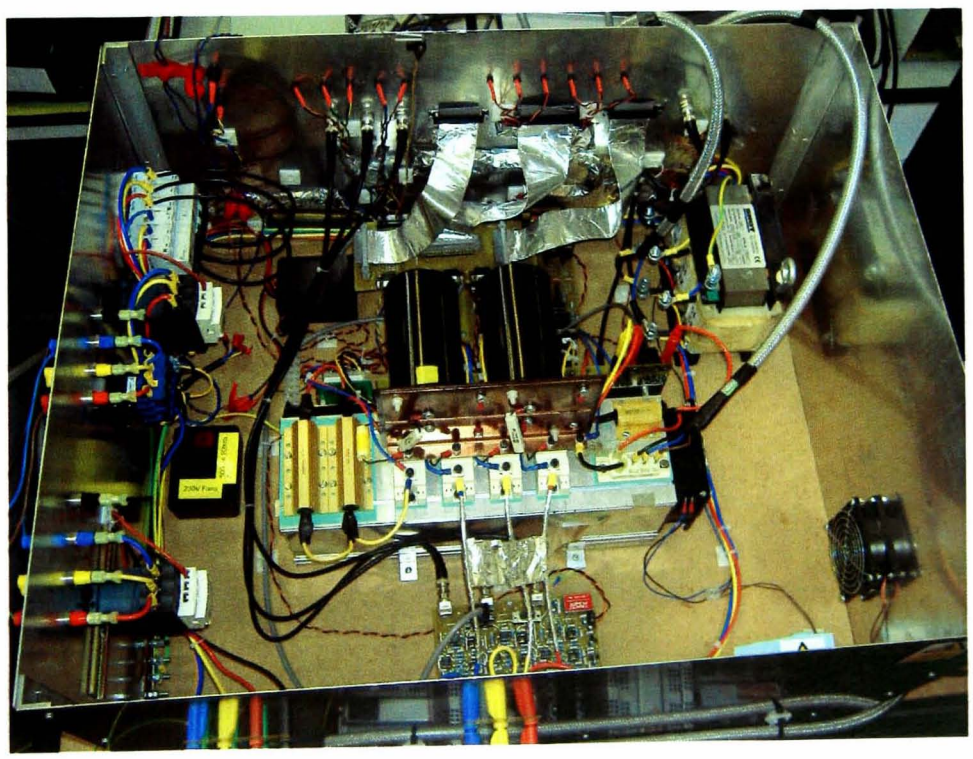

Fig. 4.3 Photograph of the experimental hardware

4.4 The DC Machine and the DC Drive

A 9 kW, 240 V, 37.5 A DC load machine is coupled to the induction machine shaft and is used as a load for the IM. The DC machine is connected in a separately excited configuration to allow separate control of the torque and speed. A 15 kW four quadrant DC drive from the Control Techniques "Mentor" range is used to control the DC machine to provide different levels of loading on the induction machine up to full load.

4.5 The Microprocessor Control System

To control the IM a dSPACE DS1103 control board is used which consists of a Power PC 604e processor running at 400 MHz, and a Slave Texas Instruments TMS320F240 DSP [86]. Used with the dSPACE Real-Time Interface (RTI) and Matlab Real Time Workshop (RTW) the Simulink model is automatically converted into C-code which is compiled and downloaded to the control board program memory. This provides a fast and easy way to implement and test control schemes in real time. RTI consists of a set of I/O interface blocks which connects the Simulink model to the real world. Experiment control is performed by ControlDesk which is used to monitor different signals and tune parameters. Interfaced with Simulink, ControlDesk performs the necessary experiment tasks using a graphical interface.

The analogue input signals from the test rig to the dSPACE system are the three phase current waveforms, the DC link voltage (V_{DC}) and current. The three phase current waveforms and the DC link voltage are sampled through 4 ×16 bit ADCs where as the DC link current waveform is sampled through 1×12 bit ADC. The load torque reference is generated from one of the eight 16 bit DAC channels.

The output from the dSPACE system gives the PWM signals for the inverter AC drive power electronics using a sinusoidal PWM technique. This output is provided from the PWM outputs of the slave TMS320F240 DSP. This signal is passed through a gate driver board before being applied to the inverter switches. The PWM switching frequency is 15 kHz with a dead time period of 1.5 μs.

To allow exchange of information between the control board and the power circuit, the dSPACE system is interfaced to the power stage via cards including a current sensing

circuit, DC link circuit, PWM circuit and gate driver board. Signal amplification and filtering and protection circuits are included into these interface cards.

LEM LA55P Hall effect current sensors were used to measure the three motor line currents with a conversion ratio of 1000:1. The sensor output is connected to a 100 Ω resistor to be transformed to measurable voltage signal of 0.1 V/A. The current sensing circuit is provided with an over-current protection using comparators. In case of over-current an error signal is sent to the gate driver to turn off the inverter IGBT's.

A potential divider is used to measure the DC link voltage giving an output of less than 5V at the maximum DC link voltage. The potential divider output is passed through an ISO124 voltage isolation amplifier and then a LPF RC filter is used to remove high frequency switching signals. The final output is obtained through a unity gain buffer amplifier.

A LAH50P current sensor is used to measure the DC link current with a conversion ratio of 2000:1. Using a 200 Ω resistor the current signal is converted to a voltage signal of 0.1 V/A.

The actual motor speed is measured by a Hohner 5000 pulses/revolution incremental optical encoder attached to the shaft of the induction machine. The encoder signal is interfaced to the dSPACE system via an incremental encoder interface. The rotor speed measurement is to allow standard *encodered* vector control operation and is employed as a reference for sensorless operation. A photograph of the whole laboratory system is shown in Fig. 4.4.

Fig. 4.4 Laboratory photograph of the experimental setup

4.6 Dead Time Compensation

Dead time is a time delay inserted in the switching signals of a PWM inverter to avoid short circuit of the DC link if two switches of the same arm are "on" at the same time. Dead time causes distortion in the output voltage waveform by introducing unwanted harmonic components making the output voltages deviate from the reference voltages [87, 88]. The effect becomes more severe in the low speed region of operation. Therefore a simple dead time compensator similar to [87, 89] is implemented. The block diagram of the rotor flux oriented control scheme with dead time compensation is shown in Fig. 4.5.

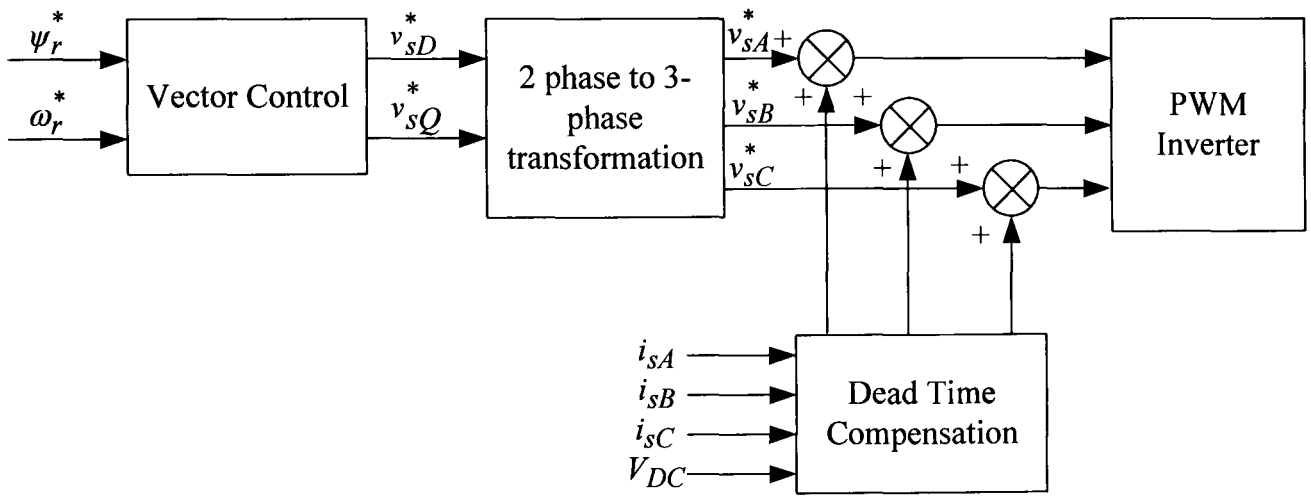

Fig. 4.5 Block diagram for vector control implementation with dead time compensation

4.7 Conclusion

This chapter has presented the experimental setup used to validate the developed schemes based on a 7.5 kW induction machine and dSPACE DS1103 control board. The main components of the hardware and software configurations of the experimental system have been described. Finally, the compensation of dead time effects in the inverter has been presented.

CHAPTER 5

DESIGN OF ADAPTATION MECHANISM FOR ROTOR FLUX-BASED MRAS

Two novel adaptation schemes are proposed to replace the classical PI controller used in model reference adaptive speed estimation schemes which are based on rotor flux. The first proposed adaptation scheme is based on SM theory. A new speed estimation adaptation law is derived using Lyapunov theory to ensure estimation stability as well as fast error dynamics. The other adaptation mechanism is based on a FL strategy. A detailed comparison between the new and conventional schemes is carried out in both open loop and sensorless modes of operation. Various simulation and experimental tests are performed to examine the performance of different schemes when the vector control IM drive is working at very low speed.

5.1 Introduction

PI controllers are widely used in industrial control systems applications. They have a simple structure and can offer a satisfactory performance over a wide range of operation. Therefore, the majority of adaptation schemes described in the literature for

MRAS speed observer employ a simple fixed gain linear PI controller to generate the estimated rotor speed as shown in Fig. 5.1. However, due to the continuous variation in the machine parameters and the operating conditions in addition to the nonlinearities present in the inverter, fixed gain PI controllers may become unable to provide the required performance. Not much attention has been devoted to study other types of adaptation mechanisms used to minimize the speed tuning signal to obtain the estimated speed.

In this chapter this point is addressed by presenting two novel nonlinear adaptation mechanisms to replace the classical PI controller used in the conventional rotor flux based-MRAS speed observer. A novel nonlinear adaptation scheme based on SM theory is proposed to improve the speed estimation performance. The new speed estimation adaptation law, which ensures estimation stability and fast error dynamics, is derived based on Lyapunov theory. Furthermore, a FLC is proposed as another nonlinear optimizer to minimize the speed tuning signal used for the rotor speed estimation. The performance of the new and conventional schemes is compared based on detailed simulation and experimental tests in both open loop and sensorless modes of operation. Focus is given to operation at low speed which represents a critical region of operation for MRAS observer.

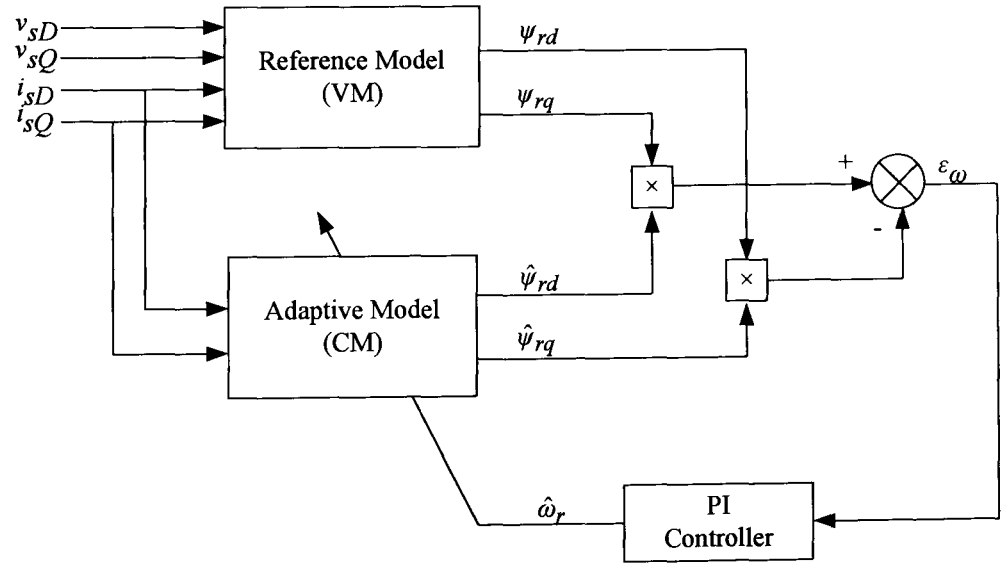

Fig. 5.1 Classical rotor flux MRAS with PI adaptation mechanism

5.2 Sliding Mode Adaptation Mechanism for MRAS Observer

Different SM strategies have been proposed to control IM drives [24, 25, 90]. Such strategies show robustness against motor parameter variation, better external

disturbance rejection, stability and fast dynamic response. However, one of the major drawbacks of the conventional SM strategy is the chattering in the steady state. In this section a new application of SMC is introduced as an adaptation mechanism for error minimization in MRAS speed observer to generate the estimated rotor speed.

5.2.1 Introduction to Sliding Mode Control

SMC is a Variable Structure Control (VSC) method with a high frequency discontinuous control action which switches between several functions depending on the system states [49]. This action forces the states of the system to slide on a predefined hypersurface (a surface embedded in the state space). The principle of SMC is to define a switching control law to drive the state trajectory onto a switching surface and to maintain this trajectory sliding on this surface for all subsequent time [91]. The sliding mode consists of a reaching phase where the state trajectory is driven to the surface $s = 0$ and reaches it in a finite time, followed by a sliding phase where it slides on the switching surface to an equilibrium point, as shown in Fig. 5.2 [24]. Usually the states x_1 and x_2 are chosen to be the error function and its derivative or integral and in this case the equilibrium point is (0, 0). The control law is defined based on Lyapunov theory to guarantee the motion of the state trajectory towards the sliding surface [91]. This is done by choosing a hitting control gain to maintain the derivative of Lyapunov function always negative definite [92].

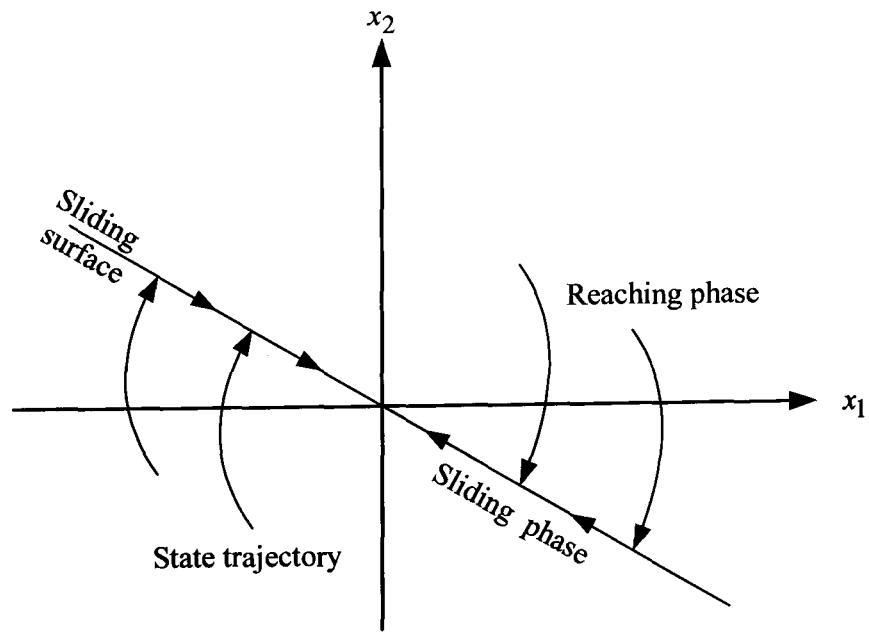

Fig. 5.2 The sliding mode principle

5.2.2 Sliding Mode MRAS Observer

The classical SM strategy applied for control applications is modified to fit with the speed estimation problem. Hence a novel SM rotor flux MRAS (MRAS-SM) is developed to replace the conventional constant gain PI controller. A new speed estimation adaptation law for the SM scheme is derived based on Lyapunov theory to ensure stability and fast error dynamics. Defining the speed tuning signal as in (3.71):

$$\varepsilon_\omega = \psi_{rq}\hat{\psi}_{rd} - \psi_{rd}\hat{\psi}_{rq} \tag{5.1}$$

Defining a switching surface s as:

$$s = \varepsilon_\omega + \int k\varepsilon_\omega \, dt \quad k > 0 \tag{5.2}$$

Such that the error dynamics at the sliding surface $s = 0$ will be forced to exponentially decay to zero. When the system reaches the sliding surface, this gives:

$$\dot{s} = \dot{\varepsilon}_\omega + k\varepsilon_\omega = 0 \tag{5.3}$$

and the error dynamics can be described by:

$$\dot{\varepsilon}_\omega = -k\varepsilon_\omega \tag{5.4}$$

The SM control law can be found using Lyapunov theory and defining the Lyapunov function candidate [92]:

$$v = \frac{1}{2}s^2 \tag{5.5}$$

According to Lyapunov theory, if the function $\dot{v}$ is negative definite, this will ensure that the state trajectory will be driven and attracted toward the sliding surface s and once reached, it will remain sliding on it until the origin is reached asymptotically [92]. The time derivative of Lyapunov function in (5.5) can be calculated as:

$$\dot{v} = s\dot{s} \Leftrightarrow s\left(\dot{\varepsilon}_\omega + k\varepsilon_\omega\right) \tag{5.6}$$

Differentiating (5.1), yields:

$$\dot{\varepsilon}_\omega = \dot{\psi}_{rq}\hat{\psi}_{rd} + \psi_{rq}\dot{\hat{\psi}}_{rd} - \dot{\psi}_{rd}\hat{\psi}_{rq} - \psi_{rd}\dot{\hat{\psi}}_{rq} \tag{5.7}$$

Substituting the CM (3.54) into (5.7) yields:

$$\begin{aligned}\dot{\varepsilon}_\omega = {} & \dot{\psi}_{rq}\hat{\psi}_{rd} - \dot{\psi}_{rd}\hat{\psi}_{rq} + \frac{L_m}{T_r}i_{sD}\psi_{rq} - \frac{1}{T_r}\hat{\psi}_{rd}\psi_{rq} \\ & - \frac{L_m}{T_r}i_{sQ}\psi_{rd} + \frac{1}{T_r}\hat{\psi}_{rq}\psi_{rd} - \hat{\omega}_r\left(\psi_{rq}\hat{\psi}_{rq} + \psi_{rd}\hat{\psi}_{rd}\right)\end{aligned} \tag{5.8}$$

By letting:

$$f_1 = \dot{\psi}_{rq}\hat{\psi}_{rd} - \dot{\psi}_{rd}\hat{\psi}_{rq} + \frac{L_m}{T_r} i_{sD}\psi_{rq} - \frac{1}{T_r}\hat{\psi}_{rd}\psi_{rq} - \frac{L_m}{T_r} i_{sQ}\psi_{rd} + \frac{1}{T_r}\hat{\psi}_{rq}\psi_{rd} \tag{5.9}$$

$$f_2 = \psi_{rq}\hat{\psi}_{rq} + \psi_{rd}\hat{\psi}_{rd} \tag{5.10}$$

Equation (5.8) can be written as:

$$\dot{\varepsilon}_\omega = f_1 - \hat{\omega}_r f_2 \tag{5.11}$$

and (5.3) can be written as:

$$\dot{s} = f_1 + k\varepsilon_\omega - \hat{\omega}_r f_2 \tag{5.12}$$

Substituting (5.12) into (5.6) yields:

$$\dot{v} = s\left(f_1 + k\varepsilon_\omega - \hat{\omega}_r f_2\right) \tag{5.13}$$

This derivative is negative definite if:

$$\left(f_1 + k\varepsilon_\omega - \hat{\omega}_r f_2\right) \begin{array}{ll} < 0 & for\ s > 0 \\ = 0 & for\ s = 0 \\ > 0 & for\ s < 0 \end{array} \tag{5.14}$$

This can be ensured if:

$$\hat{\omega}_r = \frac{f_1 + k\varepsilon_\omega}{f_2} + M\,sign(s) \quad M > 0 \tag{5.15}$$

where the sign function is defined as:

$$sign(s) = \begin{Bmatrix} -1 & for\ s < 0 \\ +1 & for\ s > 0 \end{Bmatrix} \tag{5.16}$$

Equation (5.15) represents the switching law of the SM controller and could be written in general form as:

$$\hat{\omega}_r = u_{eq} + u_s \tag{5.17}$$

where u_{eq} is the equivalent control which defines the control action that keeps the state trajectory on the sliding surface, u_s is the switching control which depends on the sign of the switching surface and M is the hitting control gain which makes (5.6) negative definite [92]. No design criterion is assigned to choose the value of M; however, its value should be selected high enough to make the manifold $s = 0$ in (5.2) attractive [51, 92]. Therefore the control law defined in (5.15) will guarantee the existence of the switching surface s in (5.2) and when the error function ε_ω reaches the sliding surface, the system

dynamics will be governed by (5.4) which is always stable [93]. The expressions for the equivalent and the switching control functions can be written as:

$$u_{eq} = \frac{f_1 + k\varepsilon_\omega}{f_2} \tag{5.18}$$

$$u_s = M\, sign(s) \quad M > 0 \tag{5.19}$$

The presence of the function f_2 in the denominator of the equivalent control u_{eq} may cause problems in the estimation performance of the proposed scheme if its value approaches zero. This problem can be avoided by allowing magnetizing of the machine before starting up and by adding a positive small value to f_2. The use of the sign function in the SM control (5.15) causes high frequency chattering due to the discontinuous control action which represents a severe problem when the system state is close to the sliding surface [92]. The block diagram of the novel MRAS observer employing SM adaptation mechanism (MRAS-SM) is shown in Fig. 5.3. Simulation and experimental results of this scheme will be given in section 5.4.

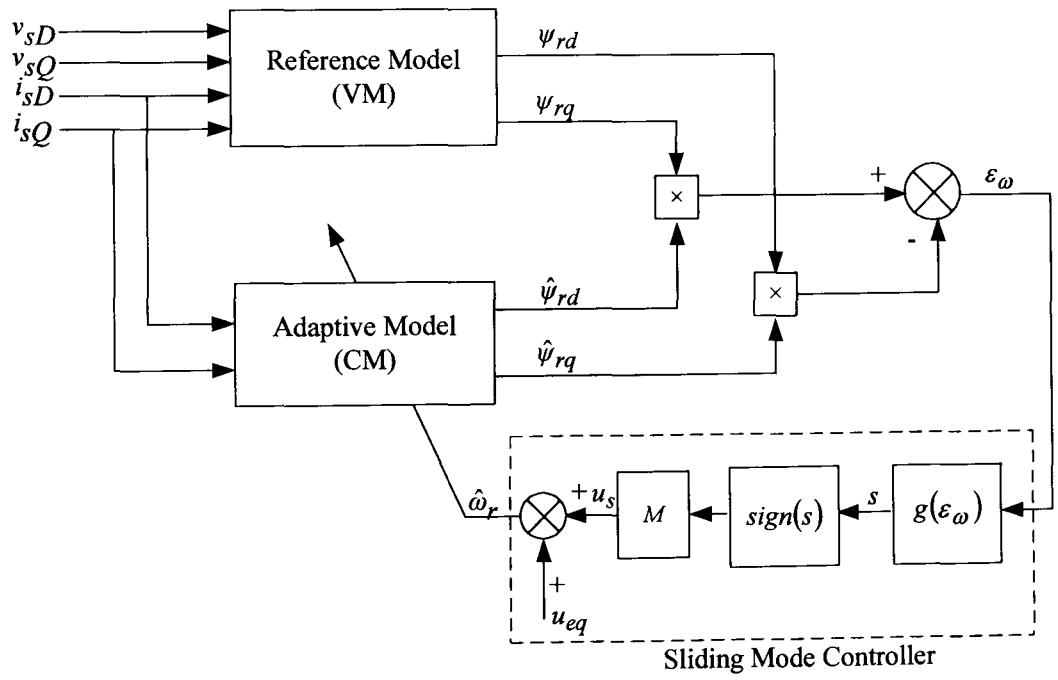

Fig. 5.3 MRAS-SM speed observer

5.3 Fuzzy Logic Adaptation Mechanism for MRAS Observer

Various applications of FL have shown a fast growth in the last few years. FLC has become popular in the field of industrial control applications for solving control, estimation and optimization problems [10]. In this section FL is proposed to replace the PI controller used for error minimization in the conventional MRAS speed observer.

5.3.1 Introduction to Fuzzy Logic

Design of classical control schemes needs an accurate model of the process to be controlled. These models could be deterministic assuming perfect model or stochastic including uncertainty and noise. However, experienced engineers may be able to control a process without needing a mathematical model based on their familiarity with its physical characteristics and their practical experience. FL mimics human reasoning to create controllers without any prior information about the mathematical model of the controlled system. This is achieved by converting the linguistic control strategy of human experience and knowledge into an automatic control strategy. Hence FL deals with linguistic variables which are in the form of words rather than numbers [94]. The idea of FL has been first introduced in 1965 by Zadeh [95] and has become an interesting field of control engineering. However, a lack of design techniques is considered as one of the major drawbacks of FLC. The most frequently used FL system is the Mamdani-type [94] which consists of three main parts: fuzzification, inference engine and defuzzification [10]. A detailed description of FLC principles is provided in Appendix B.

5.3.2 Fuzzy Logic MRAS Observer

FL technique has been applied to solve optimization problems for IM drives [30, 96-99]. It has been proposed to replace PI controllers in different error minimization applications [100, 101]. For the MRAS speed observer, the mechanism of the estimation of the rotor speed can be regarded as an optimization problem where the PI controller is generating a quantity, the estimated speed, in such a way as to minimize a specified error, which is the speed tuning signal in (5.1), in a feedback loop. Therefore, FLC can replace the conventional PI controller to solve the optimization problem.

The proposed FLC is a Mamdani-type rule base where the inputs are the speed tuning signal ε_ω in (5.1) and its change $\Delta\varepsilon_\omega$ which can be defined as:

$$\Delta\varepsilon_\omega(k) = \varepsilon_\omega(k) - \varepsilon_\omega(k-1) \tag{5.20}$$

In the z-domain this can be written as:

$$\Delta\varepsilon_\omega(z) = \left(\frac{z-1}{z}\right)\varepsilon_\omega(z) \tag{5.21}$$

These two inputs are multiplied by two scaling factors k_e and k_d respectively. The output of the controller is multiplied by a third scaling factor k_u to generate the actual value of the rate of change of the estimated speed. Finally, a discrete integration is performed to get the value of the estimated speed. Hence a PI-Type FLC is created with structure as shown in Fig. 5.4 [102, 103]. The expression for the estimated speed can be written as:

$$\hat{\omega}_r(k) = \hat{\omega}_r(k-1) + \Delta\hat{\omega}_r(k) \tag{5.22}$$

In the z-domain this can be written as:

$$\hat{\omega}_r(z) = \left(\frac{z}{z-1}\right)\Delta\hat{\omega}_r(z) \tag{5.23}$$

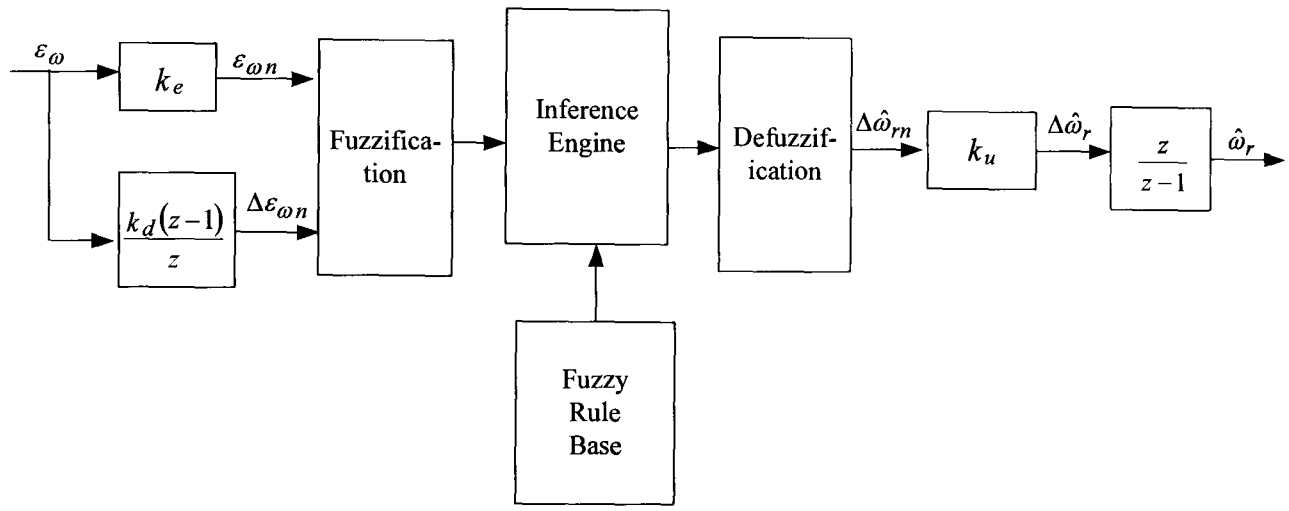

Fig. 5.4 Block diagram of PI-Type fuzzy logic controller

The choice of the values of the scaling factors greatly affects the performance of the FLC. A trial and error technique is usually used to tune these gains to ensure optimal performance of the controller [99]. Each variable of the FLC has seven membership functions. The following fuzzy sets are used: NB= NEGATIVE BIG, NM= NEGATIVE MEDUIM, NS= NEGATIVE SMALL, ZE= ZERO, PS= POSITIVE SMALL, PM= POSITIVE MEDUIM, PB= POSITIVE BIG. The universe of discourse of the inputs and outputs of the FLC are chosen between -0.1 and 0.1 with triangular membership functions as shown in Fig. 5.5. Table 5.1 shows the fuzzy rule base with 49 rules [99]. FLC is modelled using the Matlab Fuzzy Logic Toolbox graphical user interface (GUI) as described in Appendix B [94]. The overall MRAS speed observer with FL speed estimation mechanism (MRAS-FL) is shown in Fig. 5.6.

Table 5.1

Linguistic rule base for PI-Type fuzzy logic controller

$\Delta\varepsilon_\omega$ \ ε_ω	**NB**	**NM**	**NS**	**ZE**	**PS**	**PM**	**PB**
NB	NB	NM	NM	NS	NS	NS	ZE
NM	NM	NM	NS	NS	NS	ZE	PS
NS	NM	NM	NS	NS	ZE	PS	PM
ZE	NB	NM	NS	ZE	PS	PM	PM
PS	NS	NS	ZE	PS	PS	PM	PM
PM	NS	ZE	PS	PS	PS	PM	PM
PB	ZE	PS	PS	PM	PM	PB	PB

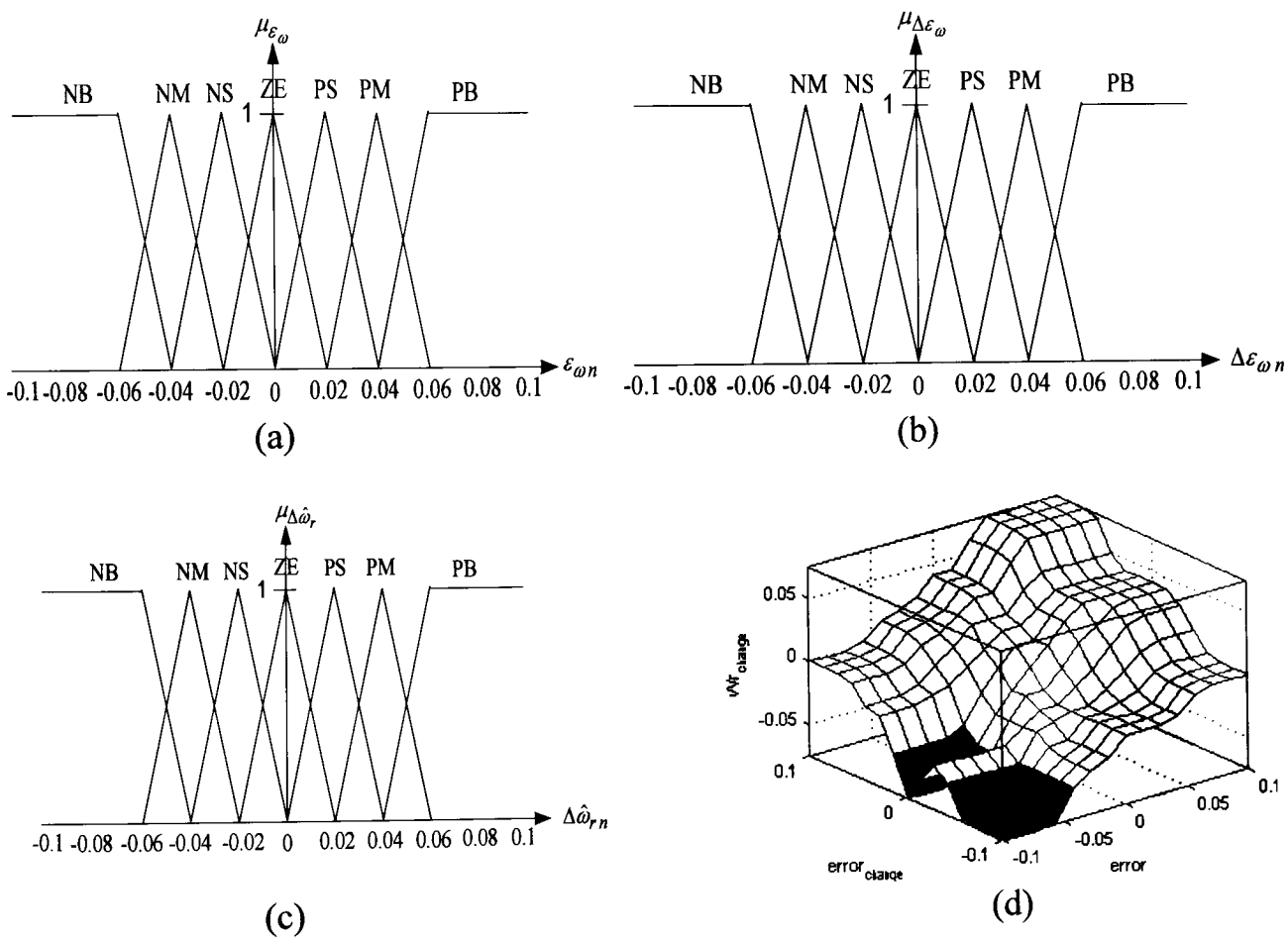

Fig. 5.5 Fuzzy controller input and output membership functions (a) error (b) error change (c) change in the estimated speed (d) surface

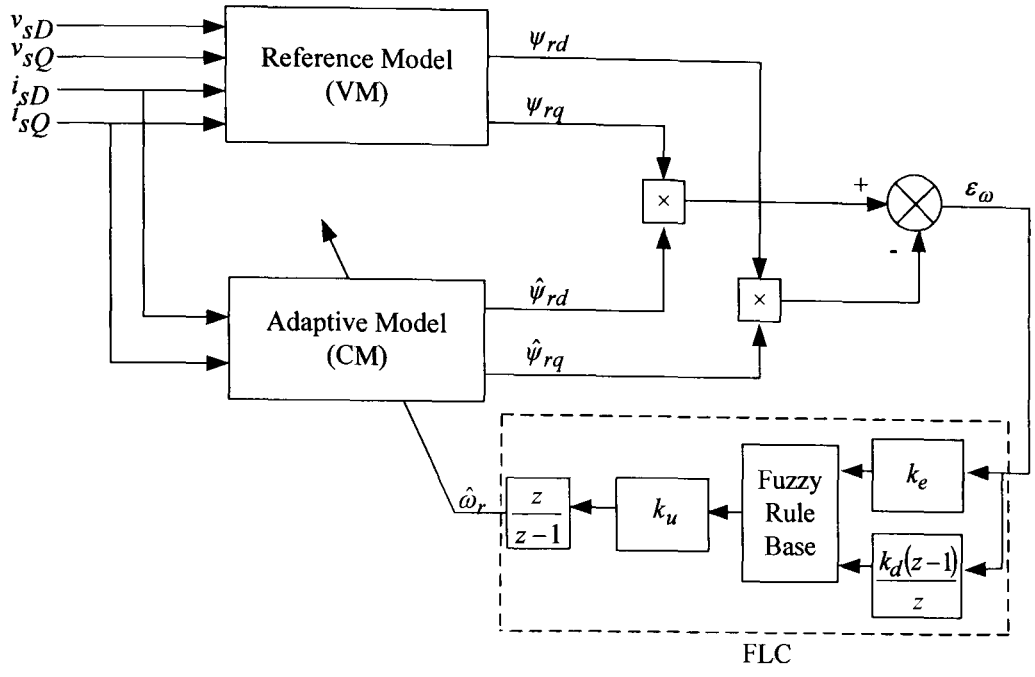

Fig. 5.6 MRAS-FL speed observer

5.4 Results

To examine the performance of the different adaptation mechanisms, simulation and experimental tests are carried out in both open loop and sensorless modes of operation. The three schemes, PI, FL and SM, are tested at different operating points when an indirect vector control IM drive is working at low speed. The PI speed and current controllers of the vector control drive are designed experimentally by a method based on Ziegler-Nichols as described in [104]. Parameters of different schemes are tuned online during experiments as will be explained later. These parameters are also used in the simulation stage. Simulation and experimental results are given in the following sections.

5.4.1 Simulation Results

As a first step of study, simulations of the proposed schemes were carried out to verify their ability to provide satisfactory speed estimation performance. The 4-pole induction machine, with parameters given in Table 4.3, was modelled using the *d-q* axis theory as described in chapter 3. The mechanical rotor speed ω_{rm} can be obtained from the mechanical model described by:

$$T_e - T_l = J\frac{d\omega_{rm}}{dt} + B\omega_{rm} \tag{5.24}$$

where the mechanical rotor speed ω_{rm} is related to its electrical value ω_r by:

$$\omega_{rm} = \frac{\omega_r}{P} \tag{5.25}$$

In (5.24), J is the motor moment of inertia that was obtained from a "run-down" test [105] and found to be approximately 0.22 Kg.m^{-2} and B is the friction coefficient that was found experimentally to be approximately 0.04 N.m/rad/s. These approximate values of the mechanical parameters are found to make the simulation results agree with the experimental results that will follow later.

The indirect vector control IM drive was developed in Matlab-Simulink environment using Simulink library blocks. The motor is directly fed from the reference voltages and hence an ideal inverter and pulse width modulator were assumed. The reference model of the MRAS observer was solved using pure integration and hence drift and initial condition problems were not considered in the simulation.

5.4.1.1 Open Loop Simulation

The performance of the proposed schemes was first investigated with open loop operation. The schematic of the open loop estimator simulation is shown in Fig. 5.7 where the MRAS observer output is not fed back into the drive system and the drive is working in *encodered* mode. The actual speed calculated from the mechanical model (5.24) is used for speed control and field angle calculation.

The vector control drive started with 100 rpm reference speed at no-load; at t=5s a 50% load was applied followed by a reference speed change to 50 rpm at t=8s. Simulation results for the MRAS estimator with the three adaptation mechanisms are shown in Figs. 5.8-5.12. Results show the superiority of the proposed adaptation mechanisms, FL and SM, over the conventional PI controller. The transient response of the two proposed schemes is faster than the PI controller. The minimum speed tuning signal was obtained from the SM scheme as shown in Fig. 5.11. However, the speed response features large chattering. The switching surface (5.2) of the SM scheme is shown in Fig. 5.12 with chattering around zero. During transients, the speed tuning signal obtained from the FL scheme is decaying to zero faster than the PI scheme. Consequently, the FL scheme shows better transient response compared to the PI scheme.

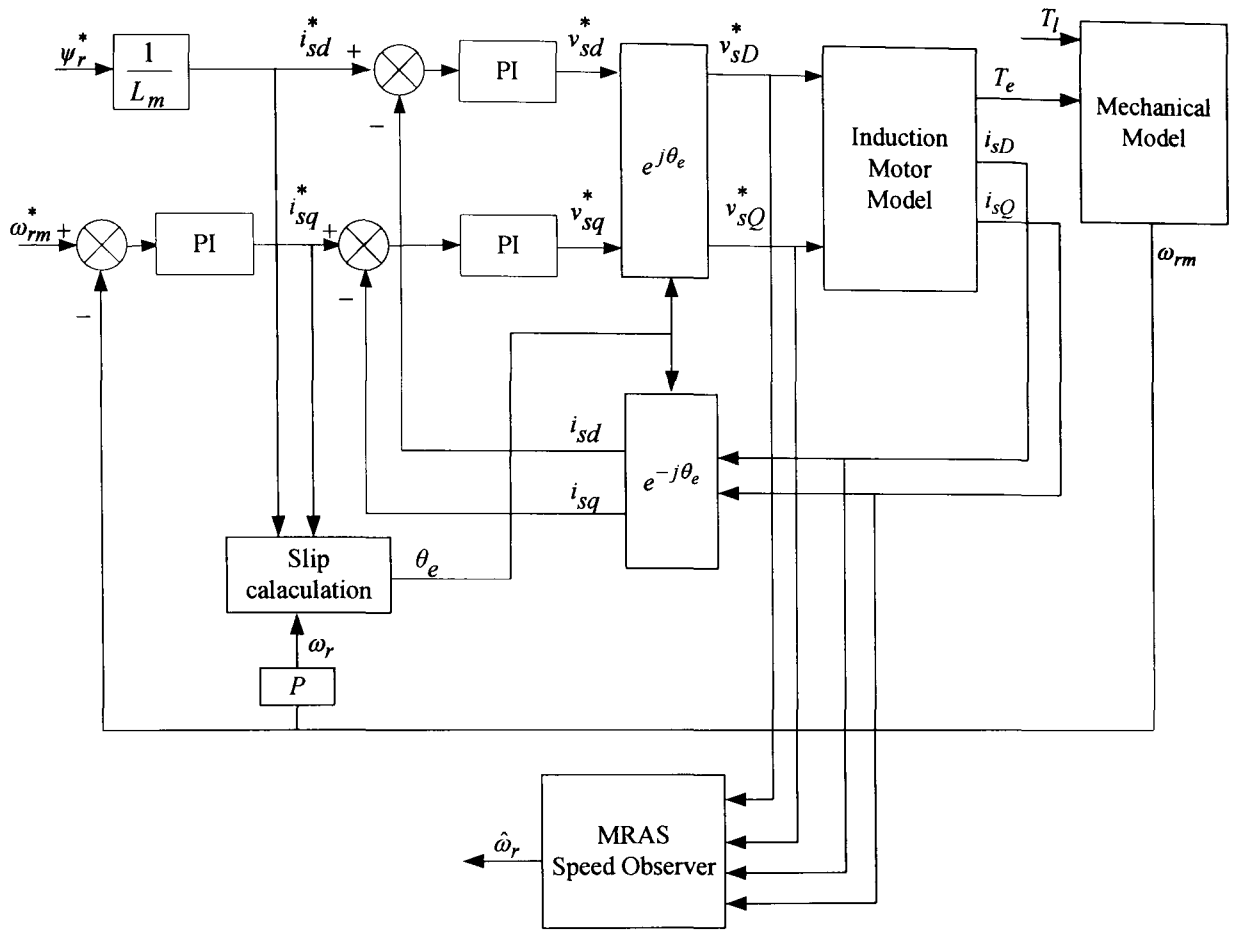

Fig. 5.7 Structure of open loop MRAS estimator simulation

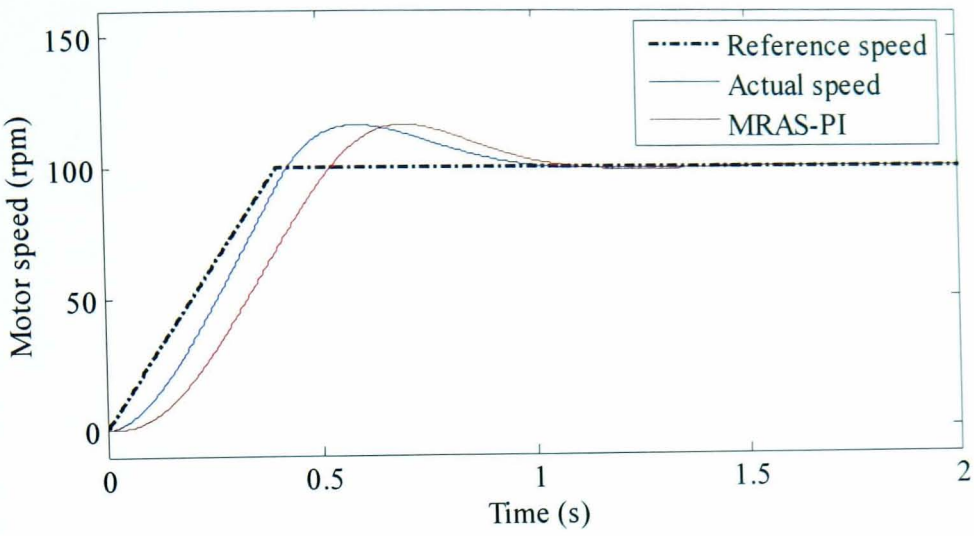

(a)

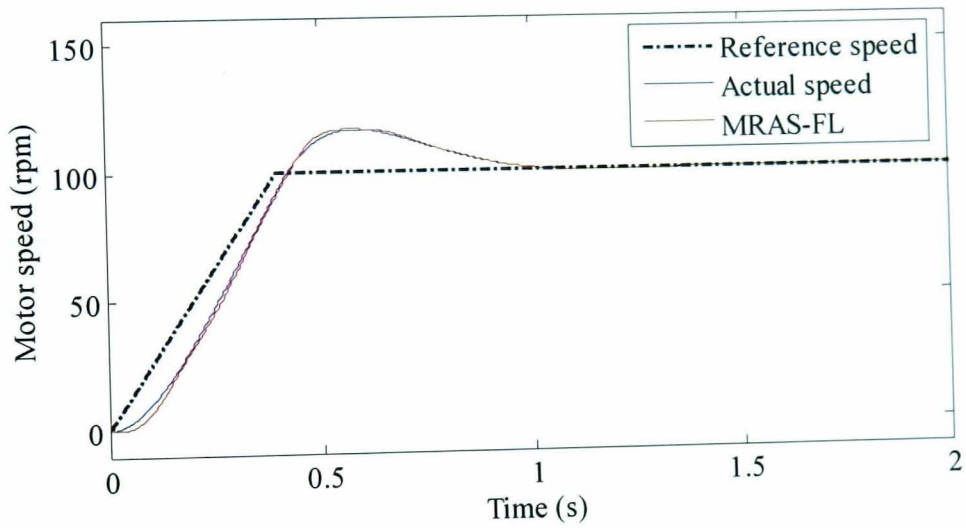

(b)

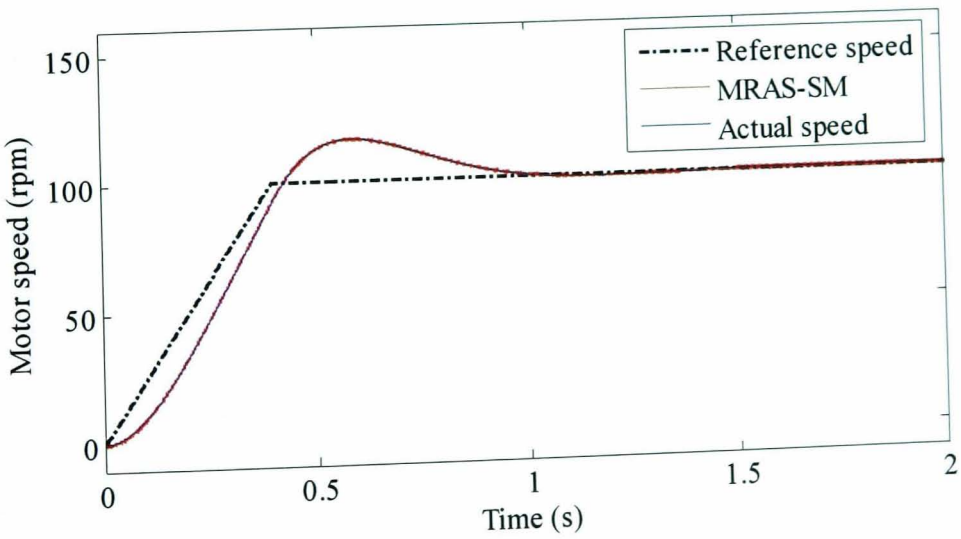

(c)

Fig. 5.8 Open loop response of MRAS estimator at 100 rpm speed reference (a) MRAS-PI (b) MRAS-FL (c) MRAS-SM

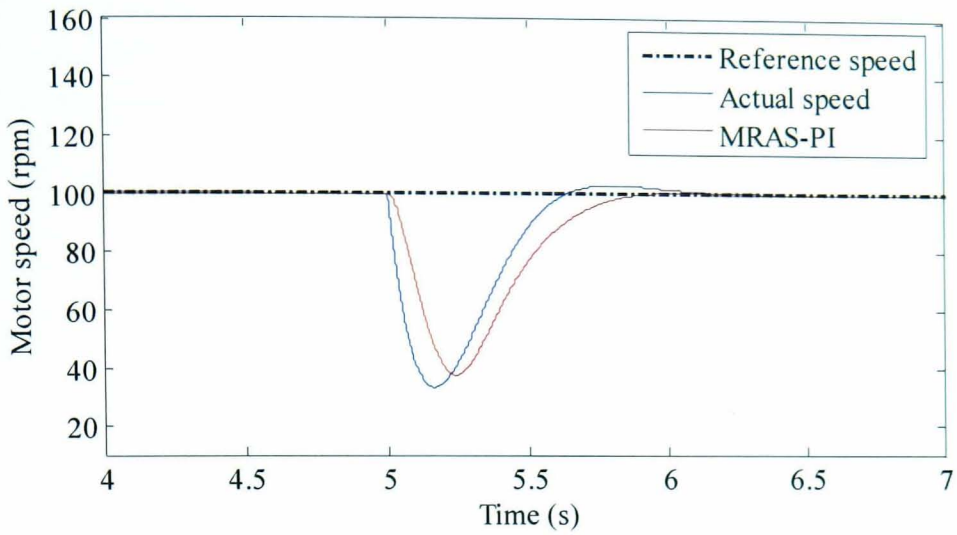

(a)

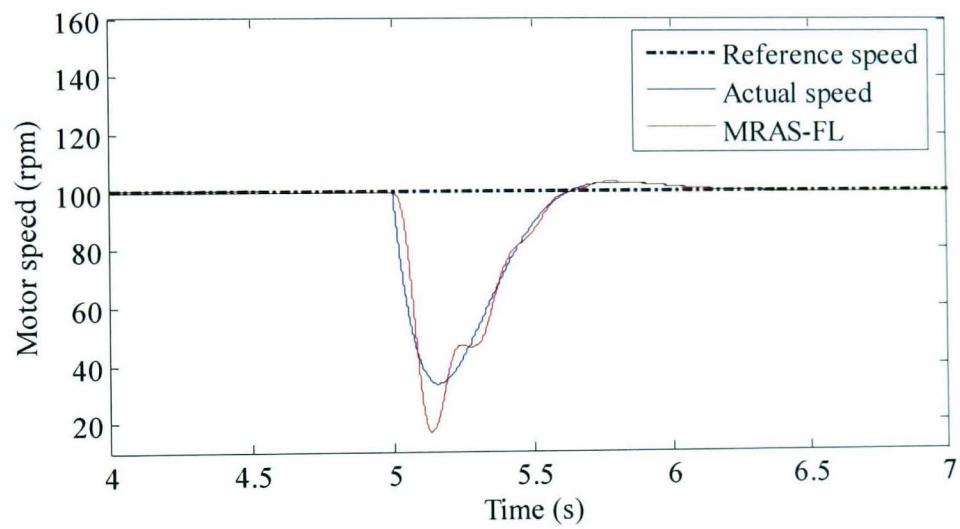

(b)

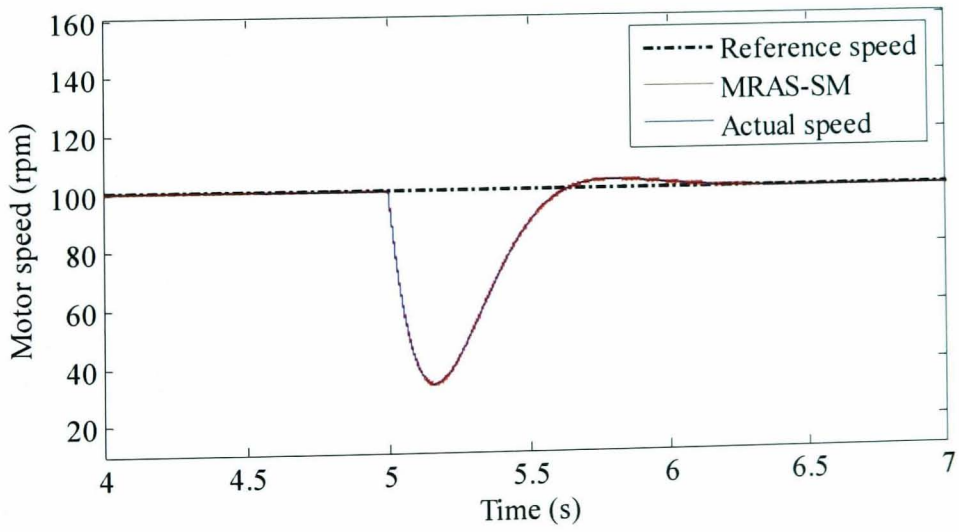

(c)

Fig. 5.9 Open loop response of MRAS estimator for 50% load disturbance rejection (a) MRAS-PI (b) MRAS-FL (c) MRAS-SM

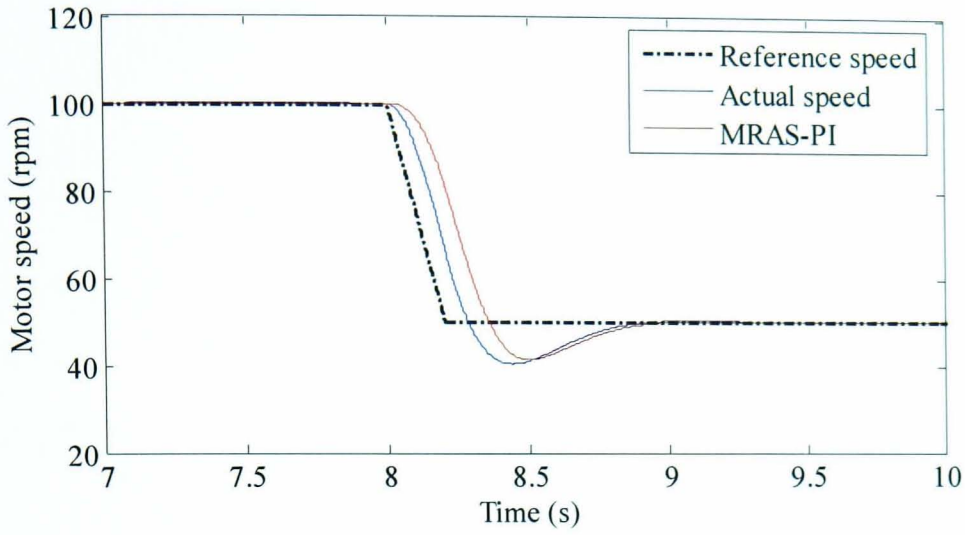

(a)

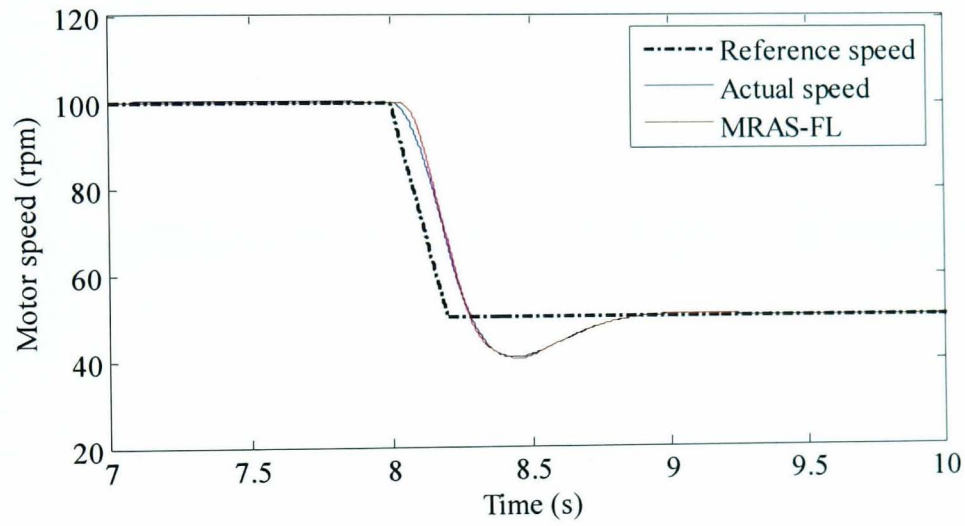

(b)

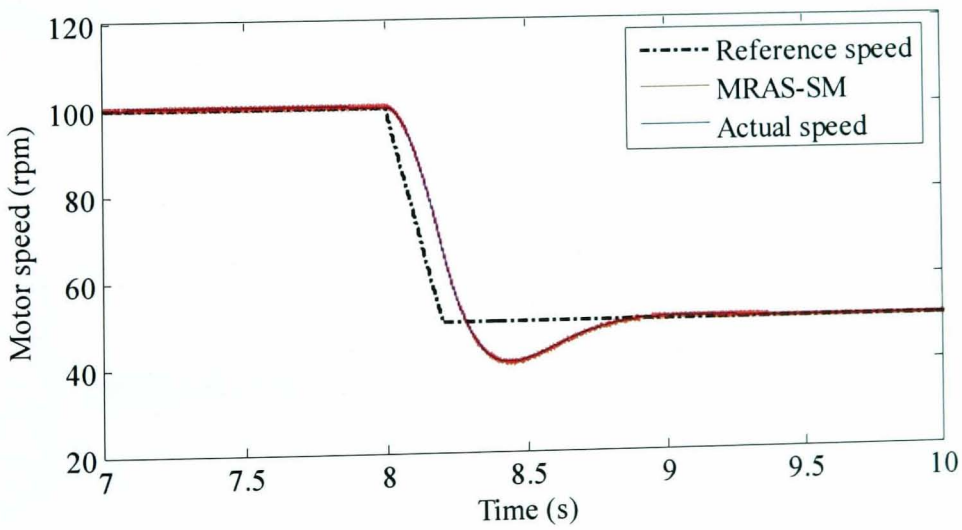

(c)

Fig. 5.10 Open loop response of MRAS estimator for reference speed change at 50% load (a) MRAS-PI (b) MRAS-FL (c) MRAS-SM

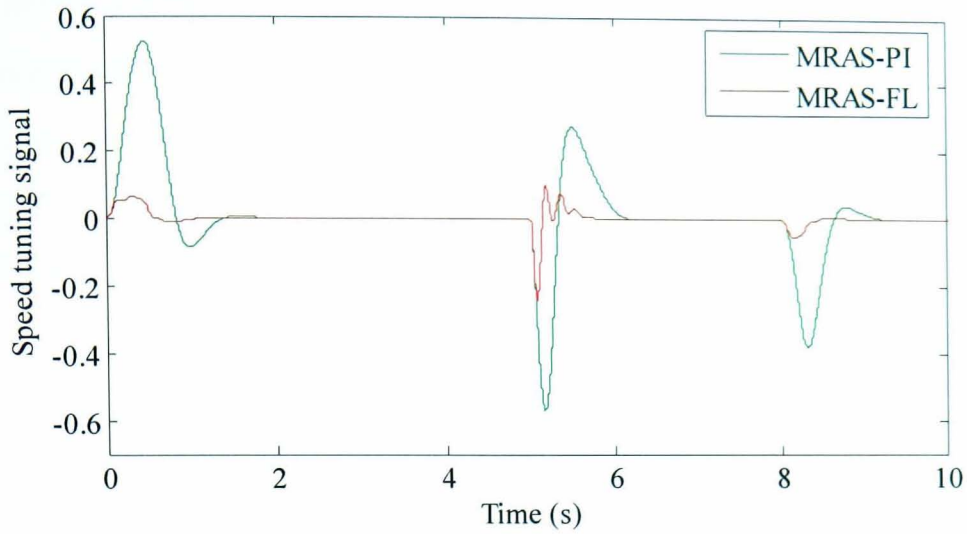

(a)

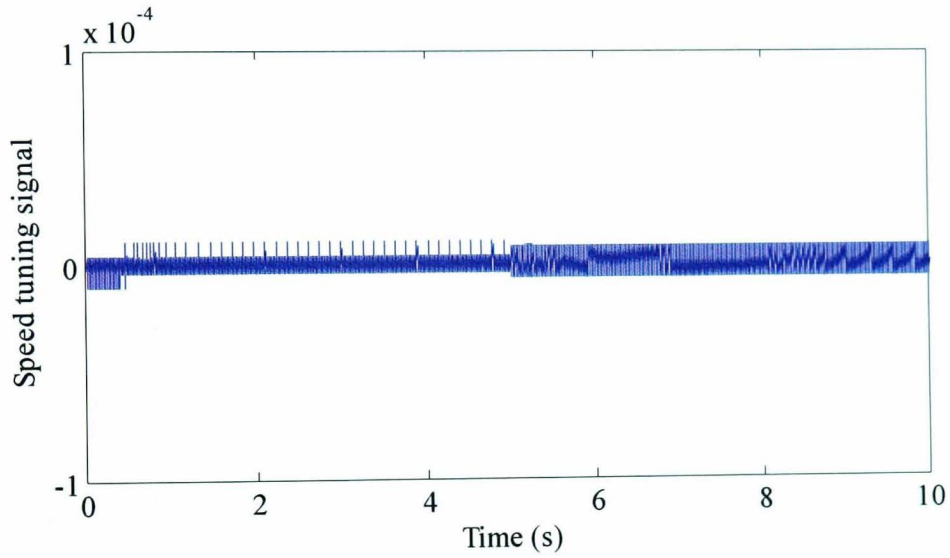

(b)

Fig. 5.11 Speed tuning signal for MRAS estimator open loop simulation (a) PI and FL (b) SM

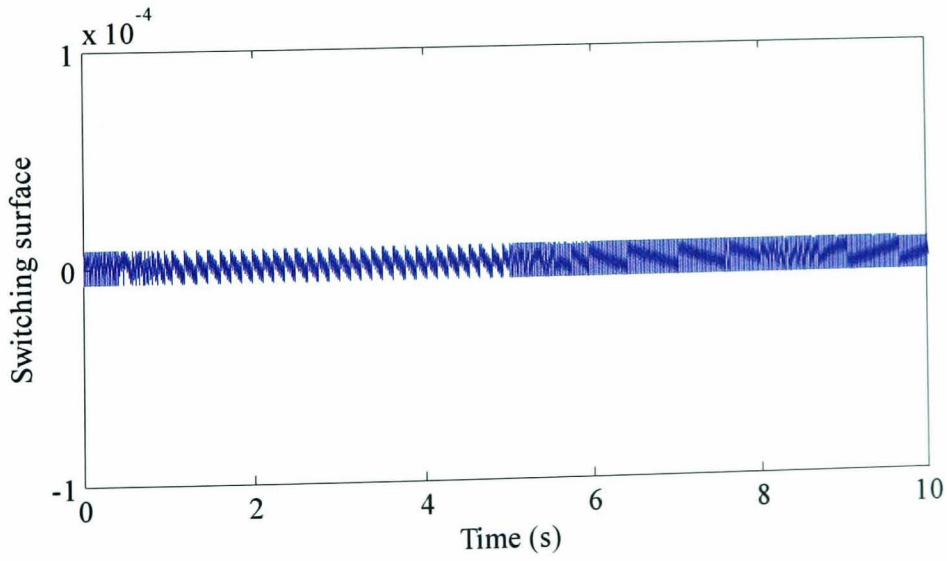

Fig. 5.12 Switching surface of SM scheme for open loop simulation

5.4.1.2 Closed Loop Simulation

After developing confidence with open loop operation, closed loop operation of the proposed schemes was considered. The schematic of the closed loop estimator simulation is shown in Fig. 5.13 where the MRAS observer output is fed back into the drive system and the drive is working in *sensorless* mode.

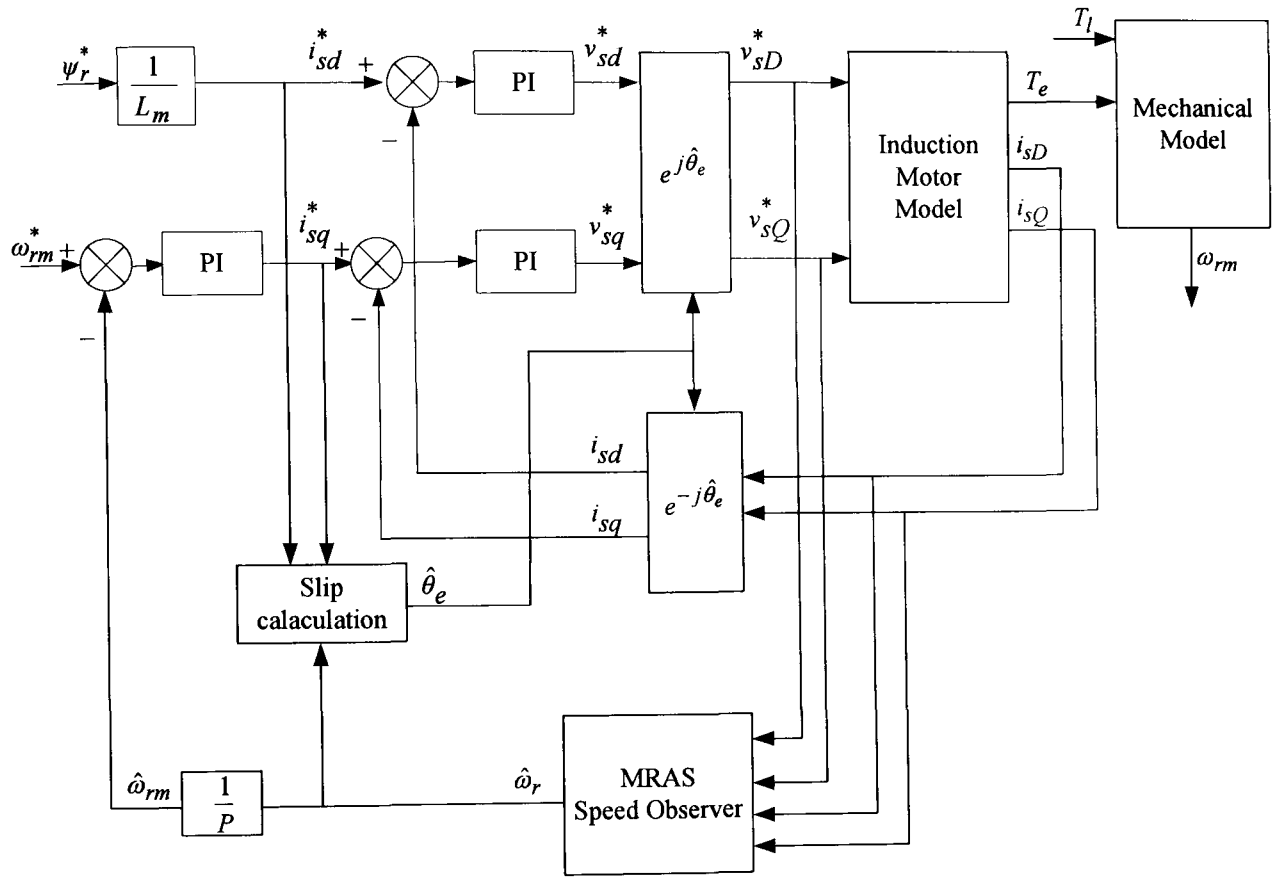

Fig. 5.13 Structure of closed loop MRAS estimator simulation

The closed loop simulation results for the MRAS estimator with the three adaptation mechanisms are shown in Figs. 5.14-5.18. The sensorless drive started with a speed command of 50 rpm at no-load followed by a 25% load torque applied at t=5s and a speed reversal command from 50 rpm to -50 rpm at 25% load. As for open loop operation, SM scheme still shows minimum speed tuning signal and FL scheme shows faster transient dynamics compared to the PI scheme.

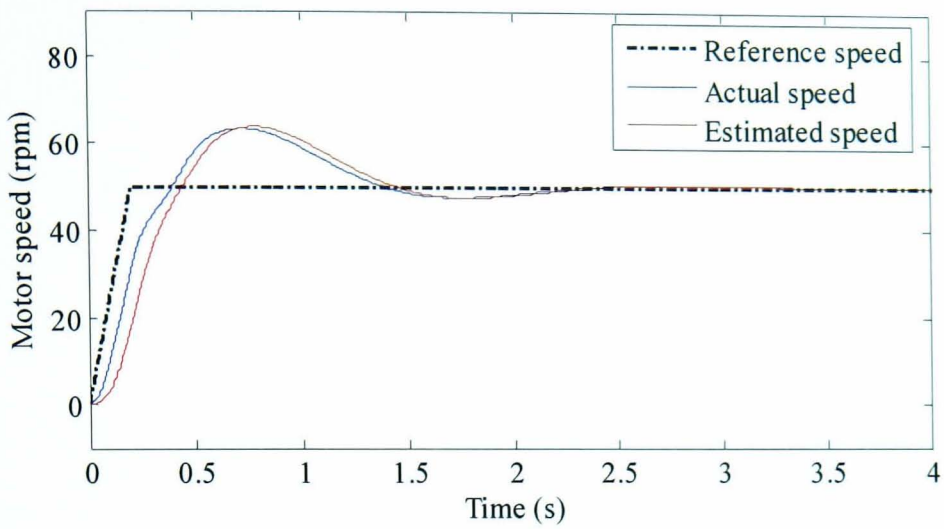

(a)

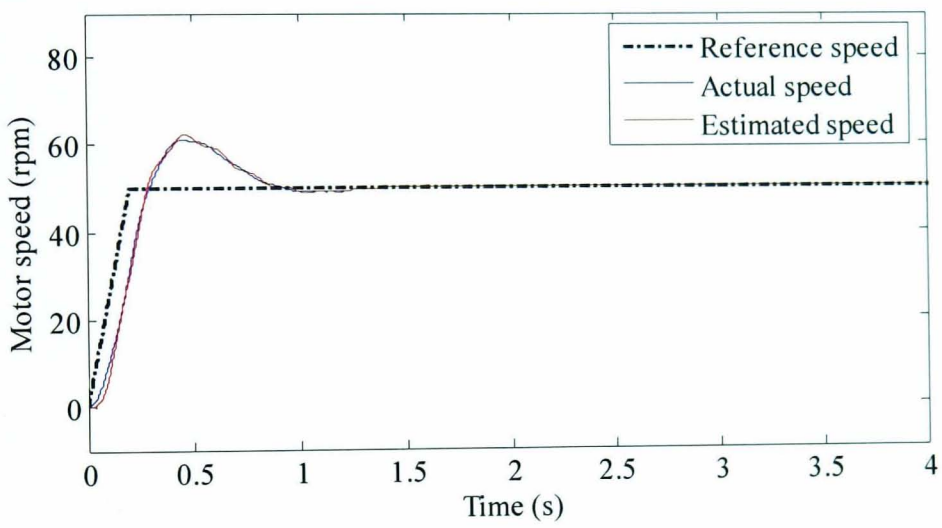

(b)

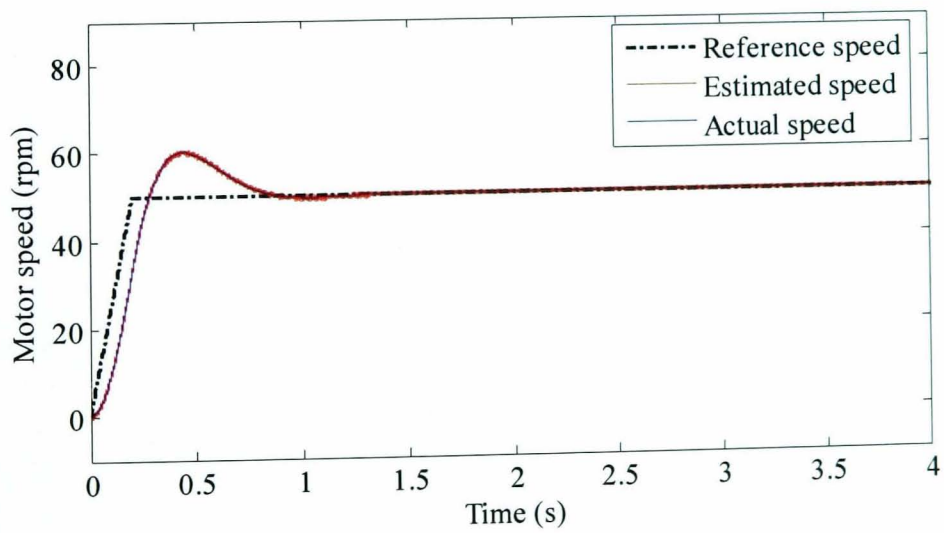

(c)

Fig. 5.14 Closed loop response of MRAS estimator at 50 rpm speed reference (a) MRAS-PI (b) MRAS-FL (c) MRAS-SM

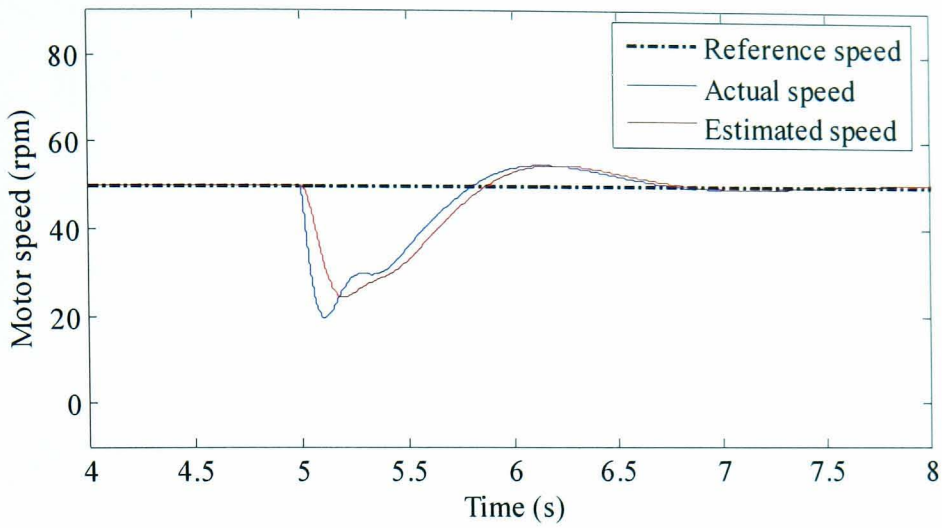

(a)

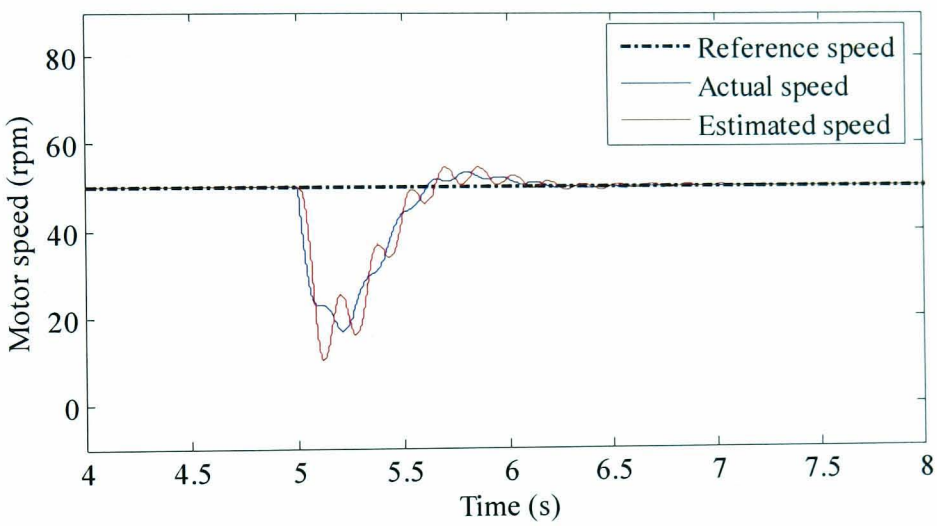

(b)

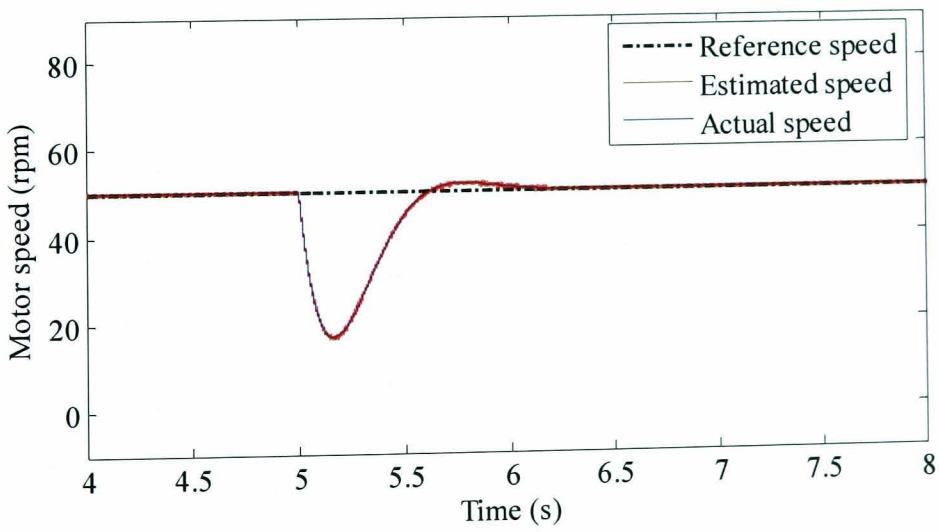

(c)

Fig. 5.15 Closed loop response of MRAS estimator for 25% load disturbance rejection

(a) MRAS-PI (b) MRAS-FL (c) MRAS-SM

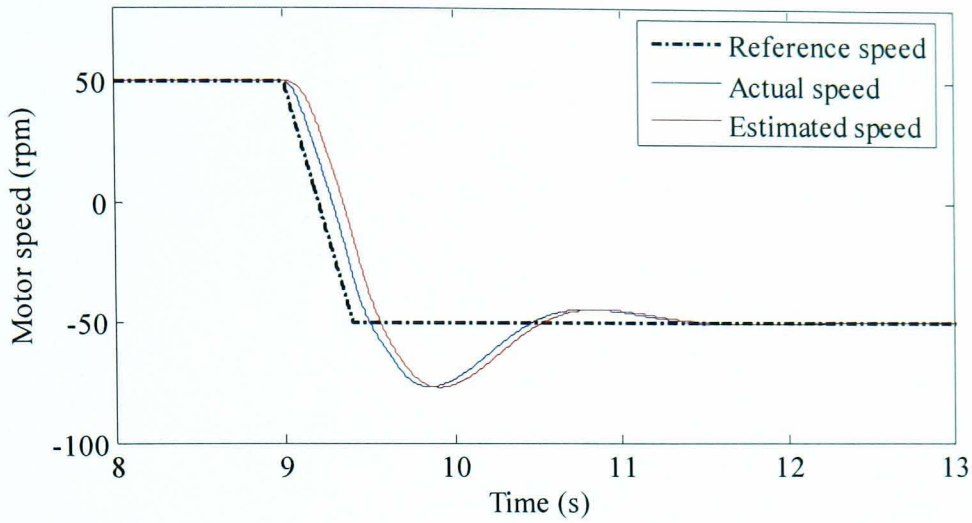

(a)

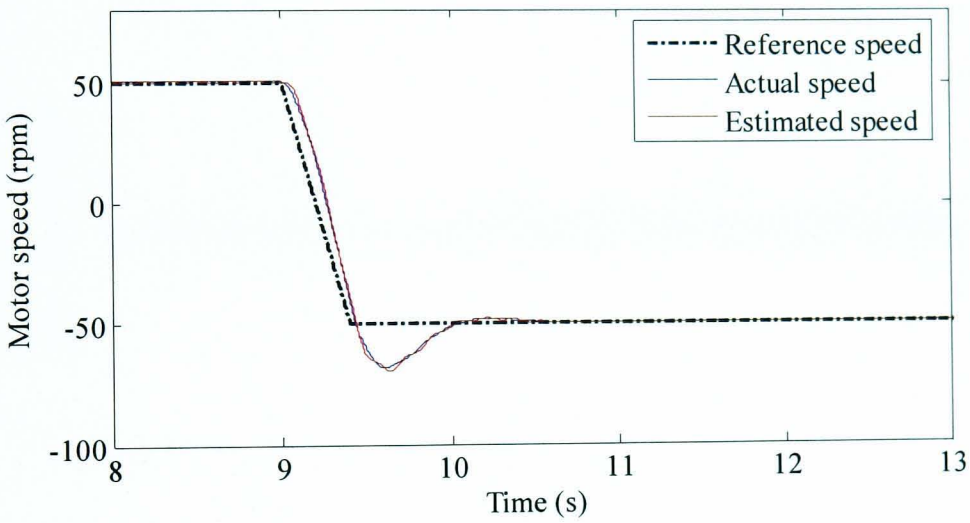

(b)

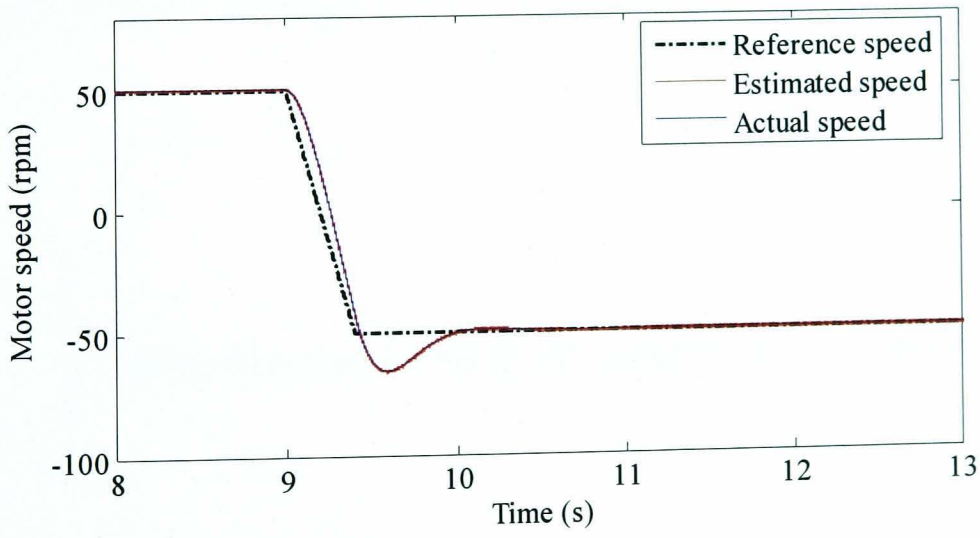

(c)

Fig. 5.16 Closed loop response of MRAS estimator for ±50 rpm speed reversal, 25% load
(a) MRAS-PI (b) MRAS-FL (c) MRAS-SM

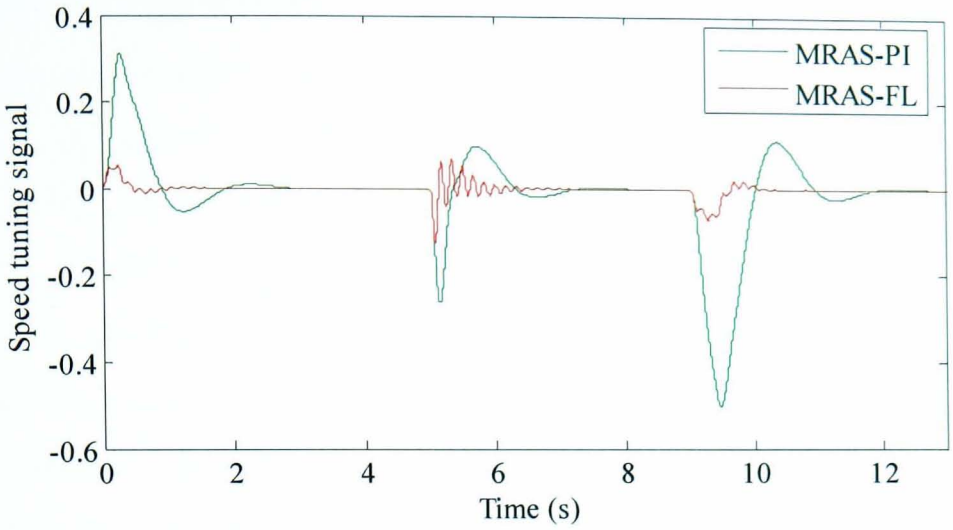

(a)

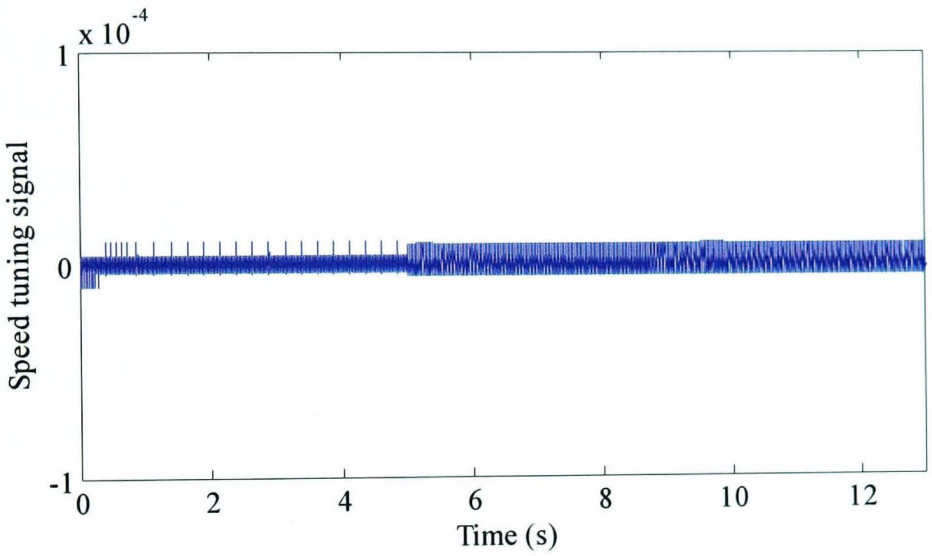

(b)

Fig. 5.17 Speed tuning signal for MRAS estimator closed loop simulation (a) PI and FL (b) SM

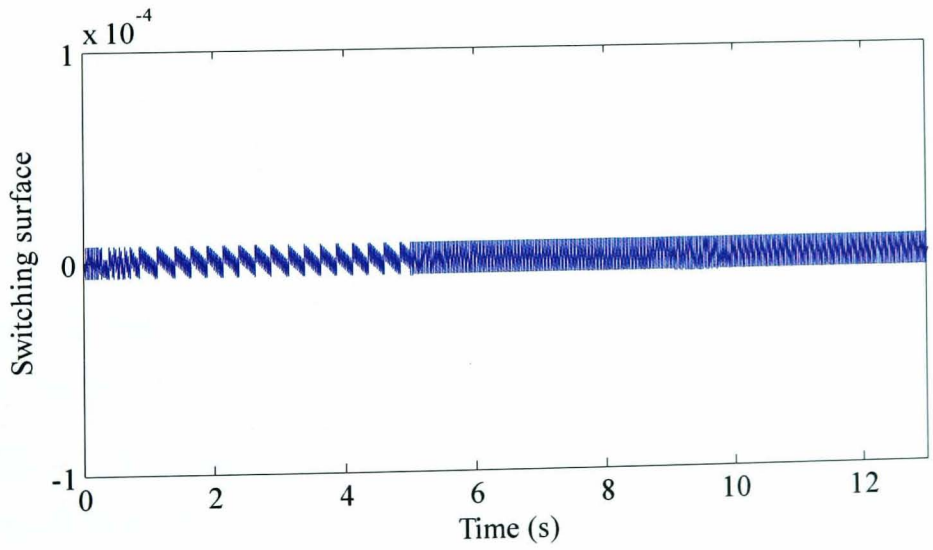

Fig. 5.18 Switching surface of SM scheme for closed loop simulation

5.4.2 Experimental Results

Extensive experimental tests were carried out to compare the three adaptation schemes; PI, FL and SM using an indirect vector control IM drive. The tests were performed in both open loop and sensorless modes of operation. The inverter switching frequency is 15 kHz and the vector control is executed with the same sampling frequency. The observer and the speed control loop have a sampling frequency of 5 kHz and the speed measurement is executed with a sampling frequency of 250 Hz.

During practical implementation of the MRAS scheme it was found necessary to cascade a low cut-off frequency High Pass Filter (HPF) at the outputs of the VM to remove integrator drift and any initial condition problems. The cut-off frequency should be selected as low as possible since the purpose is just to remove the DC component and therefore a value of 1 Hz was chosen. Reference voltages which are available in the control unit are used to avoid the need to measure the real stator voltages and will be used for the VM flux observer in (3.53).

To use the FLC in real time with the dSPACE card and Simulink, a two dimensional look-up table is generated from the FL toolbox in Matlab with a step size of 0.0005 for the inputs. The FLC implementation using a look-up table is shown in Fig. 5.19 where the saturation limits for the input saturation blocks are set to 0.1 and -0.1. Experimental results from the tests are shown in the following sections.

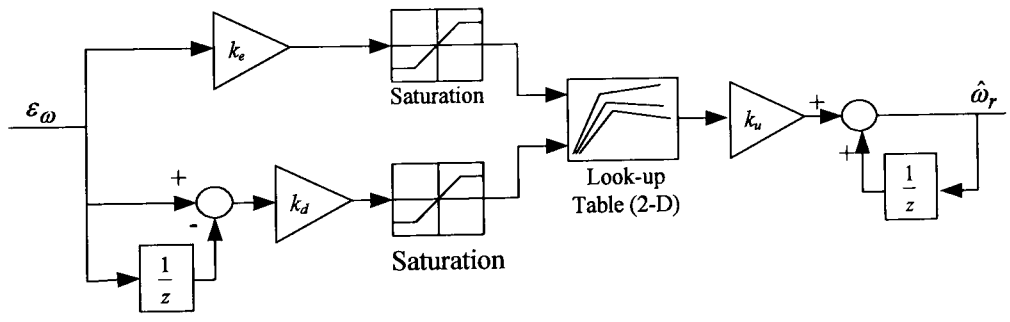

Fig. 5.19 FLC implementation using look-up tables

5.4.2.1 Open Loop Performance

The three adaptation mechanisms were tested in open loop when the drive is operated as an *encodered* vector control, i.e. the encoder speed is used for speed control and rotor flux angle estimation. The drive was subjected to different reference speed changes at various load torque levels. The PI controller gains can be selected as high as possible but are limited by the noise [2]. PI gains of $K_p = 10$; $K_i = 100$, obtained by trial and error,

were shown to provide an optimal performance for the conventional MRAS observer. These gains will be used throughout this work. To allow a fair comparison FLC gains were tuned in such a way as to obtain similar steady state performance as PI controller and are found to be: $k_e = 0.01$; $k_d = 1$; $k_u = 5$.

A LPF is used to reduce the chattering in the estimated speed obtained from the SM scheme. This LPF is found also useful to remove the spikes that may appear in the estimated speed due to the differentiation of fluxes in (5.9). The choice of the cut-off frequency for this LPF affects the observer performance. Using small values reduces the speed ripples but introduces more delay in the estimated speed. A cut-off frequency of 30 rad/s was found to be a good compromise between speed ripples and dynamic response. The parameters of the SMC are: $k = 1000$; $M = 0.1$ and are obtained by trial and error.

At low speed a steady state error in the estimated speed is observed for the MRAS observer using the three adaptation schemes. This is mainly due to the stator resistance mismatch between the motor and the observer. Moreover, since dead time effects cannot be completely removed even by complicated compensation schemes [5], the reference voltages used for the VM did not match the actual stator voltages across the machine terminals which represents another source for the steady state error in the estimated speed.

Figs. 5.20-5.24 show the speed estimation performance of both schemes for 25% load torque disturbance rejection at 60 rpm and for speed change from 30 rpm to 100 rpm at 25% load. Other results are shown in Figs. 5.25-5.29 for 50% disturbance rejection at 100 rpm and for speed reversal from -60 rpm to 100 rpm at 62.5% load. Figs. 5.30-5.32 show the results of a reference speed change from 50 rpm to 100 rpm at rated load. FL and SM schemes show better transient response compared to the PI scheme, due to an optimal speed tuning signal during transients. The switching surface of the SM scheme (5.2) corresponding to the unfiltered speed is shown for the different operating conditions. These figures show that the manifold $s = 0$ is attractive causing fast error dynamics.

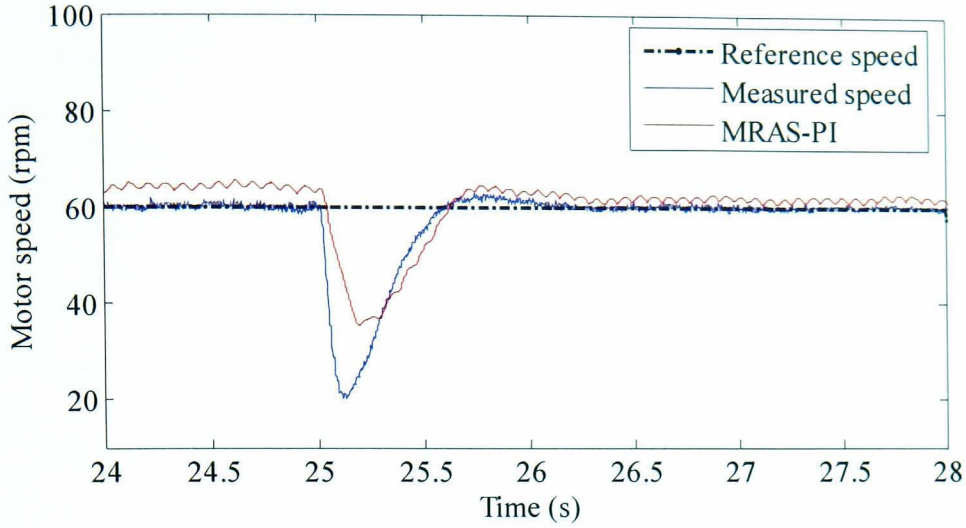

(a)

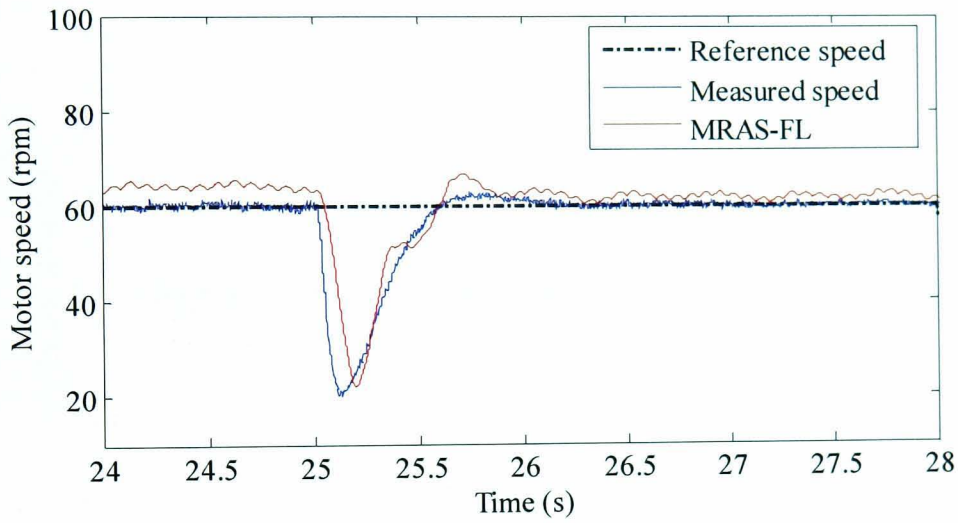

(b)

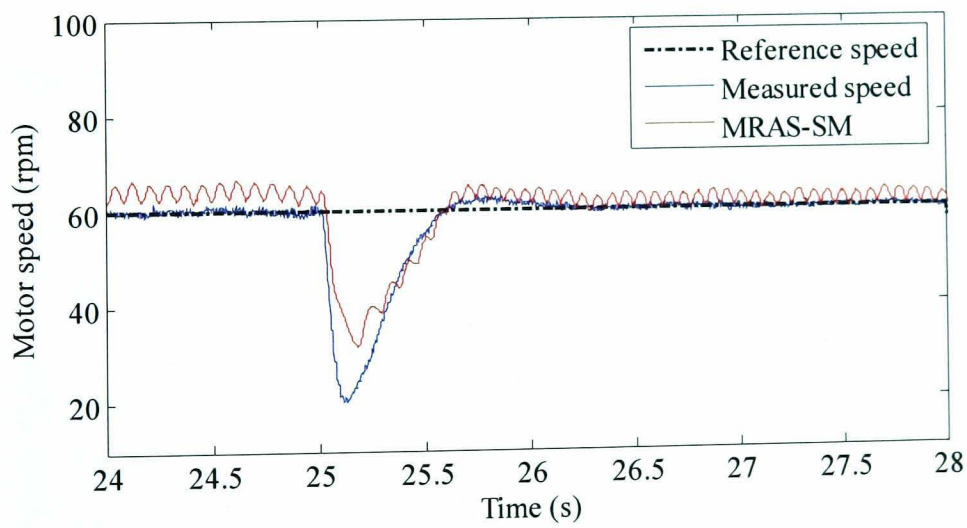

(c)

Fig. 5.20 Speed estimation performance for open loop 25% load torque disturbance rejection, 60 rpm (a) MRAS-PI (b) MRAS-FL (c) MRAS-SM

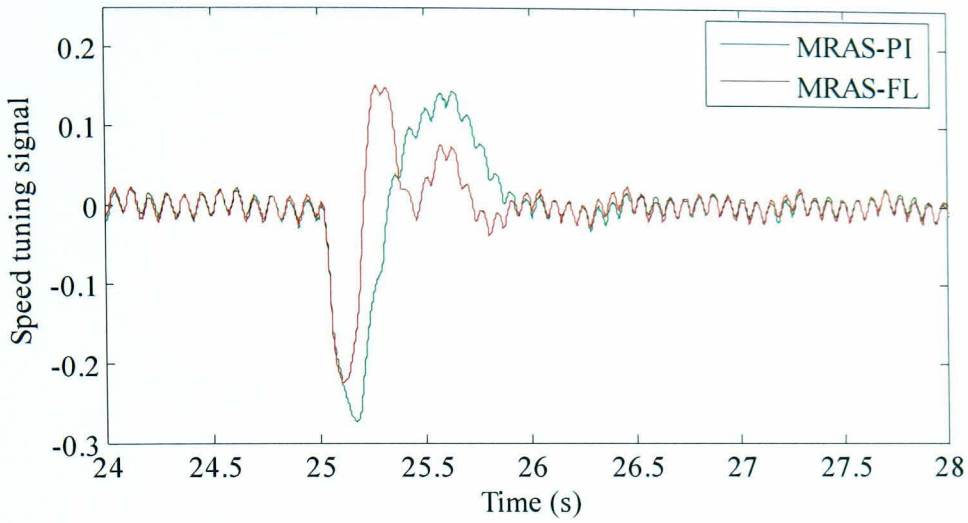

(a)

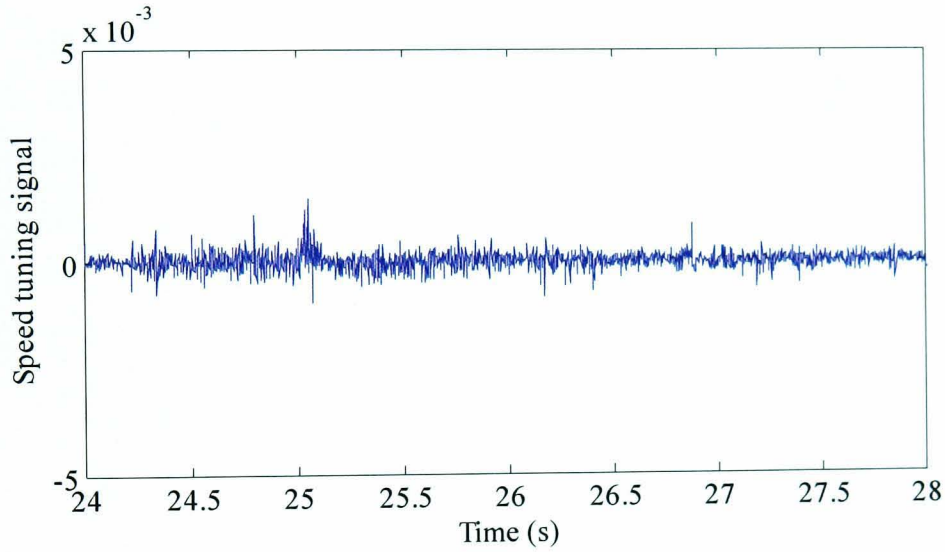

(b)

Fig. 5.21 Speed tuning signal for 25% load torque disturbance rejection, 60 rpm (a) PI and FL (b) SM

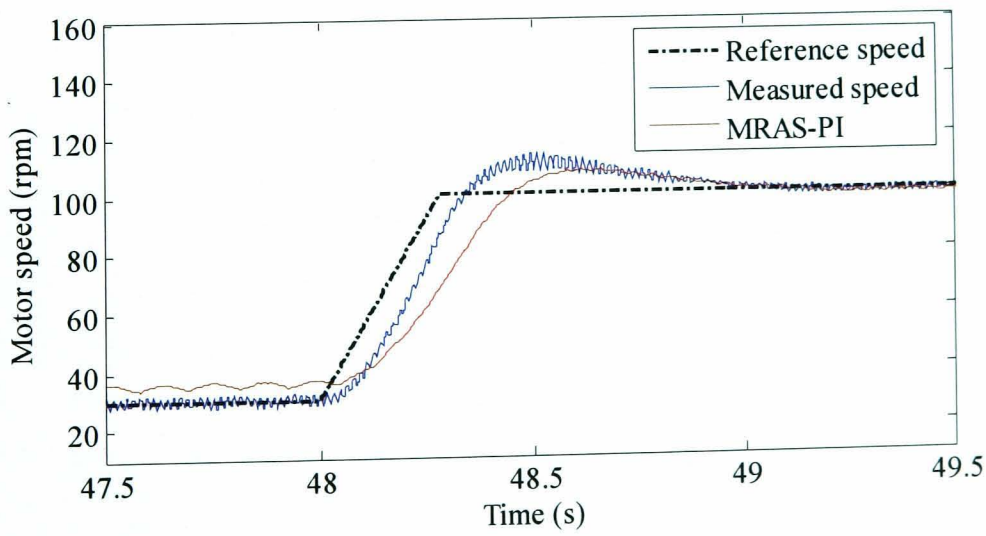

(a)

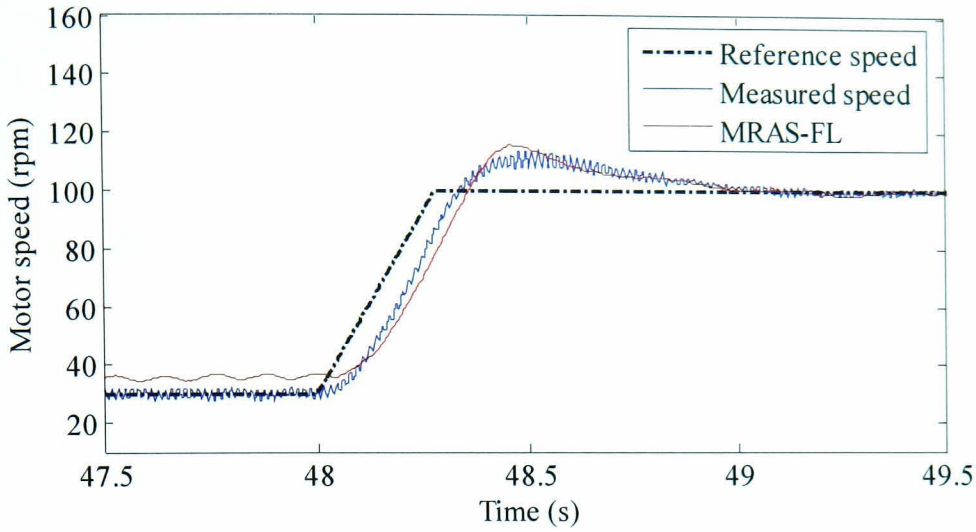

(b)

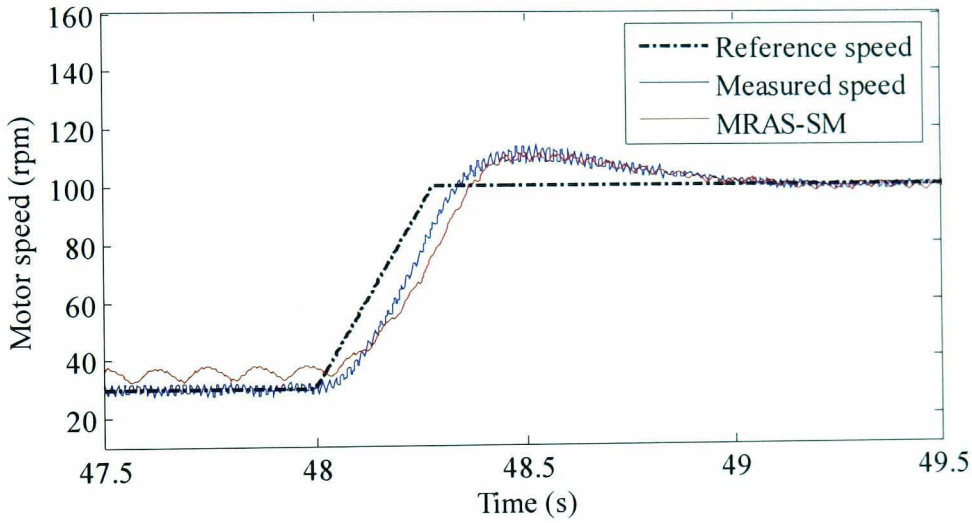

(c)

Fig. 5.22 Speed estimation performance for 30 rpm to 100 rpm reference speed change, 25% load (a) MRAS-PI (b) MRAS-FL (c) MRAS-SM

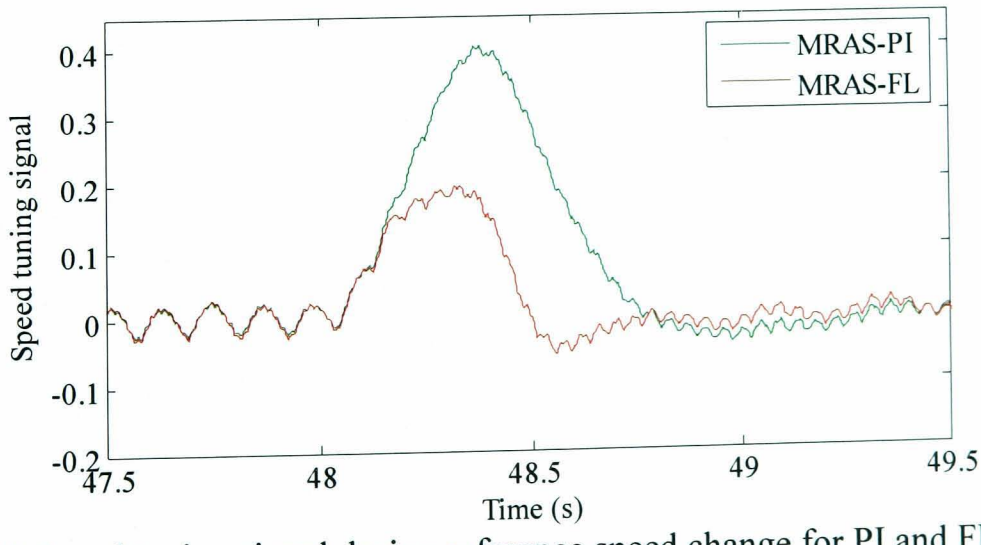

Fig. 5.23 Speed tuning signal during reference speed change for PI and FL schemes

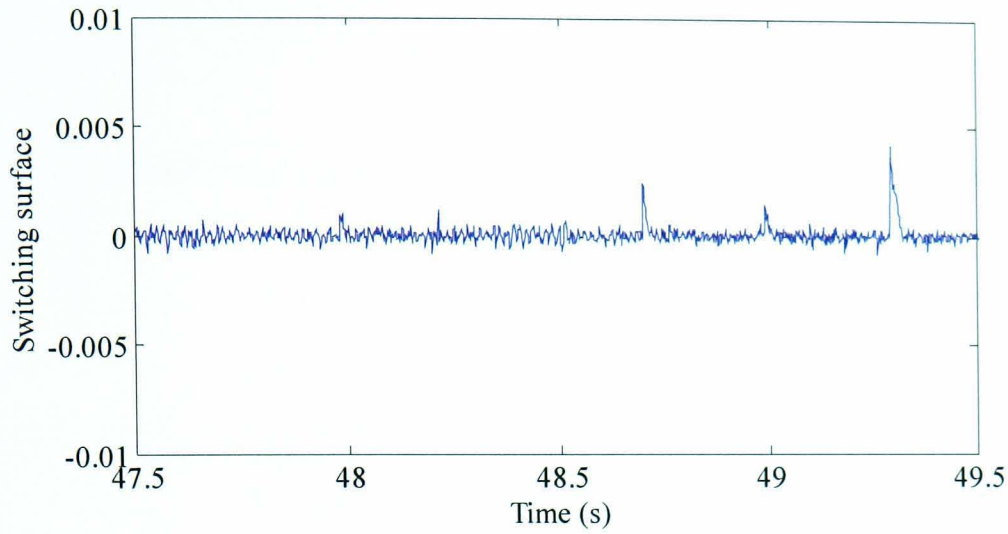

Fig. 5.24 Switching surface for SM scheme during reference speed change

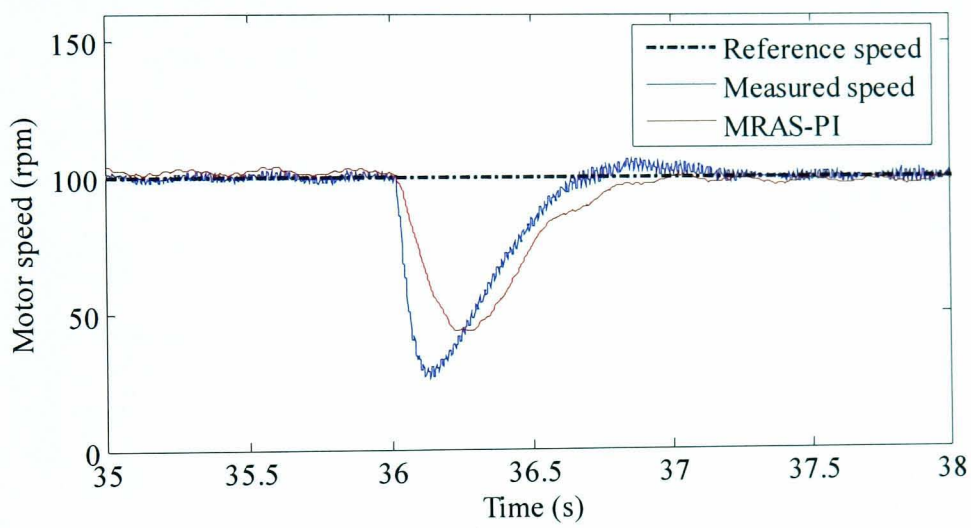

(a)

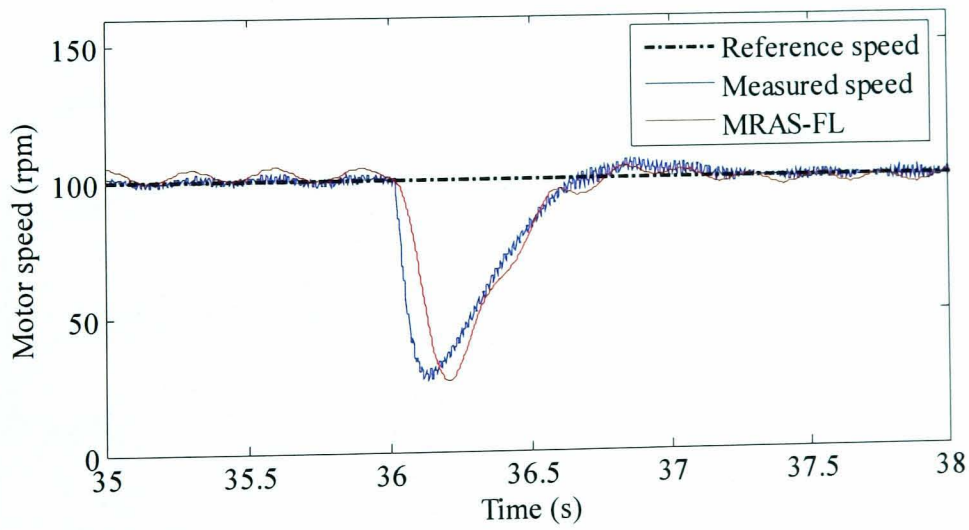

(b)

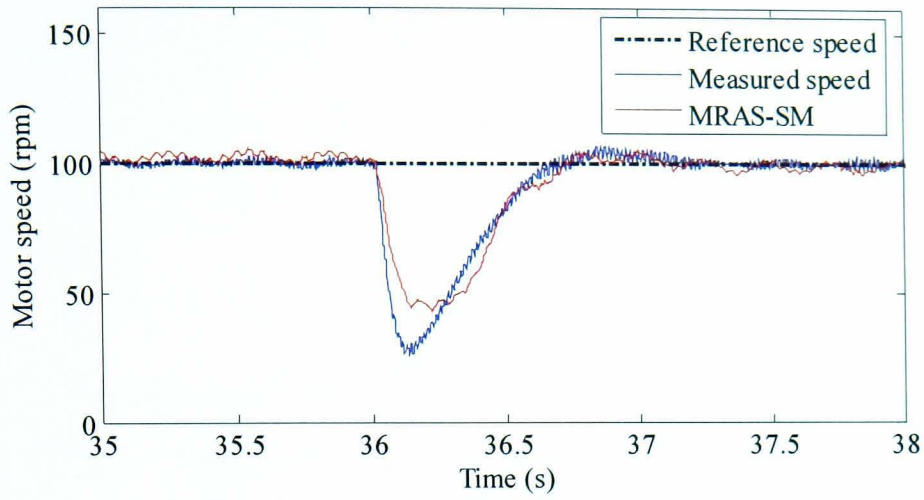

(c)

Fig. 5.25 Speed estimation performance for 50% load torque disturbance rejection, 100 rpm (a) MRAS-PI (b) MRAS-FL (c) MRAS-SM

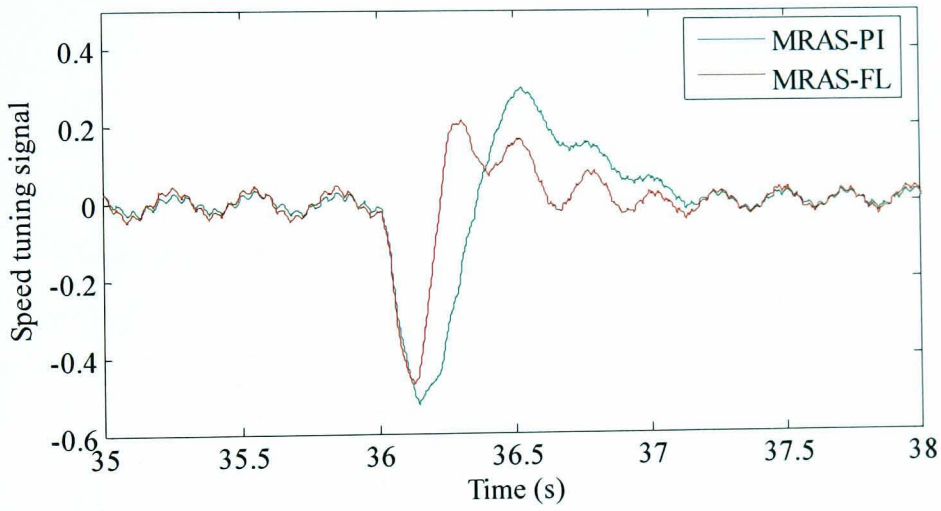

(a)

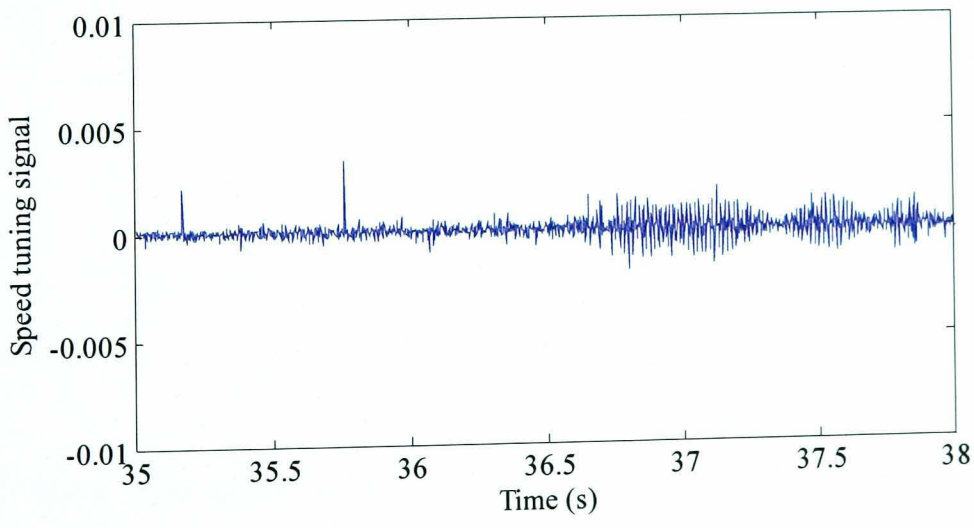

(b)

Fig. 5.26 Speed tuning signal for 50% load torque disturbance rejection (a) PI and FL (b) SM

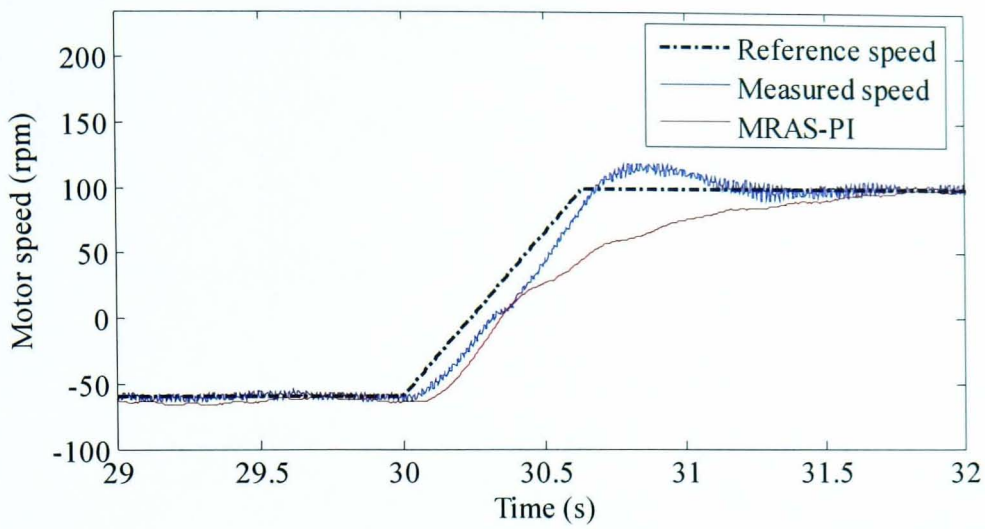

(a)

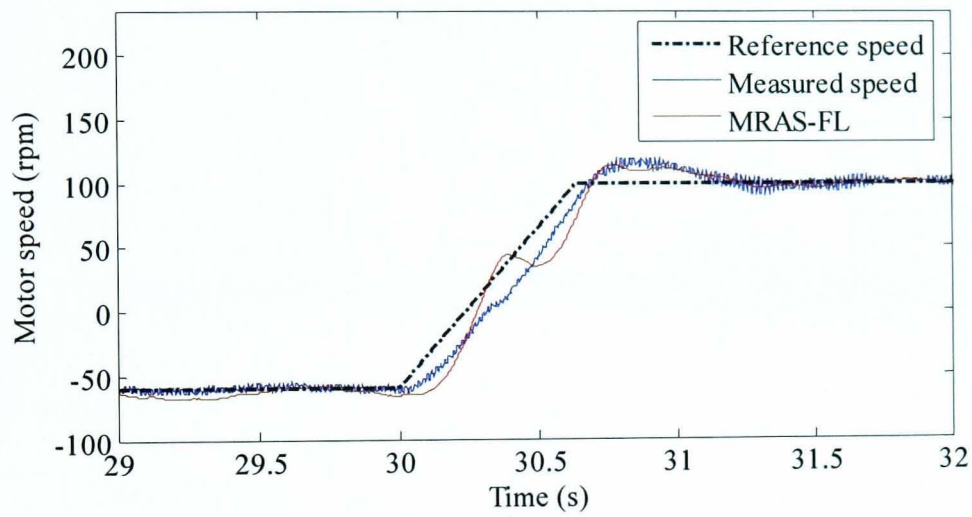

(b)

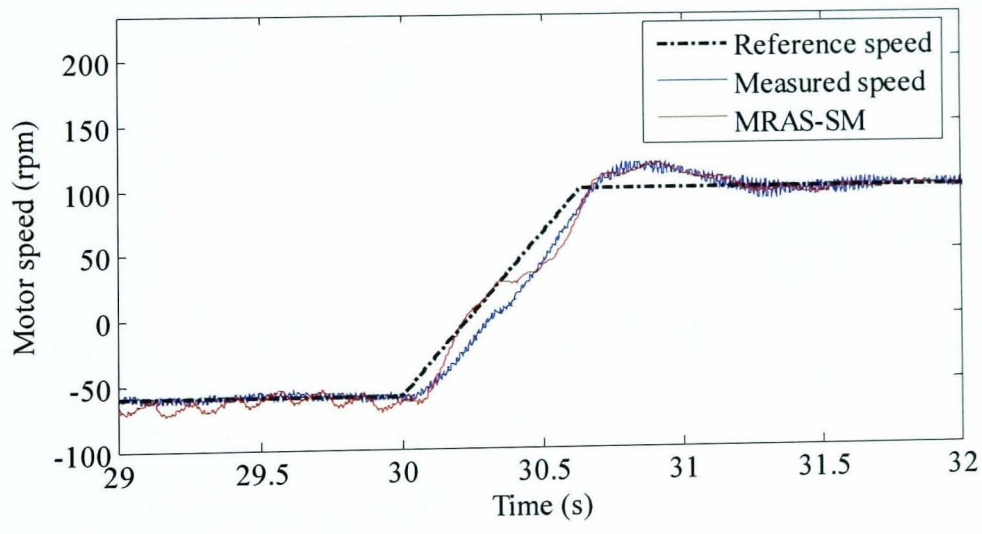

(c)

Fig. 5.27 Speed estimation performance during reference speed change from -60 to 100 rpm, 62.5% load (a) MRAS-PI (b) MRAS-FL (c) MRAS-SM

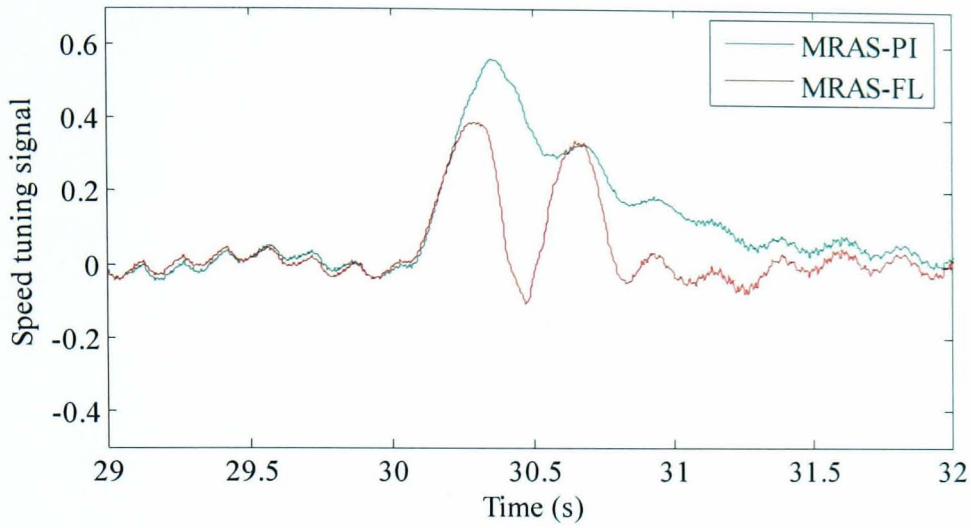

Fig. 5.28 Speed tuning signal during reference speed change from -60 to 100 rpm, 62.5% load for PI and FL

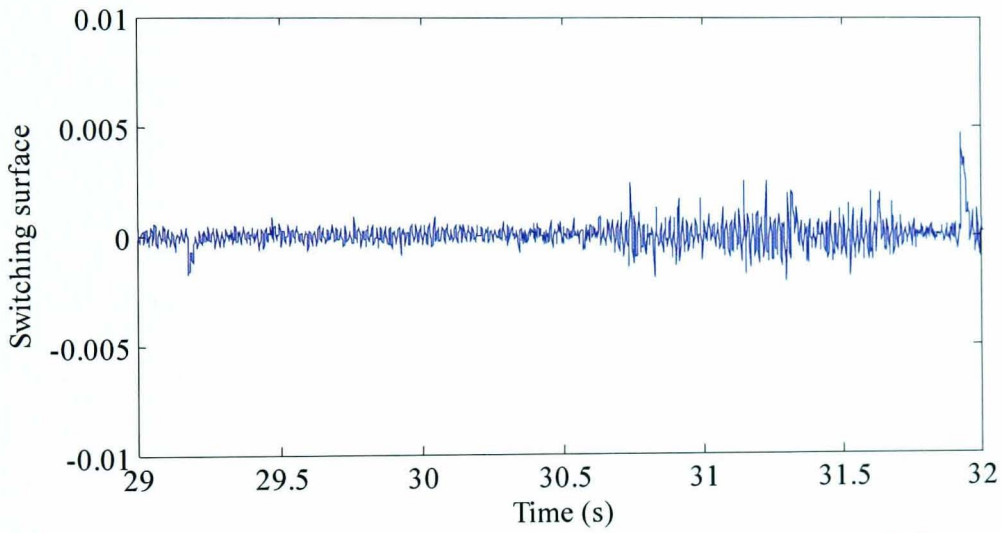

Fig. 5.29 Switching surface for SM scheme during reference speed change from -60 to 100 rpm, 62.5% load

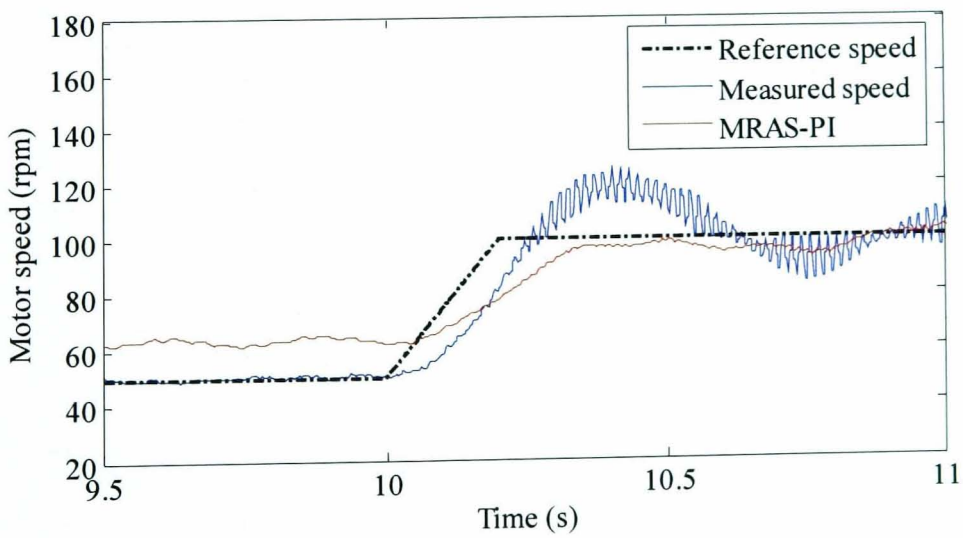

(a)

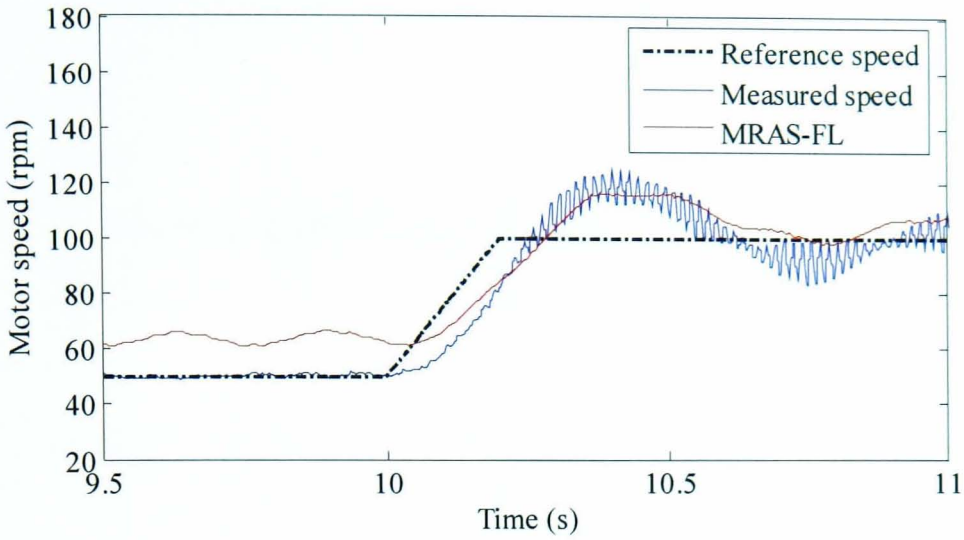

(b)

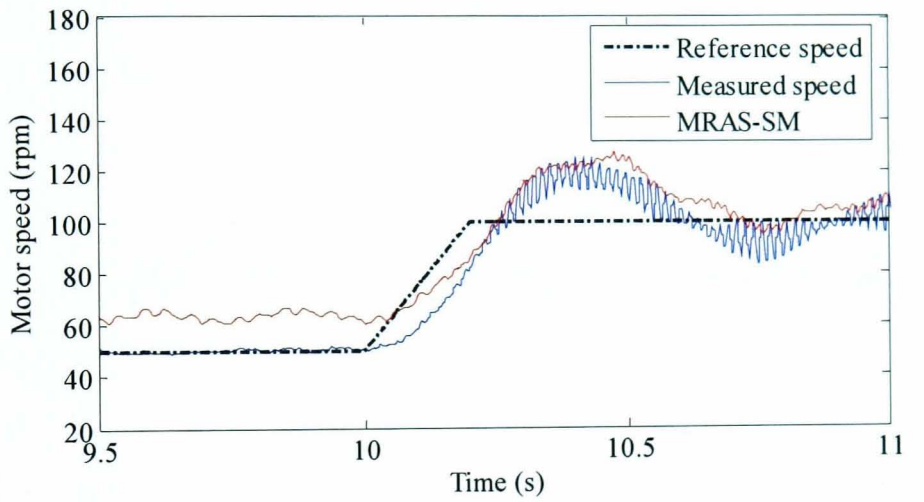

(c)

Fig. 5.30 Speed estimation performance during reference speed change from 50 rpm to 100 rpm, rated load (a) MRAS-PI (b) MRAS-FL (c) MRAS-SM

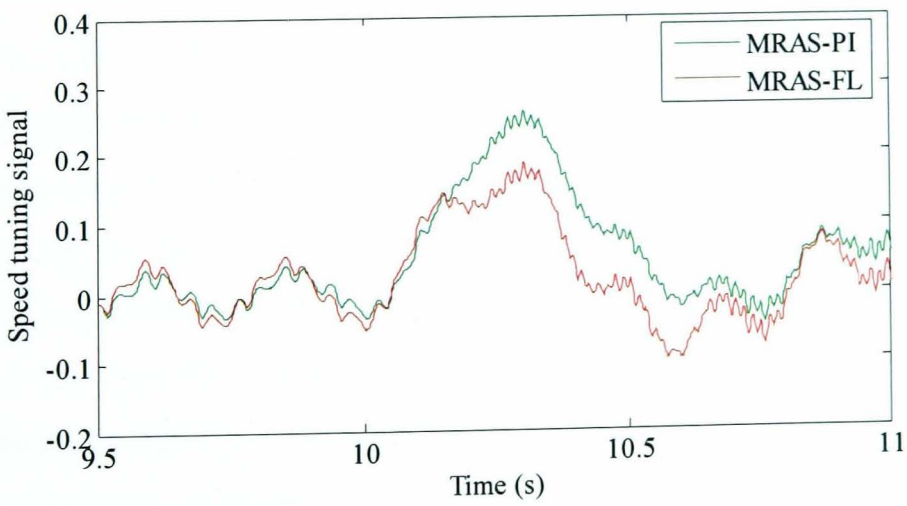

(a)

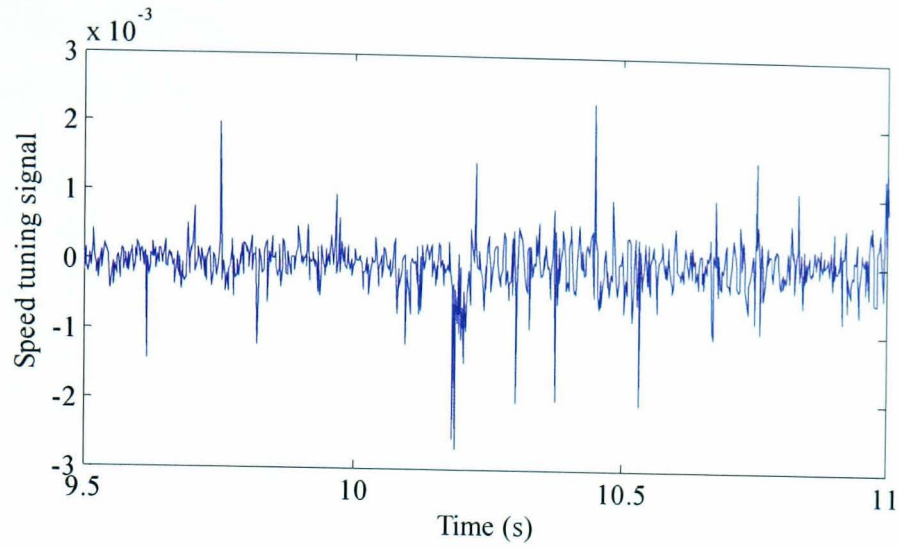

(b)

Fig. 5.31 Speed tuning signal for reference speed change at rated load (a) PI and FL (b) SM

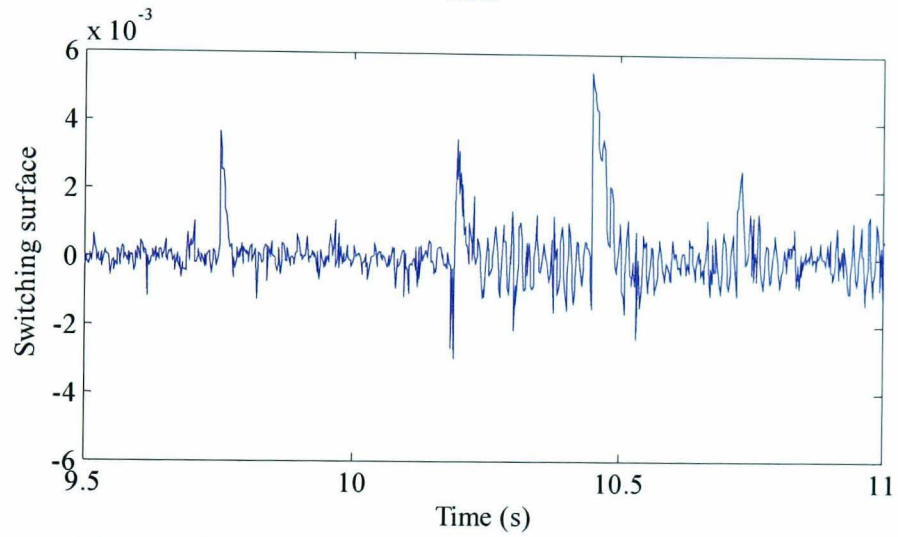

Fig. 5.32 Switching surface of SM scheme for reference speed change at rated load

5.4.2.2 Sensorless Performance

In these tests the vector control drive is working in the closed loop sensorless mode, where the estimated speed is used for both speed control and rotor flux orientation. The three schemes are compared when the drive is running with different operating conditions at very low speed.

Sensorless performance of all schemes is shown in Figs. 5.33-5.37 where the drive is subjected to a reference speed change from -30 rpm to -60 rpm at no load and 25% load torque application at 100 rpm. Other test results are shown in Figs. 5.38-5.42 for ±50 rpm speed reversal at 12.5% load and 37.5% load disturbance rejection at 50 rpm. Compared to the PI scheme, FL and SM still show a faster response during transients. Moreover, the FL scheme shows faster response compared to the SM scheme due to the need for LPF

for the SM scheme. An optimal speed tuning signal was obtained for the FL scheme compared to the PI scheme as shown in Figs. 5.39 and 5.42(a).

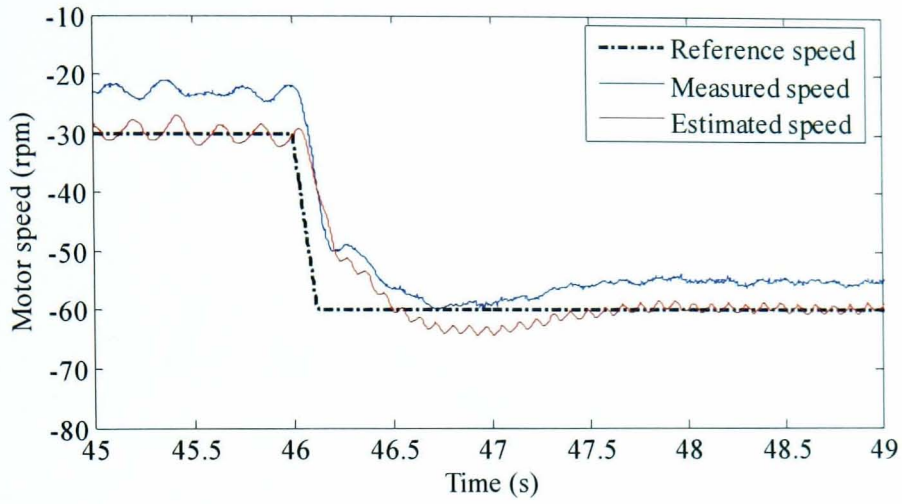

(a)

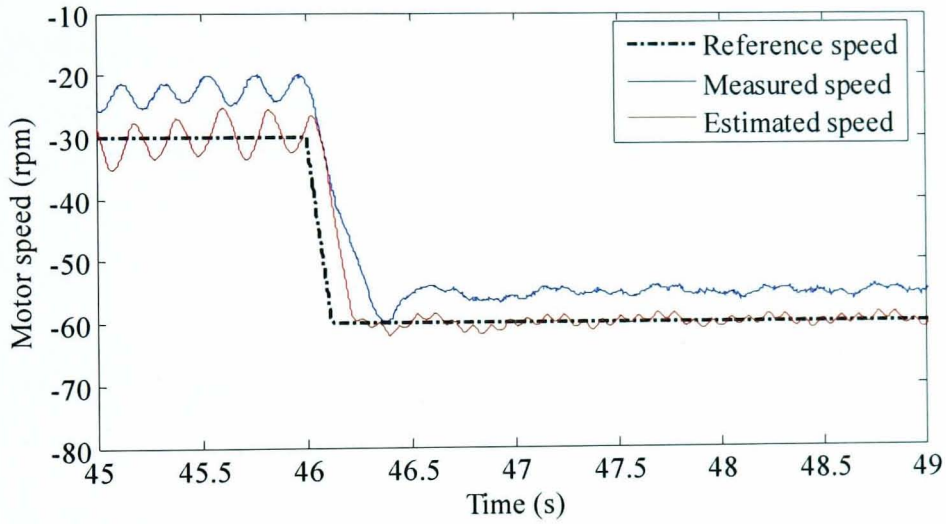

(b)

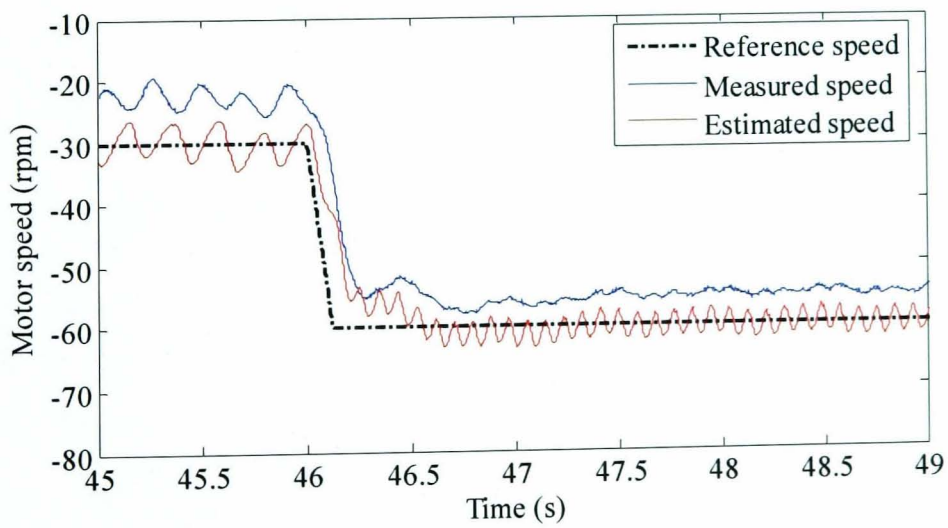

(c)

Fig. 5.33 Sensorless performance at no load (a) MRAS-PI (b) MRAS-FL (c) MRAS-SM

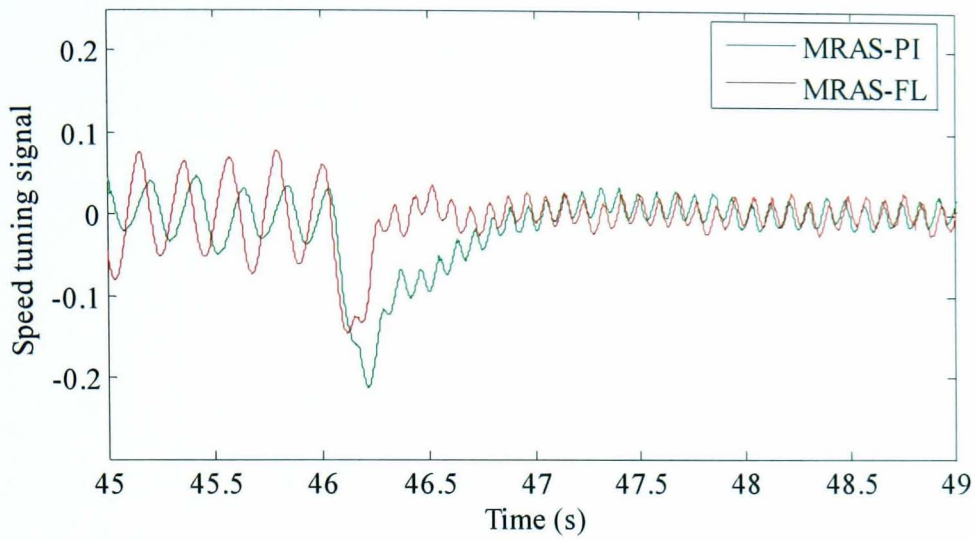

(a)

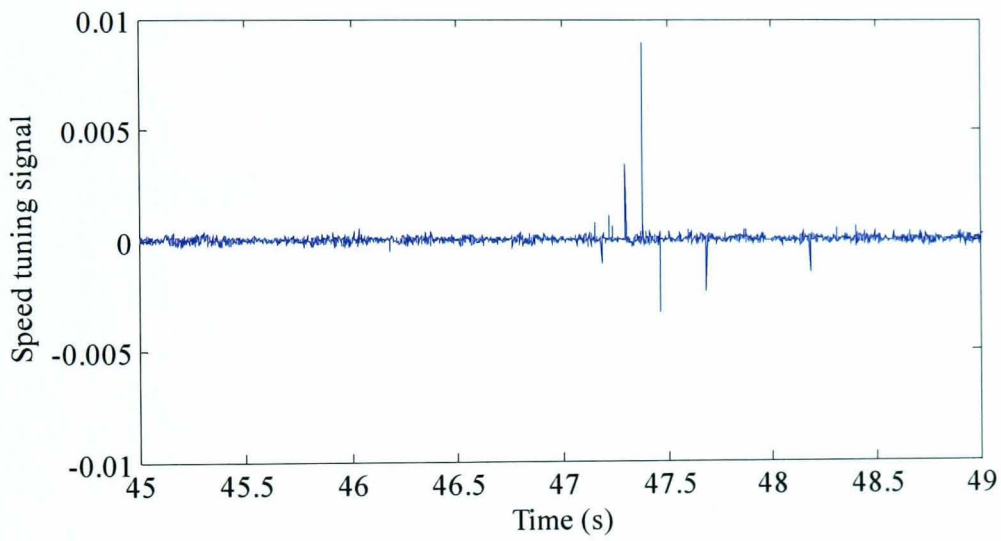

(b)

Fig. 5.34 Speed tuning signal for sensorless reference speed change (a) PI and FL (b) SM

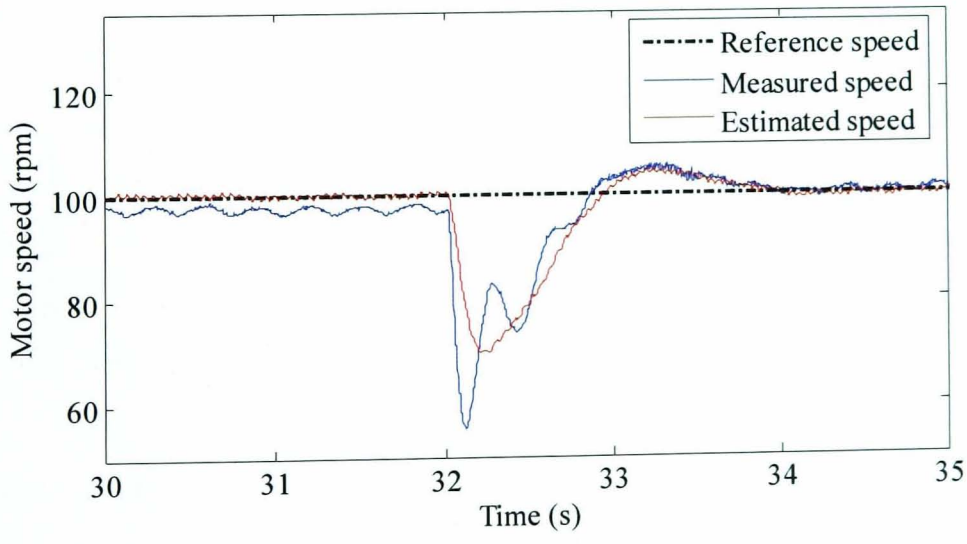

(a)

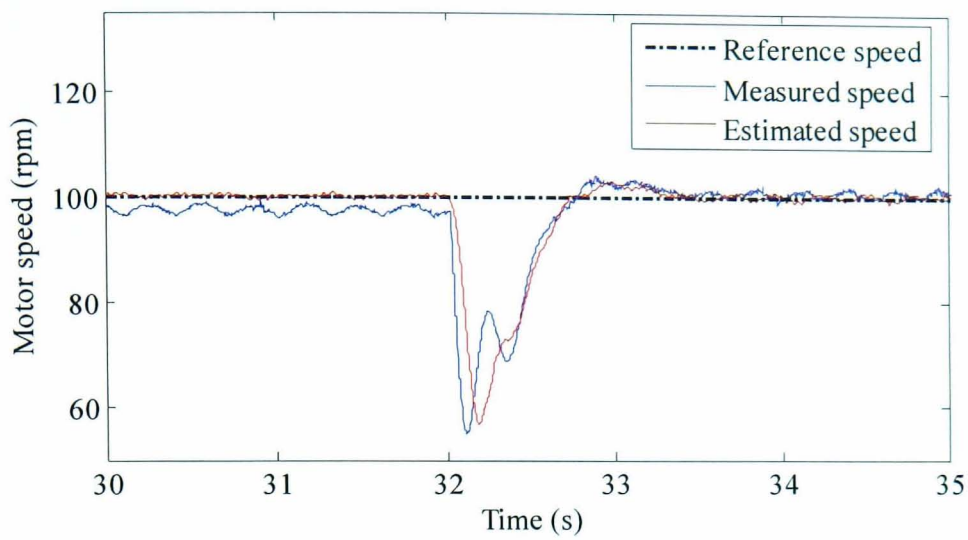

(b)

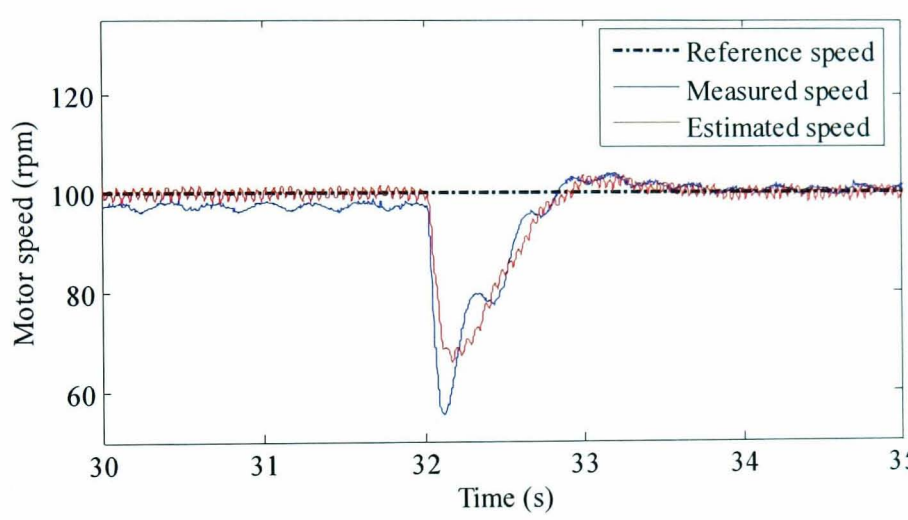

(c)

Fig. 5.35 Sensorless performance for 25% load disturbance rejection (a) MRAS-PI (b) MRAS-FL (c) MRAS-SM

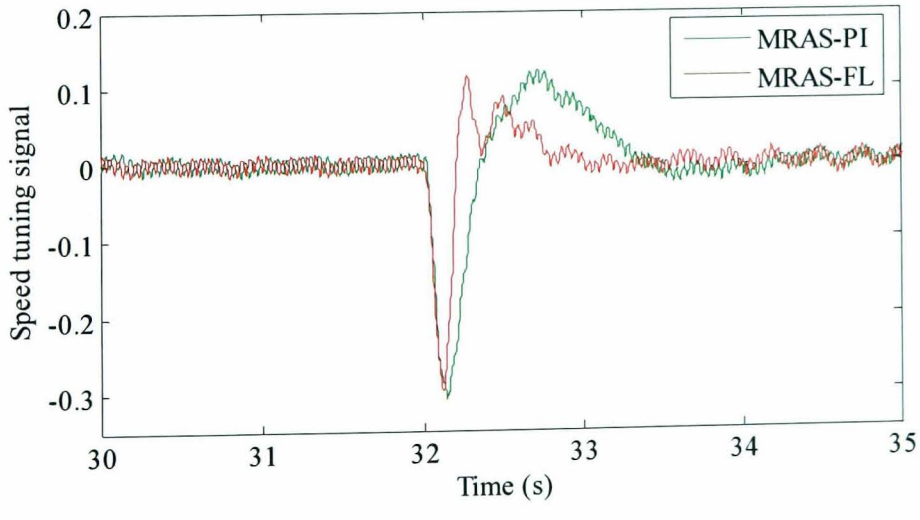

(a)

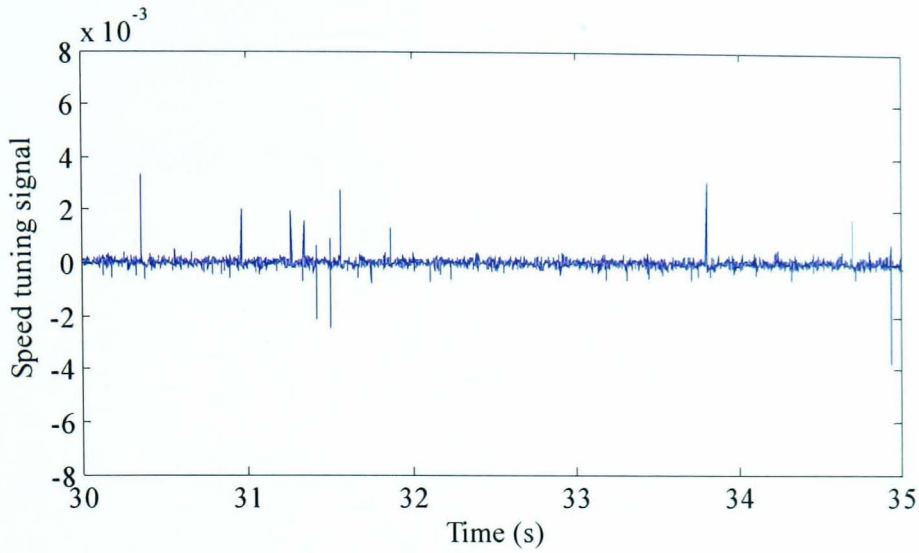

(b)

Fig. 5.36 Speed tuning signal during sensorless load torque rejection (a) PI and FL (b) SM

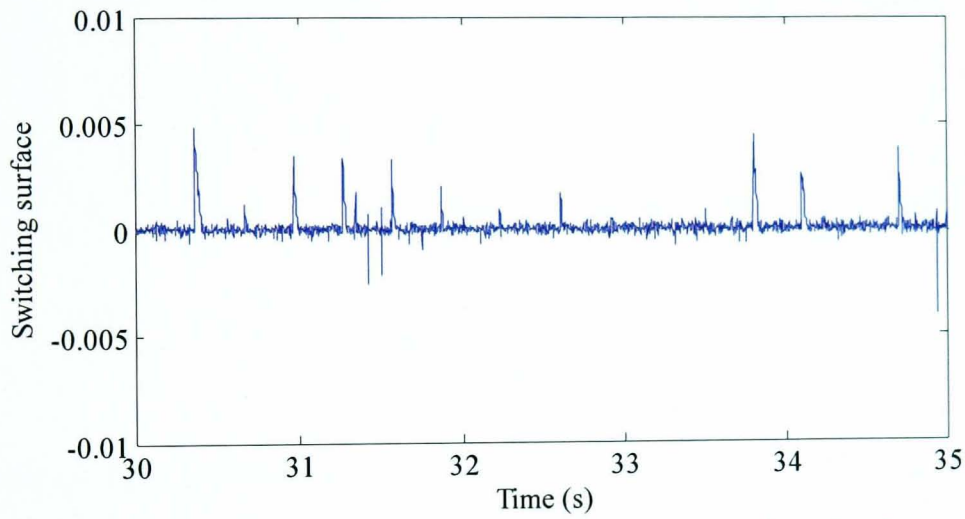

Fig. 5.37 Switching surface for SM scheme during sensorless load torque rejection

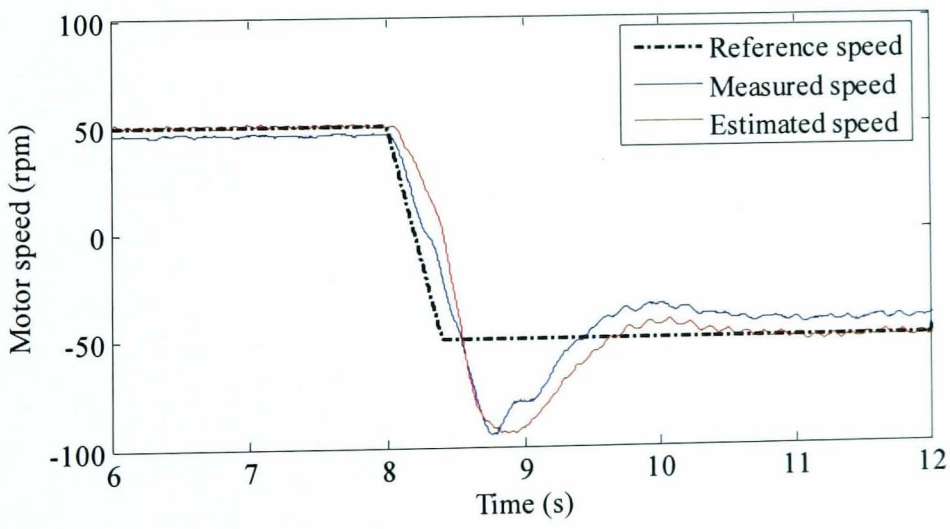

(a)

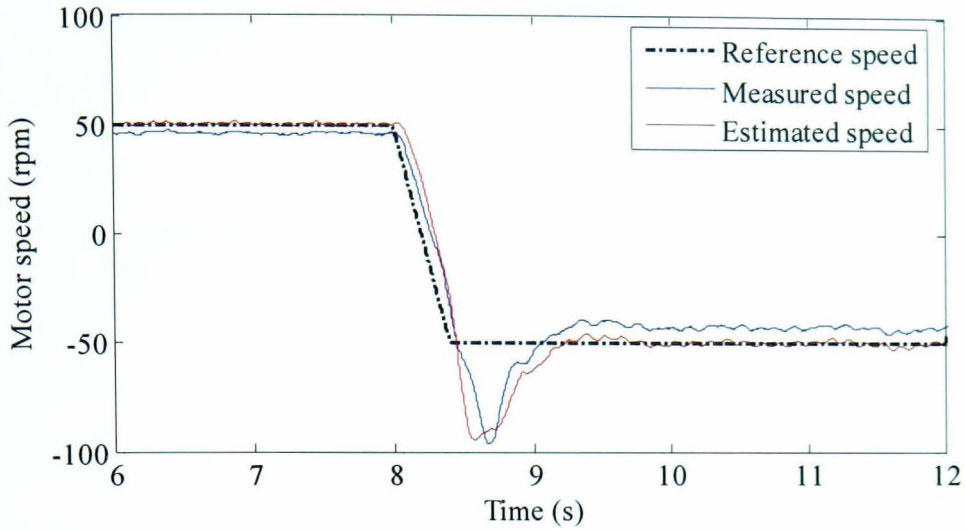

(b)

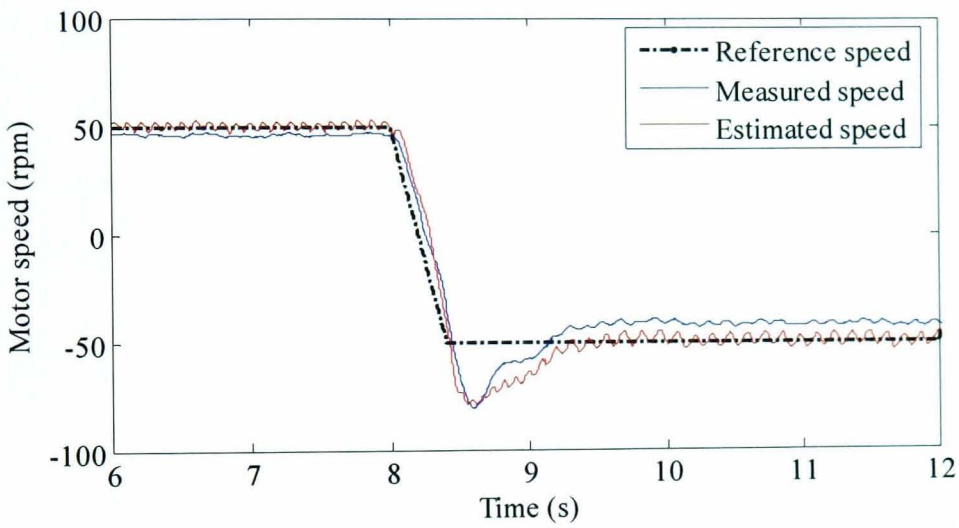

(c)

Fig. 5.38 Sensorless performance for ±50 rpm speed reversal, 12.5% load (a) MRAS-PI (b) MRAS-FL (c) MRAS-SM

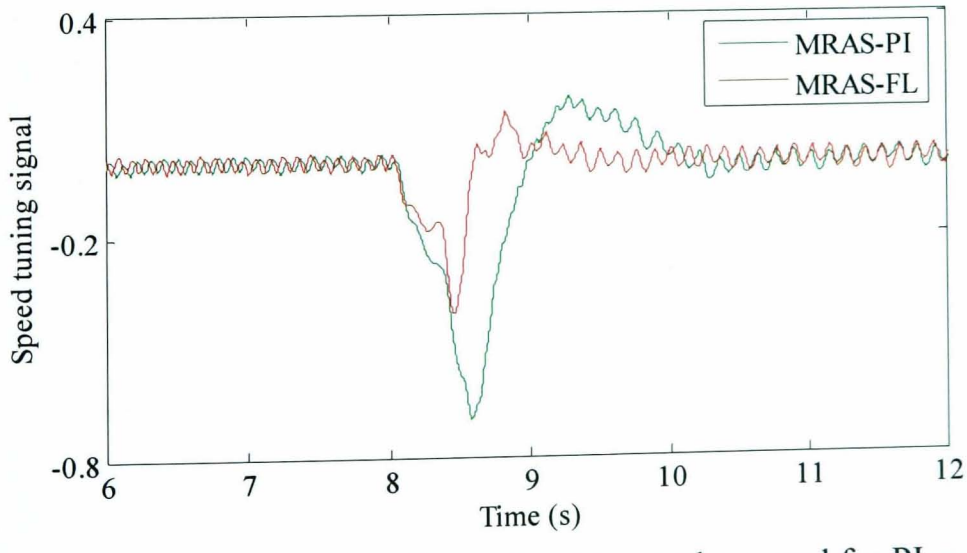

Fig. 5.39 Speed tuning signal for ±50 rpm speed reversal for PI and FL

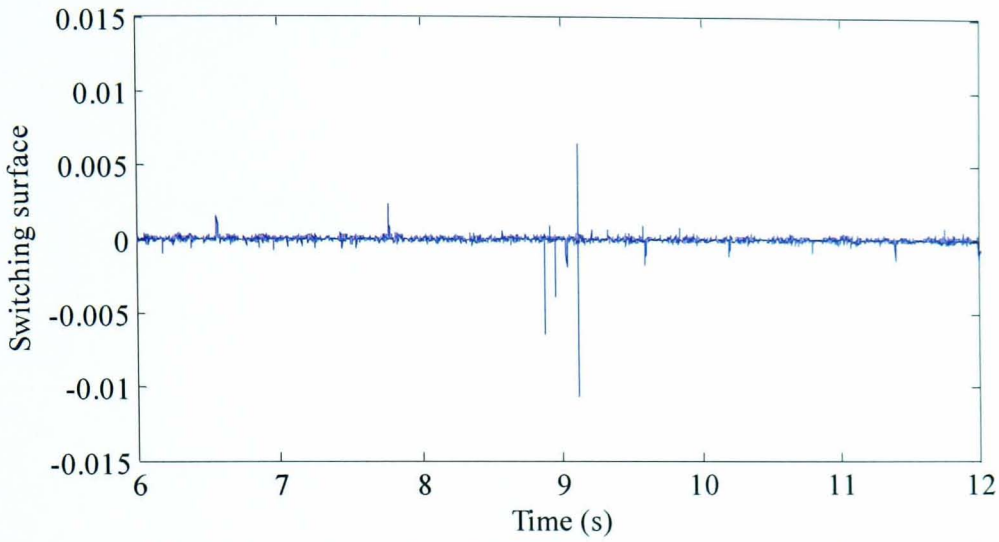

Fig. 5.40 Switching surface for SM scheme during sensorless speed reversal

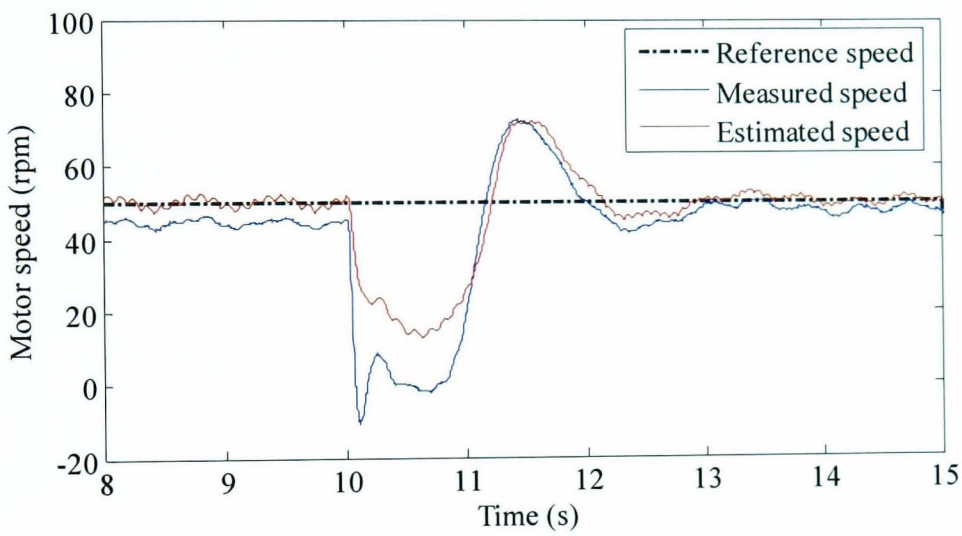

(a)

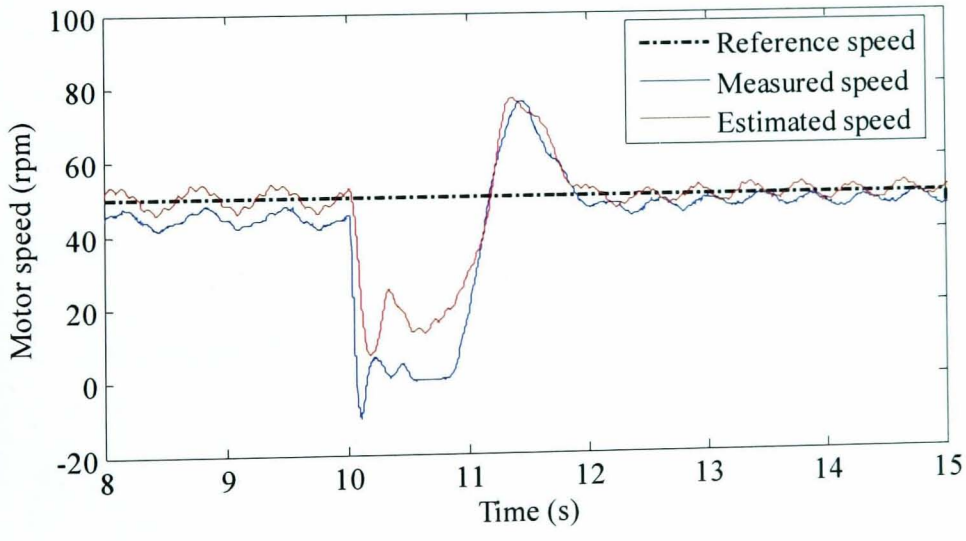

(b)

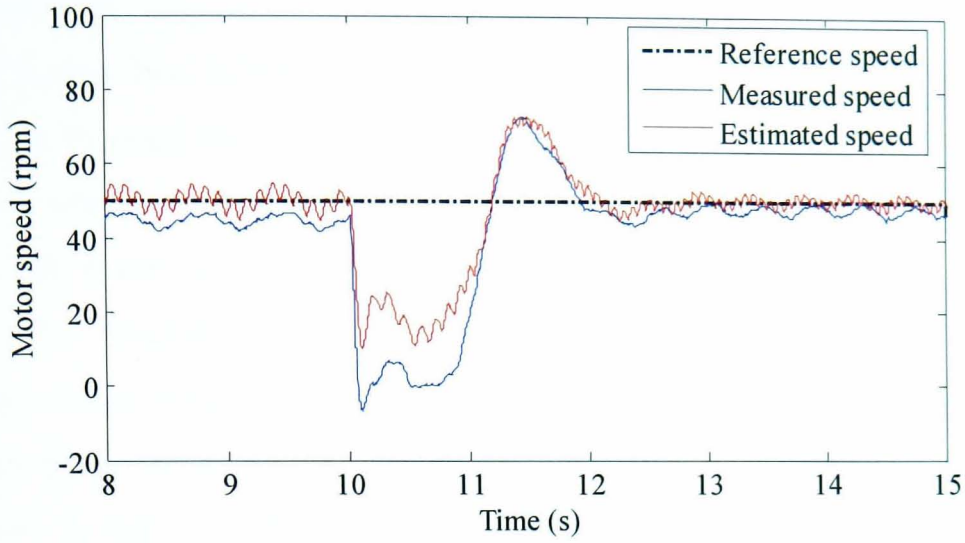

(c)

Fig. 5.41 Sensorless performance for 37.5% load disturbance rejection at 50 rpm (a) MRAS-PI (b) MRAS-FL (c) MRAS-SM

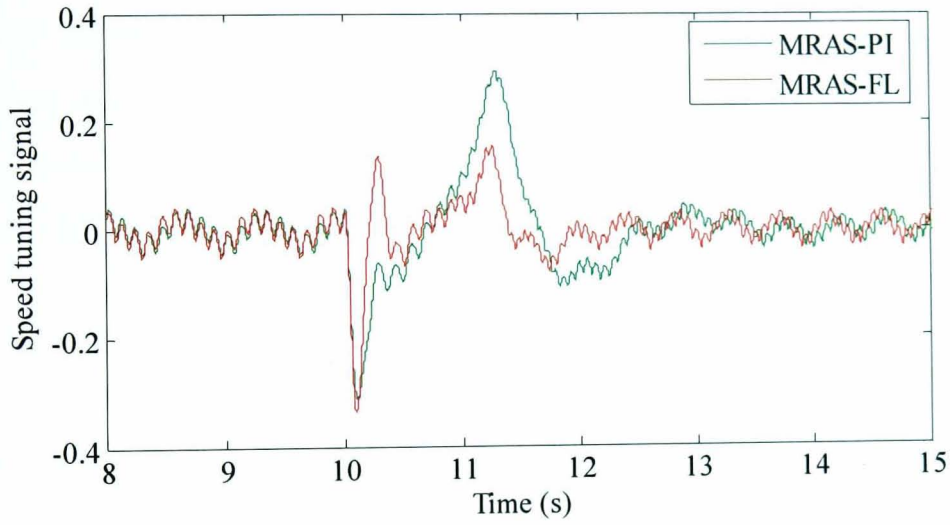

(a)

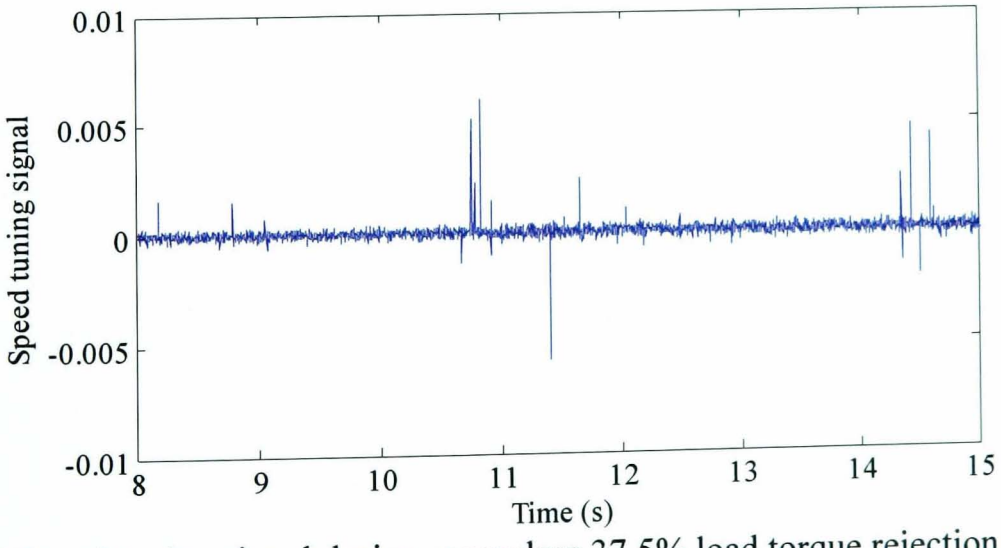

Fig. 5.42 Speed tuning signal during sensorless 37.5% load torque rejection (a) PI and FL (b) SM

5.5 Conclusion

In this chapter two novel nonlinear adaptation mechanisms are proposed to replace the fixed gain PI controller which is conventionally used for rotor flux MRAS observer. One of these schemes is based on SM theory where a novel speed estimation adaptation law is derived based on Lyapunov theory to ensure estimation stability with fast error dynamics. The second scheme is based on a FL strategy working in a nonlinear optimization mode. Parameter tuning of the PI and FL schemes has been performed in such a way as to obtain similar steady state performance. A rigorous simulation and experimental comparison between the three schemes have been carried out using an indirect vector control IM drive. Application of the new schemes shows better transient performance as well as better load torque disturbance rejection in both open loop and closed loop sensorless modes of operation. More specifically, due to the need of low pass filtering of the estimated speed obtained from the SM approach, the FL strategy shows a faster response than the SM scheme. However, the application of the new adaptation schemes does not considerably improve the steady state performance which will be the purpose of the following chapter.

CHAPTER 6

NEURAL NETWORK-BASED ROTOR FLUX MRAS SPEED OBSERVER

A new method is described which considerably improves the performance of rotor flux-MRAS based sensorless drives in the critical low and zero speed region of operation. It is applied to a vector controlled IM drive and is experimentally verified. The new technique uses a NN as a rotor flux observer to replace the conventional VM. This makes the reference model free of pure integration and less sensitive to stator resistance variations. This is a radically different way of applying NNs to MRAS schemes. The data for training the NN is obtained from experimental measurements based on the CM avoiding voltage and flux sensors. This has the advantage of considering all the drive nonlinearities. Both open loop and sensorless operations for the new scheme are investigated and compared with the conventional MRAS speed observer. The experimental results show the great improvement in the speed estimation performance for open and closed loop modes of operation including zero speed.

6.1 Introduction

Classical rotor flux MRAS observer employs a VM to produce the reference values of the rotor flux. However, VM flux observer suffers from stator resistance sensitivity, stator voltage acquisition problem and flux open loop integration which may cause dc

drift and initial condition problems [1, 5]. These problems limit the performance of the MRAS observer in the low and zero speed region of operation.

Neural Networks, with their learning and generalization capabilities, have attracted much attention in the last two decades. They have been used before with MRAS schemes as described in chapter 2. However, a completely novel application of the NN for MRAS schemes is described in this chapter. This new MRAS scheme employs a NN rotor flux observer to entirely replace the conventional VM (and not the CM as described in [28, 52]) to improve the sensorless drive performance at low and zero speed. A multilayer feedforward NN estimates the rotor flux from present and previous samples of the terminal voltages and currents. The training data for the NN is obtained from experimental measurements giving a more accurate model that includes all the drive nonlinearities. An experimental implementation of the new NN MRAS observer is described. The new NN scheme is compared with the conventional, which employs a VM for flux estimation, in both the open loop and closed loop sensorless modes for an indirect vector control IM drive. The drive performance is tested when running at very low and zero speed at various load levels. Experimental results confirm the great improvement in the performance of the new NN MRAS speed observer.

6.2 Artificial Neural Networks

Artificial NNs are based on the basic model of the human brain with capability of generalization and learning. They are frequently used as universal nonlinear function approximators to represent functions with weighted sums of nonlinear terms [106]. Multilayer feedforward NNs have shown a great capability to model complex nonlinear dynamic systems [27]. Generally, the advantages of applying NN over mathematical model-based techniques are fault tolerance, parallel processing, fast implementation speed, noise-immunity, generalization capability and insensitivity to inaccurate inputs [4, 107, 108]. On the other hand, lack of design techniques and computational effort requirement are the main drawbacks of NN. The following sections briefly describe various network topologies and training methods.

6.2.1 Structure of Artificial Neural Networks

Stimulated by the structure of the brain, a NN consists of a set of highly interconnected processing units, called *nodes* or *units*. Each unit is designed to mimic its biological counterpart, the neuron [11]. Each accepts a weighted set of inputs and responds with an output. NN resembles the biological neuron in acquiring knowledge by learning from examples and storing this information within inter-neuron connection strengths called *weights*. Fig. 6.1 shows an artificial neuron which consists basically of a summer and an activation function [11, 109].

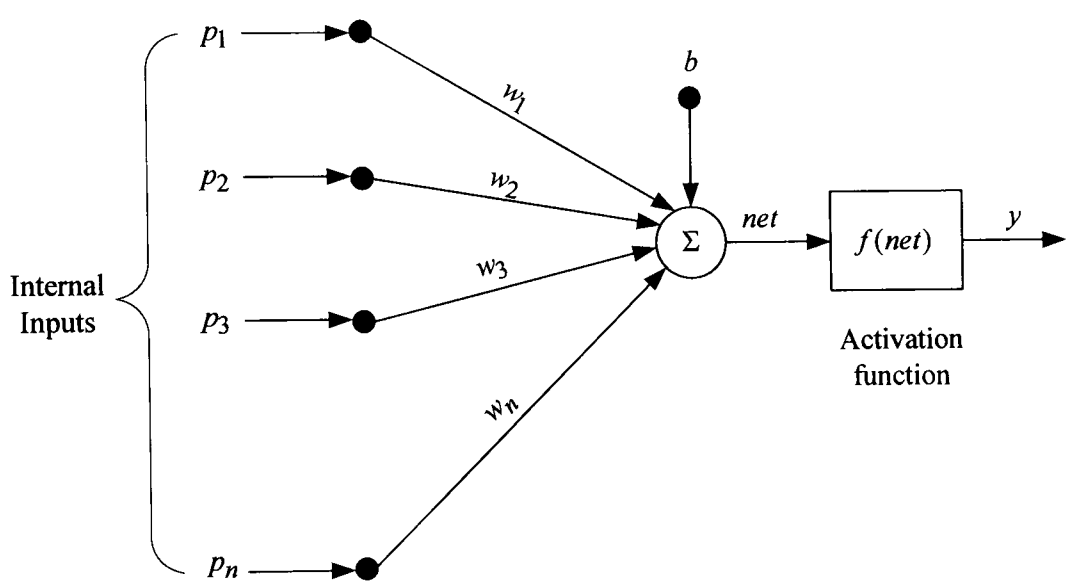

Fig. 6.1 Structure of the artificial neuron

The inputs to the neuron are $p_1, p_2, p_3, \ldots, p_n$ with corresponding weights $w_1, w_2, w_3, \ldots, w_n$ which act in such a way as to increase or decrease the input signals to the neuron. Sometimes a threshold term b is added to the inputs. All inputs are multiplied by their corresponding weights and added together to form the net input to the neuron called *net*. The mathematical expression for *net* can be simply written as:

$$net = \sum_{i=1}^{n} w_i p_i + b = w_1 p_1 + w_2 p_2 + w_3 p_3 + \ldots\ldots + w_n p_n + b \tag{6.1}$$

The neuron behaves as activation or mapping function $f(net)$ to produce an output y which can be expressed as:

$$y = f(net) = f(\sum_{i=1}^{n} w_i p_i + b) \tag{6.2}$$

where f is the neuron activation function or the neuron transfer function. Common neuron activation functions are: Linear, threshold, log-sigmoid and tan-sigmoid as shown in Fig. 6.2 [11]. In all these cases the net neuron input is mapped into values between 0 and 1 or -1 to 1 where g is the gain that adjusts the slope of the sigmoid functions [10, 11]. All these functions are squashing since they limit the neuron output to asymptotic levels [11]. Using nonlinear activation functions allows nonlinear input-output mapping of NN which can permit nonlinear function approximation.

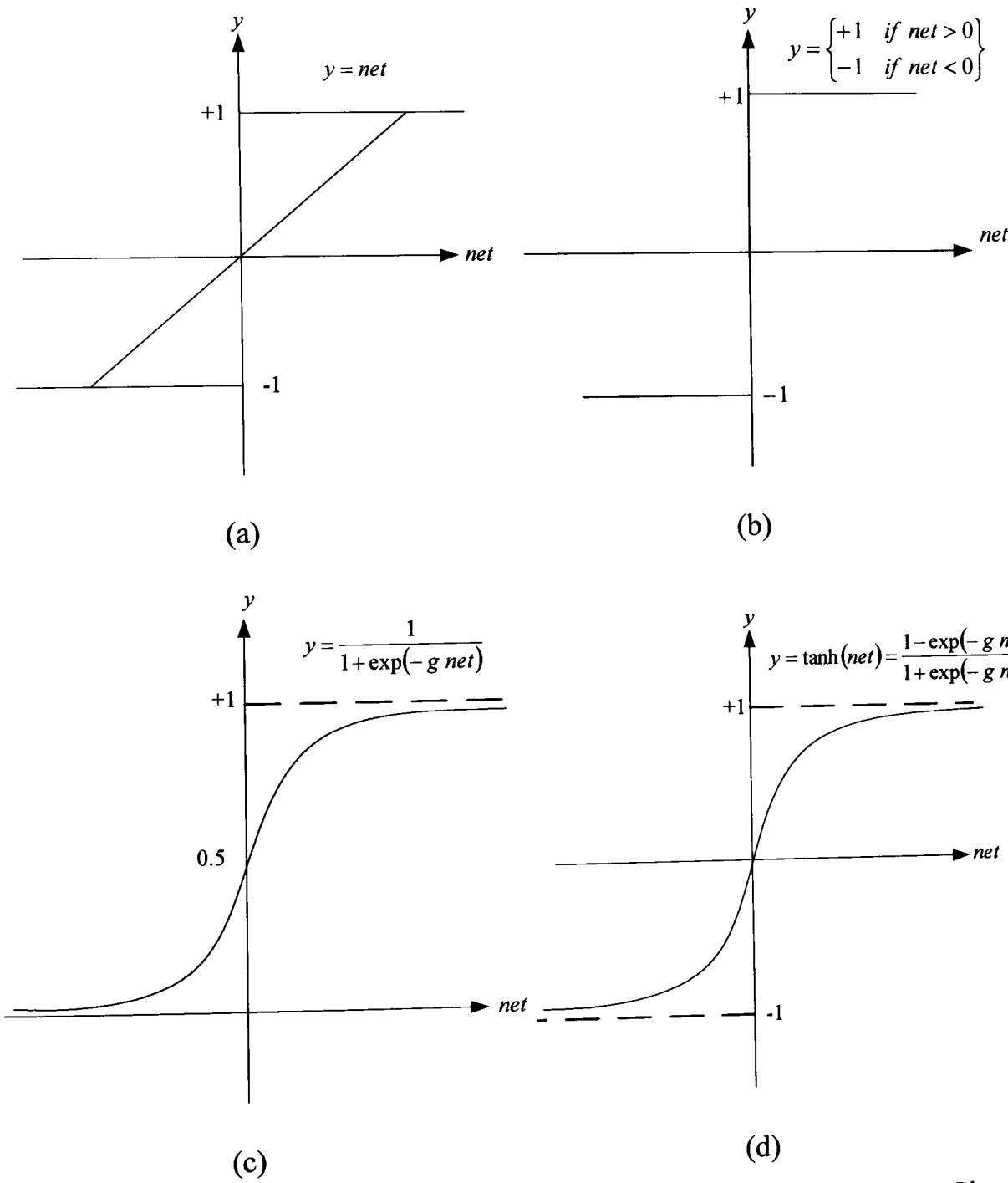

Fig. 6.2 Common neuron transfer functions (a) Linear (b) Threshold (c) Log-Sigmoid (d) Tan-Sigmoid

The most common type of NN is the multilayer feedforward network which consists of a group of interconnected neurons organised in layers: input layer, hidden layer and output layer where each layer consists of a group of neurons as shown in Fig. 6.3. It is feedforward because signals propagate only in a forward direction from the input nodes to the output nodes and no signals are allowed to be fed-back among the neurons [108]. The number of hidden layers, number of neurons in each layer totally depends on the complexity of the problem being solved by the network. This structure is commonly used in system identification and nonlinear function approximation applications.

Another architecture of NN is the recurrent network which differs from the feedforward structure by having feedback connections which propagate the outputs of some neurons back to the inputs of other neurons to carry out repeated computations on the signal as shown in Fig. 6.4 [108].

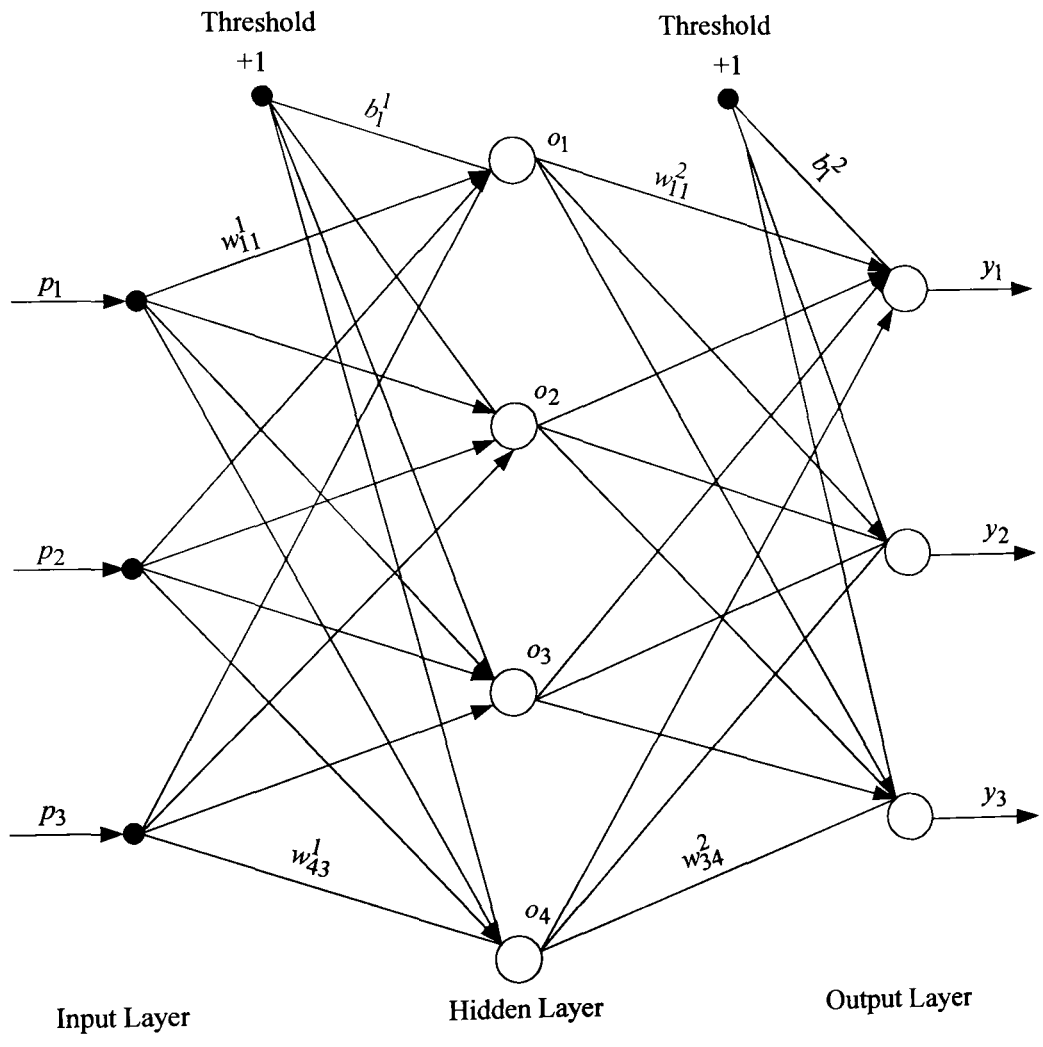

Fig. 6.3 Architecture of multilayer feedforward neural network

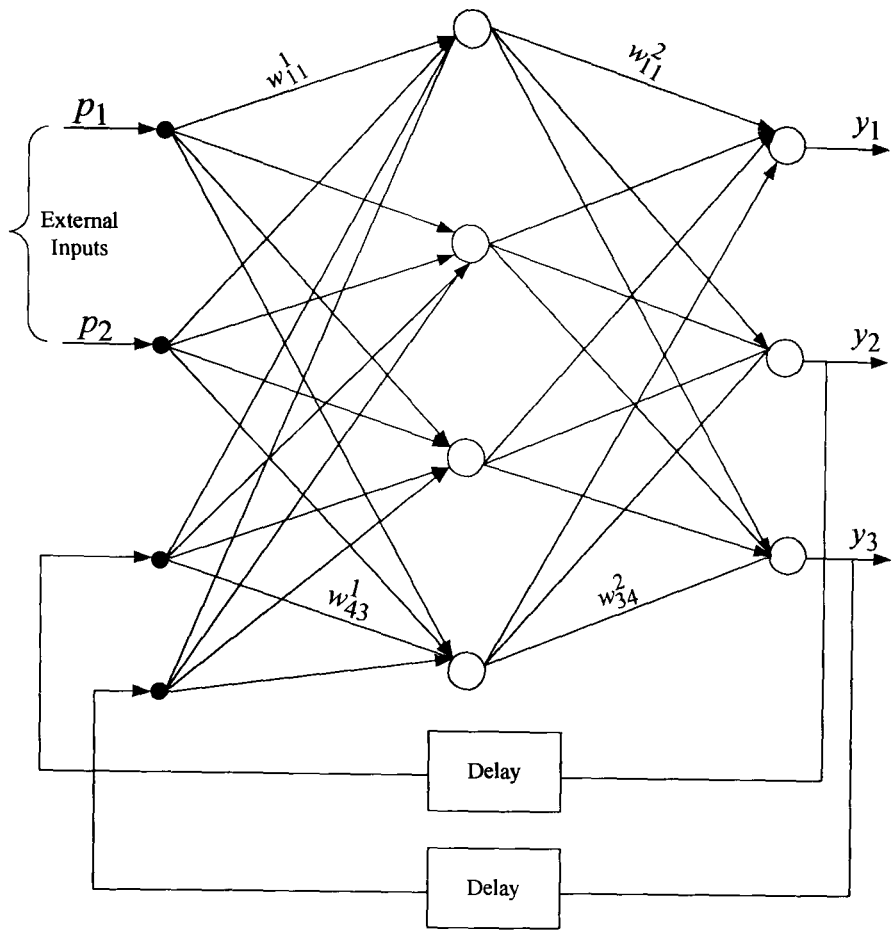

Fig. 6.4 Structure of recurrent neural network

6.2.2 Learning Techniques

The artificial NN resembles the human brain in learning through training and data storage. A training process is performed to enable the NN to understand the model to be represented. Based on learning strategy two popular techniques can be described: supervised and unsupervised learning. Supervised learning is frequently used in the majority of NN applications. Training can be performed either online or off-line. For online training, the NN weights are continuously updated during operation rather than being constant with off-line training.

6.2.2.1 Supervised Learning

In this type of learning a teacher is present during the learning process and the NN is trained through a given input/ target data which includes input pattern associated with the corresponding target or desired pattern [11]. These training data form a pool of examples used to train the NN in order to learn a specific behaviour. The presence of desired output(s) for each input in the training pattern makes this type of learning supervised.

During the learning process, the NN output is compared with the target value and a network weight correction via a learning algorithm is performed in such a way as to minimize an error function between the two values [27, 60]. This is an optimization problem in which the learning algorithm is searching for the optimal weights that can represent the solution to the approximation problem. The block diagram of the training process is shown in Fig. 6.5.

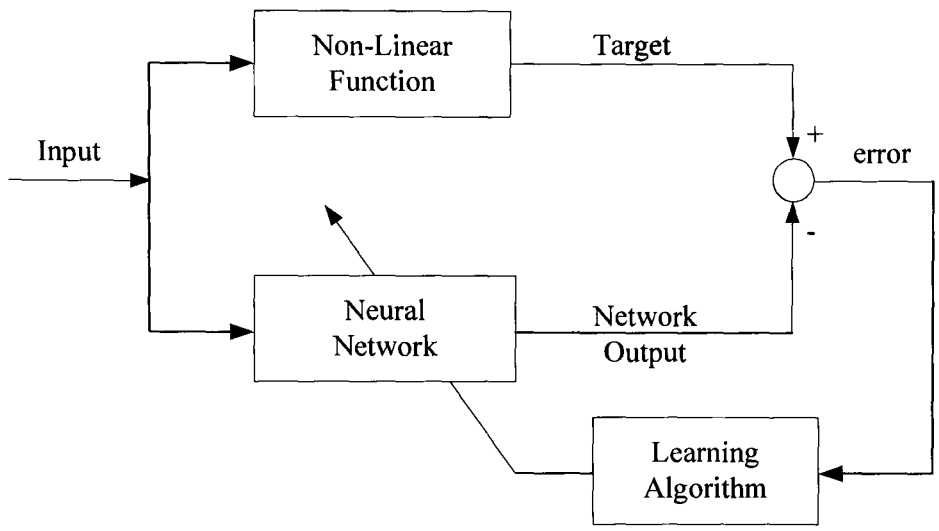

Fig. 6.5 Block diagram of neural network training using supervised learning

A commonly used error function is the Mean-Squared Error (MSE) which represents the average error between the network's output and the target value over all the example pairs. Backpropagation is a gradient descent algorithm usually used to update the network weights during training to improve the network performance. This is achieved by minimizing a performance function, the MSE, which moves the network weights along the negative of the gradient of the performance function. This algorithm can be used to train multilayer feedforward NNs either online or off-line.

6.2.2.2 Unsupervised Learning

In this type of learning, no desired or target is available to the network and only the input pattern is present, i.e. there is no teacher to learn the network. The system must learn by discovering and adapting to structured features in the input pattern [108, 109]. This is done by adapting to statistical regularities or clustering of patterns from the input training samples [108].

6.3 Neural Network MRAS Observer

To overcome the problems associated with the conventional rotor flux-MRAS observer NN is introduced as rotor flux observer to replace the conventional VM used in the classical scheme. This represents an entirely new application of NN to MRAS schemes. A multilayer feedforward NN is used to estimate the rotor flux components from current and previous samples of the stator voltages and currents. Compared to a VM flux observer, the NN does not employ pure integration and is less sensitive to motor parameter variations as will be shown later. Compared to other conventional schemes that make use of a LPF for flux estimation, the NN observer does not employ any filtering. This avoids delaying the estimated speed and prevents estimation errors below the filter cut-off frequency. The training of this network was performed using experimental data. This avoids using search coils which are not a suitable way to obtain flux measurements in most applications [106]. The outputs from the CM are used as target values for the NN to provide harmonic-free signals and an accurate output at low speed. Hence the MRAS scheme effectively uses two versions of the CM: one based on (3.54) and one based on the trained NN. This greatly improves the performance of the speed estimator as will be experimentally proved later. The offline trained NN will be used as a reference model for the MRAS observer to form a NN MRAS scheme as shown in Fig. 6.6.

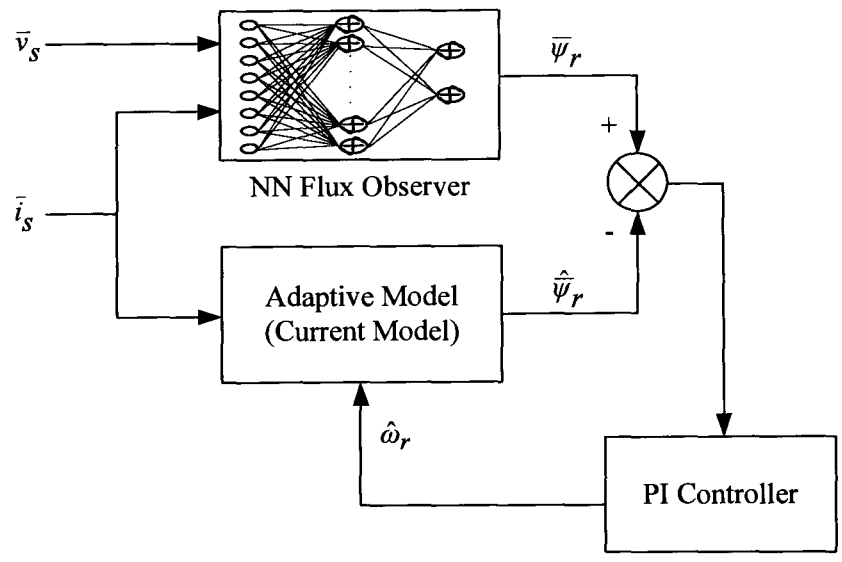

Fig. 6.6 Proposed NN MRAS speed observer

Since the performance of the conventional MRAS scheme improves at higher speeds, NN is suggested to replace the VM only in the low speed region. This will dramatically

reduce the number of training samples and consequently the training time in addition to reducing the NN size. At high speed conventional MRAS employing VM can be used. Experimental testing of the classical MRAS observer shows deterioration of the performance in ±100 rpm speed region but operation outside this range was satisfactory. Therefore the task of the proposed scheme is to improve the performance in the critical ±100 rpm region. First a NN scheme is developed which is suitable for general purpose IM drives where rated load is not required for low speed operation. In such applications the load torque is related to the rotor speed and hence a small load torque is needed at low speed. The possibility of extending the scheme to cope with low speed, rated load applications has also been discussed.

6.4 Neural Network Rotor Flux Observer

Multilayer feedforward NNs have shown great capabilities for nonlinear function approximation applications. Various attempts to model machine flux from measured quantities such as stator voltages, currents and motor speed have been discussed [10, 27, 29, 106]. In this section a multilayer feedforward NN will be presented that estimates the rotor flux components from the present and past samples of the terminal voltages and currents. The NN is trained to match the performance of the CM which is free from stator resistance dependency and dc drift problems.

It has been shown that any nonlinear function can be represented by a three layer NN, i.e. input, hidden and output layers, with a given number of neurons in each layer and that the accuracy of the approximation depends on the number of neurons in the hidden layer [10, 11]. Here an 8-25-2 multilayer feedforward NN, shown in Fig. 6.7, is used to estimate the rotor flux components in the stationary reference frame. To obtain good estimation accuracy, the inputs to the network are the present and past values of the *d-q* components of the stator voltage and current in the stationary reference frame. Compensated versions of the reference voltages are used, as discussed in chapter 4. Better performance can be obtained by increasing the number of inputs to include voltage and current samples from more than one time step in the past. However, this may require larger training data and will need more computational effort to achieve good approximation accuracy.

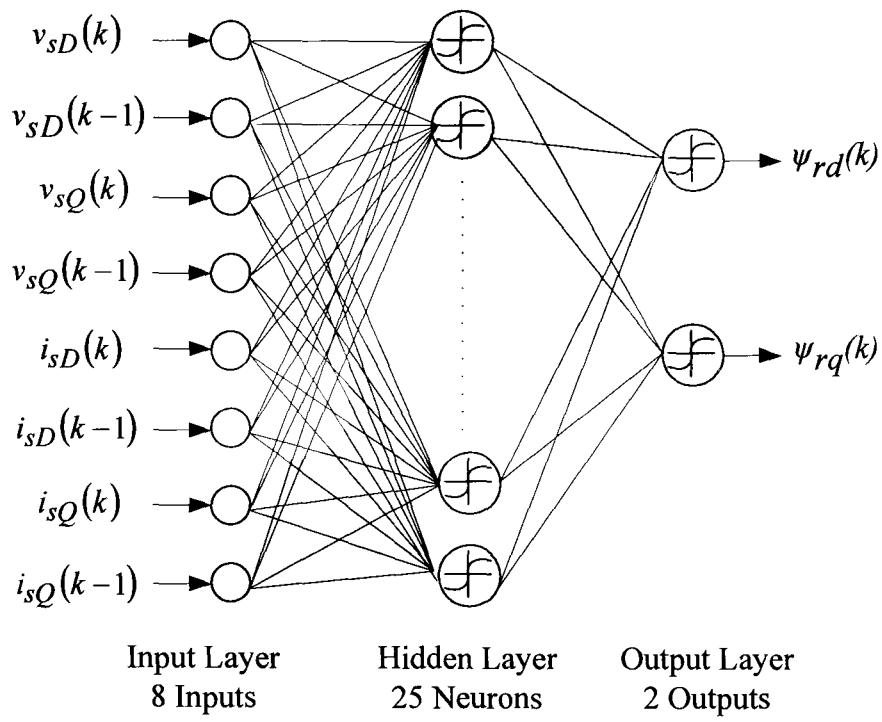

Fig. 6.7 Neural network rotor flux observer

One of the major drawbacks of NN strategy is the lack of design techniques. Hence the number of neurons in the hidden layer is chosen by a trial and error technique to compromise between computational complexity, if a larger number is selected, and approximation accuracy, if a smaller number is selected [27]. This degree of trial and error may increase the training process time. The output layer of the NN consists of two neurons representing the rotor flux components in the stationary reference frame. Since the case is approximating a nonlinear function with bipolar input/output pattern, hyperbolic tangent (Tan-Sigmoid) activation functions, Fig. 6.2(d), is used in both hidden and output layers [11]. In this case, the neuron transfer function can be written as:

$$y_j = \tanh(net_j) = \frac{1-\exp(-net_j)}{1+\exp(-net_j)} \tag{6.3}$$

6.4.1 Neural Network Training

The first step for NN development is to obtain the training data. Generation of the training set is crucial since it should adequately represent the problem to be solved by the NN. Training data can be obtained by using simulation tools or through experiments. However, experimental data is more suitable for NN to produce realistic outputs [110]. Therefore the training data for the NN flux observer are obtained from the experimental

system. This is achieved by running the encodered vector control drive with different operating conditions in the low speed region 100 rpm to -100 rpm including the zero speed. Various load levels ranging from 0 to 25% of rated load are used to suit low speed, low torque applications such as fans, centrifugal pumps and blowers. Small and large references speed changes were applied to the drive during the training phase to include all the possible operating conditions. The reference voltages and measured stator currents are transformed from 3-phase (a, b, c) to 2 phase (d, q) for the NN training data. A LPF with 40 rad/s cut-off frequency was used to remove drift and noise from the reference stator voltage signals. The present and past samples of filtered stator voltages and stator currents components are obtained which will be used as inputs to the NN model. Even using direct flux sensing via search coils [27], noise and rotor slot harmonic effects on the measurements require that a LPF be used.

The outputs from the CM, which are obtained from stator currents components and encoder speed, are used as target values for the NN. This is an effective way to obtain the correct values of the rotor flux since the obtained signals are relatively noise and harmonic-free including all the drive nonlinearities. Moreover, the CM flux observer produces accurate flux estimation at low speed [69]. The block diagram of the training data acquisition from the experimental system is shown in Fig. 6.8.

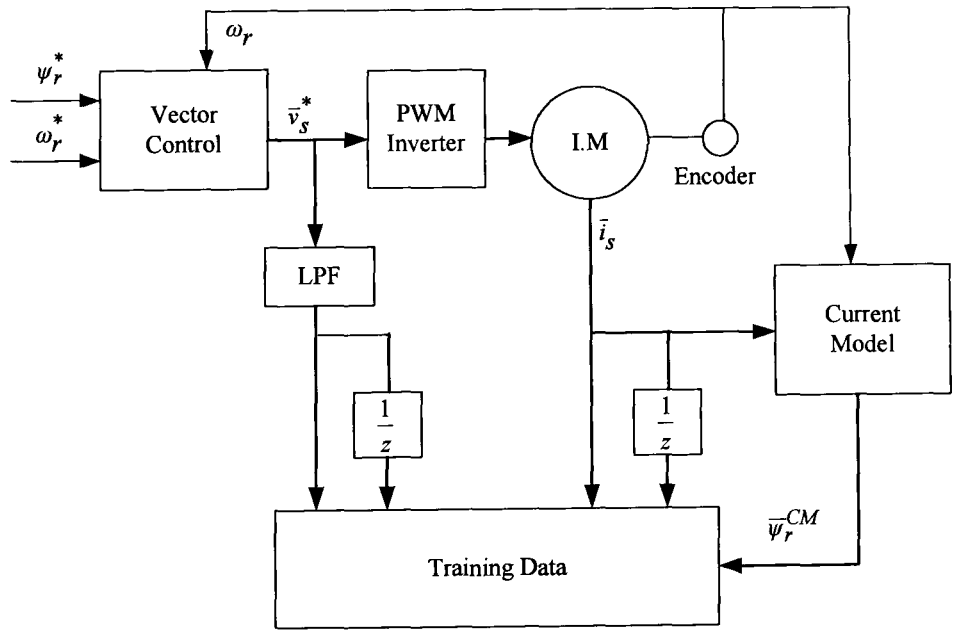

Fig. 6.8 NN Training data acquisition from experimental system

Since the measurements are generated at different scales for voltage, current and flux, scaling of the data variables is necessary to increase the numerical stability of the data

processing [110]. Furthermore, the scaling level is determined by the type of activation function being used. With hyperbolic tangent sigmoid function used in the hidden layer of the NN, training data has to be normalized to lie in the range between -1 to 1. The training is performed off-line with Matlab-Simulink using the Levenberg-Marquardt training algorithm which is faster than the gradient descent backpropagation algorithm but needs a large memory [11, 27]. This algorithm is considered to be the fastest for training moderate size feedforward NN with weights up to several hundreds [111]. Moreover, it has an efficient implementation in Matlab software [111]. A 5000 input/output pattern was used to train the NN. After the training the MSE between targets and NN outputs decays to a satisfactory level (4.5×10^{-4}) after about 2200 epochs as shown in Fig. 6.9. The training lasts for less than one hour on a Pentium ® IV PC running at 3 GHz with 512 MB of RAM.

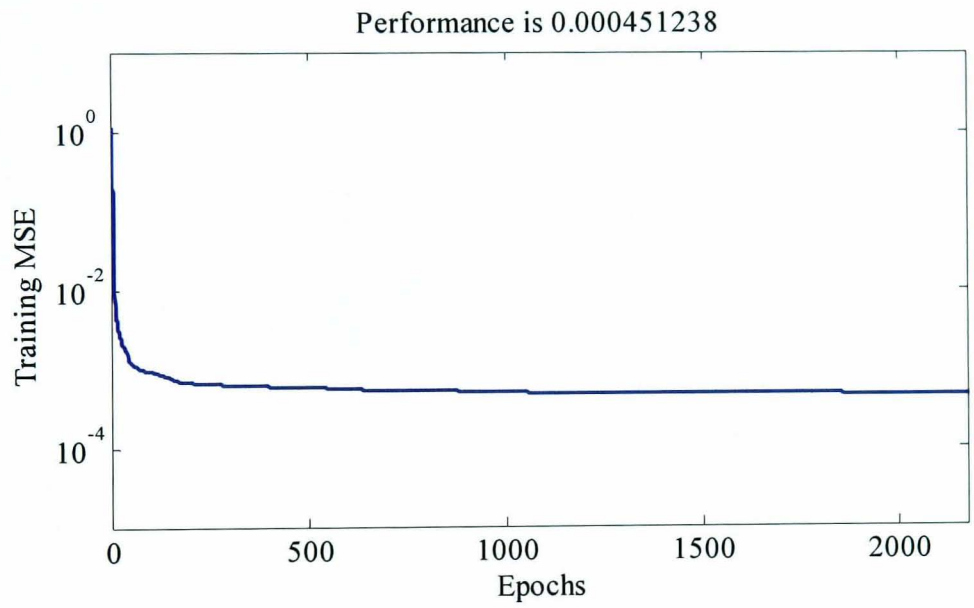

Fig. 6.9 NN performance during training

6.4.2 Neural Network Flux Observer Testing

Extensive experimental tests were carried out to test the performance of the NN observer in various operating conditions not seen during training to ensure the generalization capability of the NN model. As shown in Fig. 6.10 the trained NN is tested and compared with the conventional VM by running the encodered vector control in the low speed region under different loading conditions. The outputs of the VM and the NN flux observer will be compared with the output of the CM which represents the accurate value of the rotor flux. Compared to the VM, the NN matches the CM extremely

well in both transient and steady state conditions even when the drive is operating at low speed.

Fig. 6.11(a) shows the performance of the two rotor flux observers, the VM and the NN, compared to that of the CM when the encodered drive is performing a speed change from 100 rpm to 50 rpm at no load. More results are shown in Figs. 6.11(b)-6.11(c) for operation at 20 rpm with 10% load and -40 rpm with 20% load. Attenuation and phase delay take place in the VM mainly due to the filter effect where as NN output closely track the CM output at this very low speed.

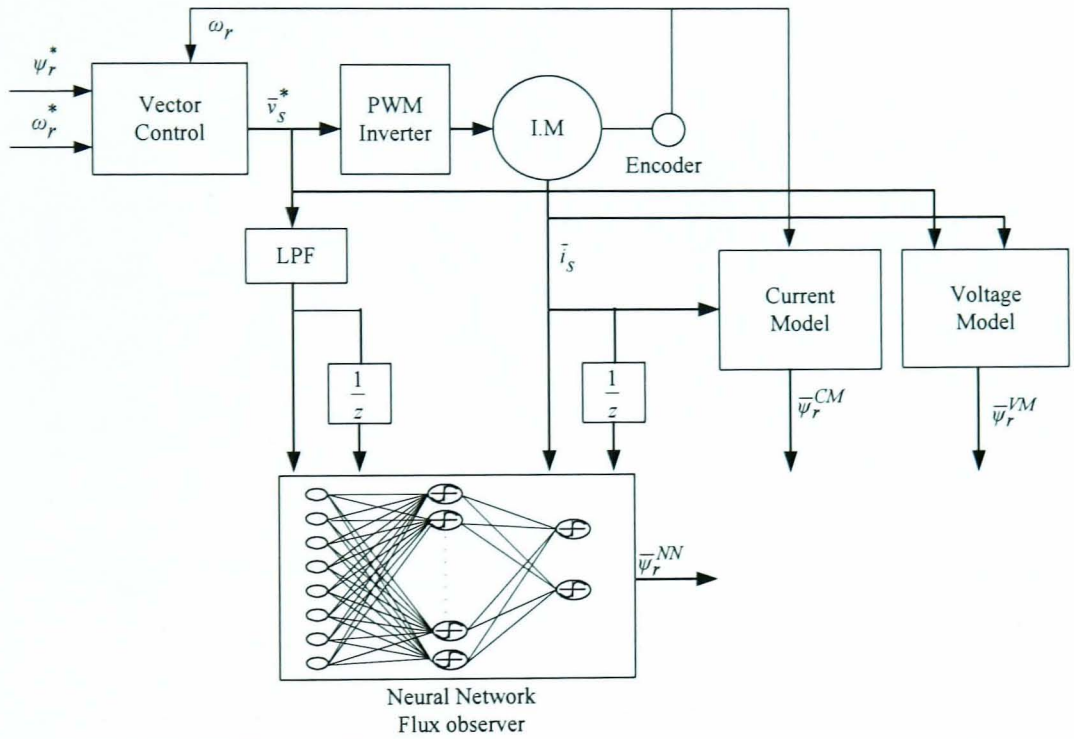

Fig. 6.10 Schematic of NN observer testing

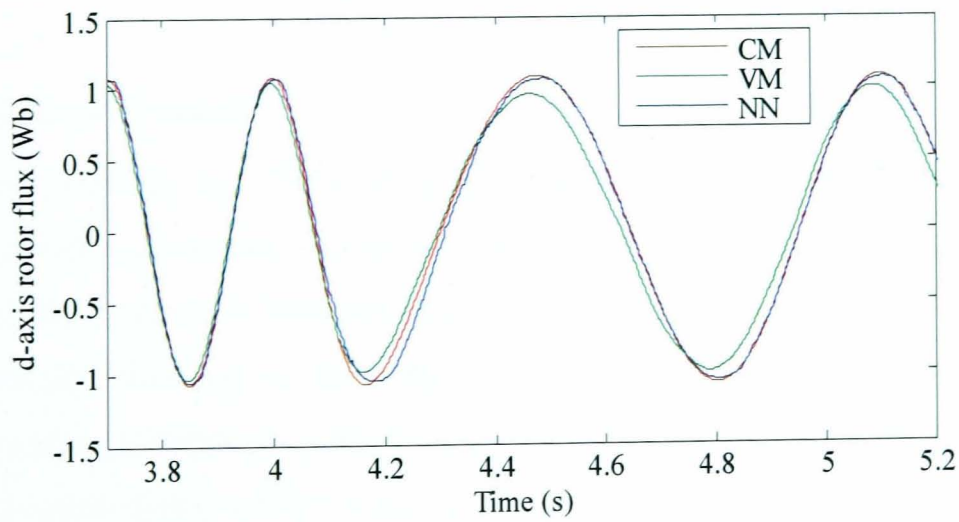

(a)

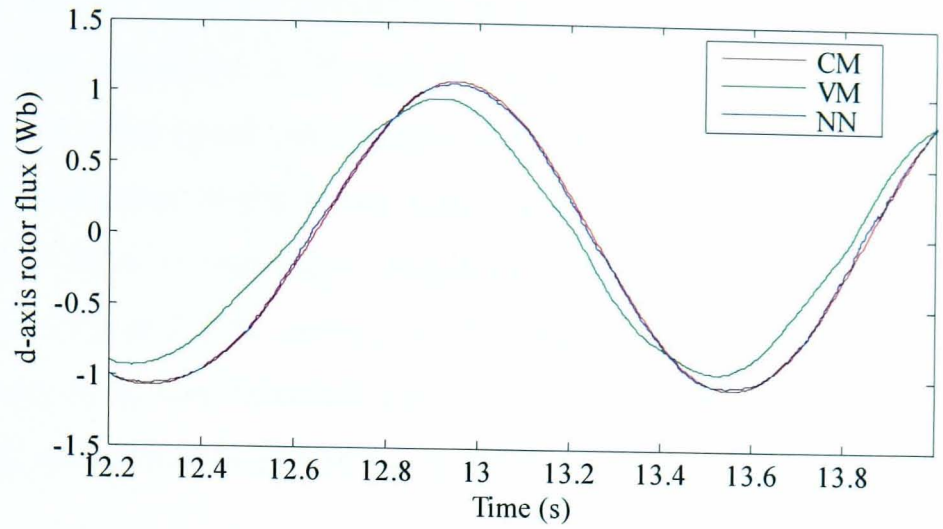

(b)

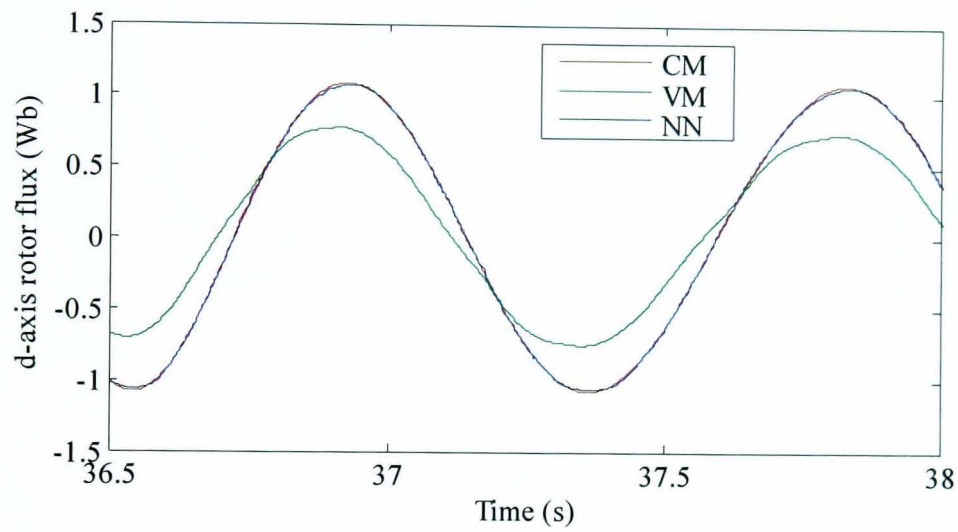

(c)

Fig. 6.11 NN observer experimental testing (a) 100 rpm to 50 rpm no load (b) 20 rpm at 10% load (c) -40 rpm at 20% load

6.5 Simulation Results

To further validate the NN observer, simulation tests were conducted to evaluate its performance when parameter variation takes place. Therefore a multilayer feedforward NN with similar structure of that introduced in the previous section has been created. The training data are obtained by simulating the vector control drive when running with different operating conditions in the low speed region. Using the same training algorithm as in the previous section a MSE between targets and NN outputs of 3.17×10^{-4} has been achieved.

To test the NN observer sensitivity to parameter variation, simulations have been conducted with variations in R_s and R_r. These two parameters are the most crucial parameters that affect speed estimation especially at low speed. The performance of both observers is compared to the actual rotor flux output from the motor model when the vector control drive is working in encodered mode. Performance of VM and NN flux observers for 25% and 50% increase in R_s is shown in Figs. 6.12(a)-6.12(b). NN shows less sensitivity to R_s variation than the VM. NN observer also shows good performance with 50% R_r variation as shown in Fig. 6.12(c).

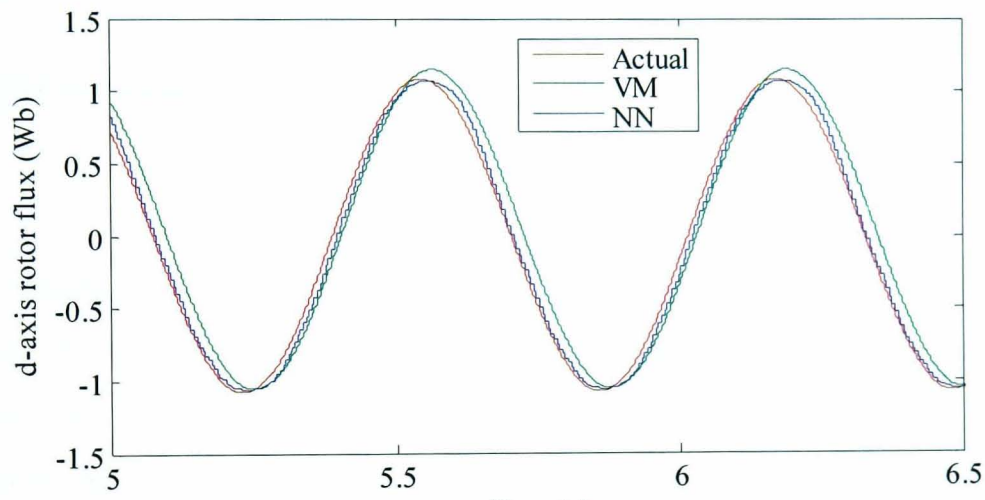

(a)

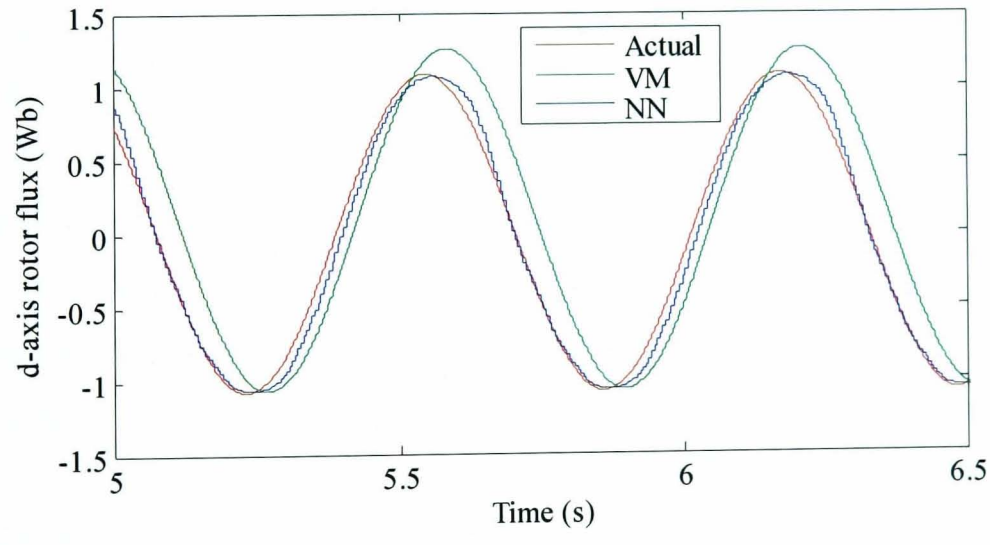

(b)

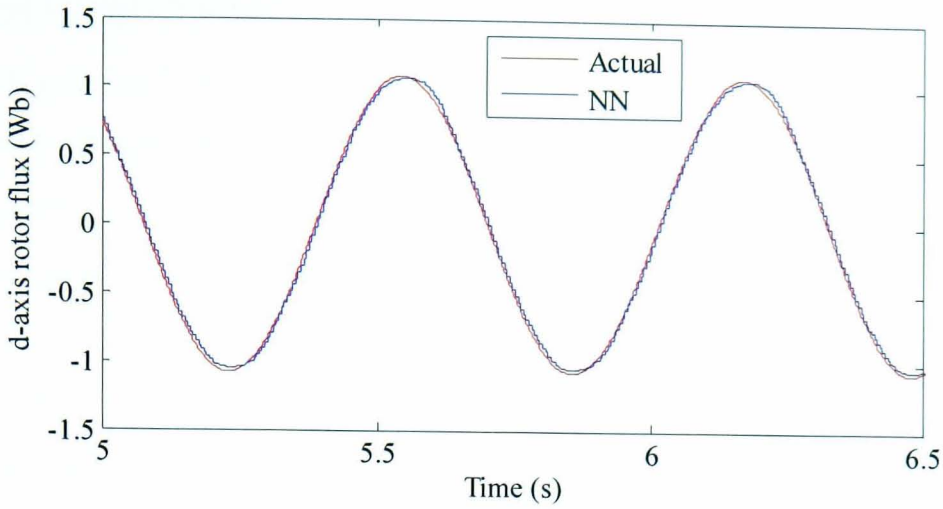

(c)

Fig. 6.12 NN observer simulation testing (a) R_s 25% variation (b) R_s 50% variation (c) R_r 50% variation

These results show that the NN can fairly handle the parameter variation problem with a good level of robustness. Consequently, for integrated drive applications, where the inverter and machine are sold as one unit, the NN observer can be trained on the actual inverter-machine combination. The NN should be able to cope with changes from these nominal parameters for other drives in the production line which is due to the manufacturer's tolerance.

However, in a mass-production environment, where the inverter can be used with several sizes of motors, the application of this technique is more difficult. In this case, a standard NN scheme becomes unsuitable unless the training is performed during commissioning for each inverter-machine combination. This may present a drawback of the proposed method. However, this could be overcome by using a range of previously trained networks where an appropriate one can be selected according to the machine nameplate rating.

6.6 Experimental Results

Once the NN is trained it is shown that it accurately matches the CM. Furthermore, NN gives a fast execution speed due to its parallel processing [11, 27]. Hence it is possible to replace the VM with the proposed NN. To further experimentally validate the proposed NN MRAS scheme, shown in Fig. 6.6, open loop and closed loop sensorless operation will be compared for the new and conventional rotor flux schemes.

6.6.1 Open Loop Operation

The new scheme was tested in open loop with the drive operated as an *encodered* vector control. The open loop performance of the conventional and the new NN MRAS speed observers is compared. PI controller gains of each scheme are tuned separately for optimal performance to allow a comparison between best performance of each scheme. Figs. 6.13-6.14 show the open loop performance of both schemes for a ±30 rpm speed reversal at 10% load and a 20% load torque disturbance rejection at 25 rpm. The NN MRAS observer demonstrates better transient and steady state performance and less sensitivity to machine parameters than the conventional scheme.

Low speed operation up to rated load can be achieved by extending the training range of the NN observer by applying various loads ranging from 0 to 100% rated load over the same speed region using the same training procedure described in section 6.4.1. After the training the MSE between targets and NN outputs decays to 0.0011. Results for 62.5% load torque rejection at 30 rpm, rated load rejection at 25 rpm and ±25 rpm speed reversal at rated load are shown in Figs. 6.15-6.17. NN MRAS scheme shows superior performance to that of the classical scheme with a negligible steady state error at higher loads up to rated load.

As discussed previously in chapter 5, the steady state error in the estimated speed at low speed for the conventional MRAS observer is mainly due to the stator resistance mismatch between the motor and the observer and dead time effects that cannot be completely removed even by complicated compensation schemes [5]. Hence the reference voltages used for the VM do not match the actual stator voltages across the machine terminals. Using the new NN MRAS scheme completely removes the steady state error in the estimated speed and improves the load torque disturbance rejection performance of the speed observer at very low speed. This improvement in the performance can be explained based on the fact that the NN estimates a flux, similar to the CM flux, which is not directly depending on the actual stator voltage, unlike the situation with using the VM in the conventional scheme. Moreover, no filters are needed in the flux observer without a pure integrator present in the NN model in addition to less sensitivity to parameter variation. As a result, the new NN MRAS scheme shows much better performance compared to the conventional MRAS observer at very low speed.

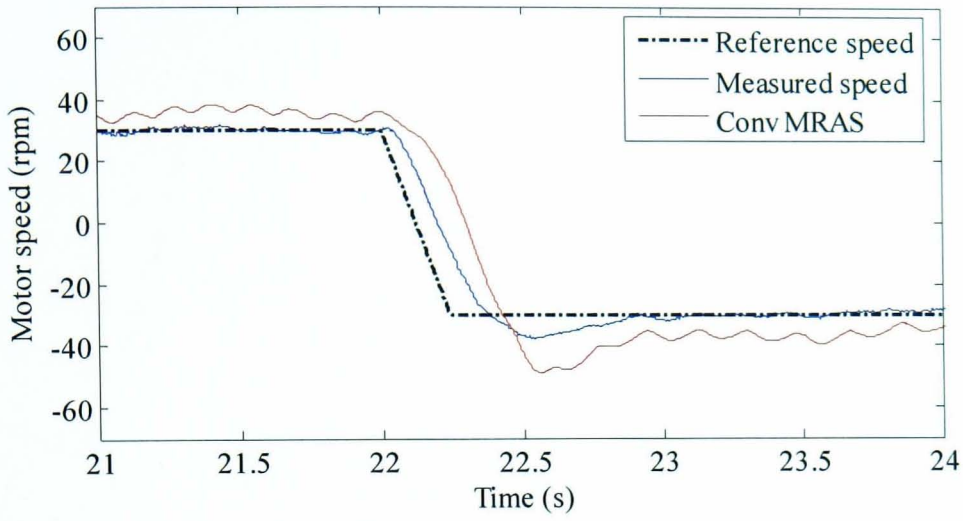
Reference speed
Measured speed
Conv MRAS
Motor speed (rpm)
Time (s)
60
40
20
0
-20
-40
-60
21
21.5
22
22.5
23
23.5
24

(a)

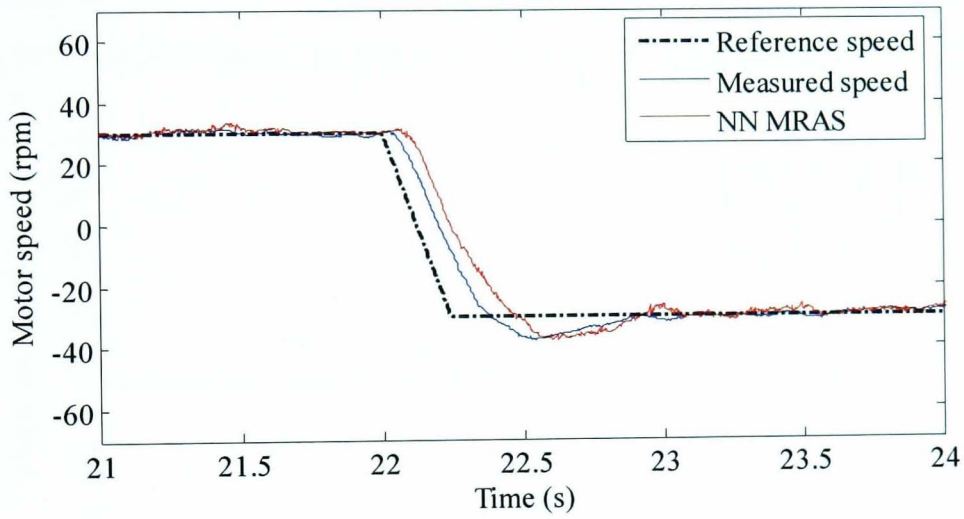
Reference speed
Measured speed
NN MRAS
Motor speed (rpm)
Time (s)
60
40
20
0
-20
-40
-60
21
21.5
22
22.5
23
23.5
24

(b)

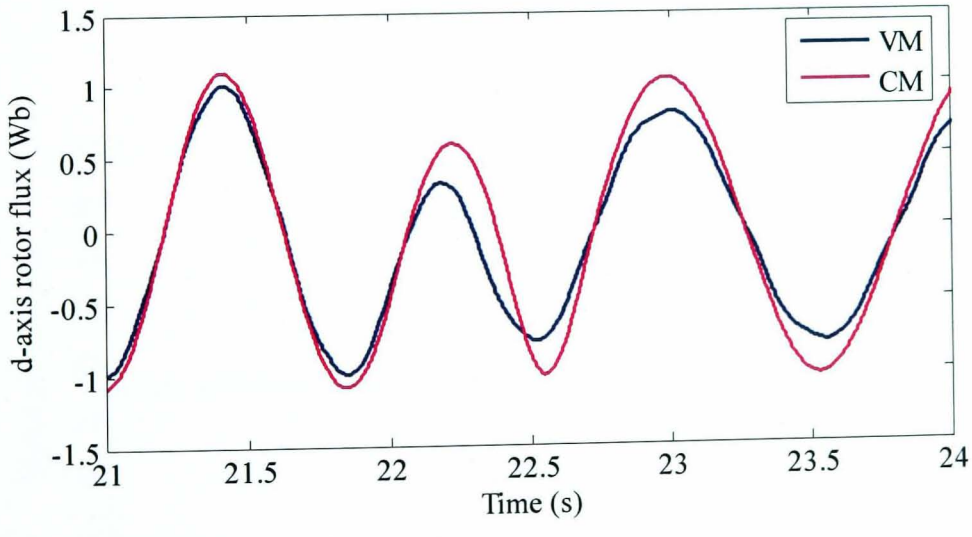
VM
CM
d-axis rotor flux (Wb)
Time (s)
1.5
1
0.5
0
-0.5
-1
-1.5
21
21.5
22
22.5
23
23.5
24

(c)

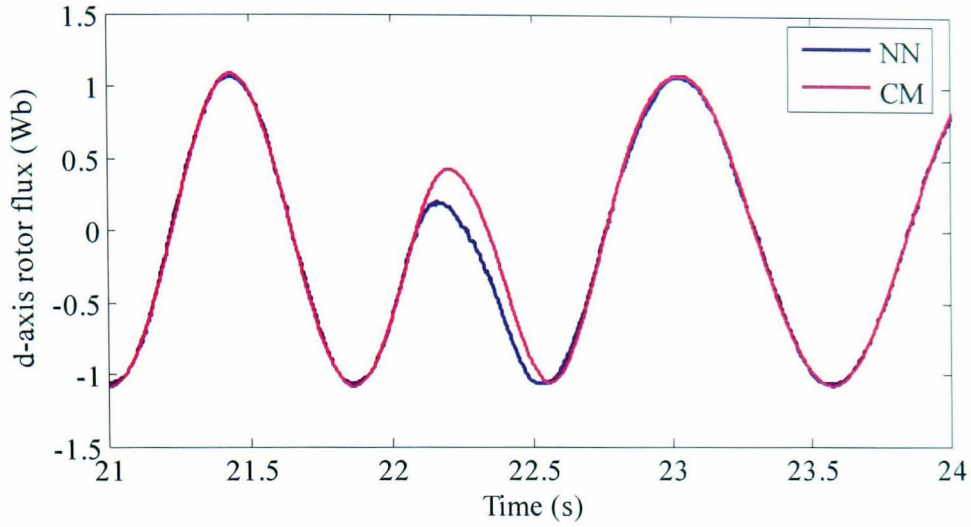

(d)

Fig. 6.13 Open loop ± 30 rpm speed reversal, 10% load. Speed: (a) Conventional MRAS (b) NN MRAS. Model outputs: (c) Conventional MRAS (d) NN MRAS

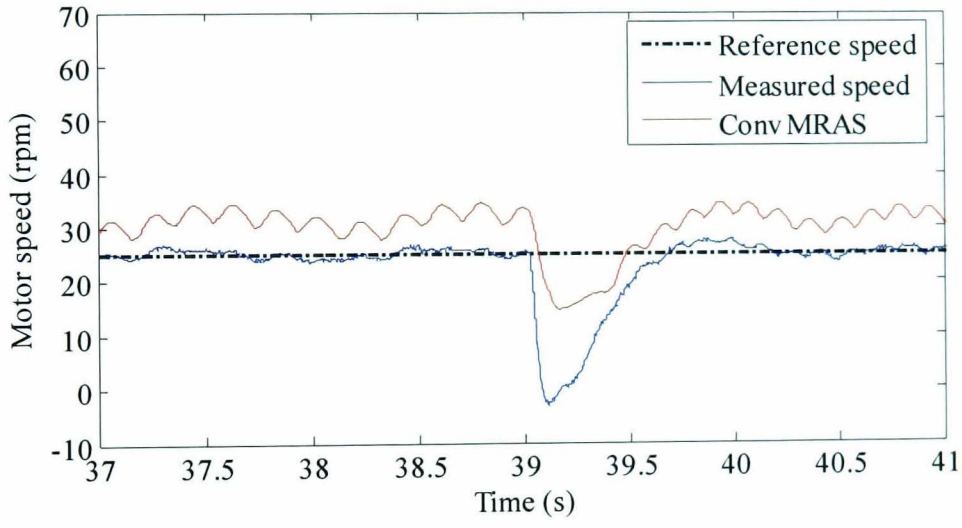

(a)

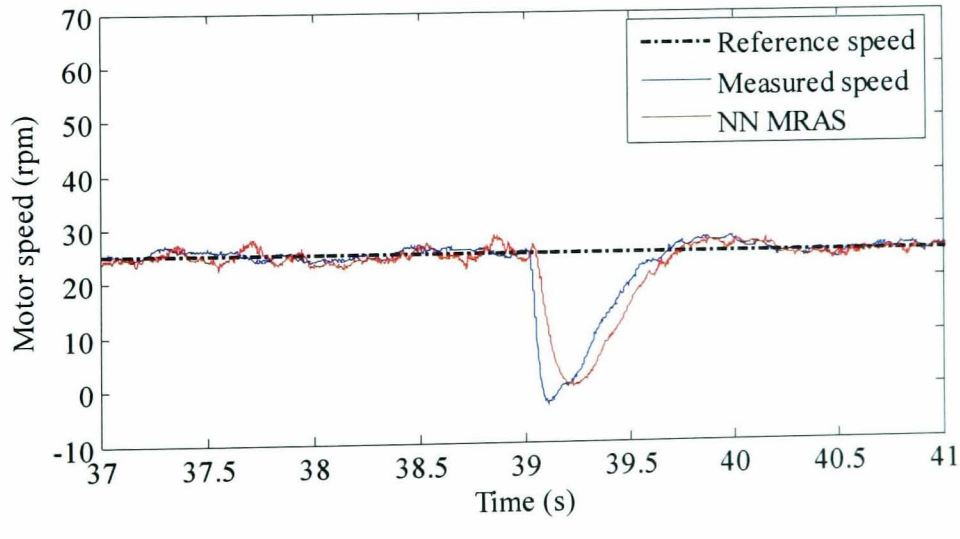

(b)

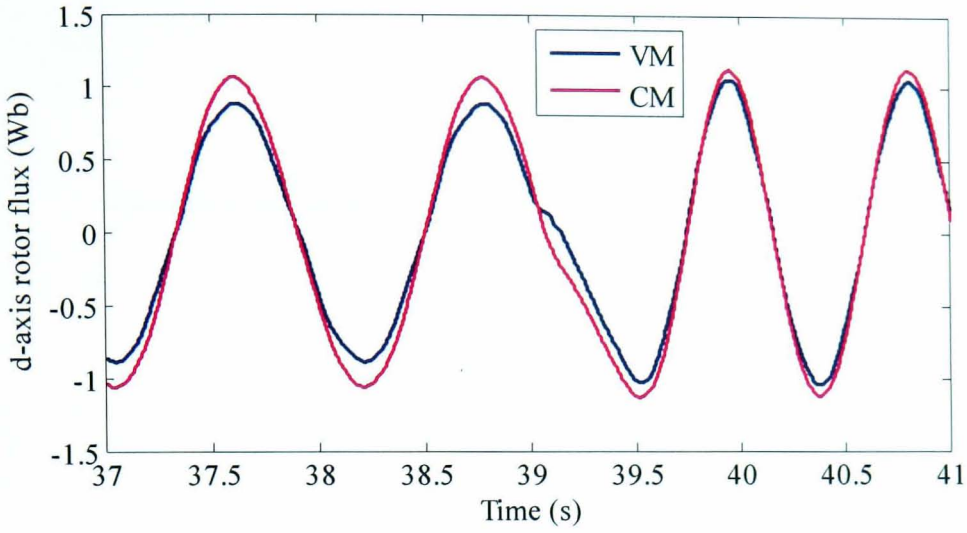

(c)

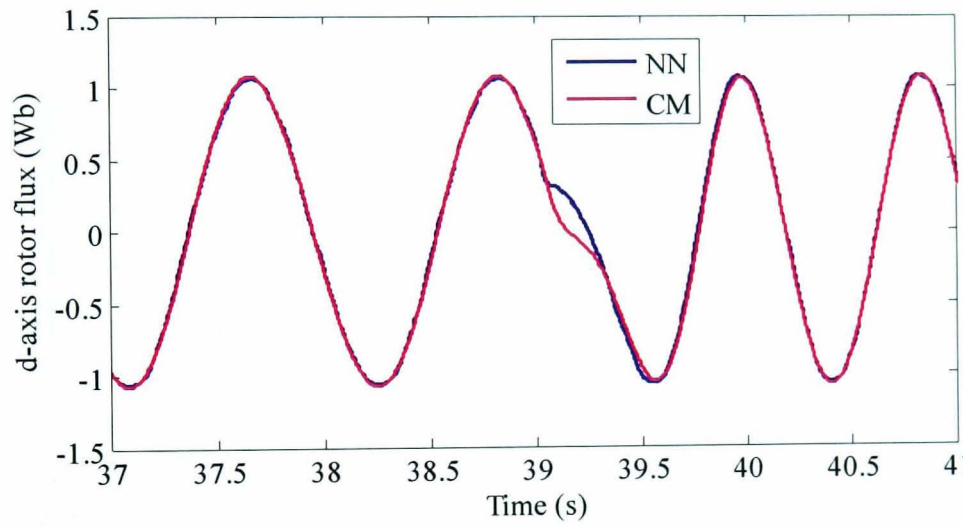

(d)

Fig. 6.14 Open loop 20% load disturbance rejection, 25 rpm. Speed: (a) Conventional MRAS (b) NN MRAS. Model outputs: (c) Conventional MRAS (d) NN MRAS

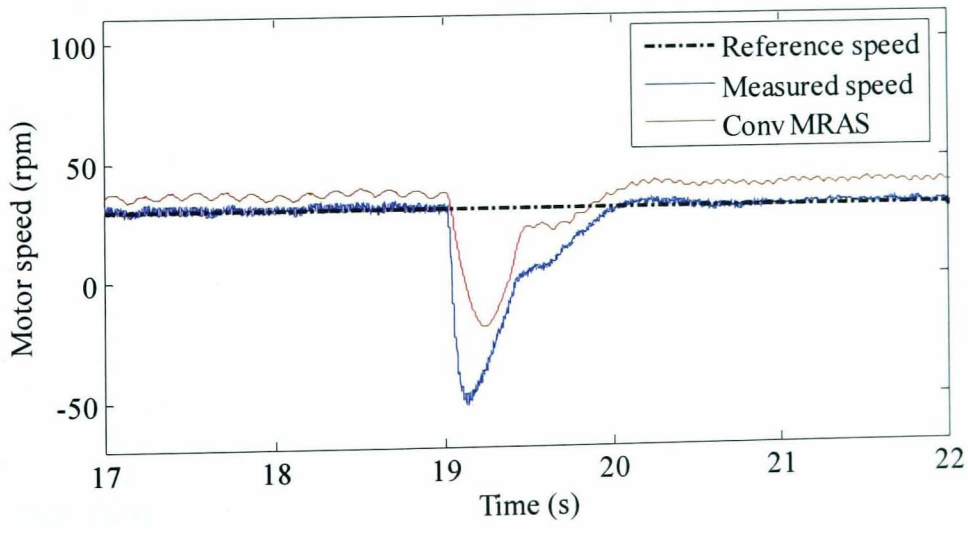

(a)

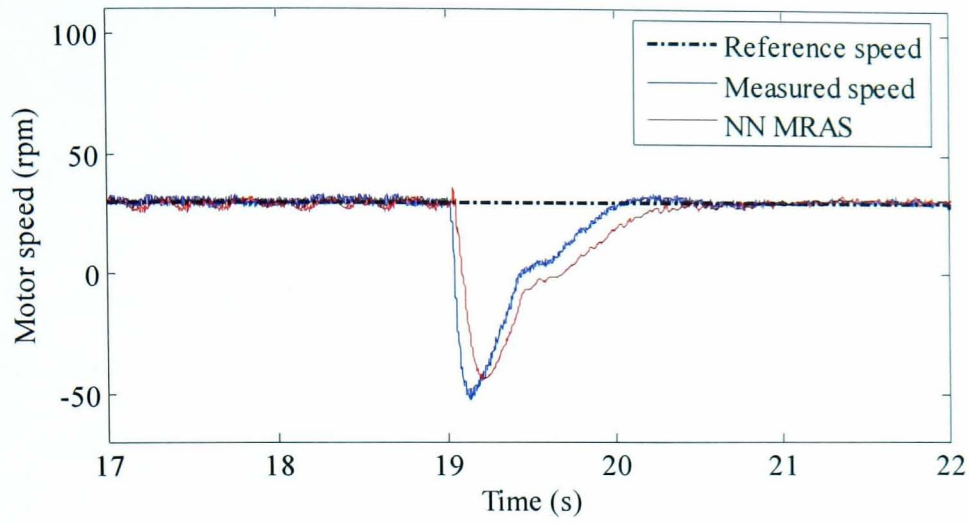

(b)

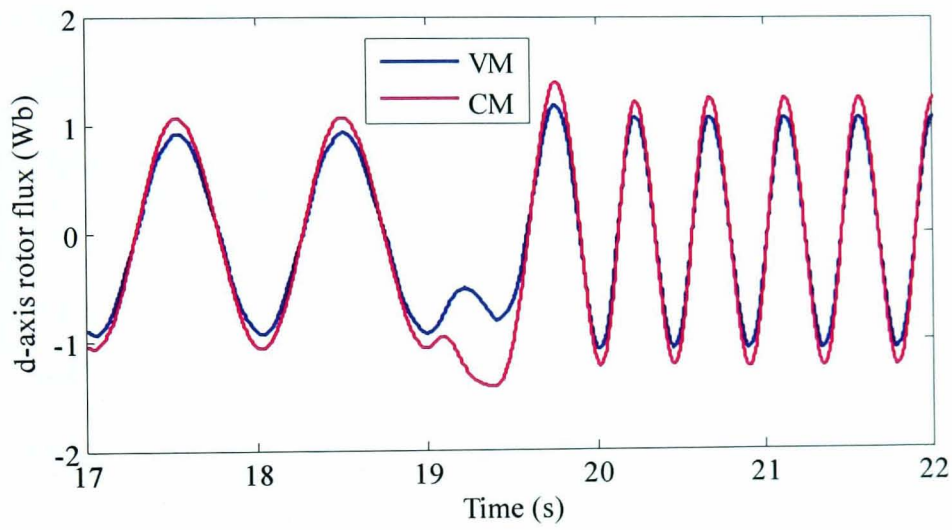

(c)

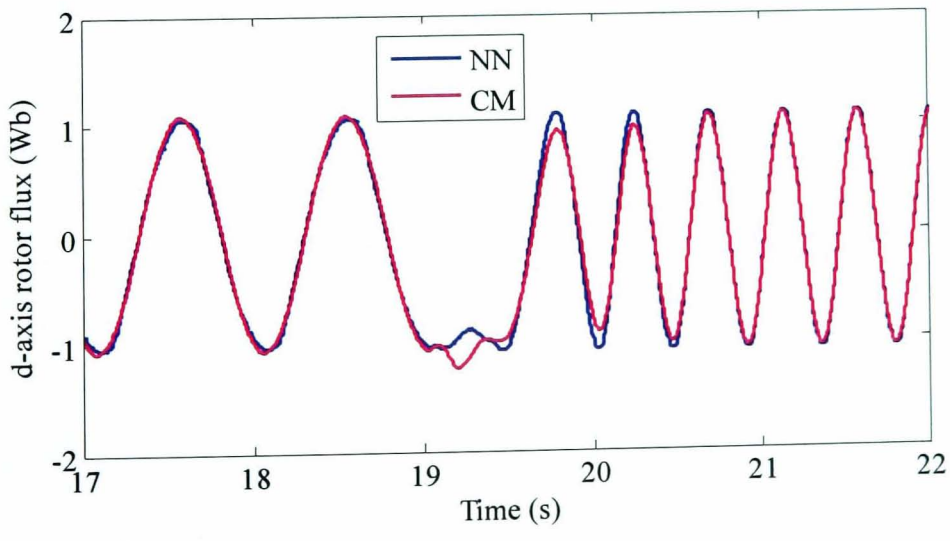

(d)

Fig. 6.15 Open loop 62.5% load disturbance rejection, 30 rpm. Speed: (a) Conventional MRAS (b) NN MRAS. Model outputs: (c) Conventional MRAS (d) NN MRAS

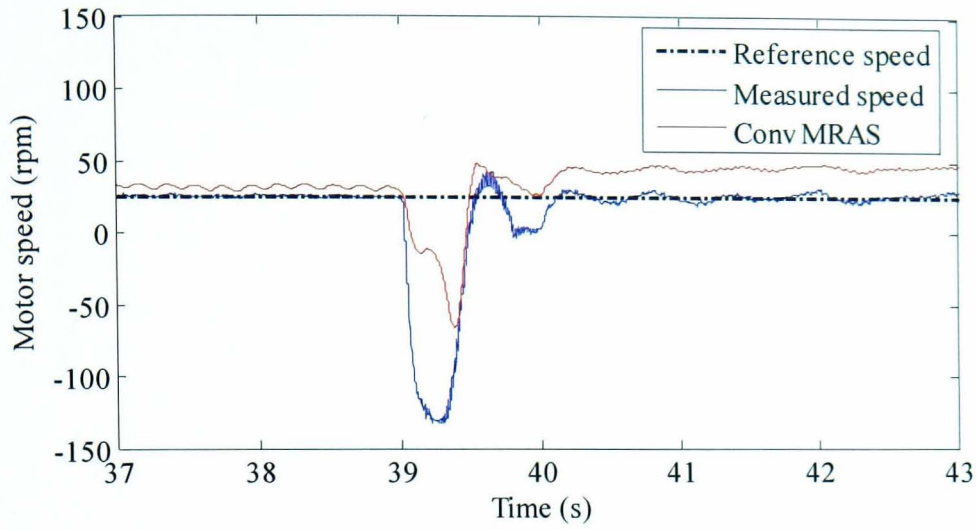
Reference speed
Measured speed
Conv MRAS
Motor speed (rpm)
Time (s)
150
100
50
0
-50
-100
-150
37
38
39
40
41
42
43

(a)

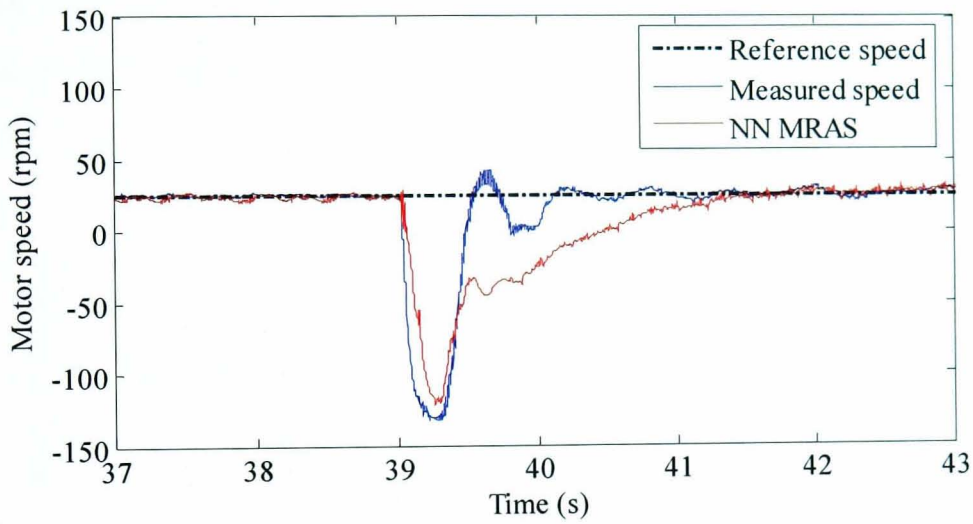
Reference speed
Measured speed
NN MRAS
Motor speed (rpm)
Time (s)
150
100
50
0
-50
-100
-150
37
38
39
40
41
42
43

(b)

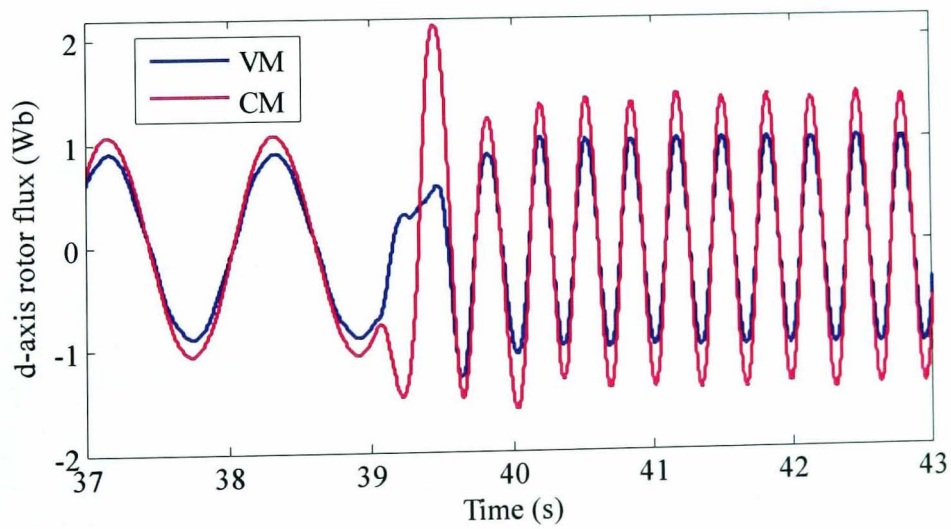
VM
CM
d-axis rotor flux (Wb)
Time (s)
2
1
0
-1
-2
37
38
39
40
41
42
43

(c)

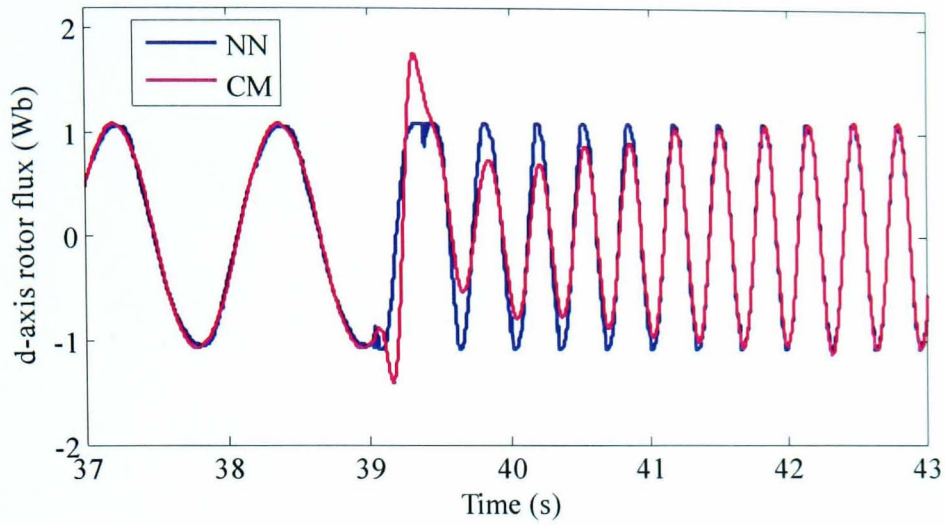

(d)

Fig. 6.16 Open loop rated load disturbance rejection, 25 rpm. Speed: (a) Conventional MRAS (b) NN MRAS. Model outputs: (c) Conventional MRAS (d) NN MRAS

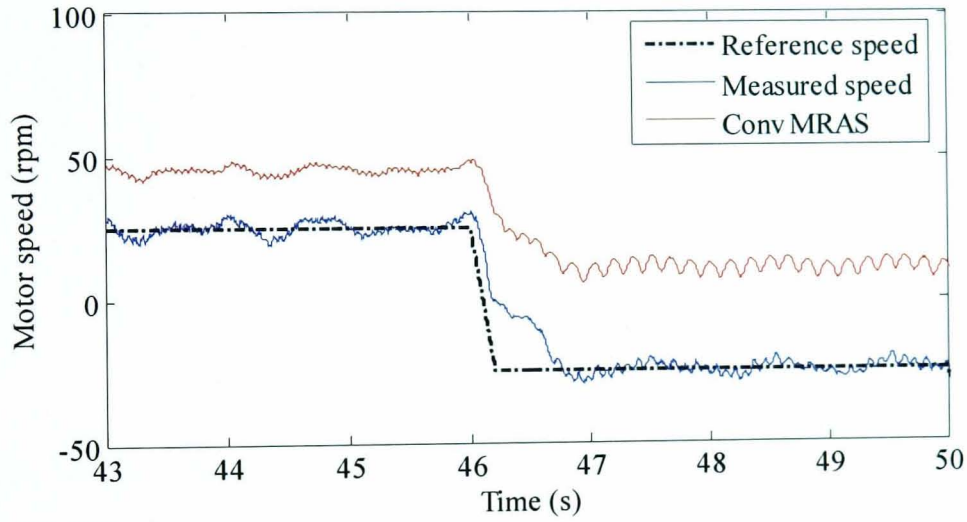

(a)

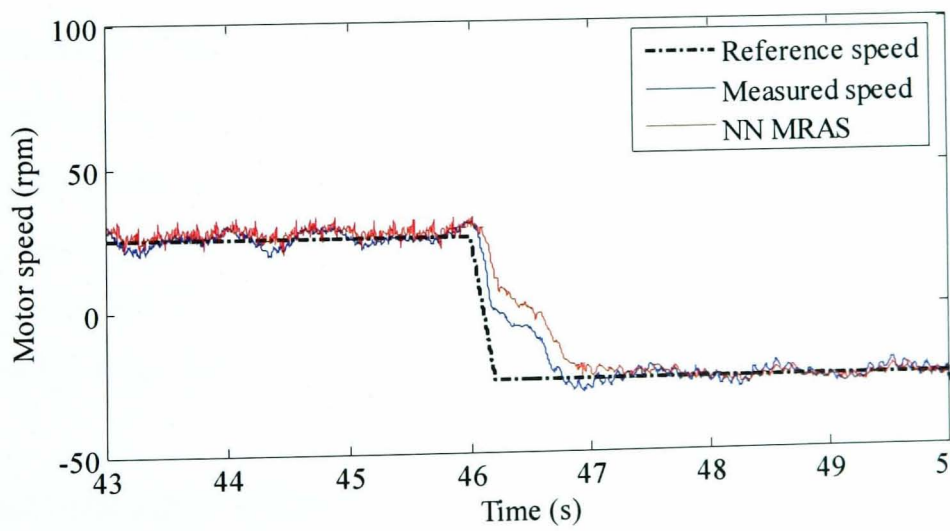

(b)

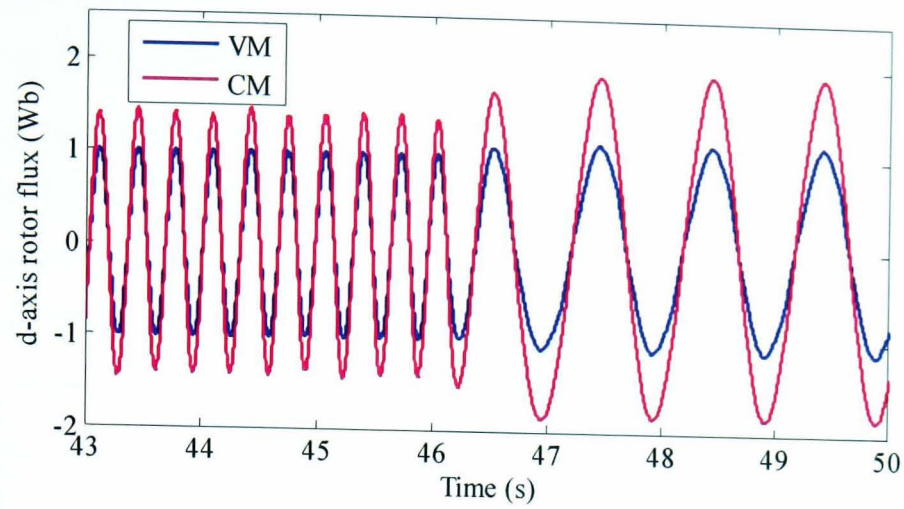

(c)

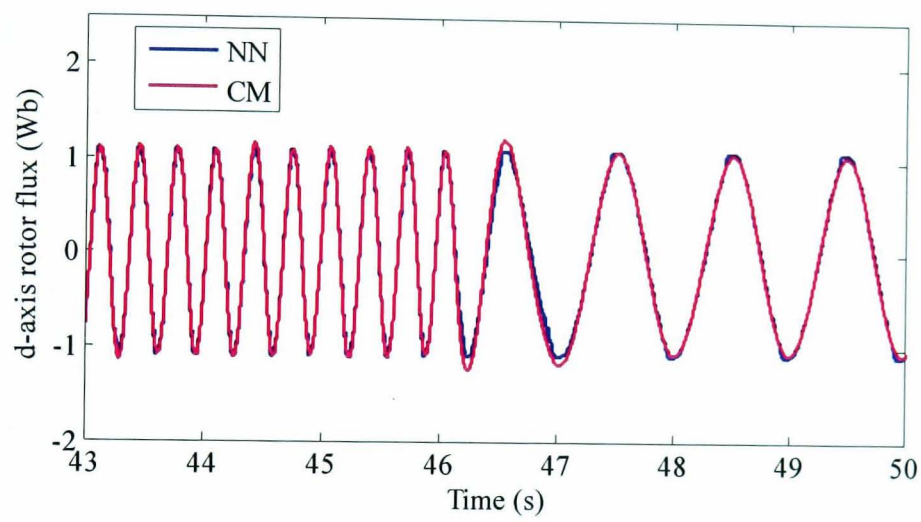

(d)

Fig. 6.17 Open loop ±25 rpm speed reversal, rated load. Estimated speed: (a) Conventional MRAS (b) NN MRAS. Model outputs: (c) Conventional MRAS (d) NN MRAS

6.6.2 Sensorless Operation

In the following tests, the IM drive is working as sensorless indirect rotor flux oriented. The encoder speed is used for comparison purposes only. Tests are conducted in the low speed and at or around the zero speed region based on some recommended benchmark tests [68, 112, 113]. Experimental results for the tests carried out using the NN described in 6.4.1 are given in this section.

Test 1: Stair case speed transients from 100rpm to 0rpm to 100 rpm:

In this test the sensorless vector control drive is subjected to stair case speed demand from 100 rpm to zero speed in a series of five steps of 20 rpm each and then back up

again to 100 rpm at no load. The performance of both schemes is shown in Fig. 6.18. The performance of the conventional MRAS deteriorates around the zero speed with speed oscillations. A steady state error between the estimated and actual speed is shown in this region of operation. NN MRAS observer shows better performance in the whole speed region. The steady state error between the estimated and actual speed has been removed with better performance around the zero speed without any oscillations. Sensorless performance around and at zero speed is shown in Fig. 6.19. MRAS model outputs are given for both schemes. With right field orientation, the NN and CM outputs match together without oscillation where as unstable behaviour is observed for the conventional MRAS outputs, the VM and CM. Better speed tuning signal is obtained from the NN MRAS scheme.

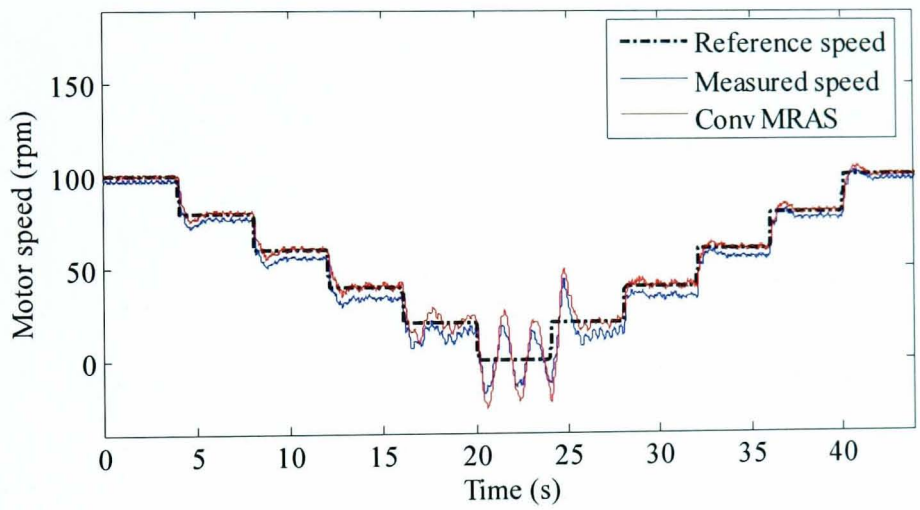

(a)

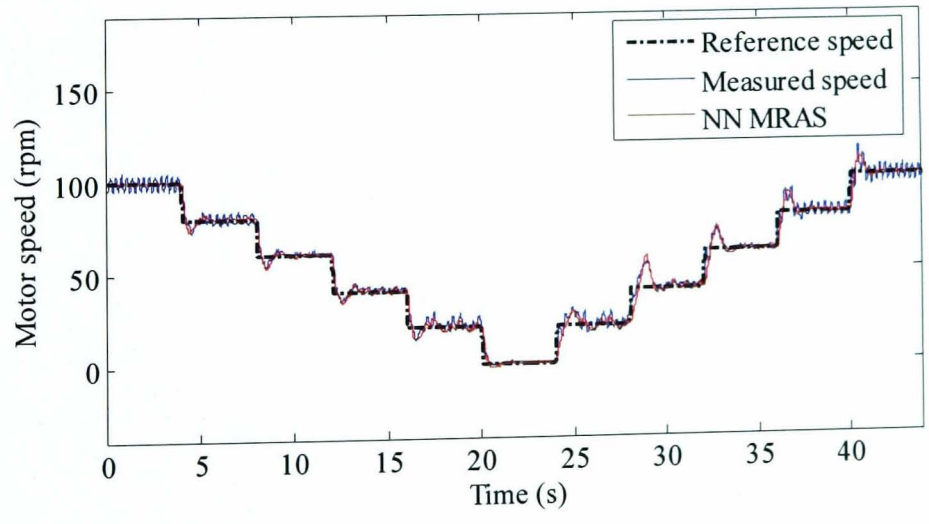

(b)

Fig. 6.18 Sensorless performance for test 1, no load. Speed response: (a) conventional MRAS (b) NN MRAS

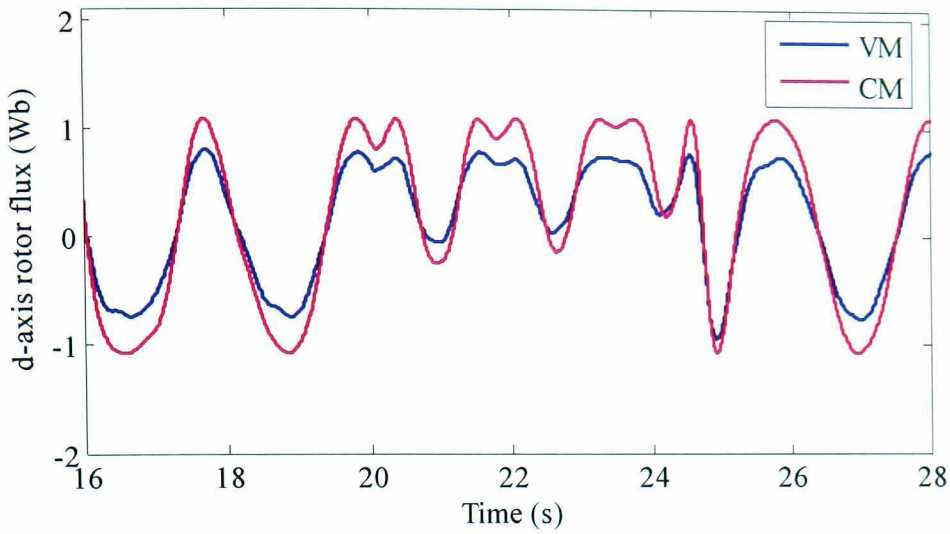
VM
CM
d-axis rotor flux (Wb)
Time (s)
2
1
0
-1
-2
16
18
20
22
24
26
28

(a)

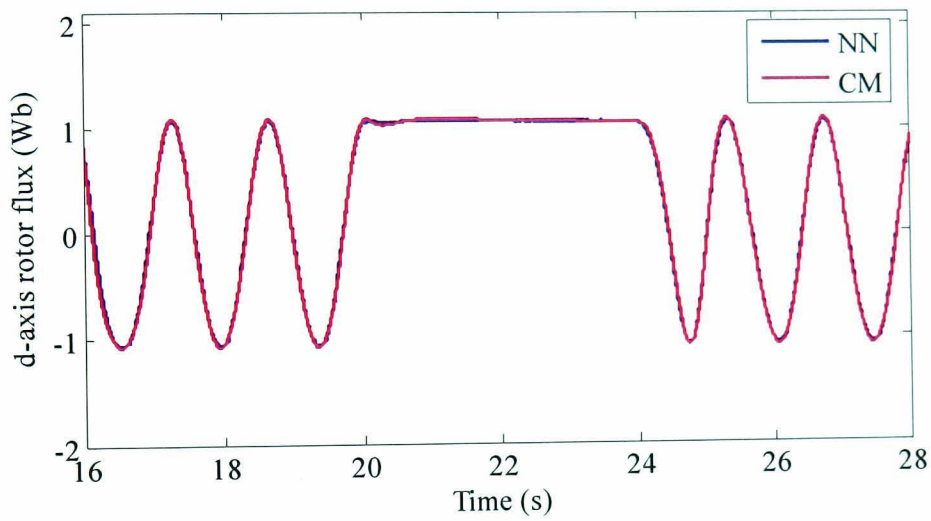
NN
CM
d-axis rotor flux (Wb)
Time (s)
2
1
0
-1
-2
16
18
20
22
24
26
28

(b)

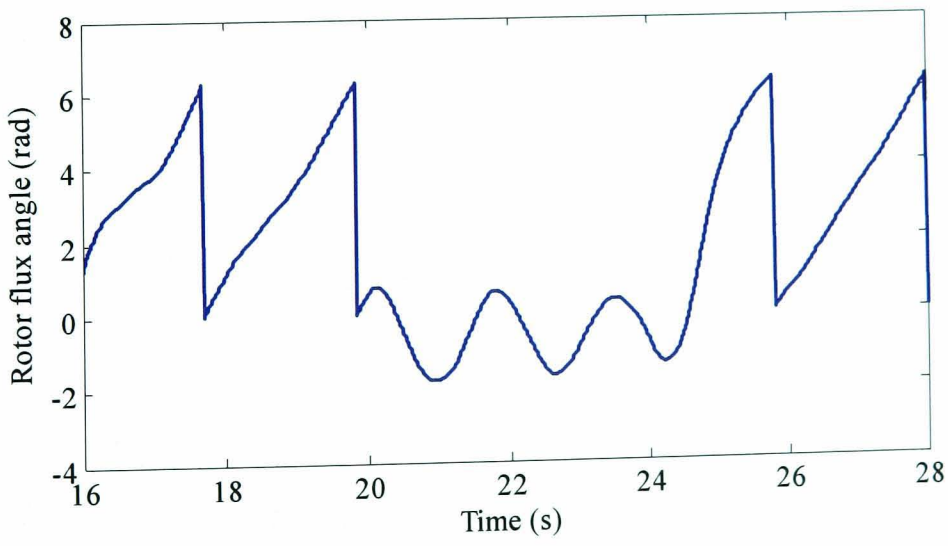
Rotor flux angle (rad)
Time (s)
8
6
4
2
0
-2
-4
16
18
20
22
24
26
28

(c)

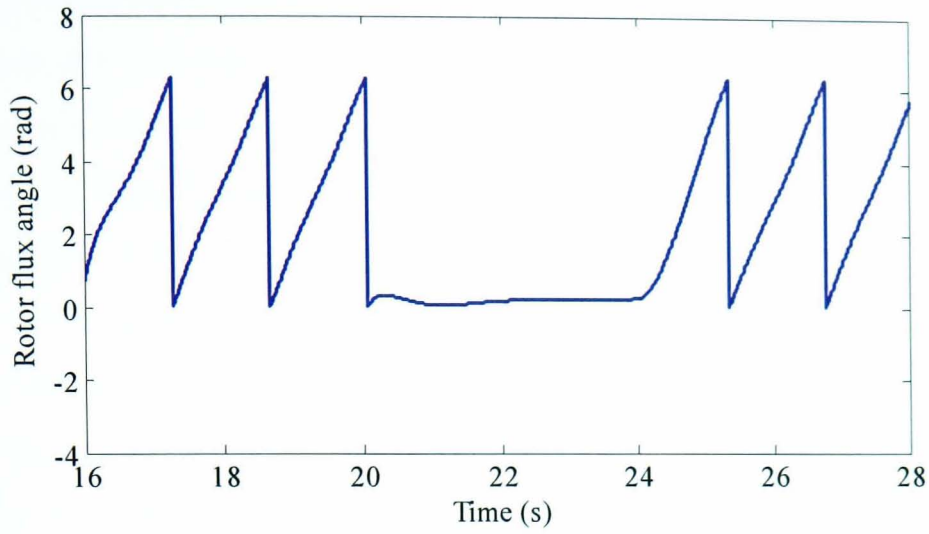

(d)

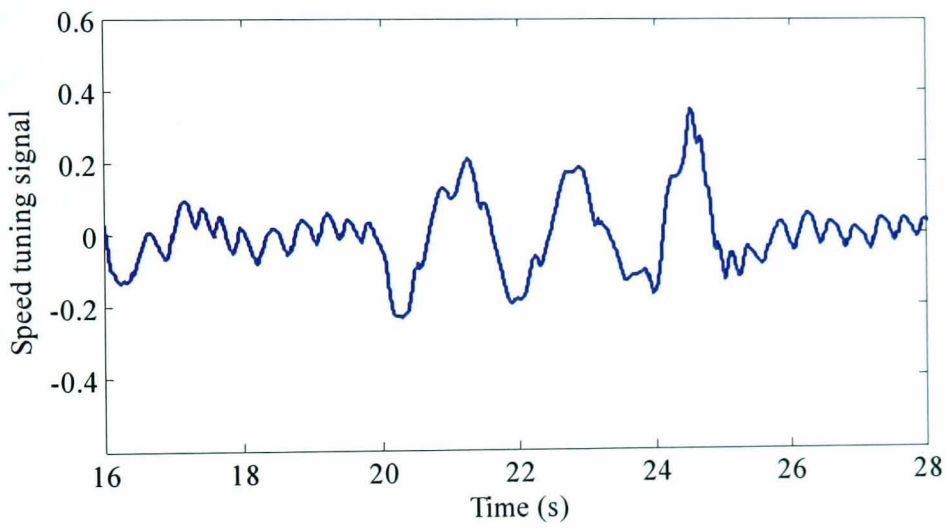

(e)

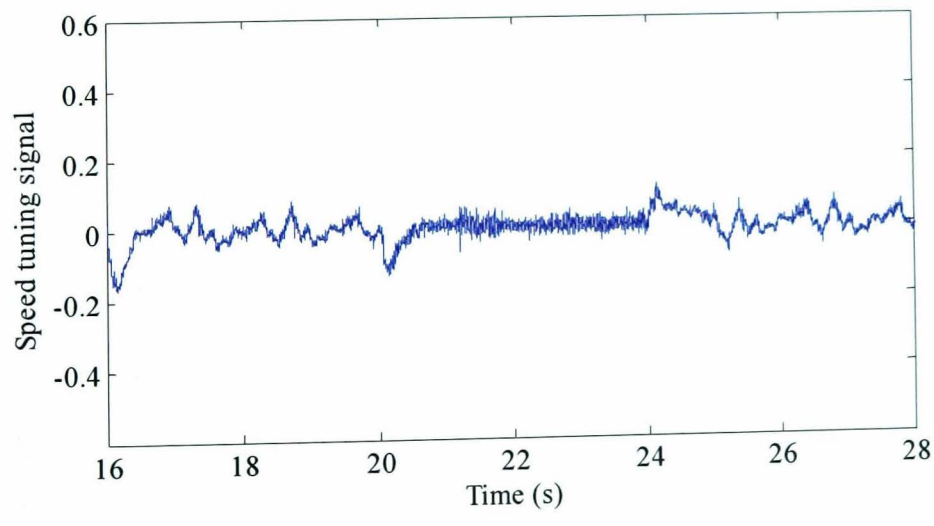

(f)

Fig. 6.19 Sensorless performance around and at zero speed, no load. Model outputs (a) conventional MRAS (b) NN MRAS. Rotor flux position (c) conventional MRAS (d) NN MRAS. Tuning signal (e) conventional MRAS (f) NN MRAS

Test 2: Stair case speed transients from 100rpm to 0rpm to -100 rpm:

In this test the sensorless vector control drive is subjected to a stair case speed demand from 100 rpm to zero speed in a series of five 20 rpm steps continuing to -100 rpm at no load. The performance of both schemes is shown in Fig. 6.20. Similar to test 1 stable operation is obtained for the NN MRAS scheme around zero speed with negligible steady state error in the low speed region. Operation around and at zero speed is demonstrated in Fig. 6.21 where NN MRAS model outputs, NN and CM, show excellent tracking performance compared to the conventional scheme model outputs, VM and CM. Consequently, NN MRAS scheme shows better speed tuning signal and estimated rotor flux position which is due to accurate speed estimation performance. NN MRAS scheme shows better and stable sensorless performance when the test is performed at 12.5% load as shown in Fig. 6.22. Operation at very low positive and negative speed around zero speed with 12.5% load is illustrated in Fig. 6.23. It is shown the performance of the sensorless drive has been greatly improved at this critical region of operation with a stable speed tuning signal. Stable performance in the regeneration mode of operation is shown by NN MRAS compared to oscillatory response from the conventional scheme.

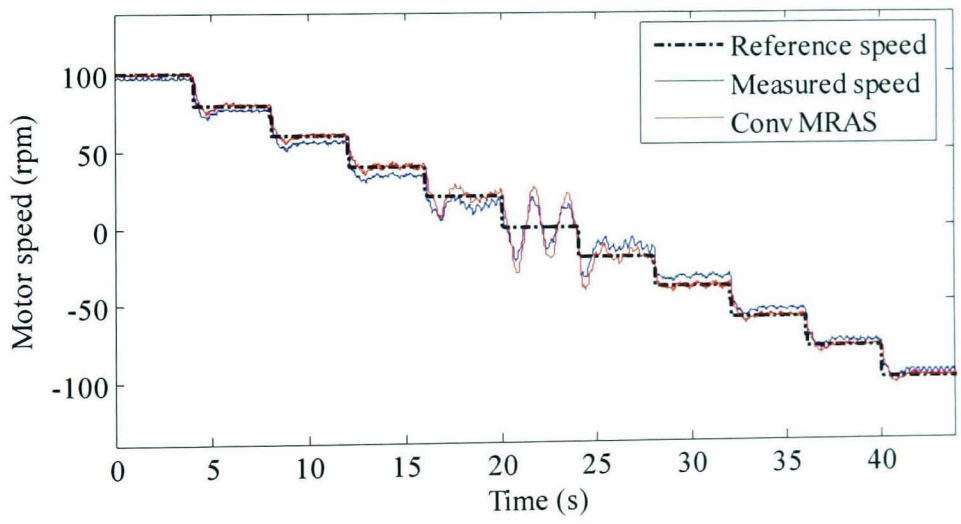

(a)

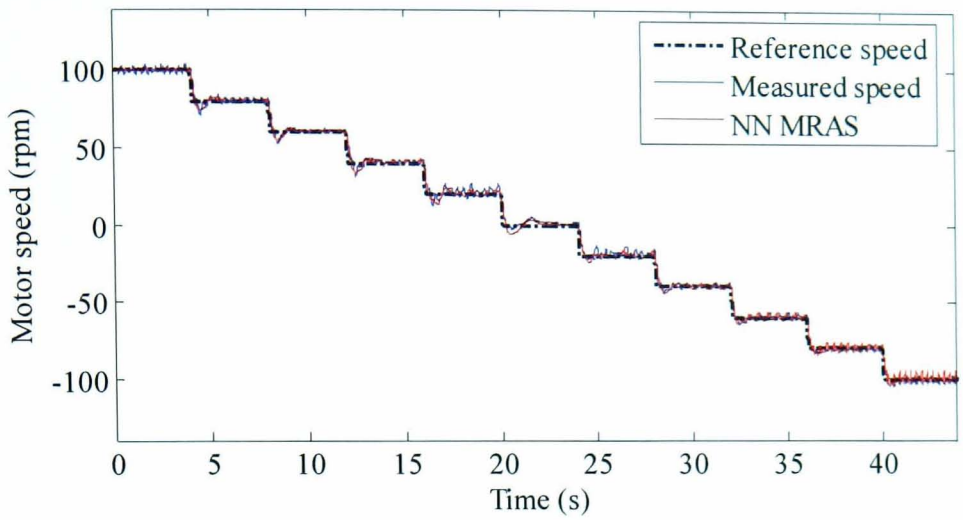

(b)

Fig. 6.20 Sensorless performance for test 2, no load. Speed response: (a) conventional MRAS (b) NN MRAS

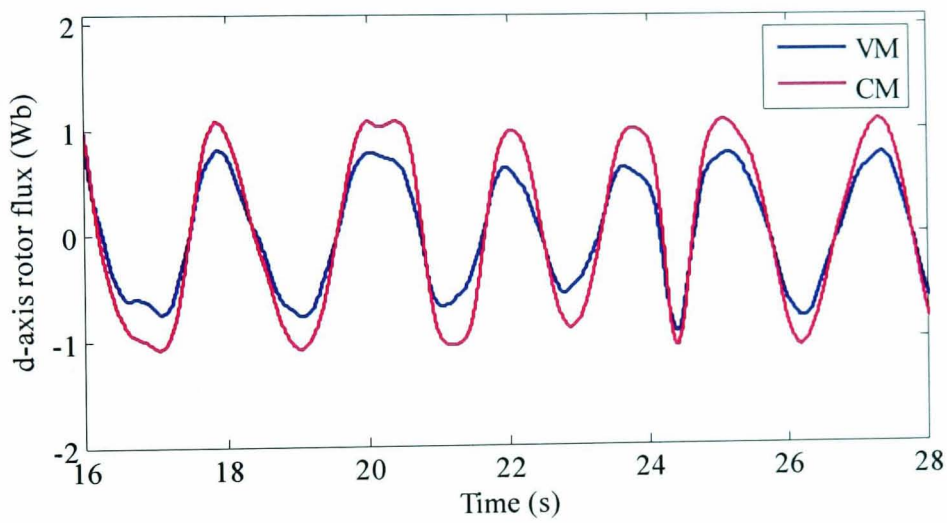

(a)

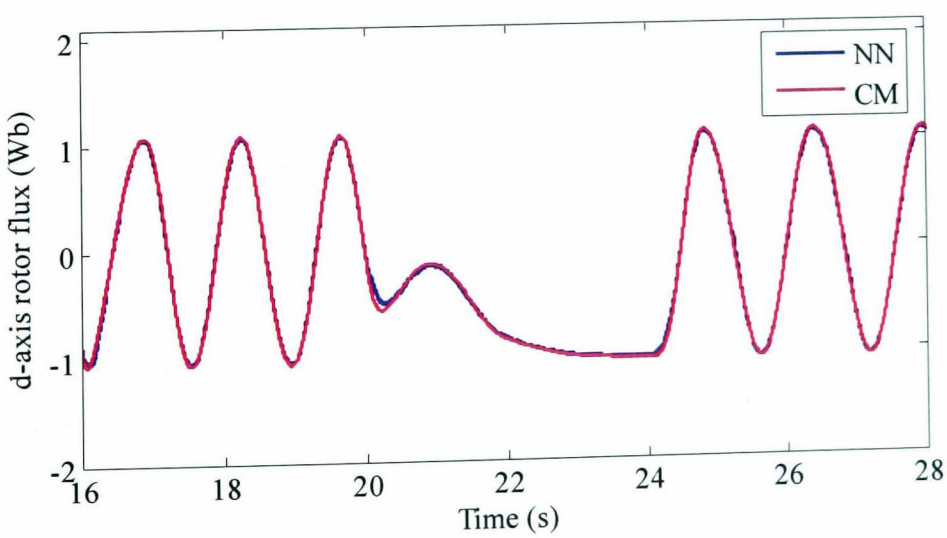

(b)

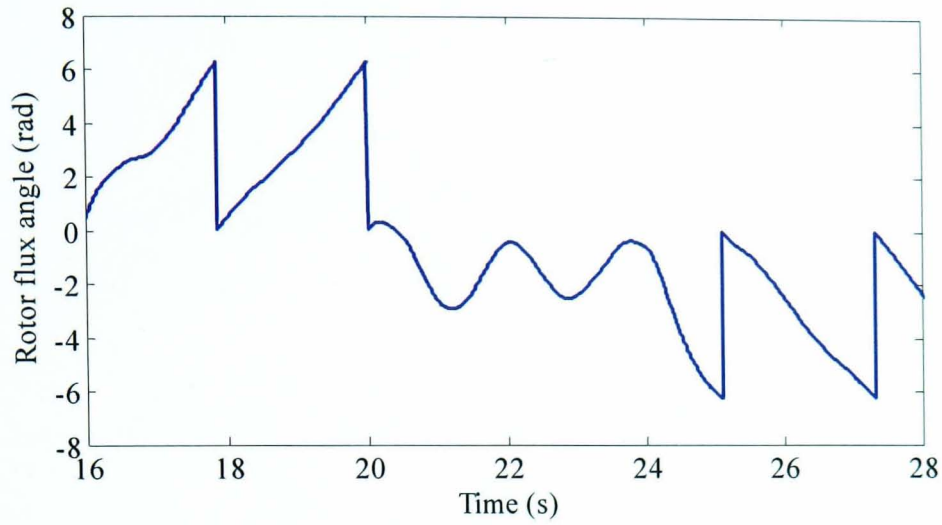
Rotor flux angle (rad)
8
6
4
2
0
-2
-4
-6
-8
16
18
20
22
24
26
28
Time (s)

(c)

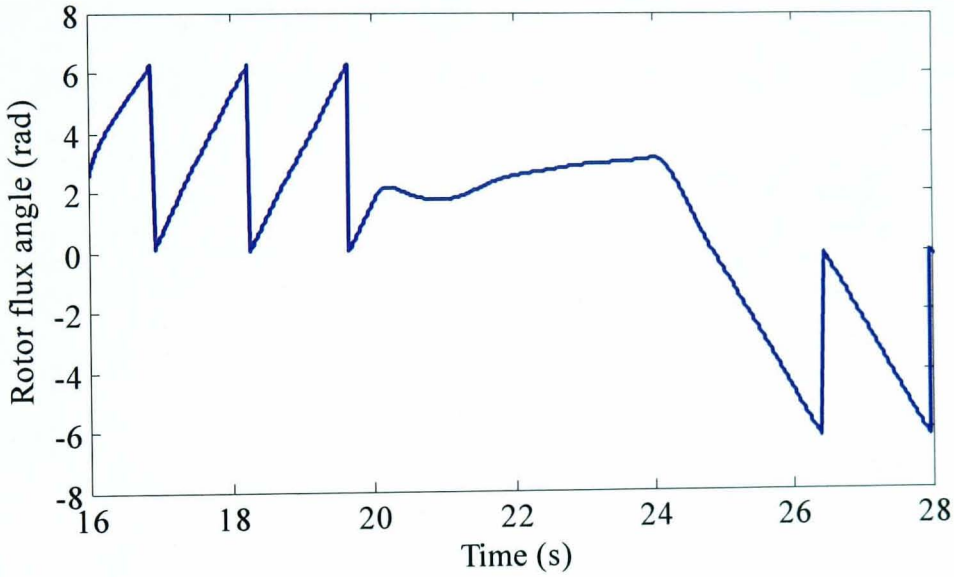
Rotor flux angle (rad)
8
6
4
2
0
-2
-4
-6
-8
16
18
20
22
24
26
28
Time (s)

(d)

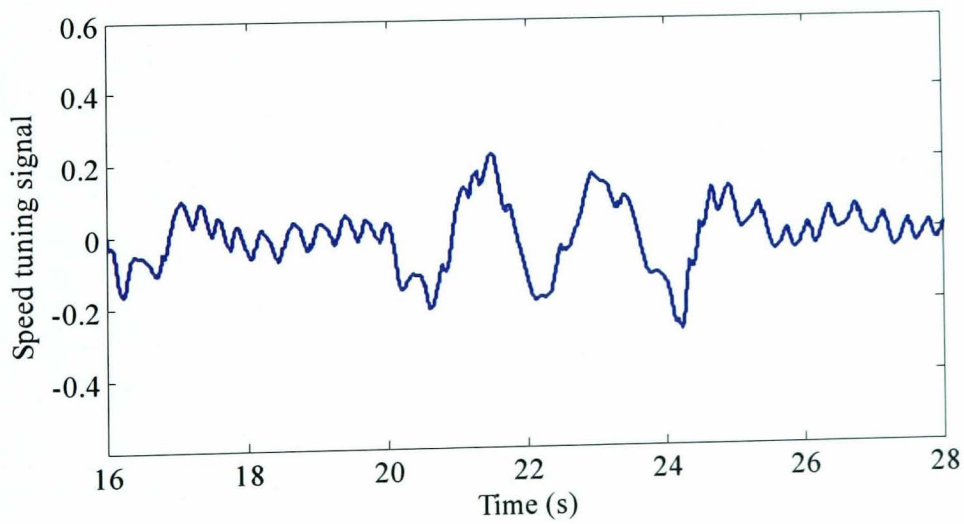
Speed tuning signal
0.6
0.4
0.2
0
-0.2
-0.4
16
18
20
22
24
26
28
Time (s)

(e)

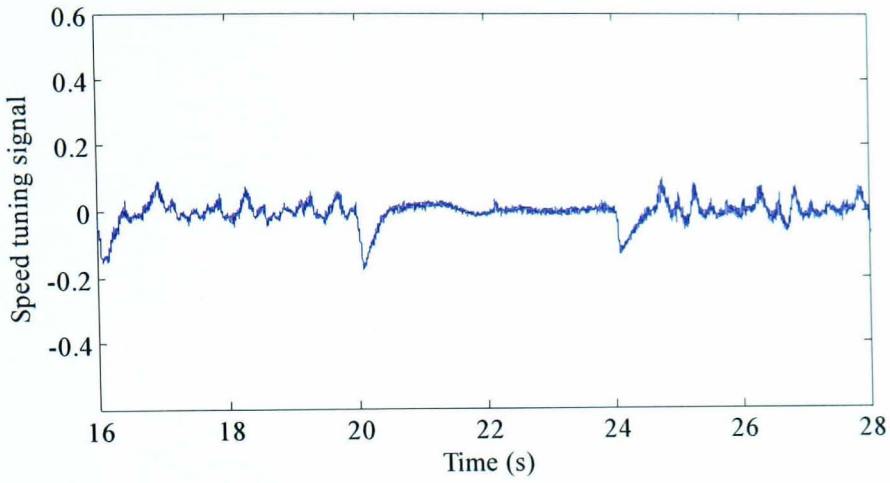

(f)

Fig. 6.21 Sensorless performance around and at zero speed, no load. Model outputs (a) conventional MRAS (b) NN MRAS. Rotor flux position (c) conventional MRAS (d) NN MRAS. Tuning signal (e) conventional MRAS (f) NN MRAS

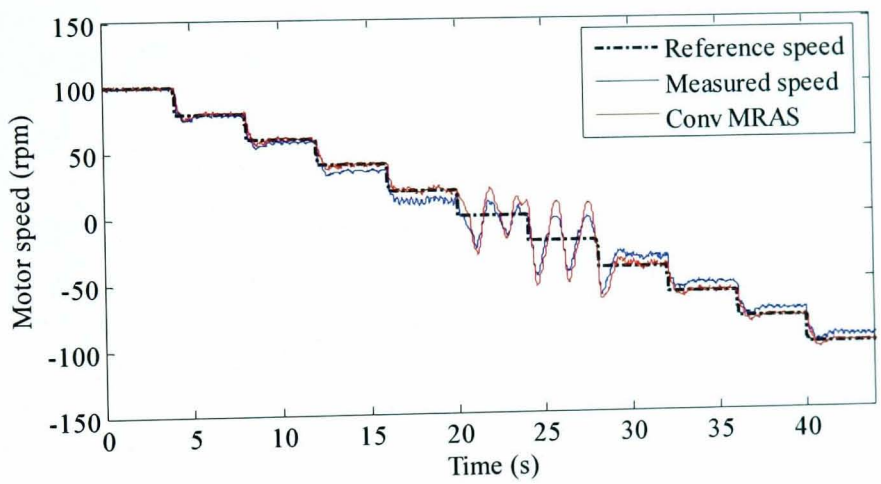

(a)

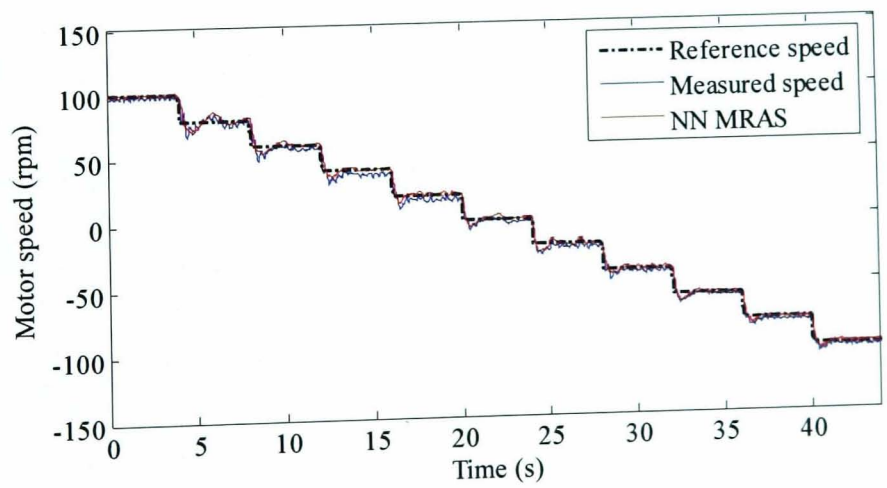

(b)

Fig. 6.22 Sensorless performance for test 2, 12.5% load. Speed response: (a) conventional MRAS (b) NN MRAS

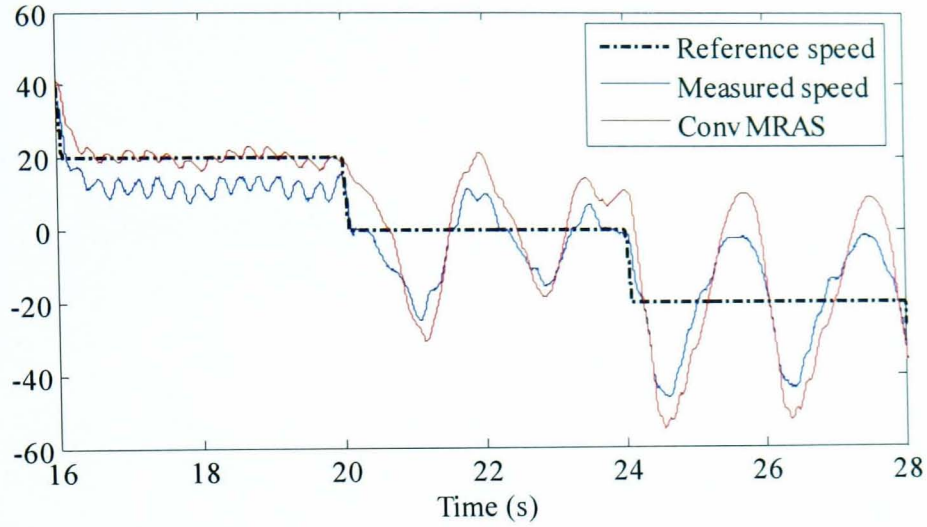
Reference speed
Measured speed
Conv MRAS
60
40
20
0
-20
-40
-60
16
18
20
22
24
26
28
Time (s)

(a)

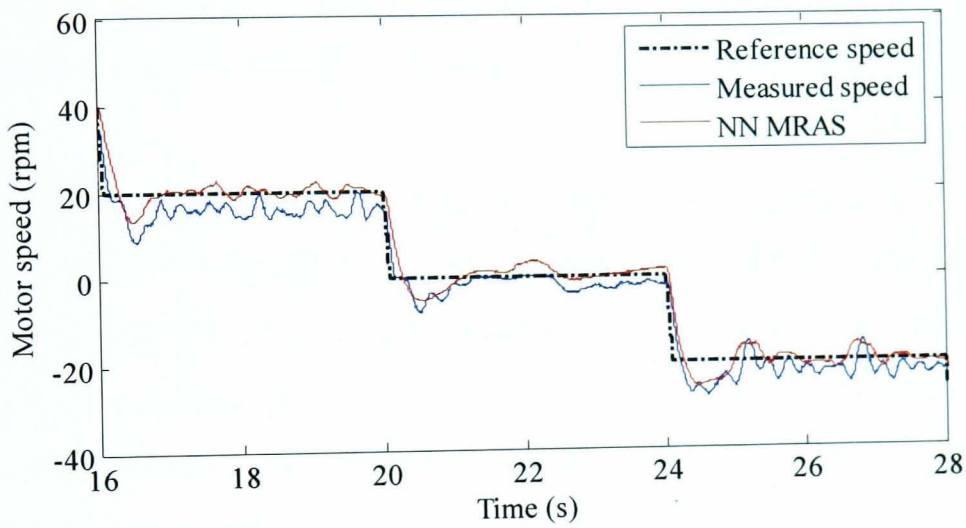
Reference speed
Measured speed
NN MRAS
Motor speed (rpm)
60
40
20
0
-20
-40
16
18
20
22
24
26
28
Time (s)

(b)

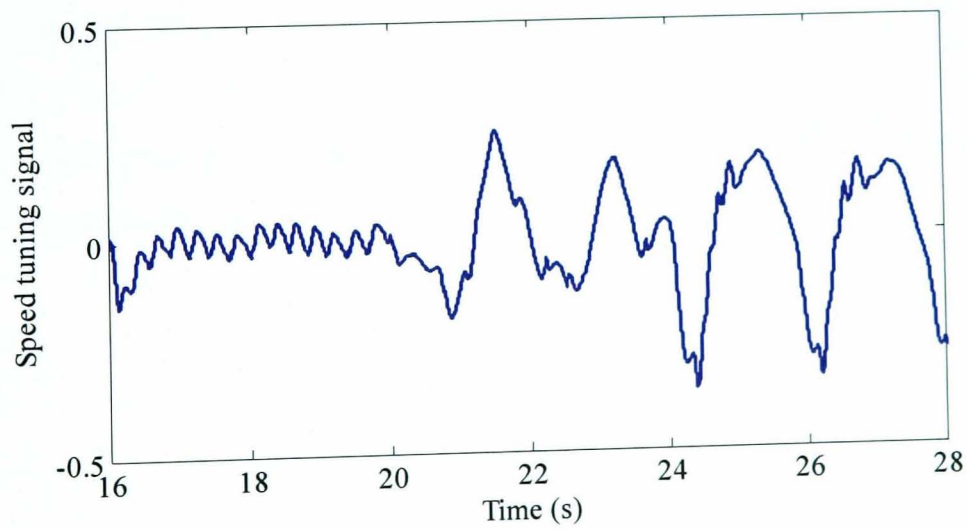
Speed tuning signal
0.5
0
-0.5
16
18
20
22
24
26
28
Time (s)

(c)

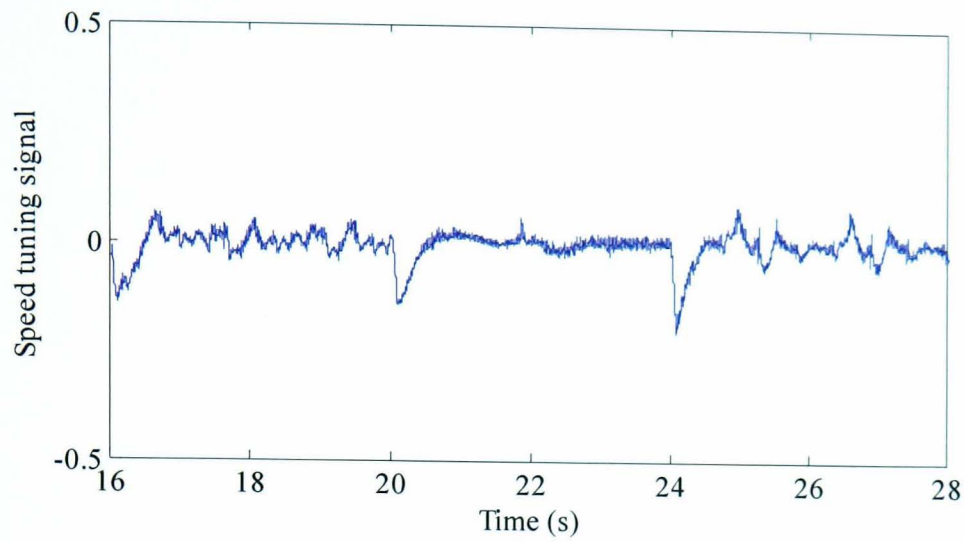

(d)

Fig. 6.23 Sensorless performance around and at zero speed, 12.5% load. Speed (a) conventional MRAS (b) NN MRAS. Tuning signal (c) conventional MRAS (d) NN MRAS

Test 3 Take off from zero speed to 100 rpm after 30 sec at zero:

This tests the drive capability to maintain field orientation at zero stator frequency followed by an application of a finite reference speed at no load. The results of this benchmark test are shown in Fig. 6.24. Unstable operation at zero speed was observed for the conventional MRAS with oscillation around zero speed. This performance affects field orientation and model outputs leading to unstable speed tuning signal. NN MRAS proves its ability to hold the zero speed at no load without any oscillations and the motor shaft is stationary. Therefore sensorless zero speed operation at no load is possible using NN MRAS scheme with stationary model flux outputs. Consequently, better field orientation angle and speed tuning signal are obtained. Both schemes succeed in taking off to 100 rpm after 30 s at zero speed.

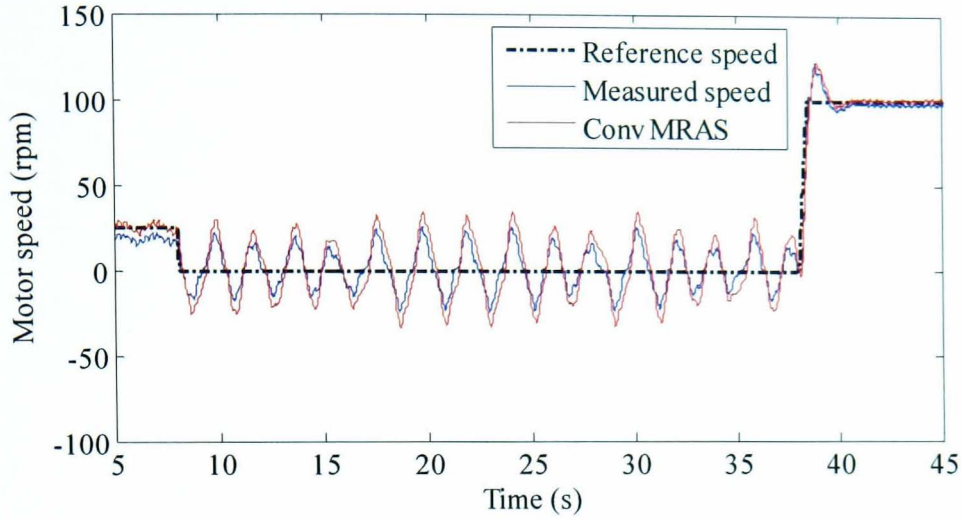
Reference speed
Measured speed
Conv MRAS
Motor speed (rpm)
Time (s)
150
100
50
0
-50
-100
5
10
15
20
25
30
35
40
45

(a)

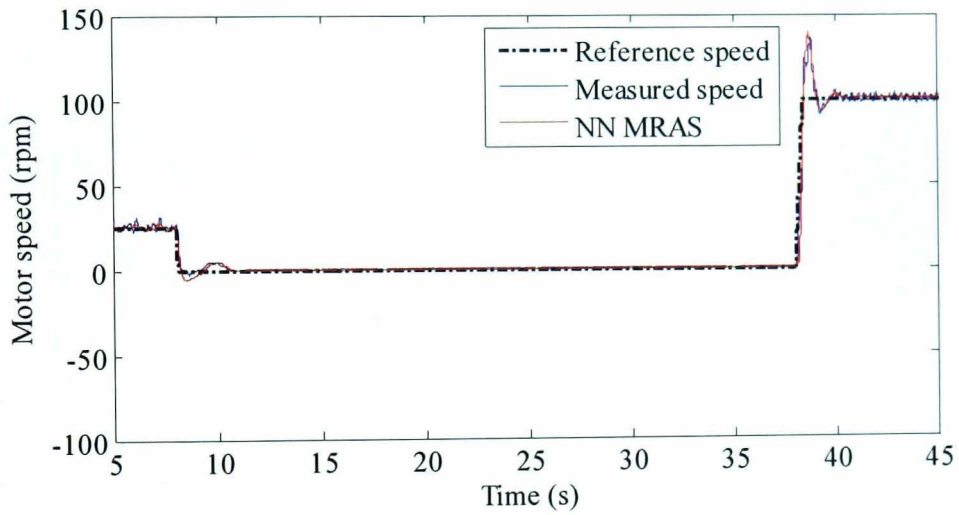
Reference speed
Measured speed
NN MRAS
Motor speed (rpm)
Time (s)
150
100
50
0
-50
-100
5
10
15
20
25
30
35
40
45

(b)

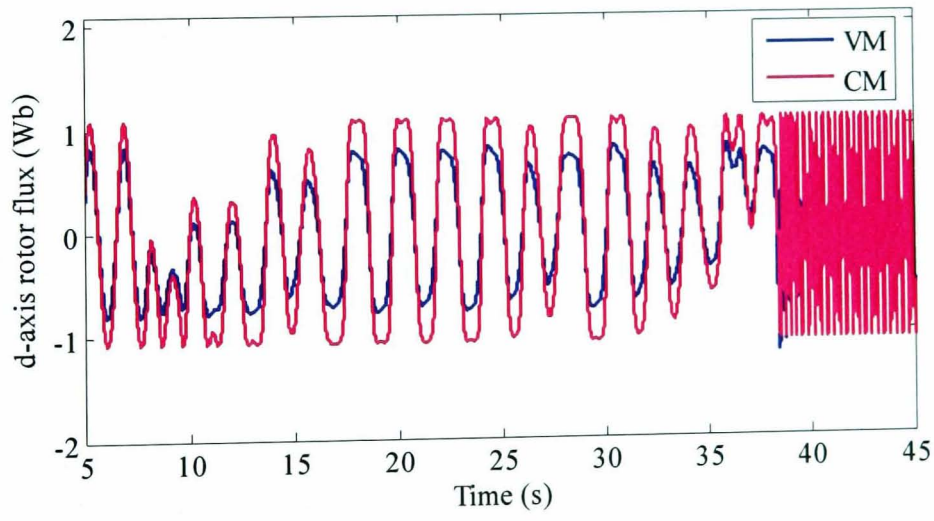
VM
CM
d-axis rotor flux (Wb)
Time (s)
2
1
0
-1
-2
5
10
15
20
25
30
35
40
45

(c)

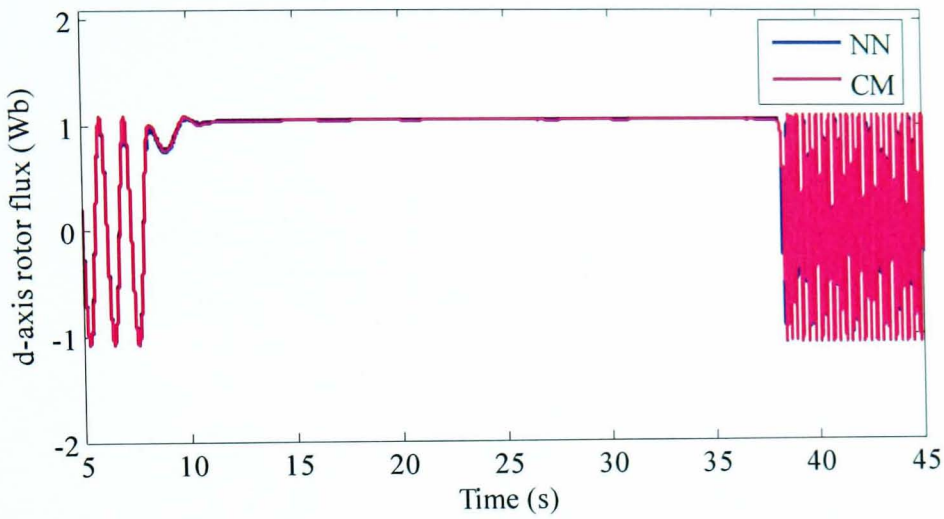
NN
CM
d-axis rotor flux (Wb)
Time (s)
2
1
0
-1
-2
5
10
15
20
25
30
35
40
45

(d)

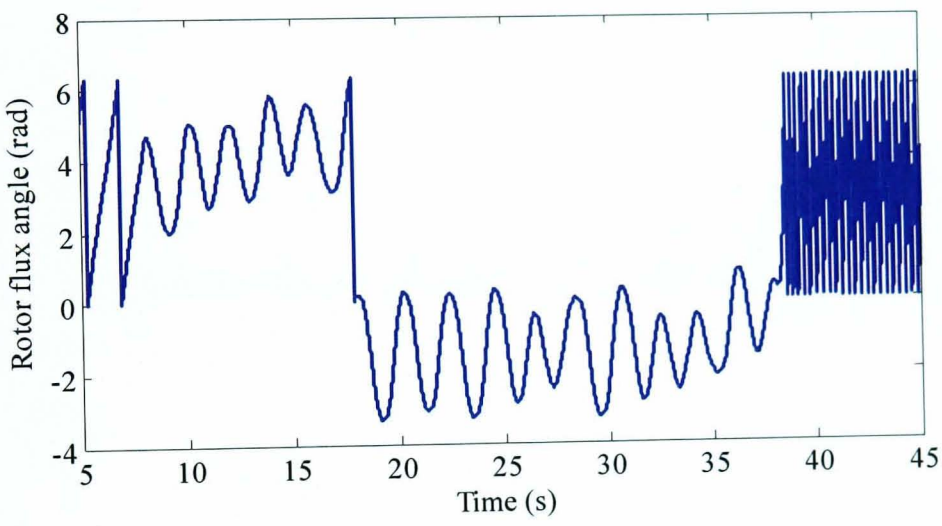
Rotor flux angle (rad)
Time (s)
8
6
4
2
0
-2
-4
5
10
15
20
25
30
35
40
45

(e)

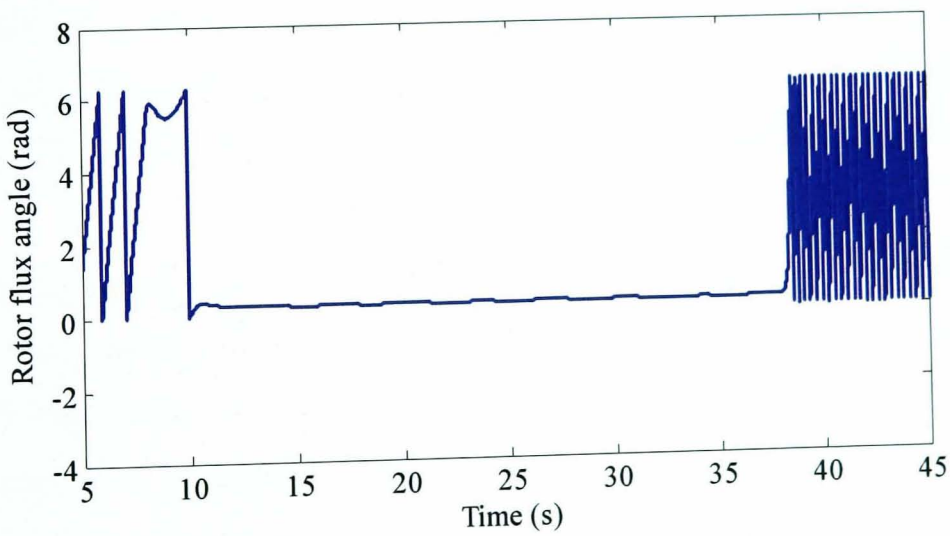
Rotor flux angle (rad)
Time (s)
8
6
4
2
0
-2
-4
5
10
15
20
25
30
35
40
45

(f)

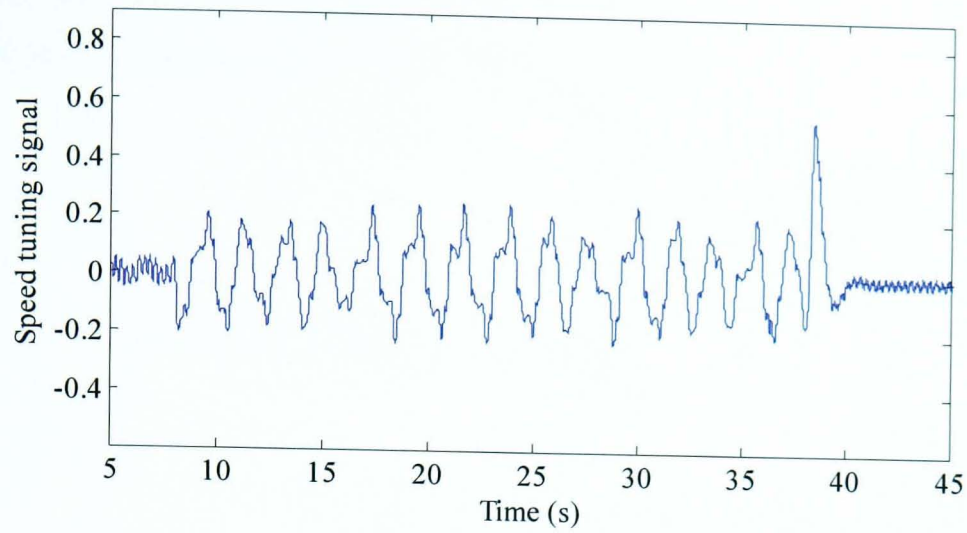

(g)

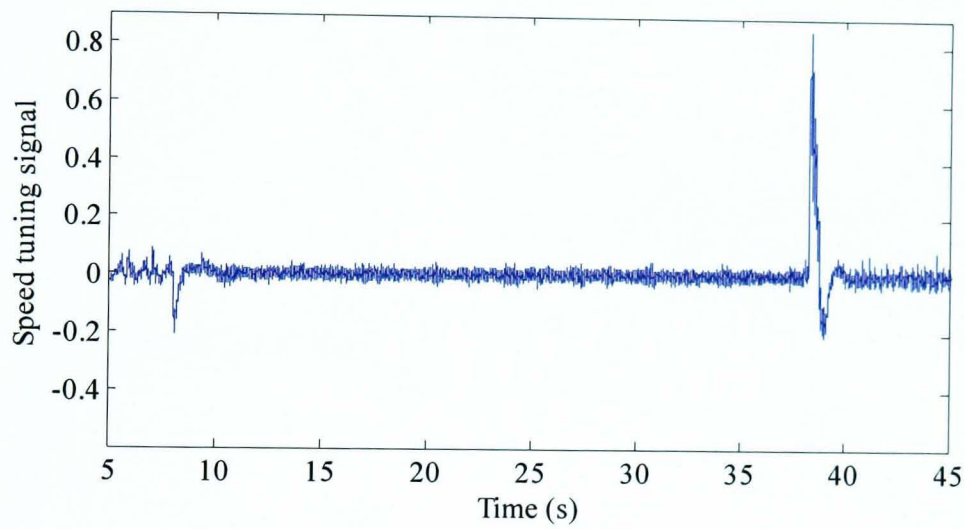

(h)

Fig. 6.24 Sensorless performance for test 3. Speed response (a) Conventional MRAS (b) NN MRAS. Model outputs (c) Conventional MRAS (d) NN MRAS. Rotor flux position (e) Conventional MRAS (f) NN MRAS. Tuning signal (g) Conventional MRAS (h) NN MRAS

Test 4: Speed step down from 20 rpm to 0 rpm in three steps each of 10 rpm:

This tests the performance of the sensorless drive at very low and zero speed at different loads. The results of this test at 10% load are shown in Fig. 6.25. At a reference speed of 20 rpm, the NN MRAS scheme was stable, showing less steady state error compared to the conventional. At such speeds and below, the conventional MRAS fails to provide stable operation giving large oscillations. NN MRAS shows better performance at this very low speed region with a very small steady state error at zero speed. Better performance is obtained from NN MRAS scheme when the test is

performed at 20% load as shown in Fig. 6.26. Results of zero speed sensorless operation at different load levels are summarized in Table 6.1.

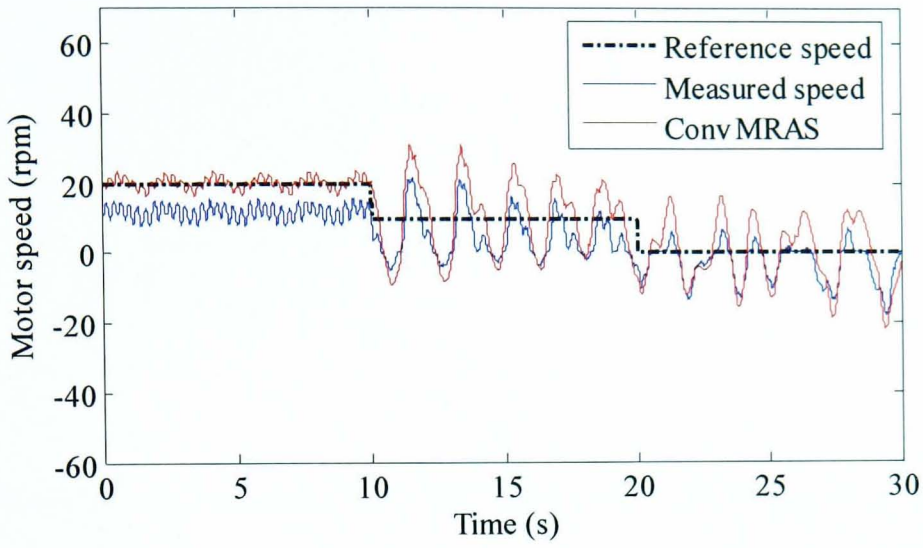

(a)

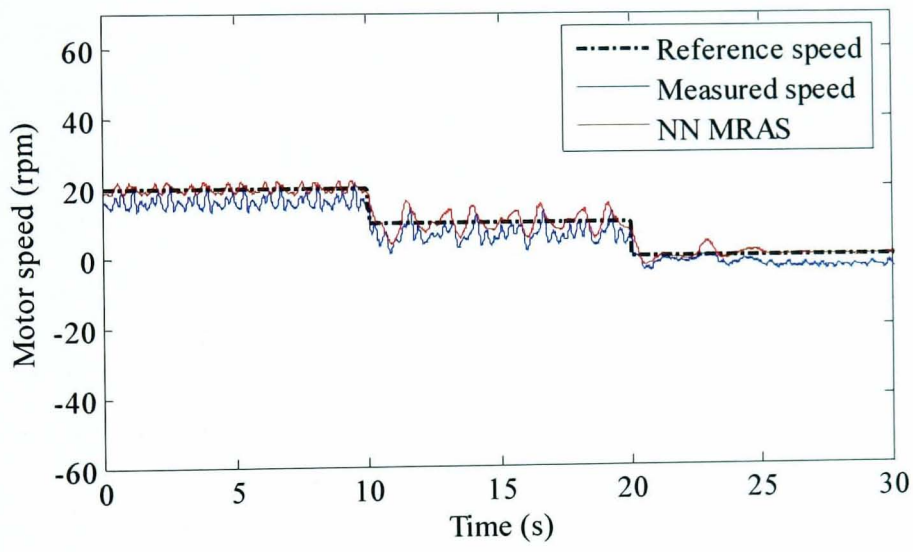

(b)

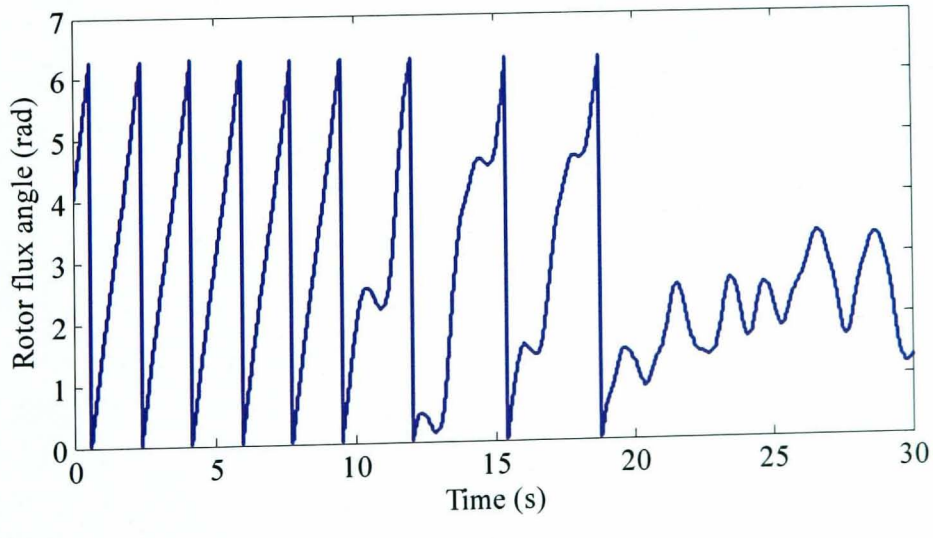

(c)

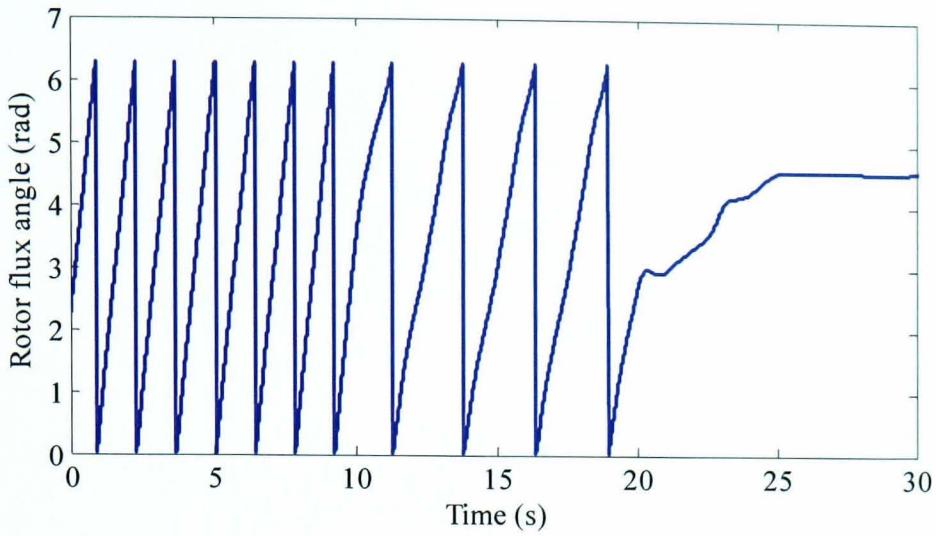

(d)

Fig. 6.25 Sensorless performance for test 4, 10% load. Speed response: (a) conventional MRAS (b) NN MRAS. Rotor flux position: (c) conventional MRAS (d) NN MRAS

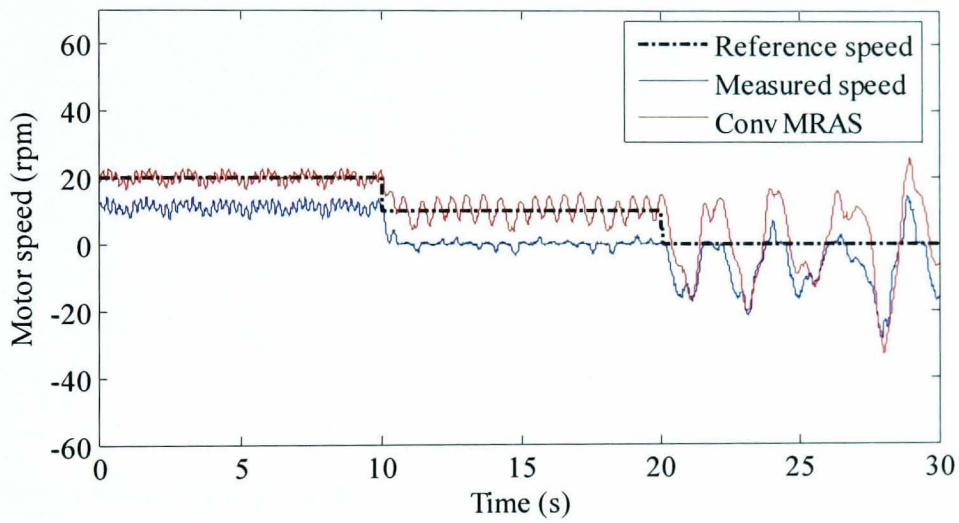

(a)

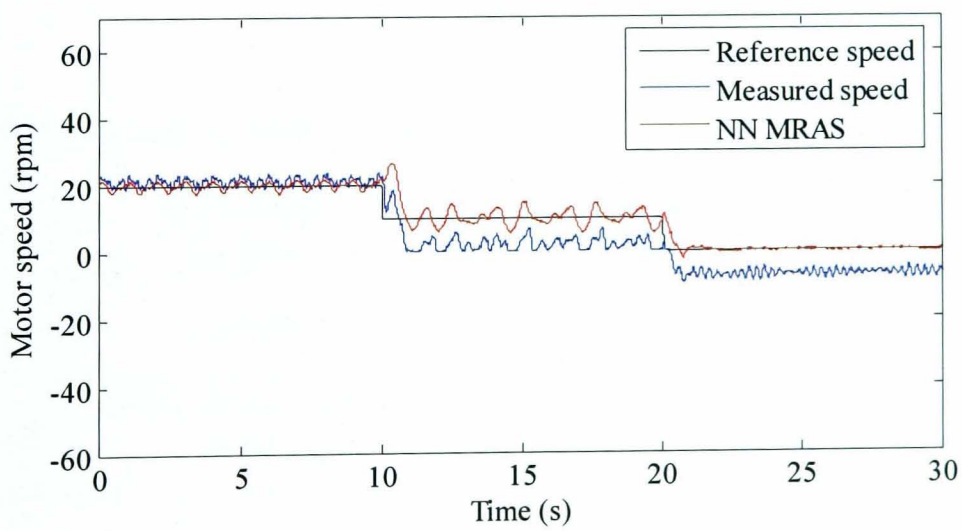

(b)

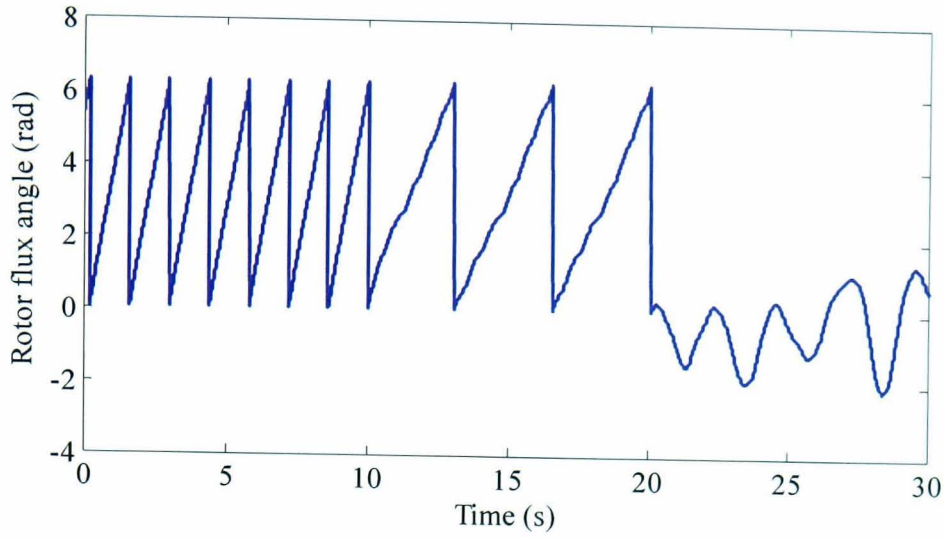

(c)

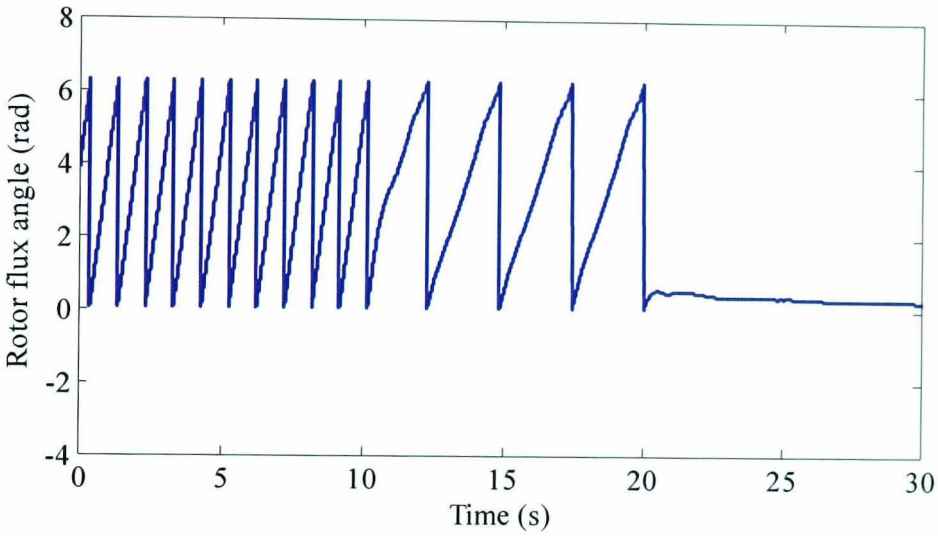

(d)

Fig. 6.26 Sensorless performance for test 4, 20% load. Speed response: (a) conventional MRAS (b) NN MRAS. Rotor flux position: (c) conventional MRAS (d) NN MRAS

Table 6.1

Summary of zero speed sensorless results

	Zero speed No load	**Zero speed 10% load**	**Zero speed 20% load**
Conv. MRAS	Unstable	Unstable	Unstable
NN MRAS	Zero steady state error	3 rpm steady state error	7 rpm steady state error

Test 5: Sensorless load torque disturbance rejection:

This test examines the load torque disturbance rejection capability of the sensorless drive. In general, load disturbance application may affect the machine parameters and increase the level of nonlinearity. Both schemes have been tested when a 20% load torque is applied at 50 rpm. The NN MRAS shows better dynamic and steady state performance with negligible steady state error between the actual and estimated speed as shown in Fig. 6.27. Furthermore, NN MRAS scheme shows better rotor field orientation performance with synchronous frame q-current component similar to that obtained from (3.48) for perfect field orientation. Inaccurate speed estimation causes wrong field orientation for the conventional scheme. More results are shown in Fig. 6.28 for a 20% load torque rejection at -50 rpm. NN MRAS scheme still shows better performance with less steady state error due to good tracking between NN and CM observers.

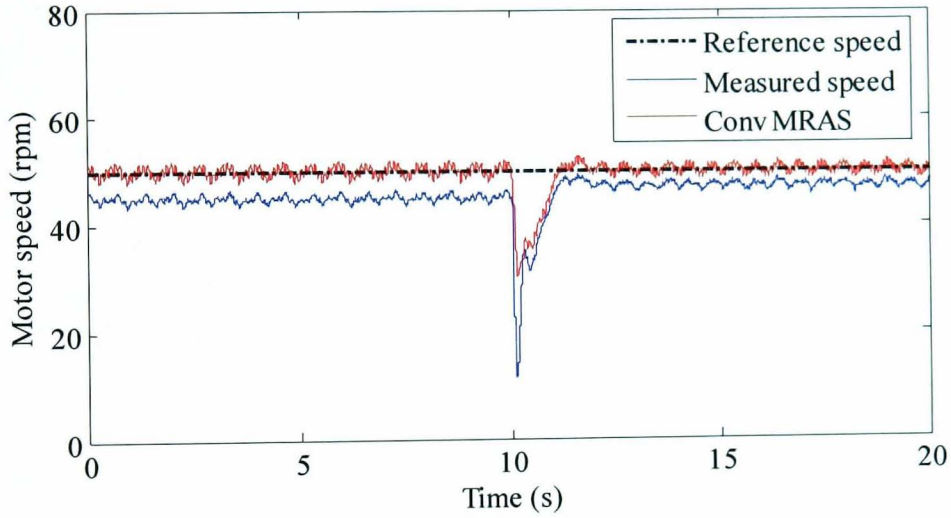

(a)

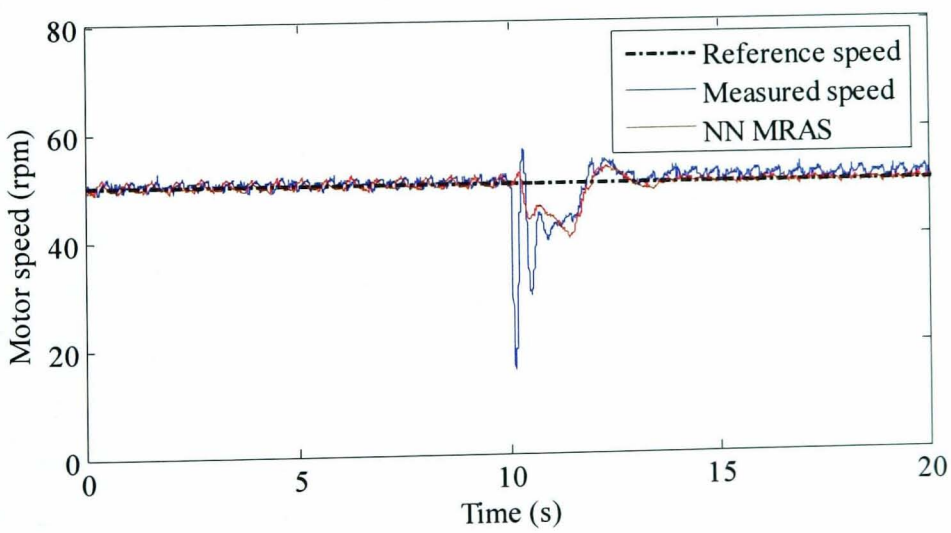

(b)

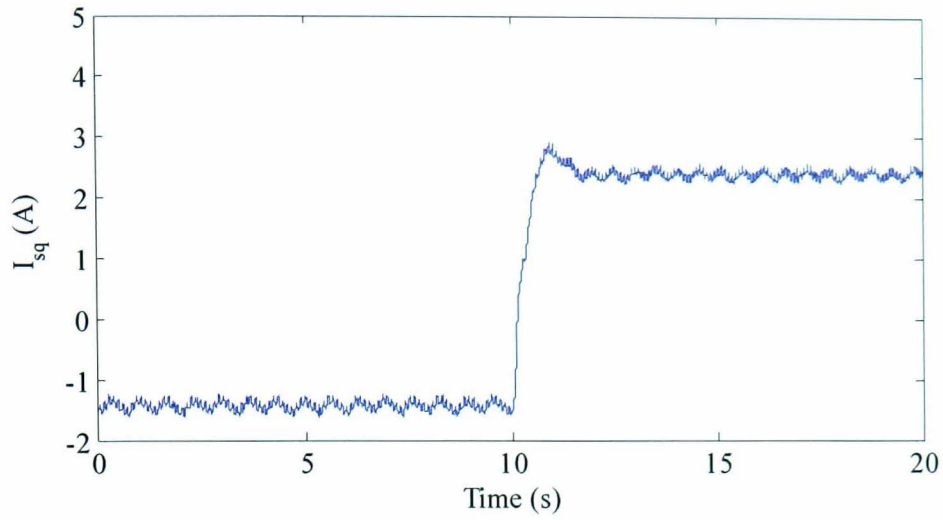

(c)

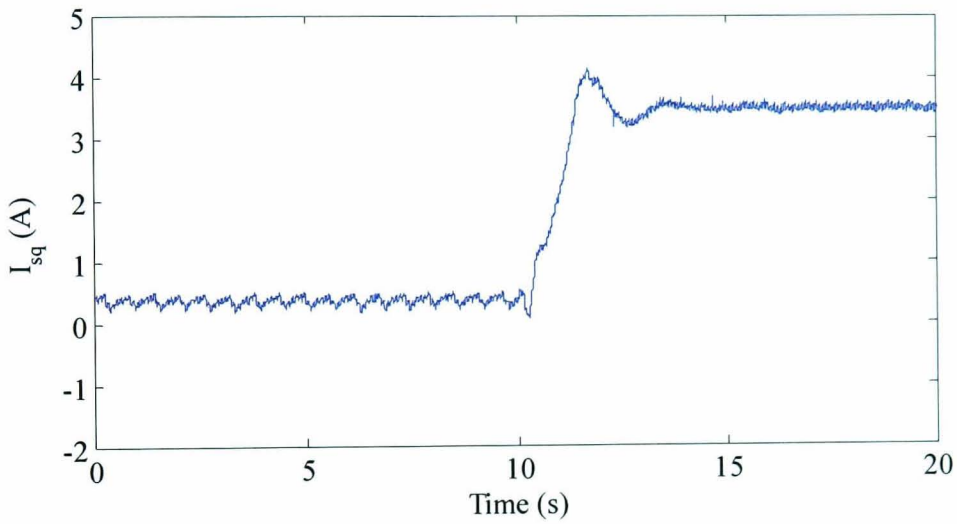

(d)

Fig. 6.27 Sensorless performance for test 5, 20% load at 50rpm. Speed response (a) conventional MRAS (b) NN MRAS. i_{sq} (c) Conventional MRAS (d) NN MRAS.

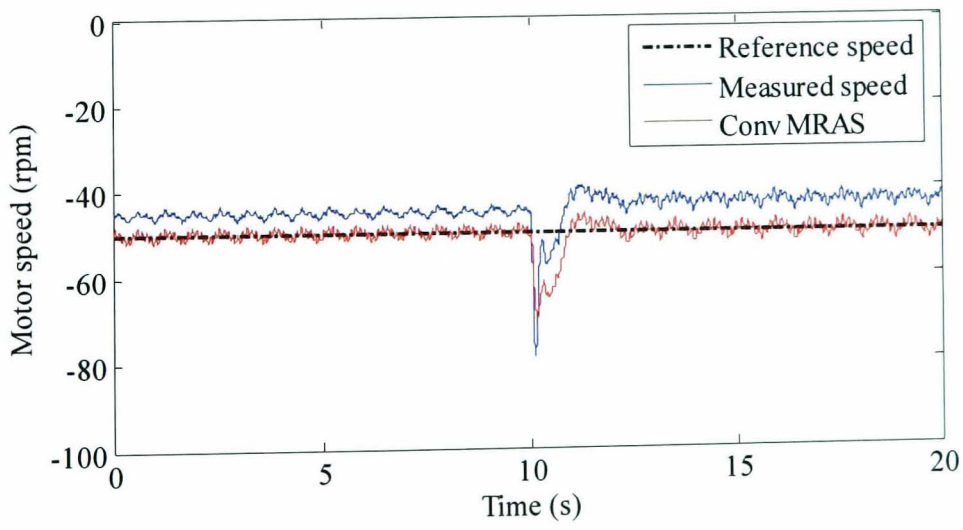

(a)

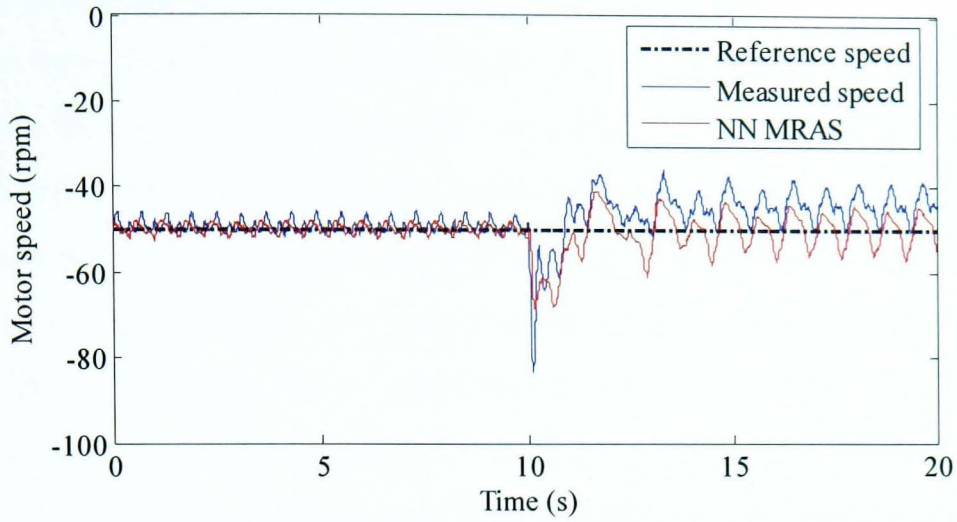

(b)

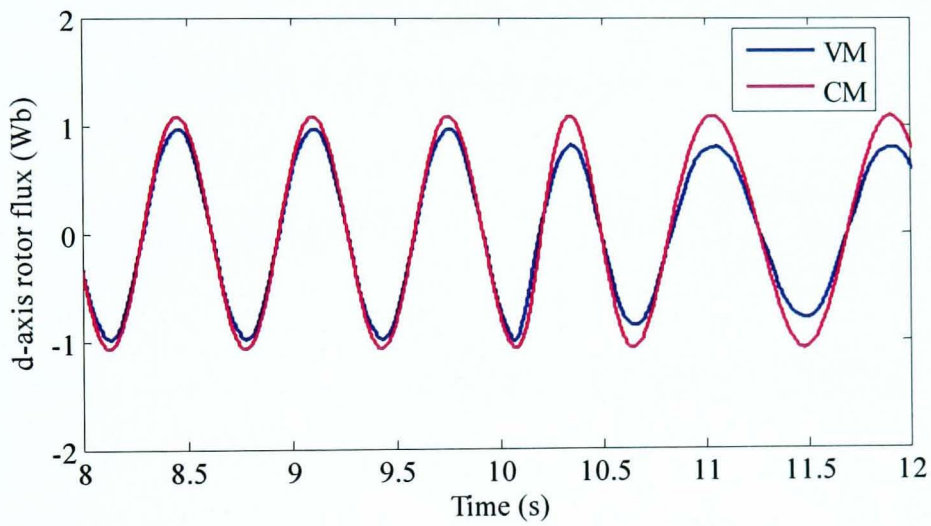

(c)

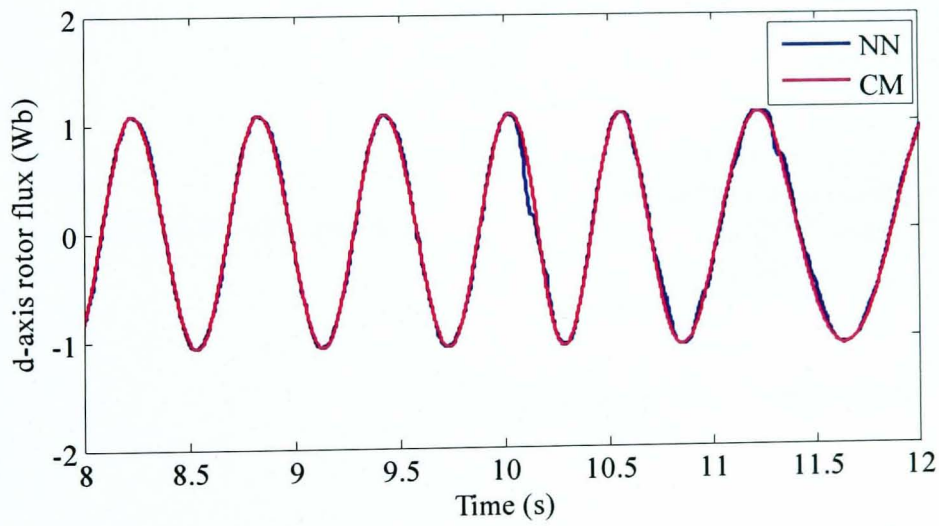

(d)

Fig. 6.28 Sensorless performance for test 5, 20% load at -50rpm. Speed response (a) conventional MRAS (b) NN MRAS. Model outputs (c) conventional MRAS (d) NN MRAS.

Test 6: Sensorless speed reversal at load:

This last test shows the drive performance for a very low speed reversal under load torque. A ±25 rpm speed reversal demand was applied to the drive when working at 10% load. Better performance with negligible steady state error was obtained from NN MRAS observer compared to the conventional MRAS scheme as shown in Fig. 6.29. This is due to excellent matching between NN MRAS model outputs, NN and CM, during transient and steady state. When the test is performed at 25% load, large speed oscillations are obtained from the conventional scheme compared to a stable performance for the NN MRA which leads to better field orientation and stable speed tuning signal. The results of this test, shown in Fig. 6.30, demonstrate the improvement of the sensorless performance in the regenerating mode of operation using NN MRAS scheme. A summary of sensorless results at different operating conditions is given in Table 6.2.

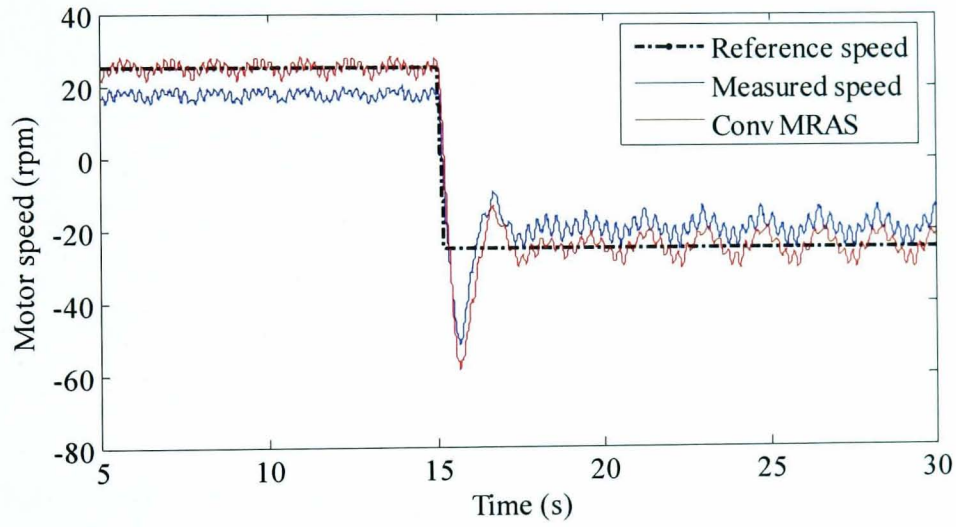

(a)

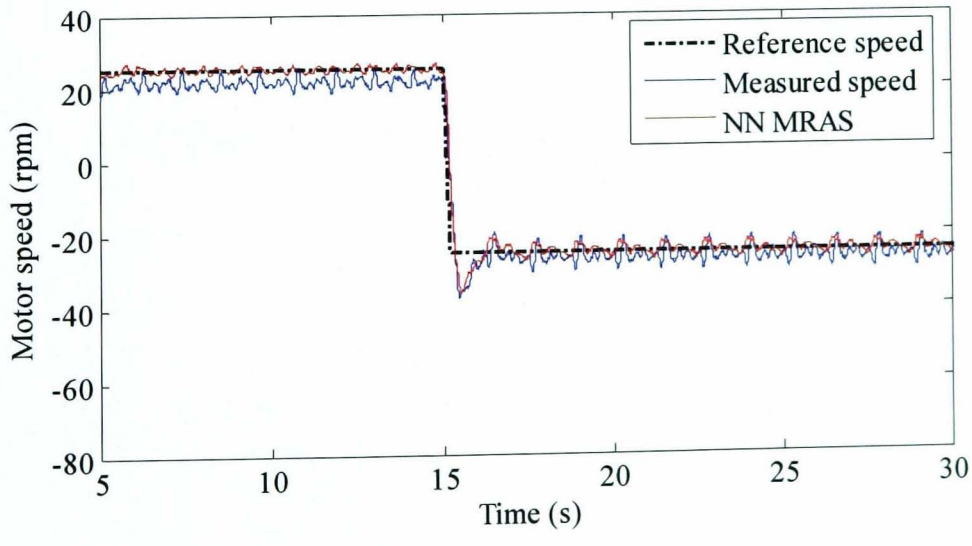

(b)

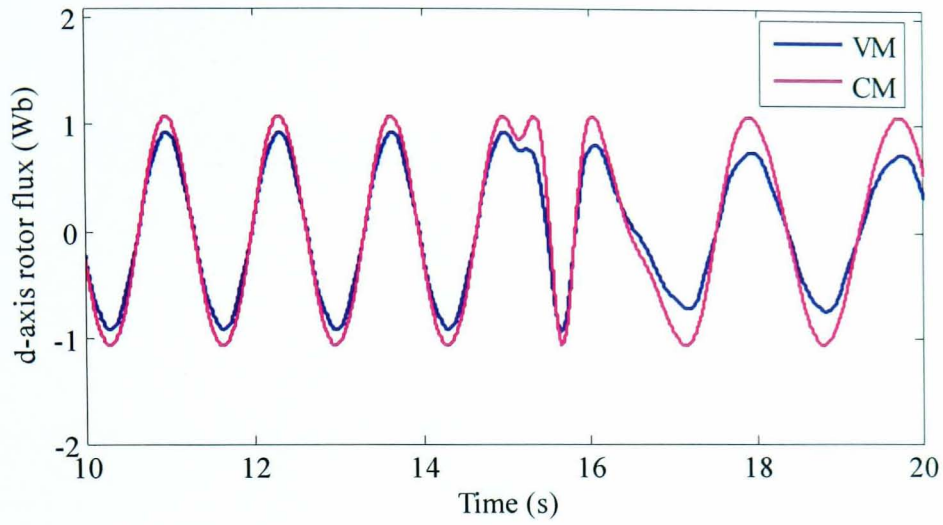

(c)

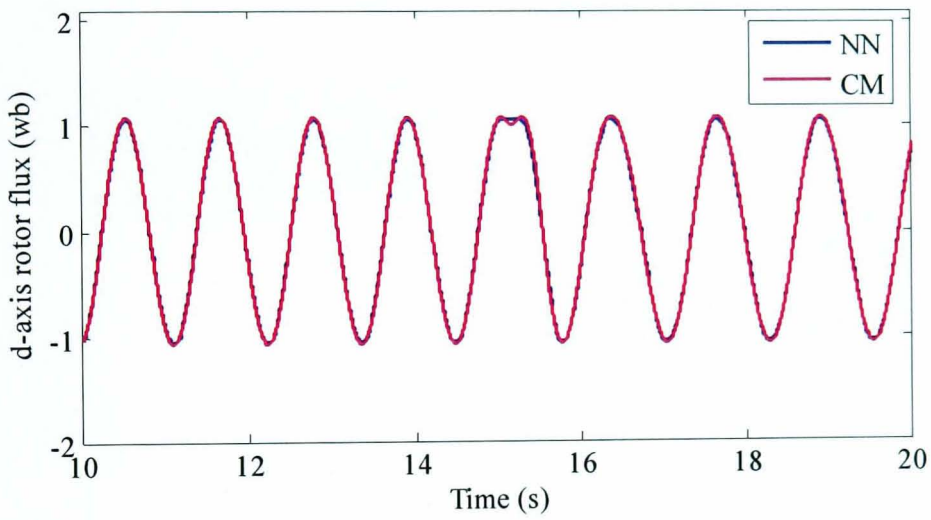

(d)

Fig. 6.29 Sensorless performance for test 6, ±25 rpm reversal, 10% load. Speed: (a) conventional MRAS (b) NN MRAS

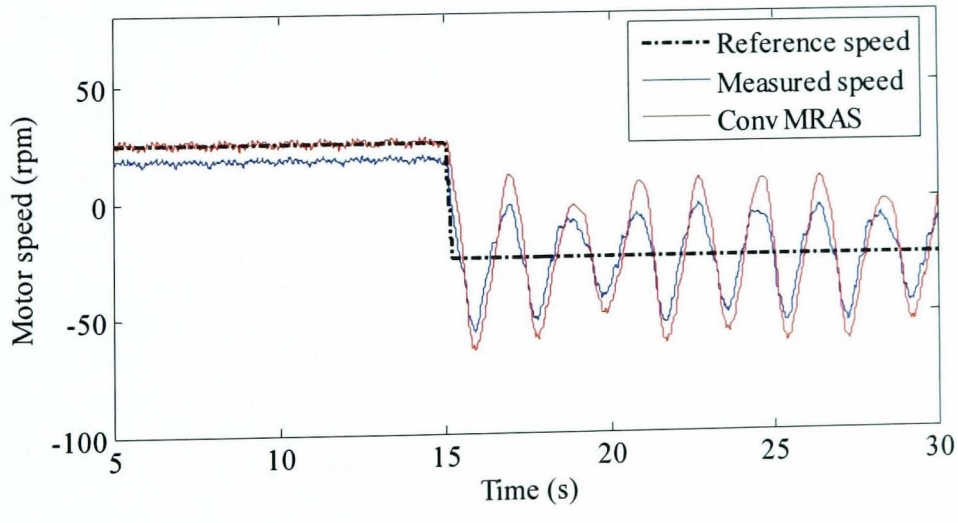

(a)

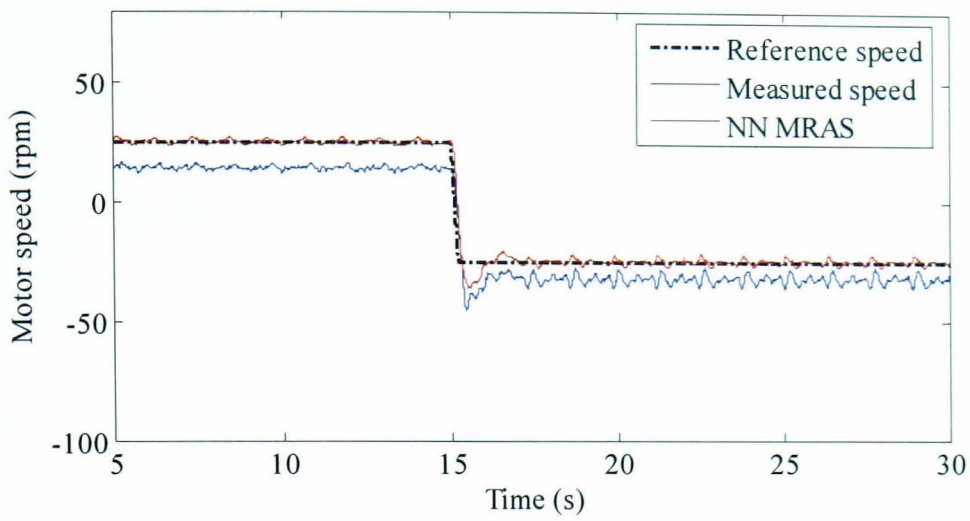
Reference speed
Measured speed
NN MRAS
Motor speed (rpm)
50
0
-50
-100
5
10
15
20
25
30
Time (s)

(b)

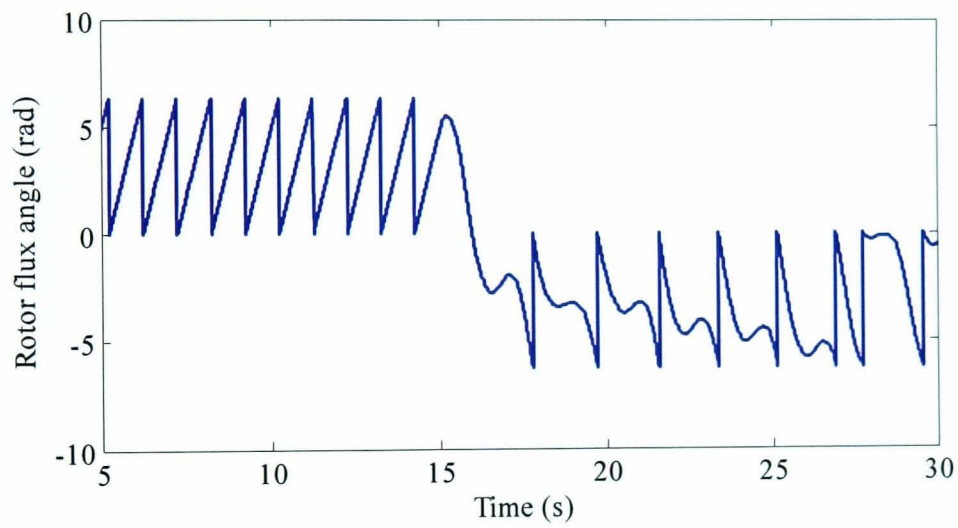
Rotor flux angle (rad)
10
5
0
-5
-10
5
10
15
20
25
30
Time (s)

(c)

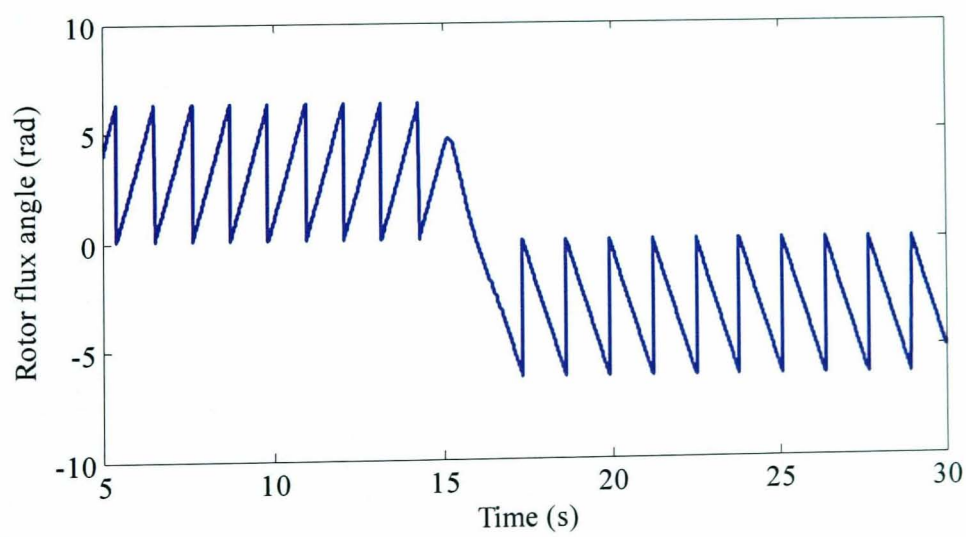
Rotor flux angle (rad)
10
5
0
-5
-10
5
10
15
20
25
30
Time (s)

(d)

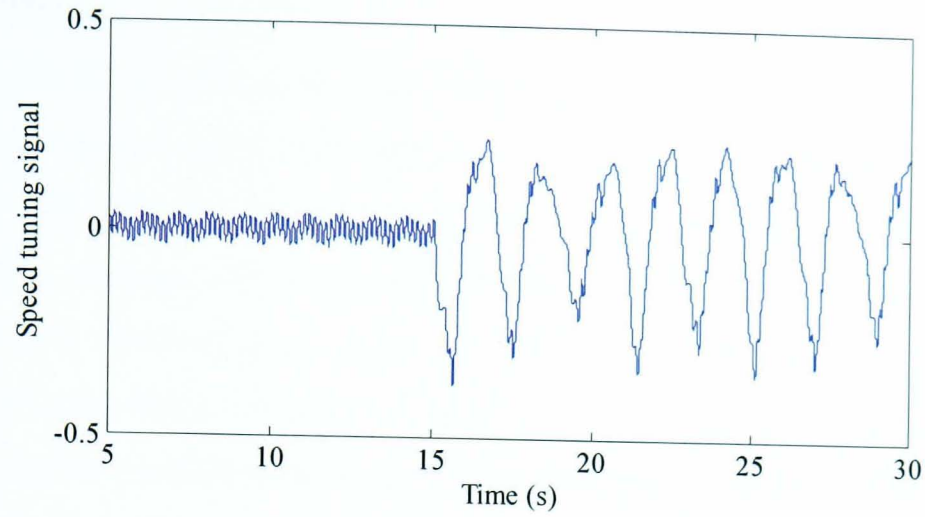

(e)

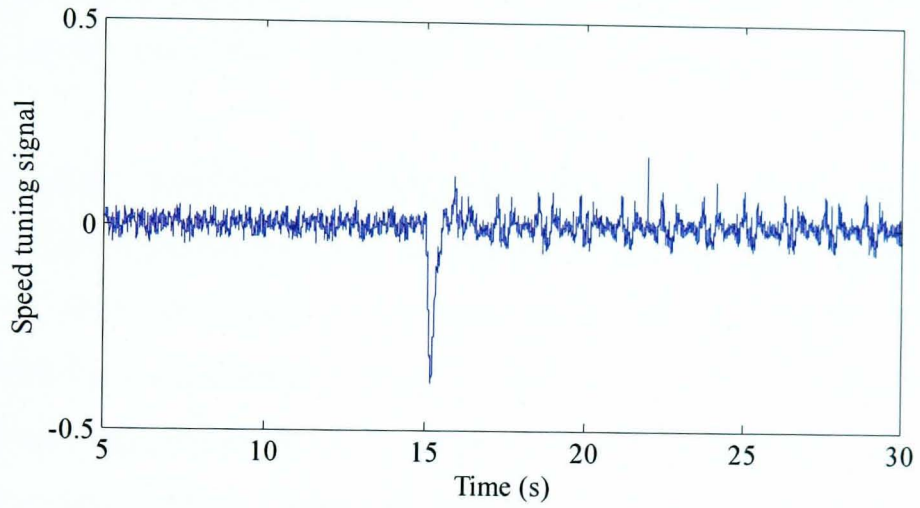

(f)

Fig. 6.30 Sensorless performance benchmark test 6 ±25 rpm reversal, 25% load. Speed response: (a) conventional MRAS (b) NN MRAS Rotor flux position: (c) conventional MRAS (d) NN MRAS Tuning signal (g) Conventional MRAS (h) NN MRAS

Table 6.2

Summary of sensorless results

	20 rpm 10% load	**10 rpm 10% load**	**50 rpm 20% load**	**-25 rpm 10% load**	**-25 rpm 25% load**
Conv. MRAS	10 rpm steady state error	Unstable	3 rpm steady state error	5 rpm steady state error	Unstable
NN MRAS	4 rpm steady state error	3 rpm steady state error	1 rpm steady state error	Negligible steady state error	7 rpm steady state error

6.7 Conclusion

This chapter has presented an entirely new application of a NN to give an improved MRAS speed observer scheme suitable for speed sensorless IM drives. A multilayer feedforward NN estimates the rotor flux components from present and past samples of reference stator voltages and measured currents. The new scheme makes use of the off-line trained NN observer as a reference model in MRAS scheme. Training data is obtained from experiments without the need for search coils. Using the new NN scheme for flux estimation eliminates the need for pure integration with less sensitivity to stator resistance variations. A NN scheme suitable for applications that require low torque at low speed such as a general purpose IM drives is first developed. A further NN extension to suit low speed rated load applications such as elevators and conveyors is also discussed.

Results obtained from a systematic set of benchmark experimental tests using a 7.5 kW IM drive system prove the great improvement of the sensorless drive performance around and at zero speed. Open loop tests show that the steady state error in the estimated speed has been totally removed compared to the conventional observer using a VM. Closed loop sensorless operation is greatly improved at very low and zero speed especially at no load without using voltage sensors. Experimental and simulation results reveal some interesting features of NN and show that the network has good potential for use as an alternative to VM used in classical MRAS speed observer.

CHAPTER 7

NEURAL NETWORK-BASED STATOR CURRENT MRAS OBSERVER

A novel MRAS speed observer for IM drives based on stator current is presented. The measured stator currents are used as reference model for the MRAS observer to avoid the use of a pure integrator. A two-layer NN stator current observer is used as the adaptive model which requires the rotor flux information. This can be obtained from the voltage or current models but instability and dc drift can downgrade the overall observer performance. To overcome these problems an off-line trained multilayer feedforward NN is proposed here as a rotor flux observer. Speed estimation performance of the new MRAS scheme using the different rotor flux observers is studied and compared with the conventional rotor flux MRAS when applied to an indirect vector control IM drive. Promising results have been obtained when using the NN flux observer with better low speed performance and stability in the regenerating mode of operation.

7.1 Introduction

Recently a stator current MRAS scheme has been introduced for stator resistance identification for IM drives [76]. In this scheme the reference model comprises the measured stator current components. This makes the reference model free of pure

integration problems and insensitive to motor parameter variations. A two layer linear NN stator current observer is used as an adaptive model where the stator resistance is one of the NN weights. A backpropagation learning algorithm is used to train the NN online to update the value of the stator resistance. A conventional CM is used for rotor flux estimation.

In this chapter the NN based MRAS observer described in [76] is used for online motor speed identification instead of stator resistance estimation. The NN weight corresponding to motor speed is updated online using the backpropagation learning algorithm in such a way as to minimize the error between the measured and estimated currents. Rotor flux is needed for the stator current estimation in the adaptive model and conventionally a CM flux observer has been employed. However, as will be shown, the use of such a model gives instability in the regenerating mode of operation. Therefore the off-line trained multilayer feedforward NN proposed in chapter 6 is suggested to solve the flux estimation problem. By using this NN the flux estimation is independent of the rotor speed and does not require the use of pure integration. Superior results have been obtained from the NN flux observer scheme in terms of stator resistance sensitivity and stability over the whole speed control range.

7.2 Neural Network Stator Current MRAS Scheme

For the stator current MRAS observer, the reference model will consist of the measured stator currents [76], and hence the IM itself will work as a reference model. This has the advantages of avoiding pure integration and the estimator is less sensitive to parameters. A stator current observer can be represented by a linear two layer NN where the motor speed is expressed as one of its weights. A backpropagation learning algorithm is used in order to minimize the error in current estimation and hence generating the estimated speed.

7.2.1 Neural Network Stator Current Observer

As described in chapter 3, the rotor flux can be expressed either based on stator equations (3.53) or rotor equations (3.54). Rearranging (3.53) gives:

$$\sigma L_s p i_{sD} = v_{sD} - R_s i_{sD} - \frac{L_m}{L_r} p\psi_{rd} \tag{7.1}$$

$$\sigma L_s p i_{sQ} = v_{sQ} - R_s i_{sQ} - \frac{L_m}{L_r} p\psi_{rq} \tag{7.2}$$

Substituting (3.54) into (7.1) and (7.2) yields:

$$\sigma L_s p i_{sD} = v_{sD} - R_s i_{sD} - \frac{L_m}{L_r}\left\{-\frac{1}{T_r}\hat{\psi}_{rd} - \omega_r\hat{\psi}_{rq} + \frac{L_m}{T_r} i_{sD}\right\} \tag{7.3}$$

$$\sigma L_s p i_{sQ} = v_{sQ} - R_s i_{sQ} - \frac{L_m}{L_r}\left\{-\frac{1}{T_r}\hat{\psi}_{rq} + \omega_r\hat{\psi}_{rd} + \frac{L_m}{T_r} i_{sQ}\right\} \tag{7.4}$$

Hence the *d-q* stator current equations in the stator reference frame can be written as:

$$\sigma L_s p i_{sD} = v_{sD} - R_s i_{sD} + \frac{L_m}{L_r T_r}\hat{\psi}_{rd} + \frac{L_m}{L_r}\omega_r\hat{\psi}_{rq} - \frac{L_m^2}{L_r T_r} i_{sD} \tag{7.5}$$

$$\sigma L_s p i_{sQ} = v_{sQ} - R_s i_{sQ} + \frac{L_m}{L_r T_r}\hat{\psi}_{rq} - \frac{L_m}{L_r}\omega_r\hat{\psi}_{rd} - \frac{L_m^2}{L_r T_r} i_{sQ} \tag{7.6}$$

Equations (7.5) and (7.6) represent the stator current observer. The discrete form of (7.5) and (7.6) can be obtained by using the backward difference method as [2]:

$$p\hat{i}_{sD} = \frac{\hat{i}_{sD}(k) - \hat{i}_{sD}(k-1)}{T} \tag{7.7}$$

$$p\hat{i}_{sQ} = \frac{\hat{i}_{sQ}(k) - \hat{i}_{sQ}(k-1)}{T} \tag{7.8}$$

where T is the sampling time. Substituting (7.7) and (7.8) into (7.5) and (7.6) yields:

$$\begin{aligned}\hat{i}_{sD}(k) = &\left\{1 - \frac{TR_s}{\sigma L_s} - \frac{TL_m^2}{\sigma L_s L_r T_r}\right\}\hat{i}_{sD}(k-1) + \frac{TL_m}{\sigma L_s L_r T_r}\hat{\psi}_{rd}(k-1) \\ &+ \frac{TL_m}{\sigma L_s L_r}\omega_r\hat{\psi}_{rq}(k-1) + \frac{T}{\sigma L_s} v_{sD}(k-1)\end{aligned} \tag{7.9}$$

$$\begin{aligned}\hat{i}_{sQ}(k) = &\left\{1 - \frac{TR_s}{\sigma L_s} - \frac{TL_m^2}{\sigma L_s L_r T_r}\right\}\hat{i}_{sQ}(k-1) + \frac{TL_m}{\sigma L_s L_r T_r}\hat{\psi}_{rq}(k-1) \\ &- \frac{TL_m}{\sigma L_s L_r}\omega_r\hat{\psi}_{rd}(k-1) + \frac{T}{\sigma L_s} v_{sQ}(k-1)\end{aligned} \tag{7.10}$$

Defining the following weights:

$$
\begin{aligned}
w_1 &= 1 - \frac{TR_s}{\sigma L_s} - \frac{TL_m^2}{\sigma L_s L_r T_r} \\
w_2 &= \frac{TL_m}{\sigma L_s L_r T_r} \\
w_3 &= \frac{TL_m}{\sigma L_s L_r}\omega_r \\
w_4 &= \frac{T}{\sigma L_s}
\end{aligned}
\tag{7.11}
$$

Substituting (7.11) into (7.9) and (7.10) yields:

$$\hat{i}_{sD}(k) = w_1\hat{i}_{sD}(k-1) + w_2\hat{\psi}_{rd}(k-1) + w_3\hat{\psi}_{rq}(k-1) + w_4 v_{sD}(k-1) \tag{7.12}$$

$$\hat{i}_{sQ}(k) = w_1\hat{i}_{sQ}(k-1) + w_2\hat{\psi}_{rq}(k-1) - w_3\hat{\psi}_{rd}(k-1) + w_4 v_{sQ}(k-1) \tag{7.13}$$

Equations (7.12) and (7.13) can be represented by a two layer linear NN with weights as defined in (7.11) as shown in Fig. 7.1 [76]. This NN will represent the adaptive model for the stator current MRAS scheme where w_3, which contains the rotor speed information, is adjusted online in such a way as to minimize the error between actual and estimated currents.

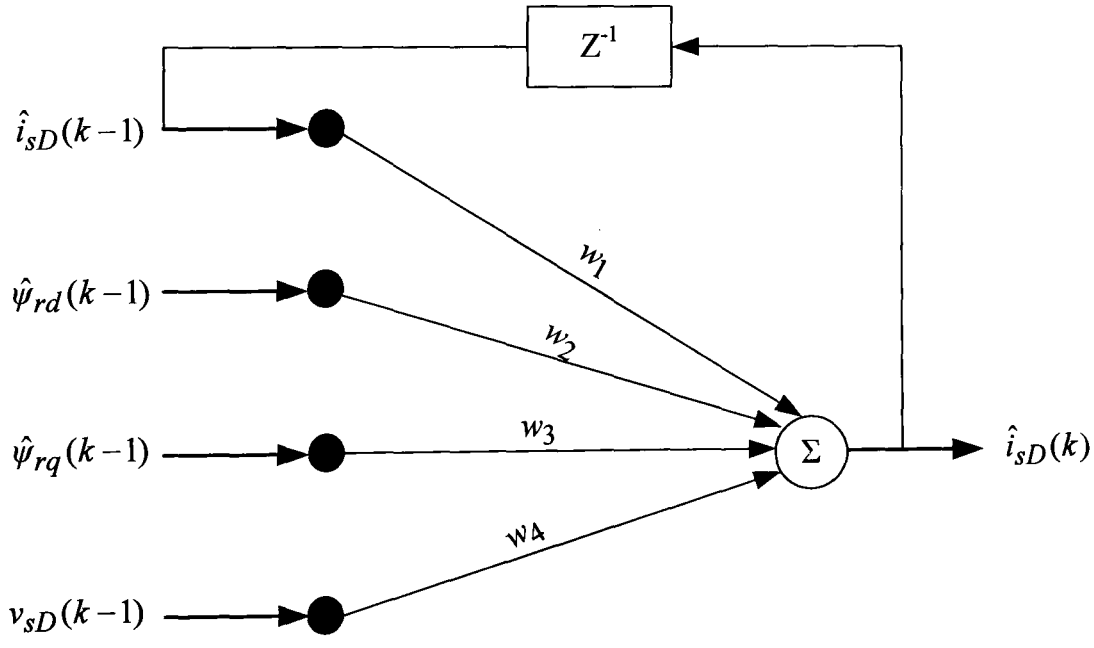

(a)

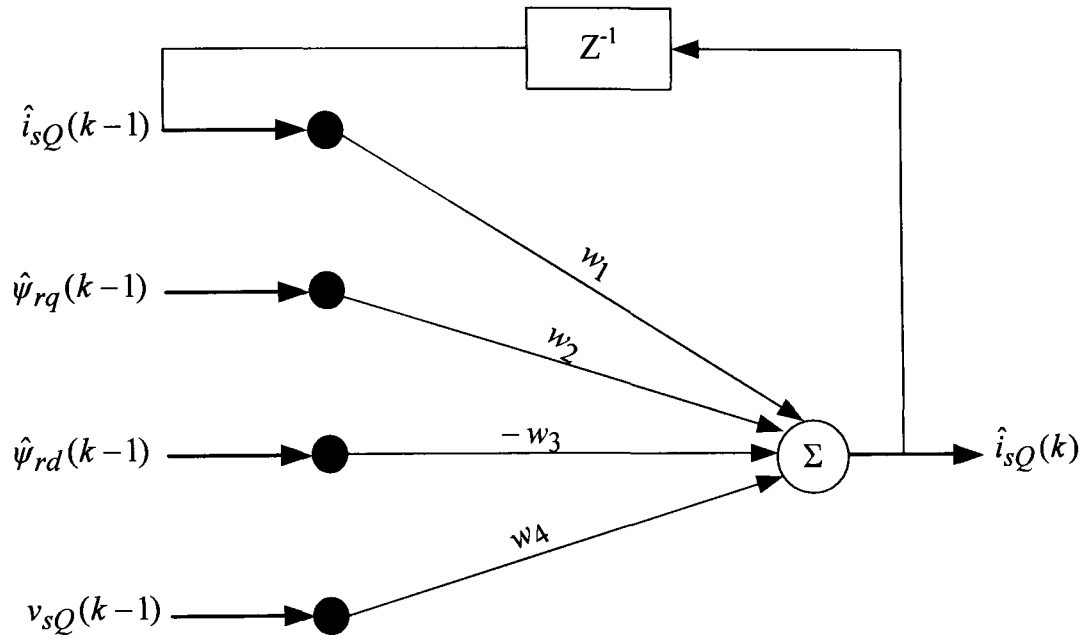

(b)

Fig. 7.1 NN-based stator current observer (a) *d*-axis (b) *q*-axis

7.2.2 Rotor Speed Estimation Algorithm

To derive the weight adjustment law of the NN stator current observer, define the energy function E to be minimized:

$$E = \frac{1}{2}\varepsilon_i^2(k) \tag{7.14}$$

where:

$$\begin{aligned}\varepsilon_i(k) &= \bar{i}_s(k) - \hat{\bar{i}}_s(k) \\ &= \left[i_{sD}(k) - \hat{i}_{sD}(k)\;\; i_{sQ}(k) - \hat{i}_{sQ}(k)\right]^T = \left[\varepsilon_{iD}(k)\;\; \varepsilon_{iQ}(k)\right]^T\end{aligned} \tag{7.15}$$

and where $\bar{i}_s$ and $\hat{\bar{i}}_s$ are the measured and the estimated stator current vectors which can be defined as:

$$\bar{i}_s(k) = \left[i_{sD}(k)\;\; i_{sQ}(k)\right]^T \tag{7.16}$$

$$\hat{\bar{i}}_s(k) = \left[\hat{i}_{sD}(k)\;\; \hat{i}_{sQ}(k)\right]^T \tag{7.17}$$

To obtain a minimum squared error between actual and estimated stator current the weight adjustment has to be proportional to the negative of the error gradient with respect to the weight as [2]:

$$\Delta w_3 \propto -\frac{\partial E}{\partial w_3} \tag{7.18}$$

Using the chain rule (7.18) can be written as:

$$-\frac{\partial E}{\partial w_3} = -\frac{\partial E}{\partial \hat{\bar{i}}_s(k)} \frac{\partial \hat{\bar{i}}_s(k)}{\partial w_3} \tag{7.19}$$

By using the definition of E given in (7.14), the term $\frac{\partial E}{\partial \hat{\bar{i}}_s(k)}$ which is present in the right hand side of (7.19) can be expressed as:

$$\begin{aligned} \frac{\partial E}{\partial \hat{\bar{i}}_s(k)} &= \frac{1}{2} \frac{\partial}{\partial \hat{\bar{i}}_s(k)} \left[\bar{i}_s(k) - \hat{\bar{i}}_s(k)\right]^2 \\ &= -\left[\bar{i}_s(k) - \hat{\bar{i}}_s(k)\right] = -\varepsilon_i{}^T(k) \end{aligned} \tag{7.20}$$

Based on stator current observer equations (7.12) and (7.13) the other term of the right hand side of (7.19) $\frac{\partial \hat{\bar{i}}_s(k)}{\partial w_3}$ can be expressed as:

$$\frac{\partial \hat{\bar{i}}_s(k)}{\partial w_3} = \left[\hat{\psi}_{rq}(k-1) \;\; -\hat{\psi}_{rd}(k-1)\right]^T \tag{7.21}$$

Substituting (7.20) and (7.21) into (7.19) yields:

$$\begin{aligned} -\frac{\partial E}{\partial w_3} &= \varepsilon_i{}^T(k).\left[\hat{\psi}_{rq}(k-1) \;\; -\hat{\psi}_{rd}(k-1)\right]^T \\ &= \varepsilon_{iD}(k)\hat{\psi}_{rq}(k-1) - \varepsilon_{iQ}(k)\hat{\psi}_{rd}(k-1) \end{aligned} \tag{7.22}$$

The mathematical expression for the weight adjustment law (7.18) can be written as [2]:

$$\begin{aligned} \Delta w_3(k) &= -\eta \frac{\partial E}{\partial w_3} \\ &= \eta\left\{\varepsilon_{iD}(k)\hat{\psi}_{rq}(k-1) - \varepsilon_{iQ}(k)\hat{\psi}_{rd}(k-1)\right\} \end{aligned} \tag{7.23}$$

where η is a positive constant called the learning rate. Large values of η may accelerate the NN learning and consequently leads to fast convergence but may cause oscillations in the network output where as low values can cause slow convergence. Therefore, the value of η has to be chosen carefully to avoid instability [2]. The new weight can be written as [2]:

$$w_3(k) = w_3(k-1) + \Delta w_3(k) \tag{7.24}$$

To ensure accelerated convergence, the last weight change is added to the weight update as [2]:

$$w_3(k) = w_3(k-1) + \Delta w_3(k) + \alpha\, \Delta w_3(k-1) \tag{7.25}$$

where α is a positive constant called the momentum constant. Due to simple structure of the NN stator current observer, the weight adjustment can be performed online and the motor speed can be estimated from the weight w_3 as:

$$\omega_r(k) = \frac{\sigma L_s L_r}{T L_m} w_3(k) \tag{7.26}$$

7.3 Rotor Flux Estimation Problem

Since rotor flux estimation is required for the stator current MRAS scheme, a VM and CM flux observers can be used. However, the VM was shown to be unsuitable for low speed operation as described in chapter 6. Therefore the CM can be used to avoid the low speed problems but it shows poor stability margins as it will be shown later. The block diagram of the NN-based stator current MRAS scheme using a CM rotor flux observer is shown in Fig. 7.2.

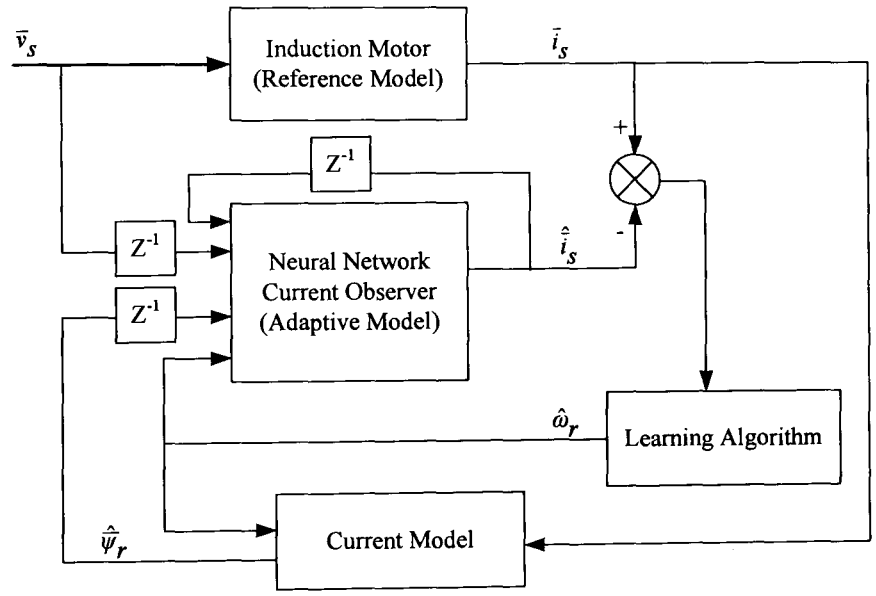

Fig. 7.2 NN-based stator current MRAS speed observer using CM flux observer

As will be shown in the next section the use of a CM to estimate the rotor flux causes instability at the regenerating region. To overcome this problem another way to estimate the rotor flux needed for the stator current MRAS scheme is proposed here which uses an off-line trained NN. To estimate the rotor flux components in the stationary reference frame the multilayer feedforward NN proposed in chapter 6 can be used. The block diagram of the stator current MRAS scheme employing a NN for rotor flux estimation is

shown in Fig. 7.3. In this scheme two NN are used, an online trained linear NN for stator current estimation and an offline trained nonlinear NN for rotor flux estimation.

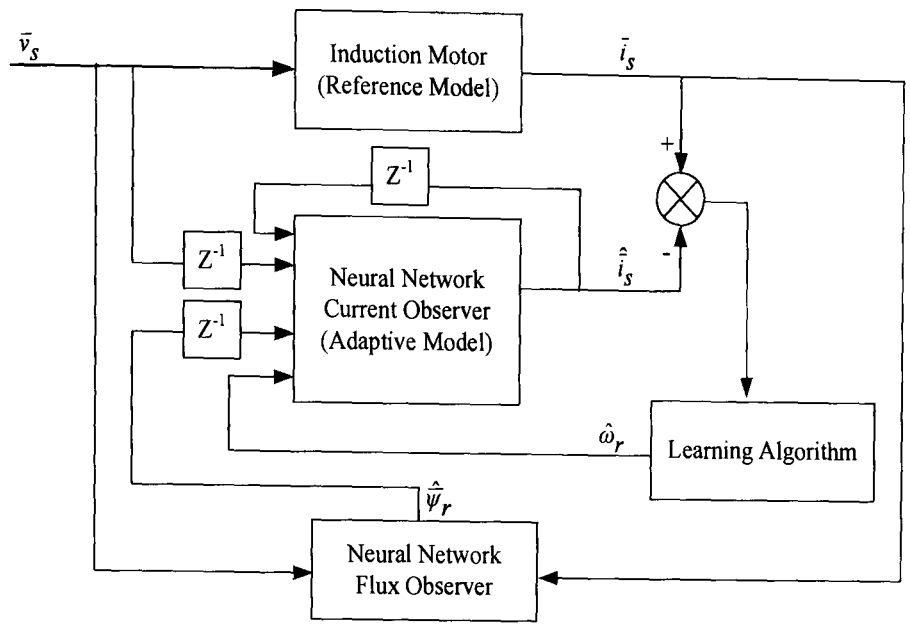

Fig. 7.3 NN-based stator current MRAS speed observer with NN flux observer

7.4 Simulation Results

To test the NN-based stator current MRAS observer performance, the 7.5 kW induction machine with parameters given in Table 4.3 is simulated using Matlab-Simulink. The drive is running under indirect vector control with different reference speed and various loading levels. The NN described in section 6.5 will be used for the simulation study. The stator current MRAS scheme using the three rotor flux observers, VM, CM and NN, is tested for sensitivity to stator resistance variation for reference speed changes and load torque application. Furthermore, speed estimation performance is investigated at different operating conditions in the low speed region of operation including the regenerating mode. In the following simulations the estimated speed (7.26) is compared with the actual speed calculated from the mechanical model (5.24). Rotor flux and stator current estimates are compared with their actual values obtained from the machine state space model (3.26).

7.4.1 Sensitivity to Stator Resistance Variation

The purpose of this test is to compare the speed estimation performance of the MRAS observer for motor parameter variation. The vector control drive is run with a 25% increase in the motor stator resistance and subjected to a reference speed change

from 50 rpm to 75 rpm at no load at t =5s followed by a 25% load torque application at t=8s. The speed estimation performance using the three different rotor flux observers is shown in Fig. 7.4.

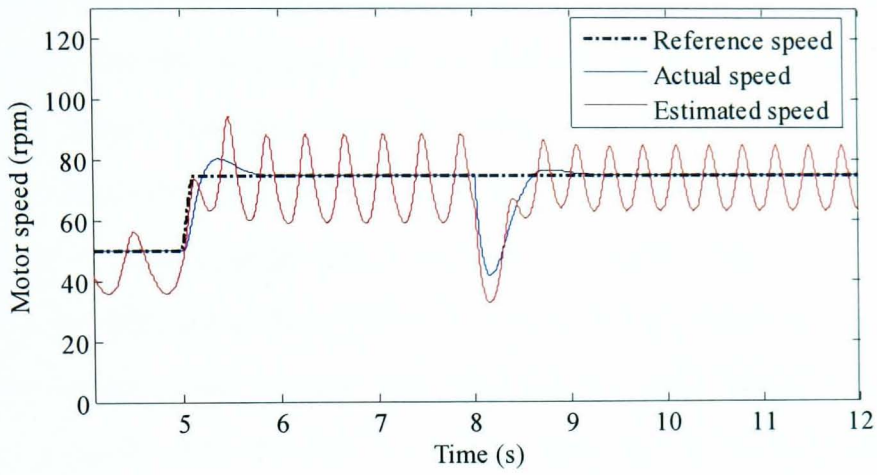

(a)

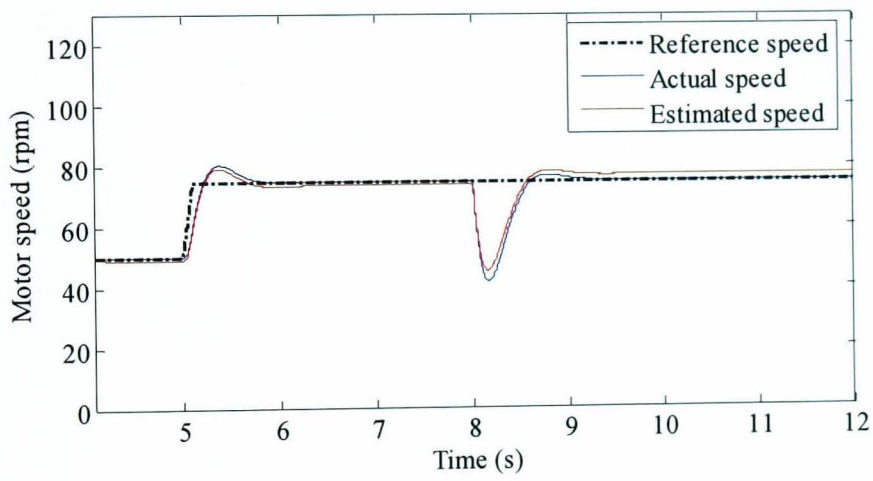

(b)

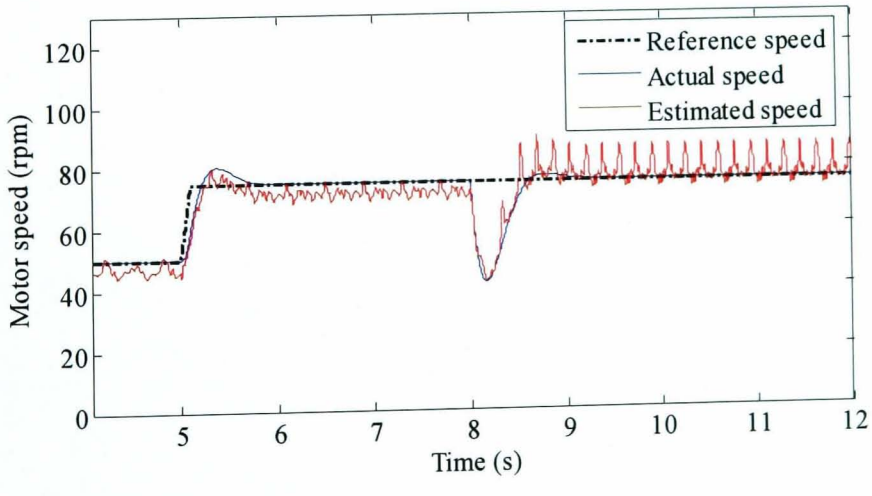

(c)

Fig. 7.4 NN stator current MRAS speed estimation performance with 25% increase in R_s

(a) VM flux observer (b) CM flux observer (c) NN flux observer

Due to the presence of R_s in the stator current observer equations (7.9)-(7.10), speed estimation for all schemes is affected by the variation in R_s. The effect of R_s change on the VM is more serious and causes oscillations in the estimated speed due to the presence of R_s in the flux estimation equation as well. Although R_s is not present in the CM observer equation, the flux estimation is still affected since the model makes use of the estimated speed which deviates from the actual. The NN flux observer shows less sensitivity to R_s variations compared to the VM without being dependent on the estimated speed. Therefore it shows good speed estimation performance close to that obtained when using a CM. The rotor flux and stator current estimation performance using the three observers during speed change and load torque disturbance rejection is shown in Figs. 7.5-7.8. As can be seen the VM is the most affected by the R_s variation compared to the CM and NN observers.

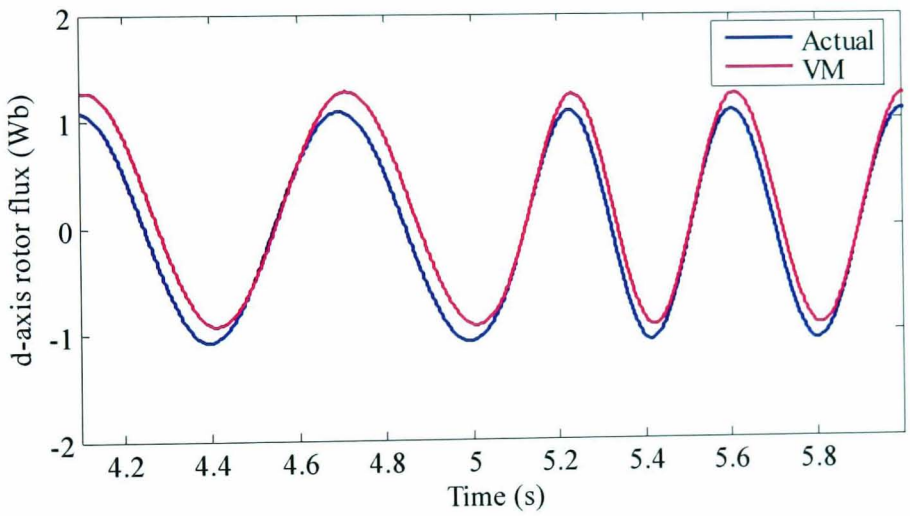

(a)

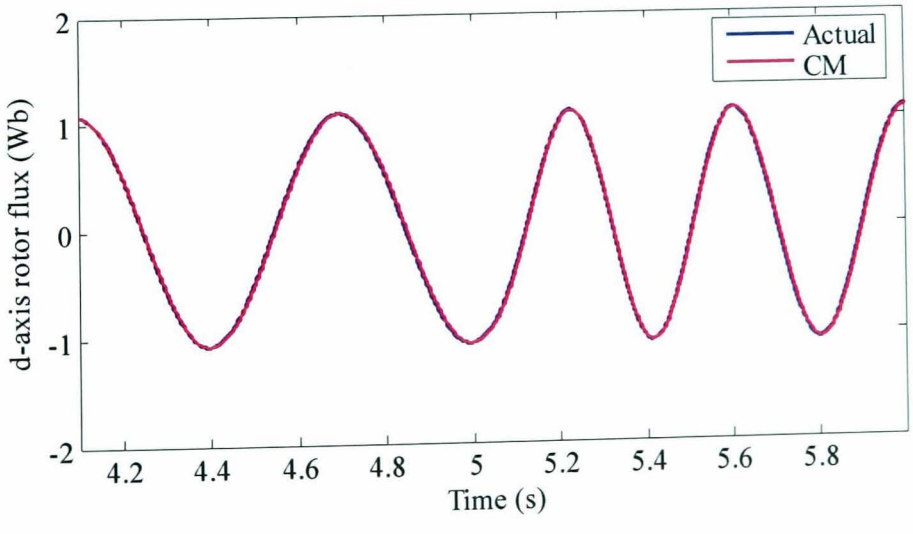

(b)

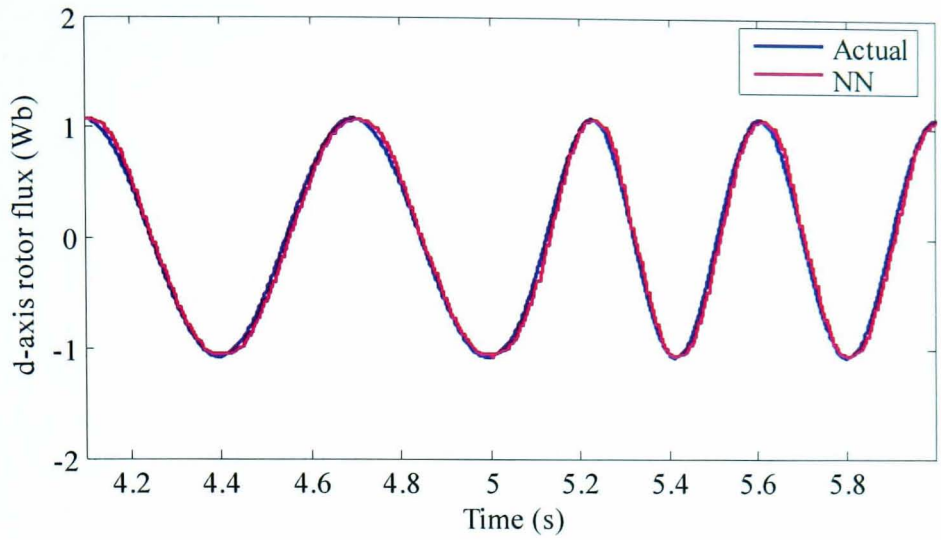

(c)

Fig. 7.5 Rotor flux estimation performance during speed change with 25% increase in R_s

(a) VM flux observer (b) CM flux observer (c) NN flux observer

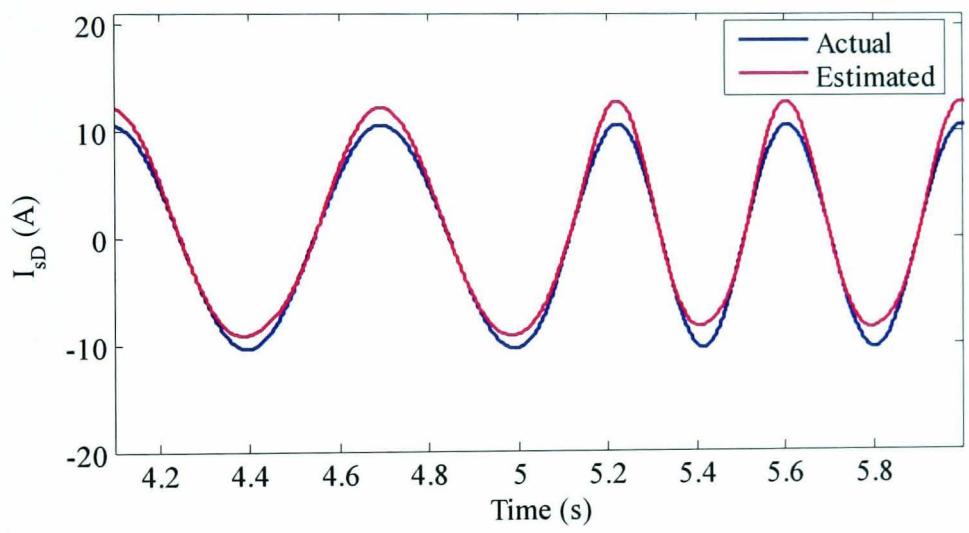

(a)

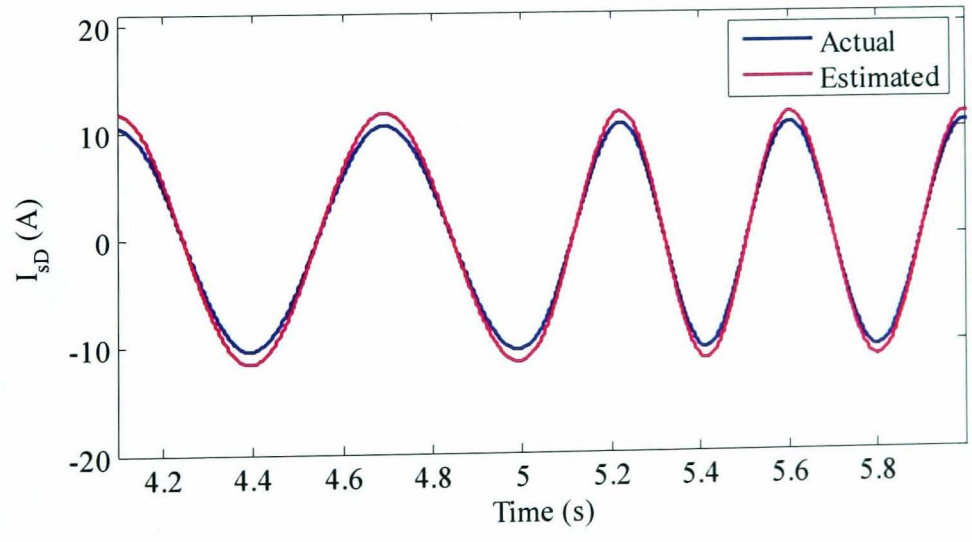

(b)

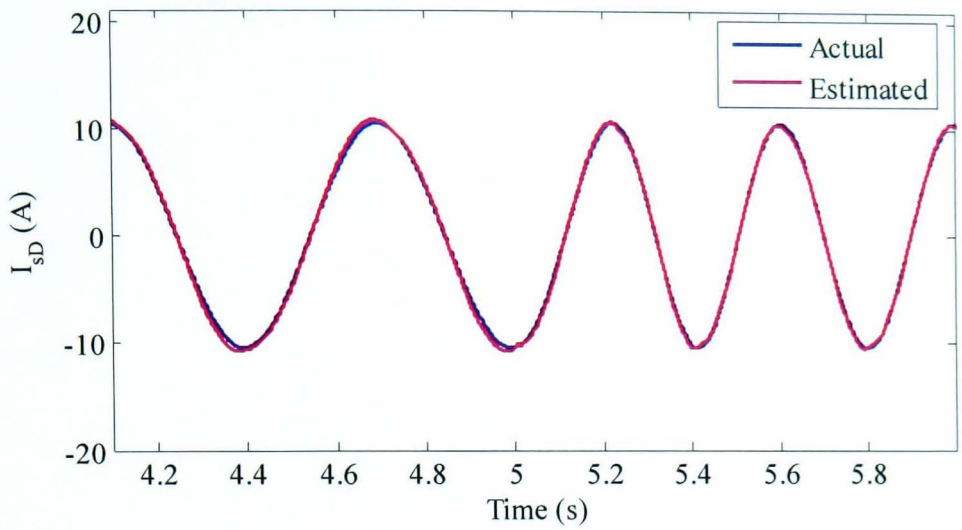

(c)

Fig. 7.6 Stator current estimation performance during speed change with 25% increase in R_s (a) VM flux observer (b) CM flux observer (c) NN flux observer

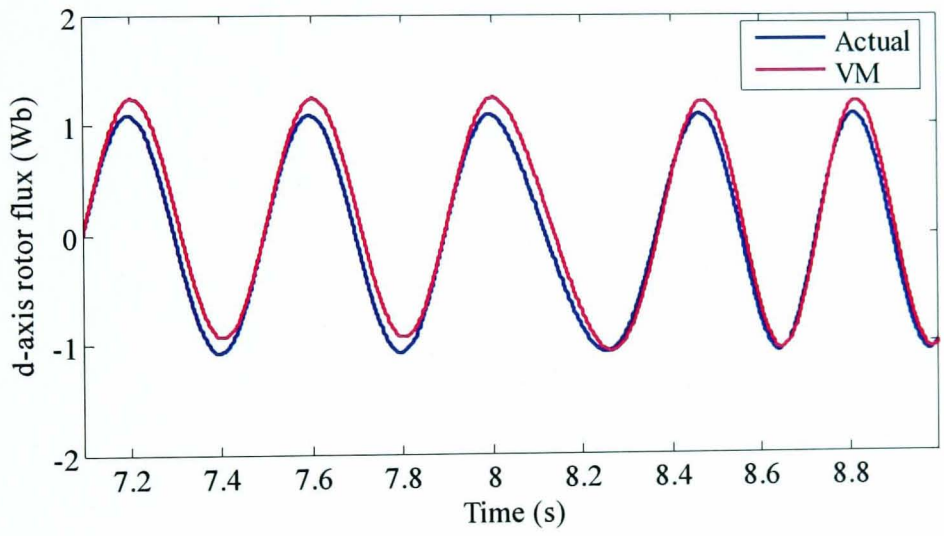

(a)

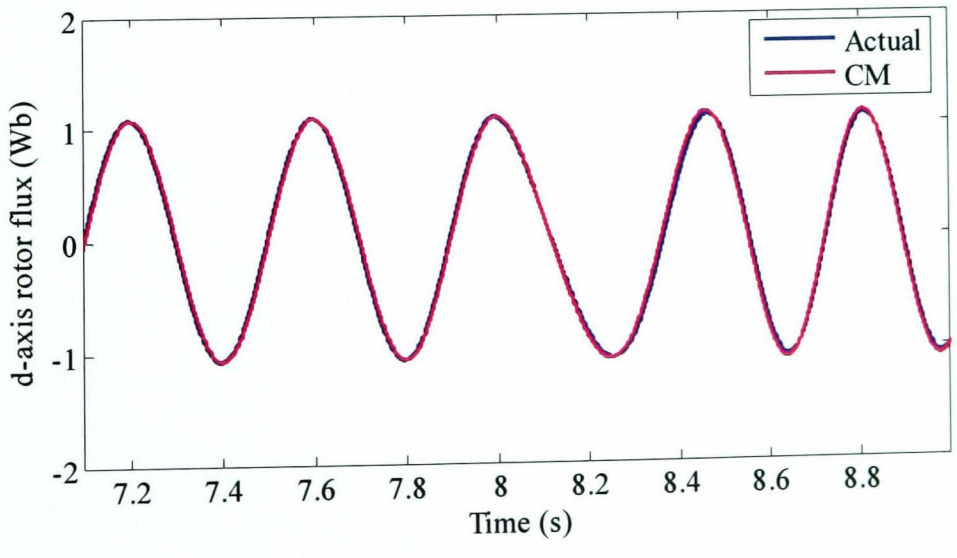

(b)

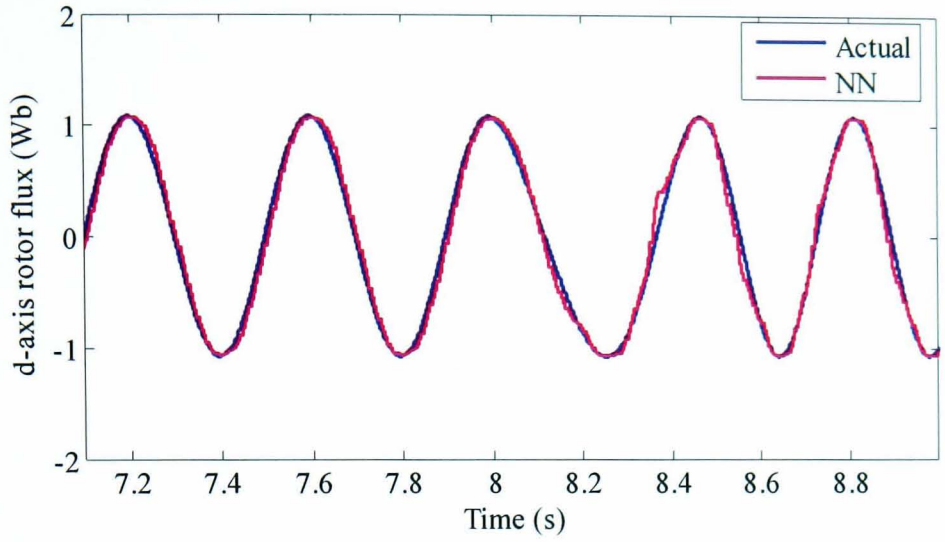

(c)

Fig. 7.7 Rotor flux estimation performance during disturbance rejection with 25% increase in R_s (a) VM flux observer (b) CM flux observer (c) NN flux observer

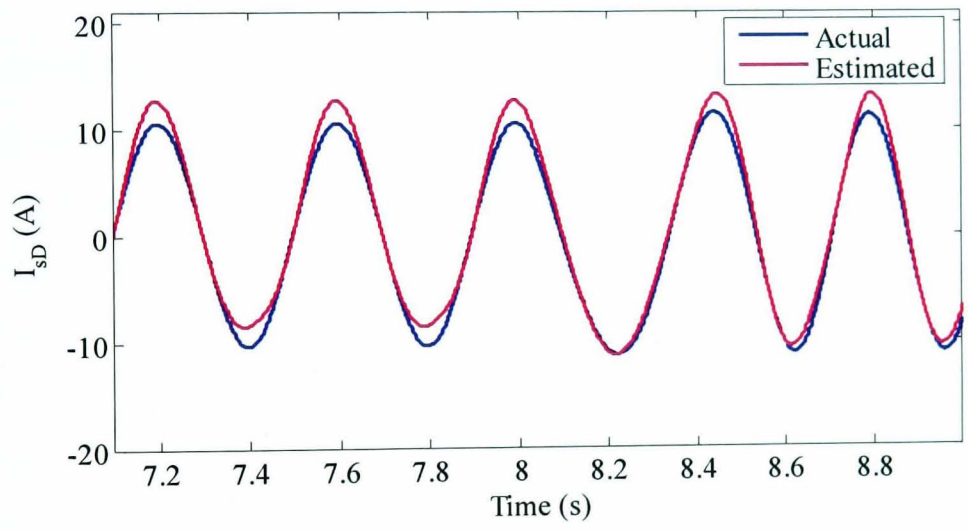

(a)

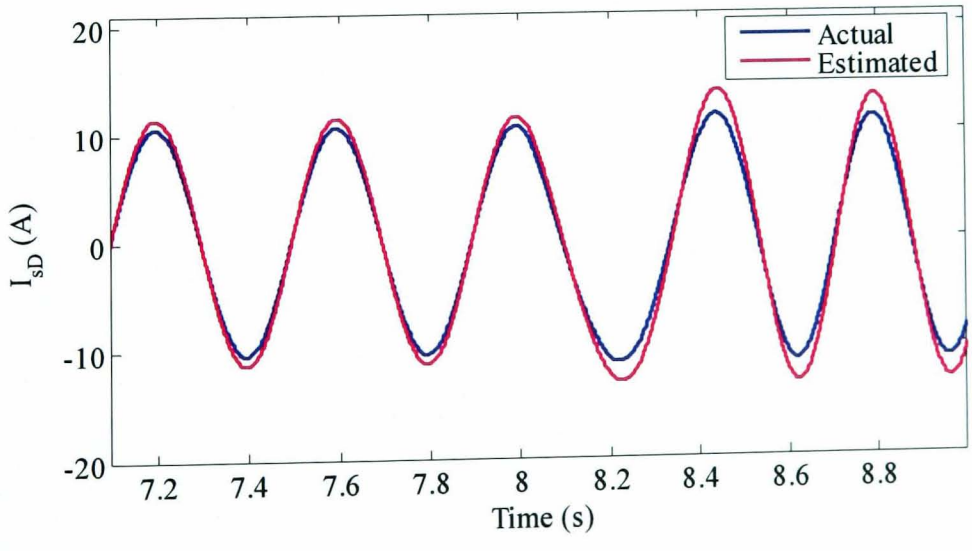

(b)

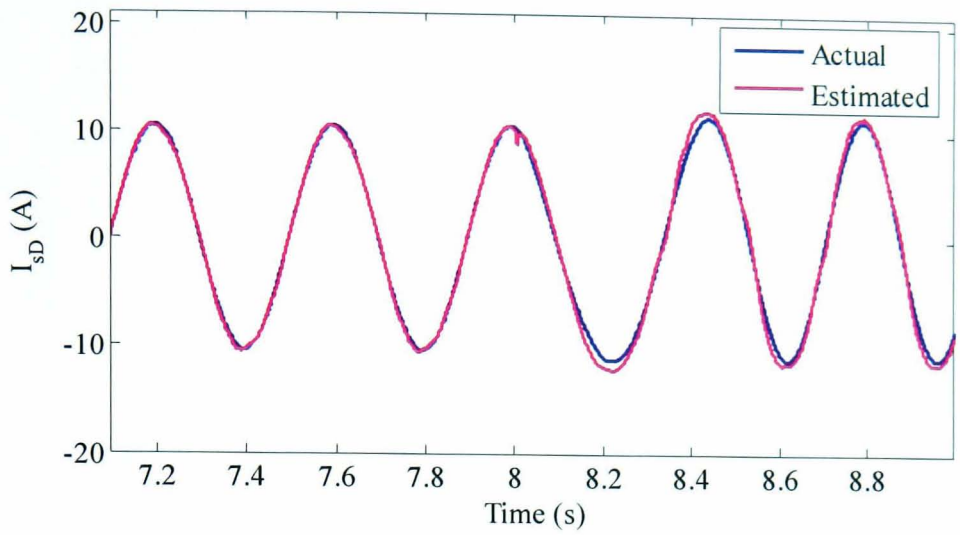

(c)

Fig. 7.8 Stator current estimation performance during disturbance rejection with 25% increase in R_s (a) VM flux observer (b) CM flux observer (c) NN flux observer

7.4.2 Stability in the Regenerating Mode

In this test the stability of the stator current MRAS schemes is tested in the regenerating mode of operation. In this region of operation the motor is running at negative speed with a positive load torque applied. Unstable performance was obtained using the CM flux observer in the regenerating mode. Results showing this unstable behaviour are obtained when the drive is subjected to a speed reversal command from 40 rpm to -40 rpm at 25% load torque with nominal machine parameters. The speed estimation performance of the stator current MRAS scheme using the CM and NN rotor flux observers is shown in Fig. 7.9.

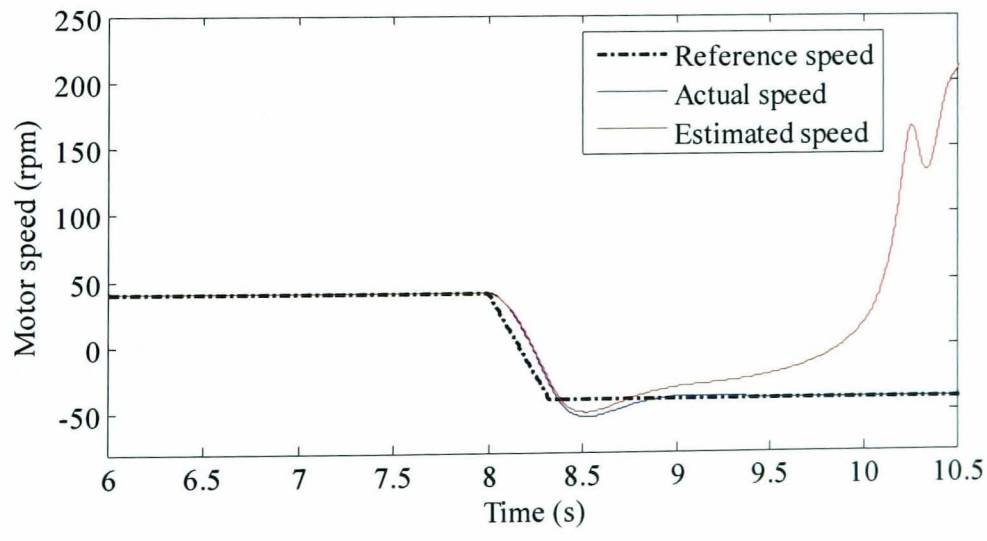

(a)

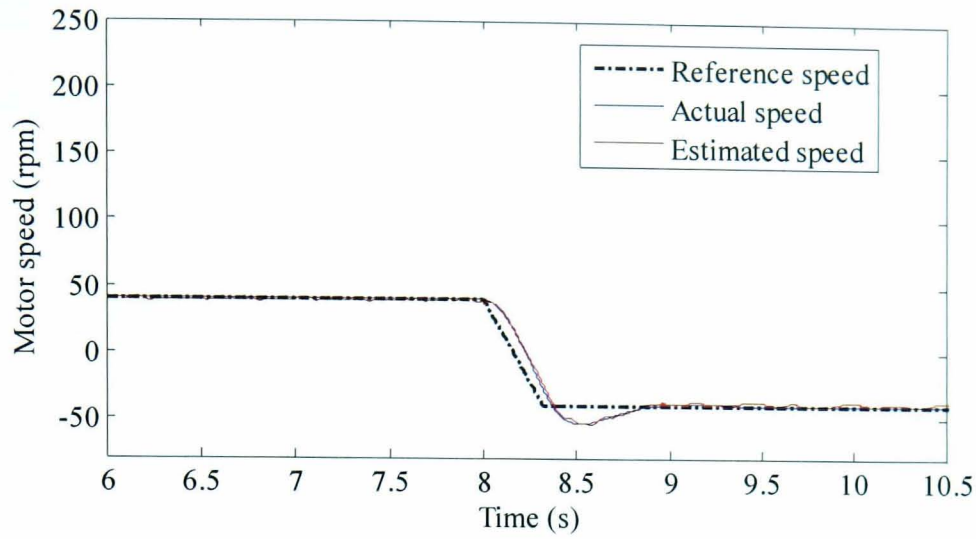

(b)

Fig. 7.9 NN stator current MRAS speed estimation performance in the regenerating mode (a) CM flux observer (b) NN flux observer

Since rotor flux estimation using a CM depends on the estimated speed, any deterioration in the speed estimation is fed back to the flux observer causing instability in the regenerating mode of operation. Using a NN for rotor flux estimation gives stable speed estimation performance in the regenerating mode since flux estimation is independent of the estimated speed. Rotor flux and stator current estimation performance using the two observers, CM and NN, is shown in Figs. 7.10-7.11. Deterioration of rotor flux estimation affects the stator current tracking causing instability of the speed estimation using the CM flux observer. By contrast the NN flux observer follows the actual flux which improves stator current tracking leading to stable speed estimation performance.

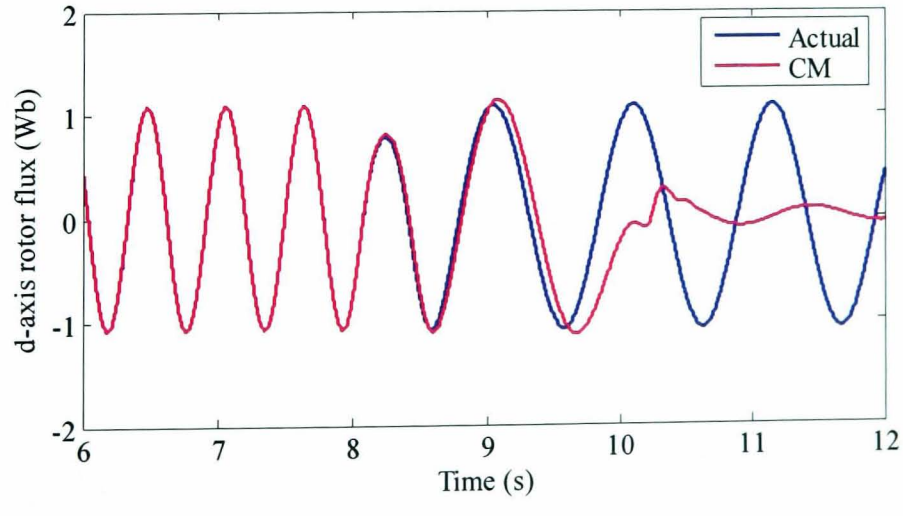

(a)

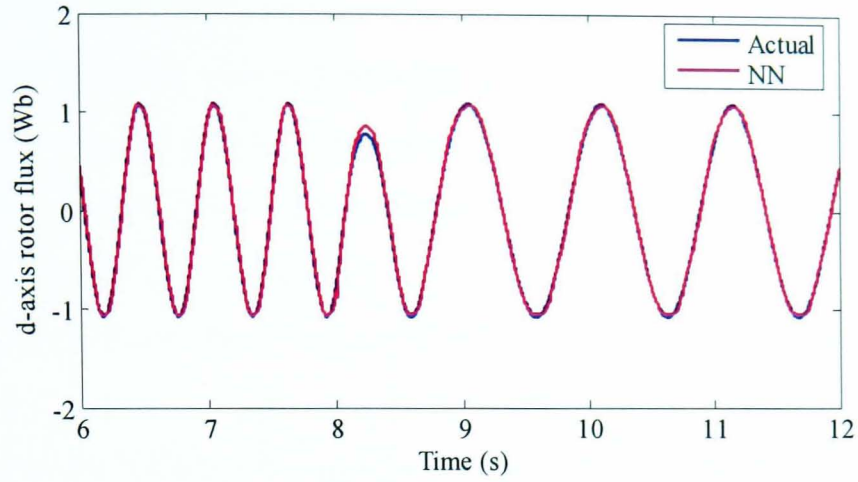

(b)

Fig. 7.10 Rotor flux estimation performance in the regenerating mode (a) CM flux observer (b) NN flux observer

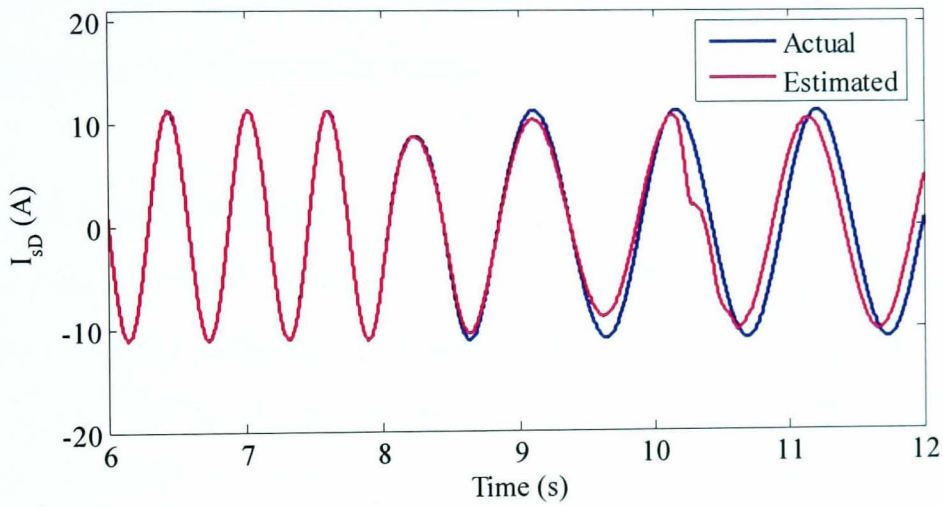

(a)

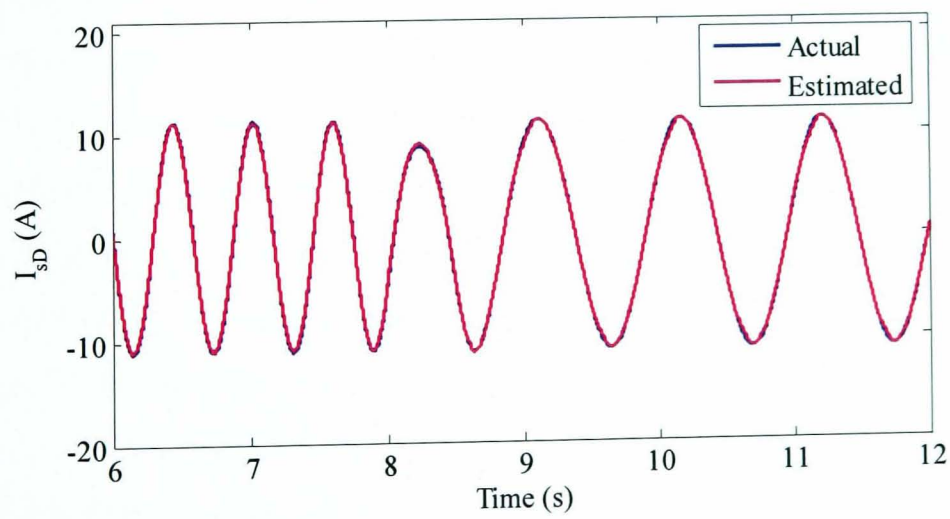

(b)

Fig. 7.11 Stator current estimation performance in the regenerating mode (a) CM flux observer (b) NN flux observer

7.5 Experimental Results

In this section the new stator current MRAS scheme based on CM and NN flux observers will be experimentally demonstrated to overcome the problems of the conventional rotor flux MRAS scheme. As illustrated in chapter 6, the NN flux observer is trained to match the performance of the CM which is free from stator resistance dependency and dc drift problems. Once the NN is trained it was shown that it accurately matches the CM. However, unlike the CM, the NN is able to estimate the values of the rotor flux components without needing the rotor speed information. Hence it is possible to use the proposed NN for rotor flux estimation in the new MRAS scheme. To further experimentally validate the proposed schemes open and closed loop sensorless operations will be compared for the new and conventional schemes. The speed estimation performance is investigated at different operating conditions in the low speed region of operation including the regenerating mode.

7.5.1 Open Loop Operation

The new schemes were tested in open loop with the drive operated as an *encodered* vector control. The open loop performance of the conventional rotor flux MRAS and the new stator current MRAS speed observers is compared. The two structures of the new scheme will be compared: Current MRAS-CM using CM flux observer and Current MRAS-NN using NN rotor flux observer that was described in section 6.4.1. Estimated speed and currents will be compared with measured rotor speed and stator currents.

The sampling time for the NN stator current observer is 1/5000s with η=0.0005 and α=0.001. These values have been obtained experimentally by trial and error to ensure optimal performance of the NN-based stator current schemes and were also used in the simulation stage. The estimated speed from stator current MRAS schemes is obtained through a LPF with 30 rad/s cut-off frequency. Figs. 7.12-7.14 show the open loop performance of all schemes for -40 rpm to 40 rpm speed reversal, 40 rpm to 20 rpm speed change at no load and a 25% load torque disturbance rejection at 30 rpm. Both stator current schemes demonstrate better transient and steady state performance compared to the conventional rotor flux MRAS where the use of the VM is dependant on the stator voltage. Hence errors between actual and reference stator voltage at low speed

worsen the speed estimation performance. On the other hand, NN and CM based schemes are not directly affected by stator voltage errors for flux estimation and hence have better performance at low speed with less steady state error.

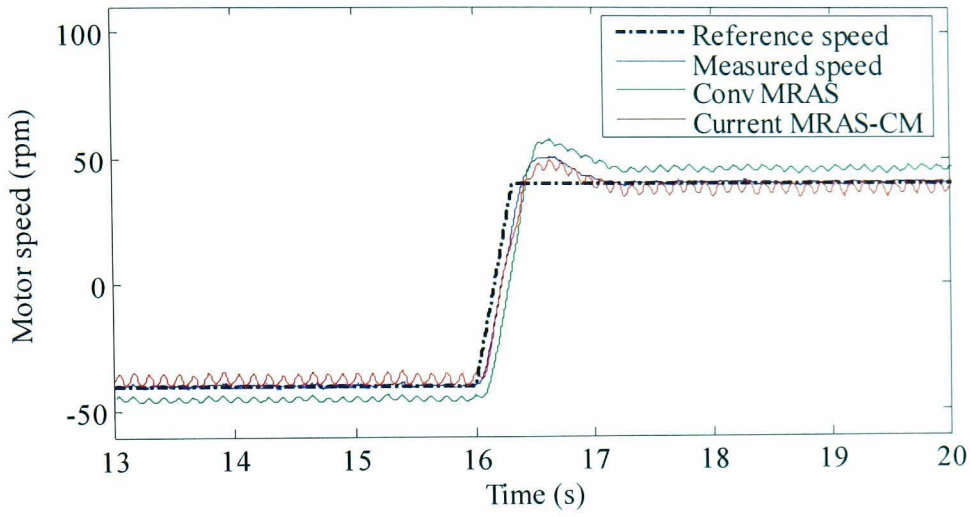

(a)

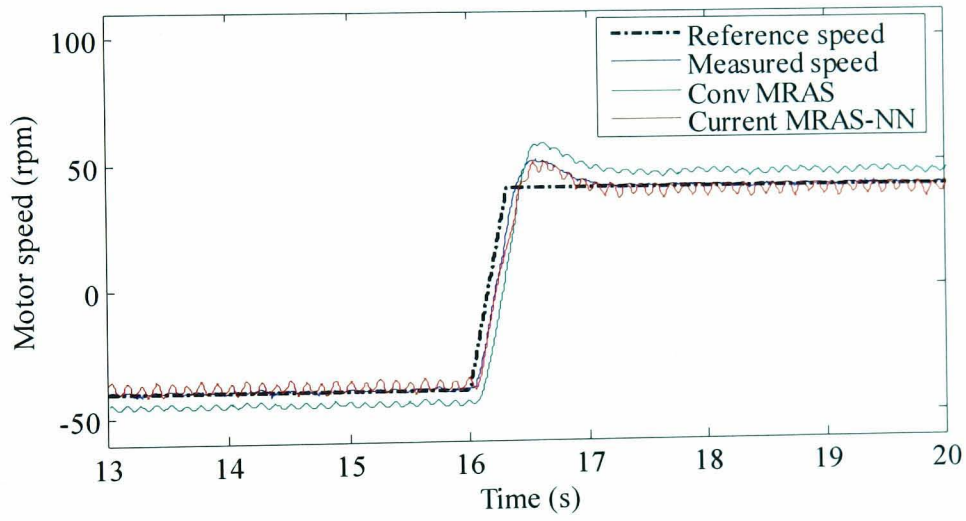

(b)

Fig. 7.12 Open loop -40 rpm to 40 rpm reversal, no load (a) Stator current MRAS-CM (b) Stator current MRAS-NN

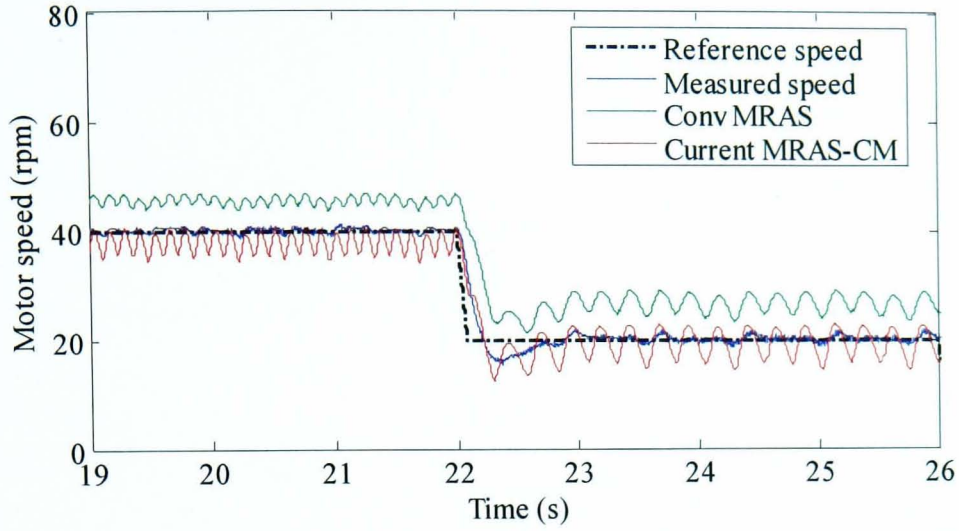

(a)

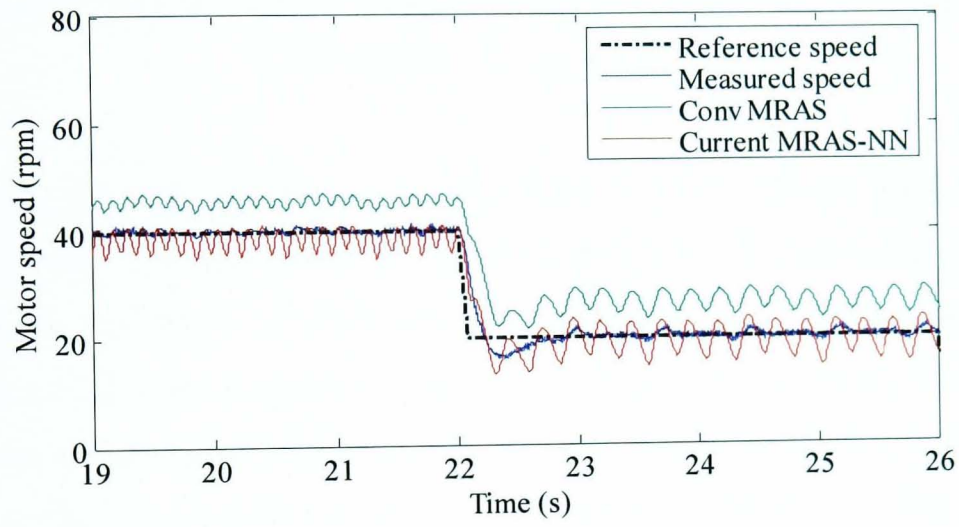

(b)

Fig. 7.13 Open loop 40 rpm to 20 rpm speed change, no load (a) Stator current MRAS-CM (b) Stator current MRAS-NN

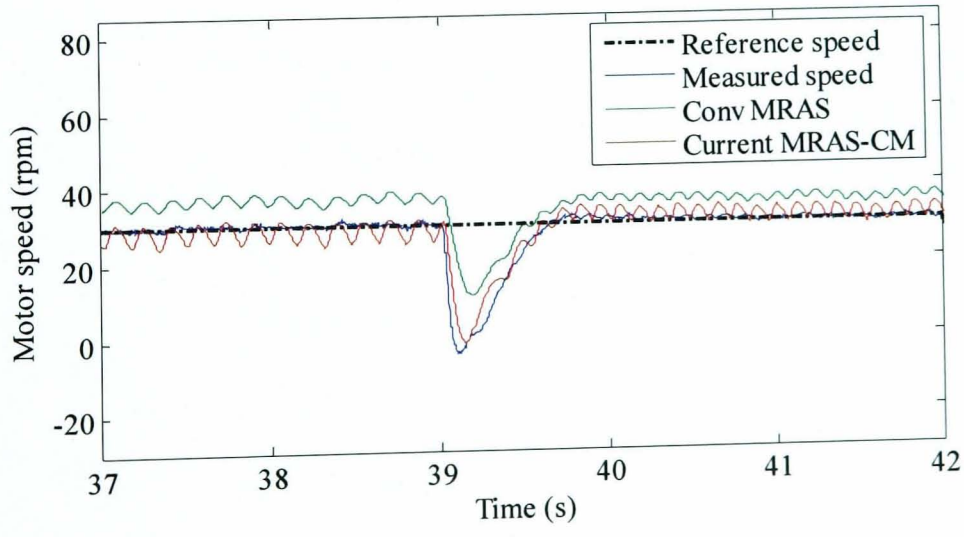

(a)

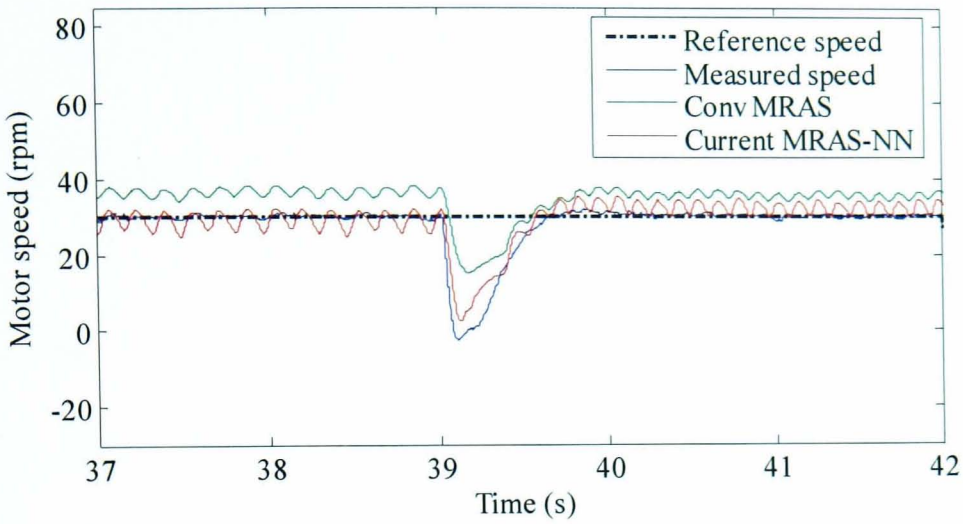

(b)

Fig. 7.14 Open loop 25% load disturbance rejection, 30 rpm (a) Stator current MRAS-CM (b) Stator current MRAS-NN

However, stability problems of the stator current MRAS-CM occur in the regenerating mode. Stable operation is obtained using the stator current MRAS-NN scheme which still shows a better response compared to the conventional rotor flux MRAS scheme. Results of speed and rotor flux estimation are shown in Fig. 7.15 for a series of step speed change from 30 rpm to -30 rpm to -60 rpm to 60 rpm at 25% load.

More results for operation at regeneration using CM and NN flux observers are shown in Fig. 7.16 for ±100 rpm speed reversal at 20% load torque. NN provides stable flux estimation compared to CM leading to better stator current and rotor speed estimation.

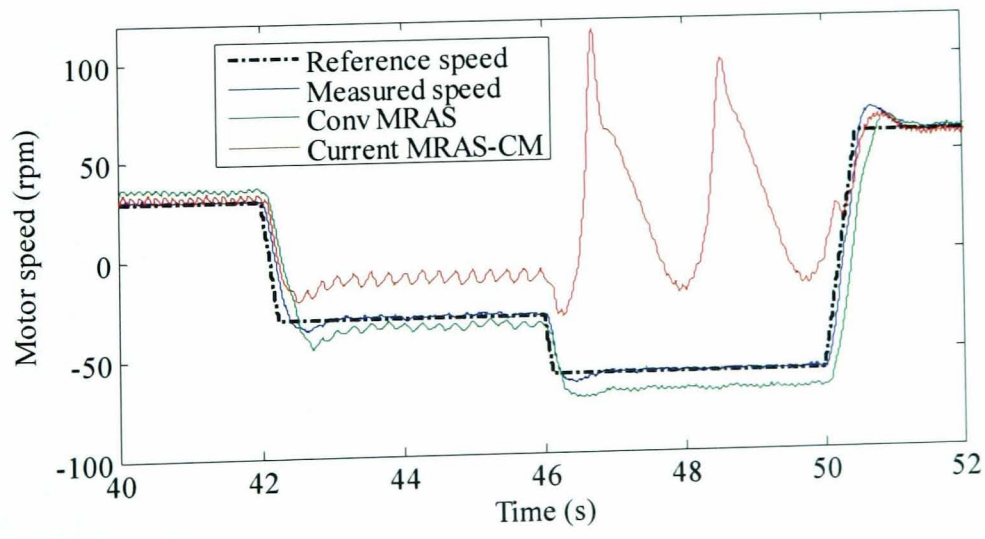

(a)

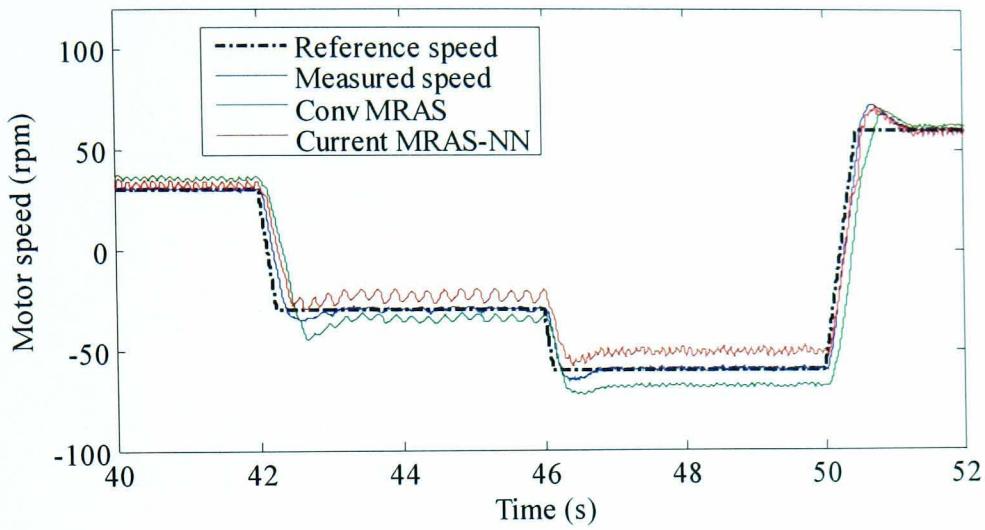

(b)

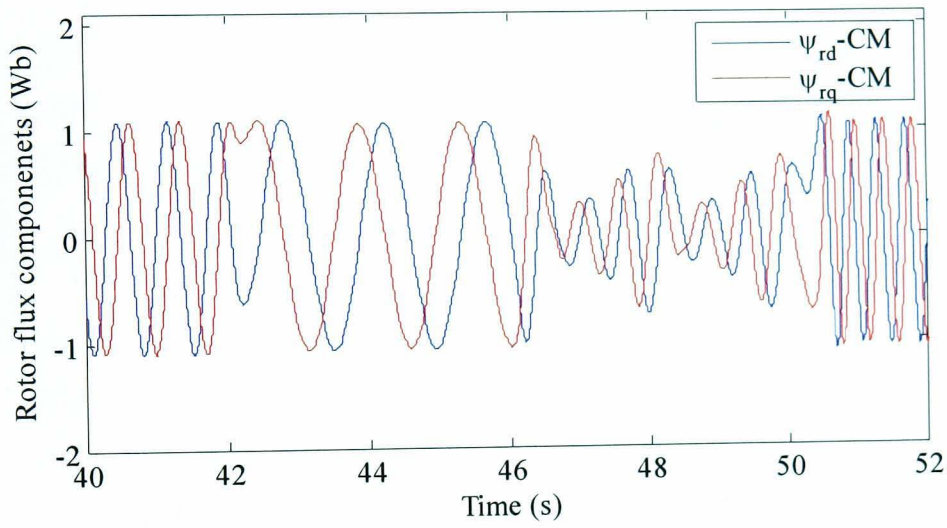

(c)

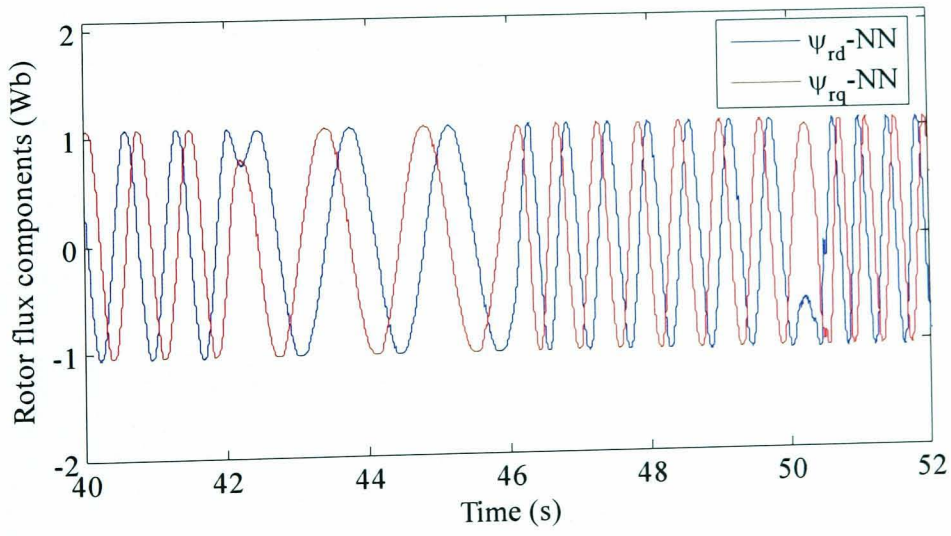

(d)

Fig. 7.15 Open loop performance at regeneration. Speed (a) Stator current MRAS-CM (b) Stator current MRAS-NN. Rotor flux (c) CM (d) NN

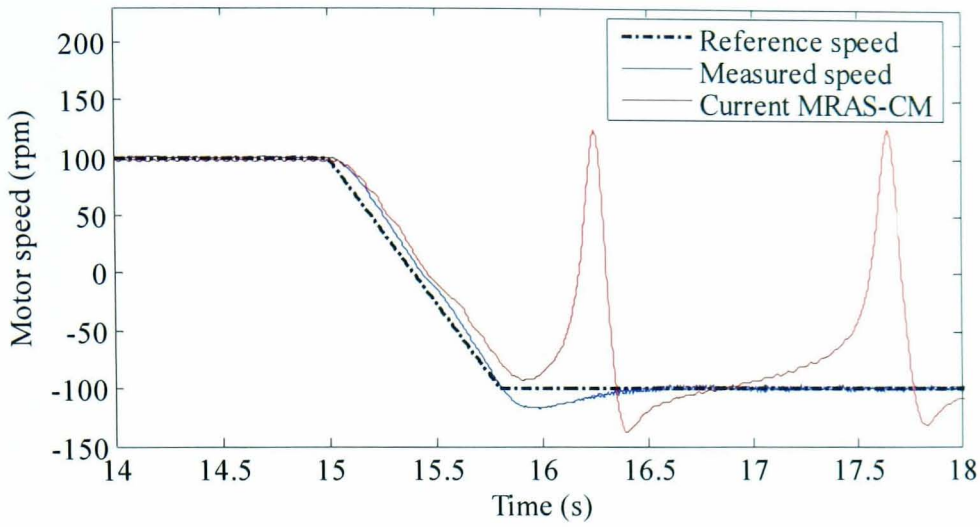
Reference speed
Measured speed
Current MRAS-CM
Motor speed (rpm)
Time (s)
200
150
100
50
0
-50
-100
-150
14
14.5
15
15.5
16
16.5
17
17.5
18

(a)

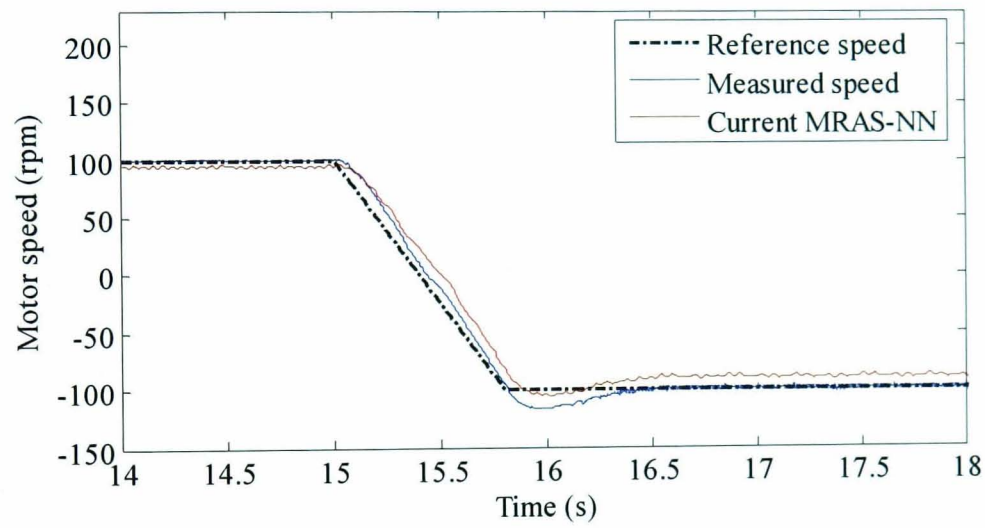
Reference speed
Measured speed
Current MRAS-NN
Motor speed (rpm)
Time (s)
200
150
100
50
0
-50
-100
-150
14
14.5
15
15.5
16
16.5
17
17.5
18

(b)

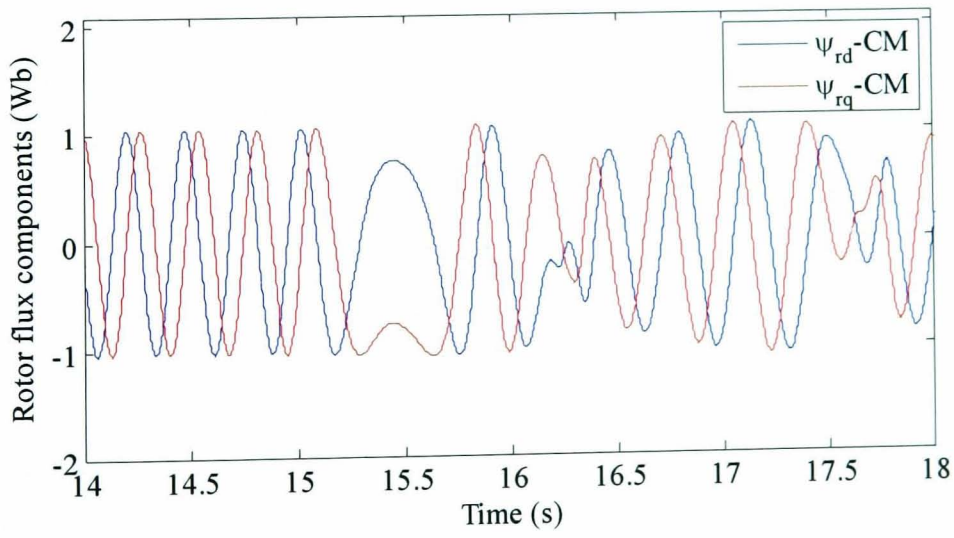
ψrd-CM
ψrq-CM
Rotor flux components (Wb)
Time (s)
2
1
0
-1
-2
14
14.5
15
15.5
16
16.5
17
17.5
18

(c)

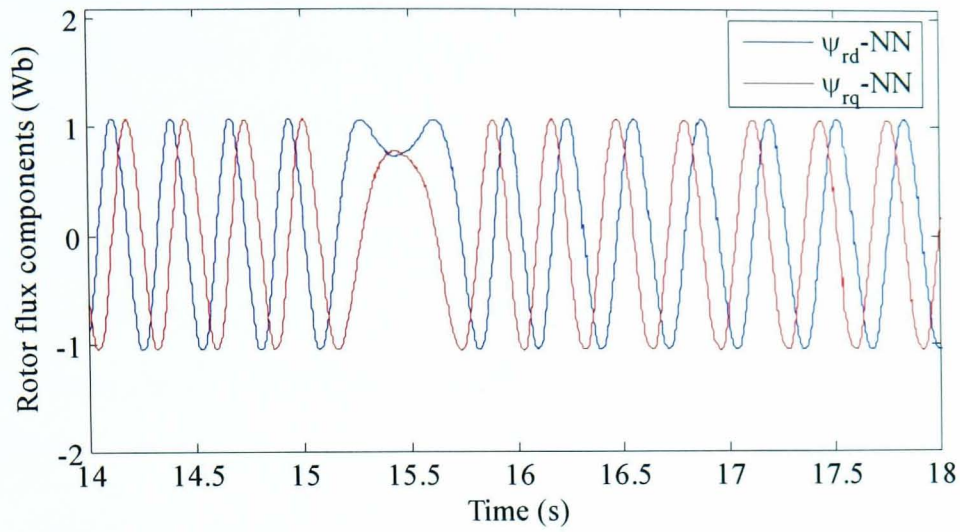

(d)

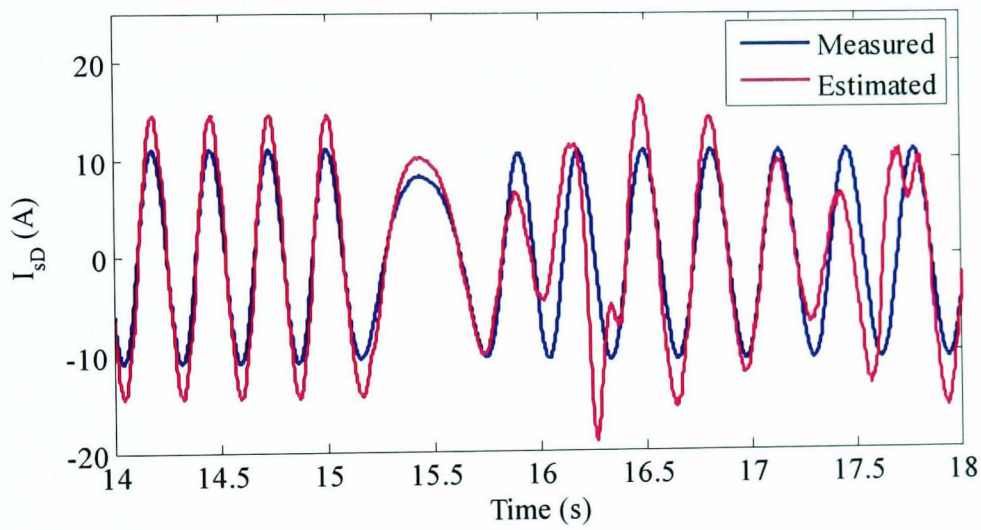

(e)

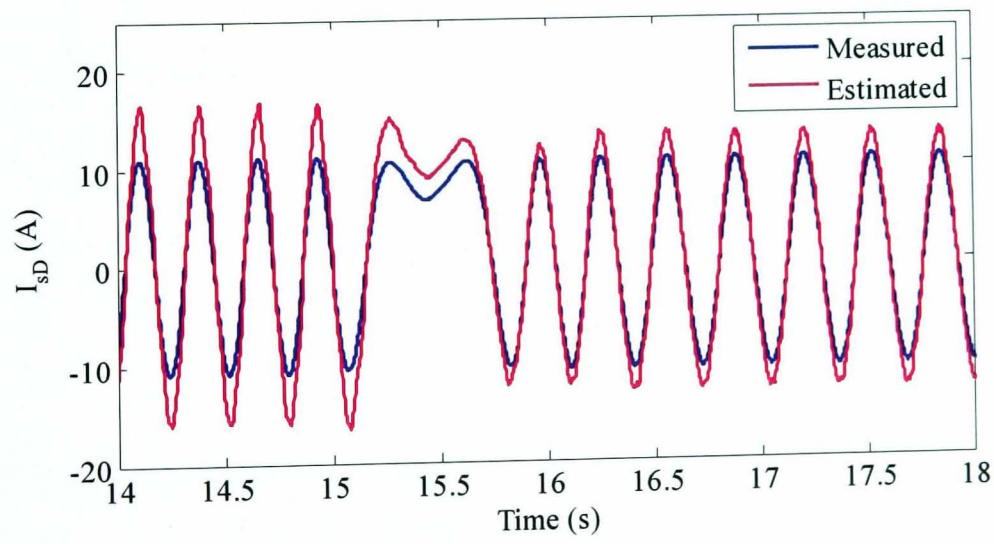

(f)

Fig. 7.16 Open loop ±100 rpm speed reversal, 20% load. Speed (a) Stator current MRAS-CM (b) Stator current MRAS-NN. Rotor flux (c) CM (d) NN. Current (e) CM (f) NN

Results at rated load for the stator current MRAS-NN scheme can be obtained by using the extended version of the NN flux observer described in chapter 6 where the training range covers the full torque region. Figs. 7.17-7.18 show the speed estimation performance of the stator current MRAS observer, using CM and NN flux observers, for rated load disturbance rejection at 40 rpm and reference speed change from 40 rpm to 10 rpm at rated load. Compared to conventional rotor flux MRAS, both new schemes show better performance at very low speed and rated load with less steady state error in the estimated speed.

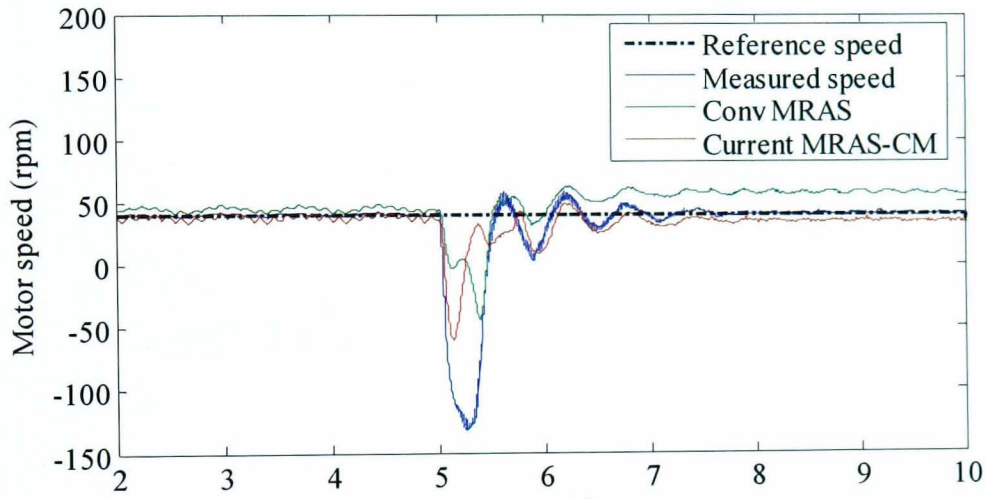

(a)

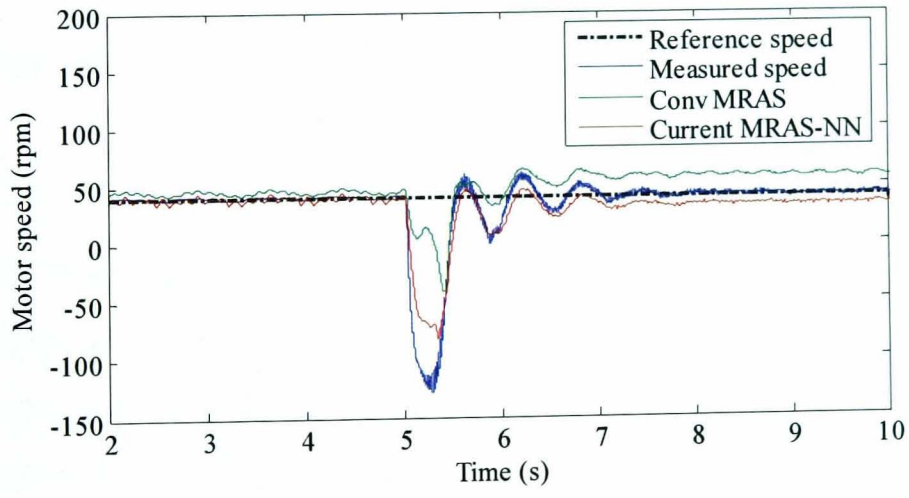

(b)

Fig. 7.17 Open loop rated load disturbance rejection, 40 rpm (a) Stator current MRAS-CM (b) Stator current MRAS-NN

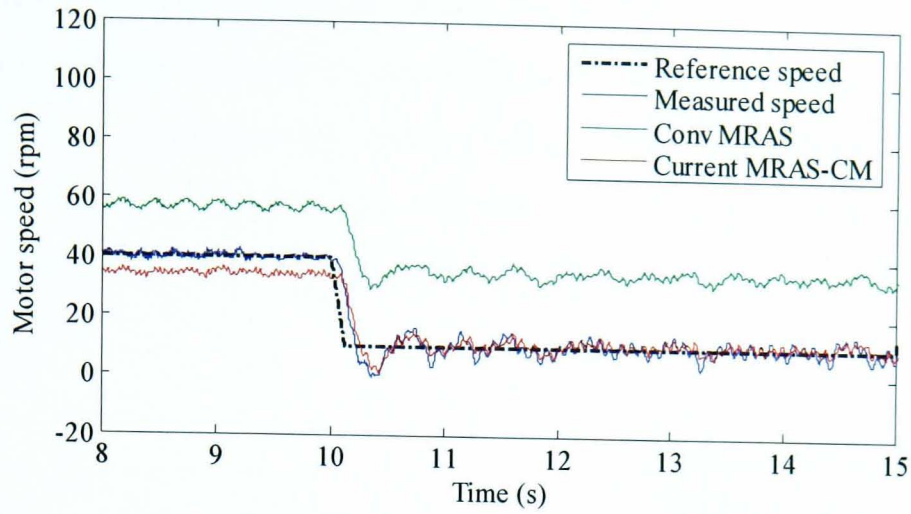

(a)

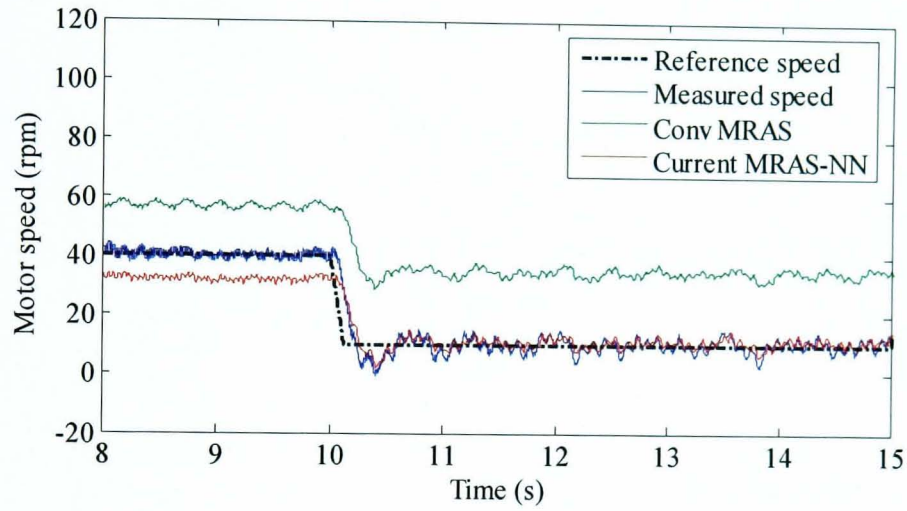

(b)

Fig. 7.18 Open loop 40 rpm to 10 rpm speed change, rated load (a) Stator current MRAS-CM (b) Stator current MRAS-NN

7.5.2 Sensorless Operation

In this section the proposed stator current based MRAS schemes are tested in sensorless mode of operation following the same procedure described in chapter 6. Results are given for the NN that was developed in section 6.4.1.

Test 1: Stair case speed transients from 100rpm to 0rpm to 100 rpm:

This sensorless test, described in chapter 6, was performed at no load. The performance of NN-stator current MRAS scheme, based on CM and NN flux observers, is shown in Fig. 7.19. Both stator current MRAS schemes show better low and zero speed performance compared to the conventional rotor flux MRAS scheme shown in Fig.

6.18 (a) but not as good as that of the NN-based rotor flux MRAS shown in Fig. 6.18 (b). Moreover, the NN flux observer shows better flux estimation at zero speed compared to the CM observer. Consequently, better stator current estimation and zero speed performance is obtained from the stator current MRAS-NN. Rotor flux and stator current estimation performances for CM and NN-based schemes around and at zero speed are shown in Fig. 7.20.

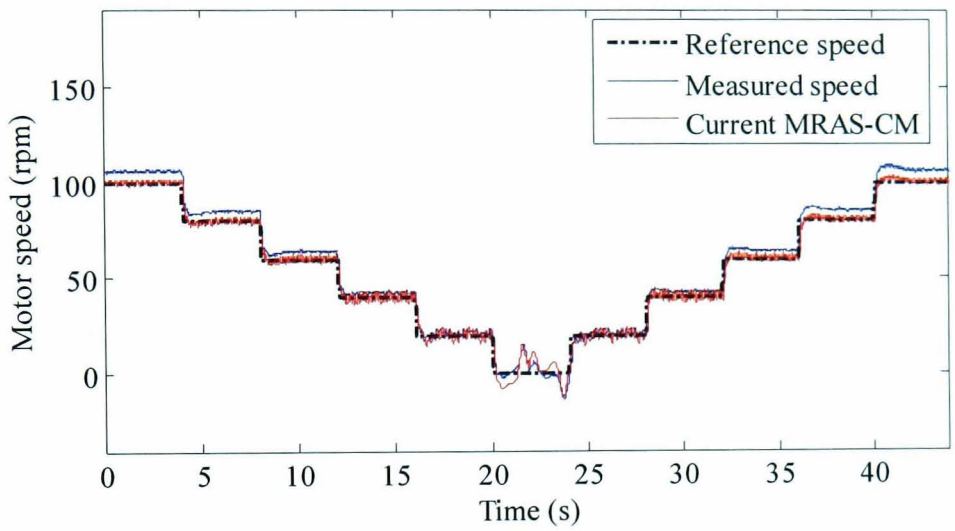

(a)

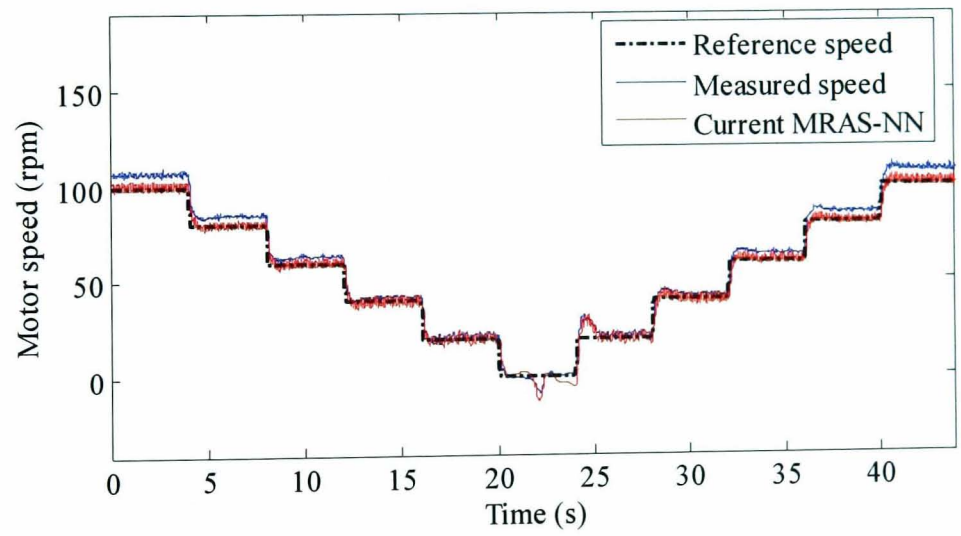

(b)

Fig. 7.19 Sensorless performance for test 1, no load (a) Stator current MRAS-CM (b) Stator current MRAS-NN

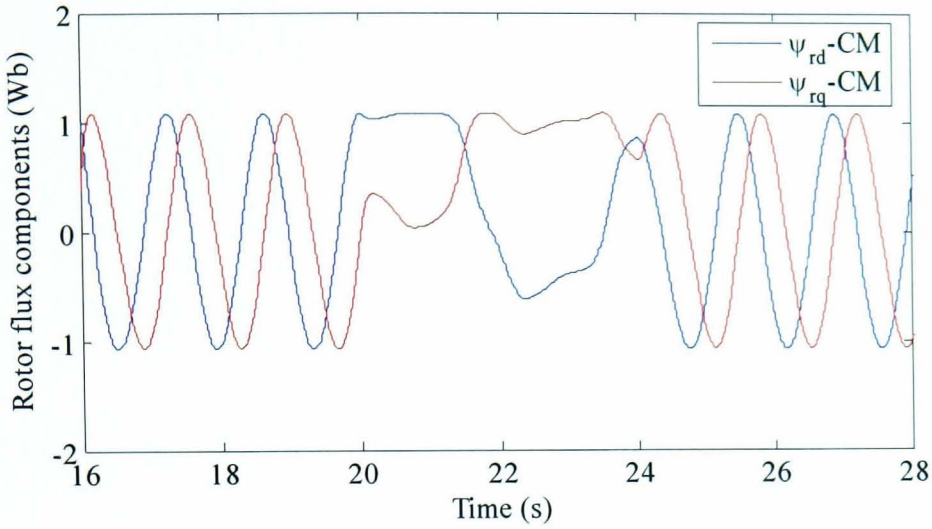
Rotor flux components (Wb)
Time (s)
ψrd-CM
ψrq-CM

(a)

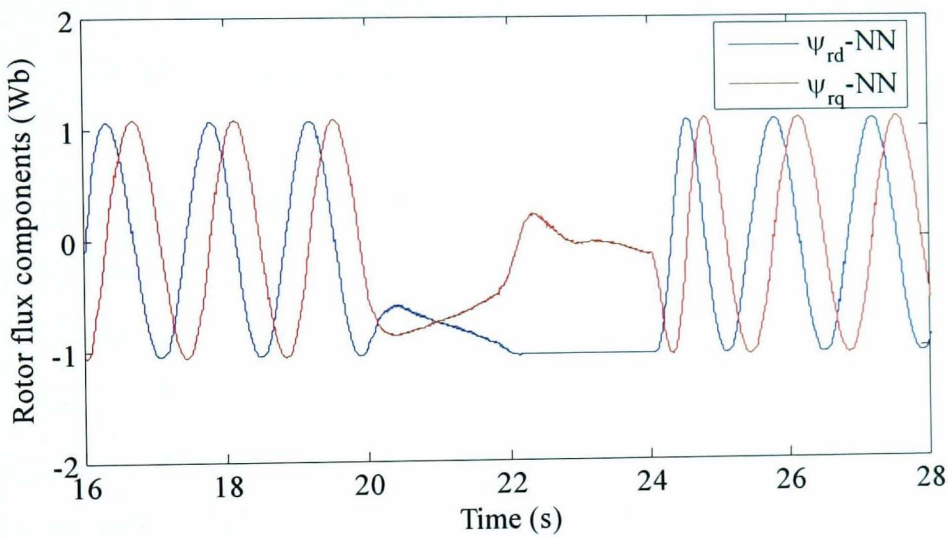
Rotor flux components (Wb)
Time (s)
ψrd-NN
ψrq-NN

(b)

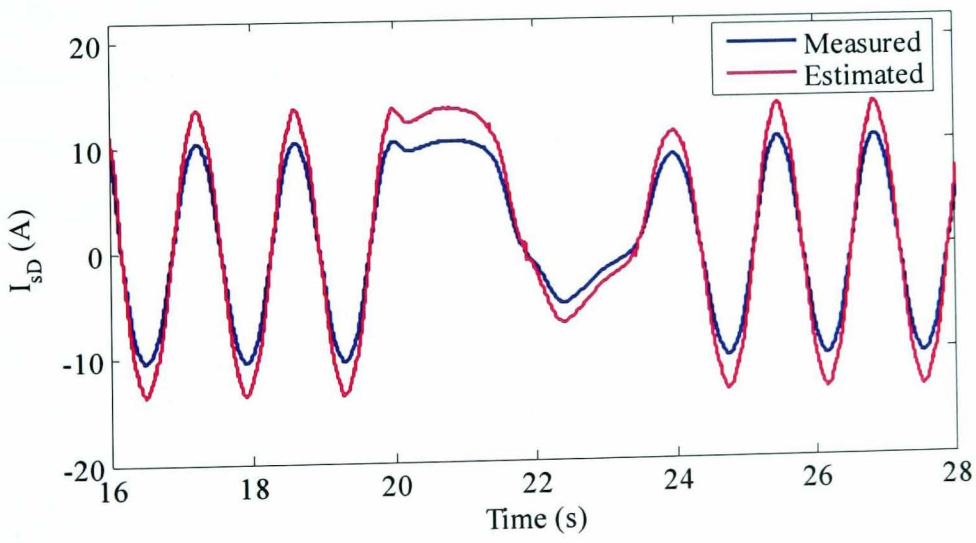
I_{sD} (A)
Time (s)
Measured
Estimated

(c)

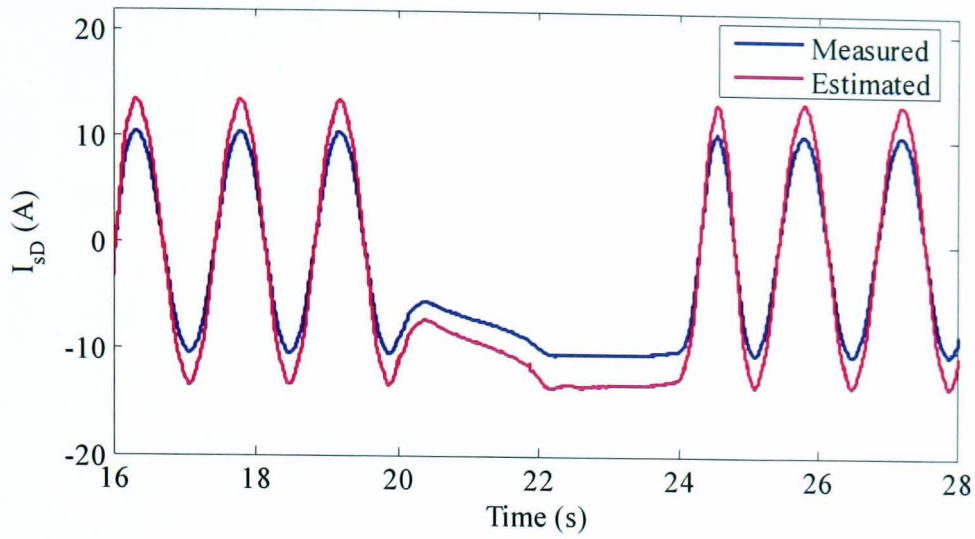

(d)

Fig. 7.20 Performance around and at zero speed at no load. Rotor flux estimation (a) CM (b) NN. Stator current estimation (c) CM-based scheme (d) NN-based scheme

Test 2: Stair case speed transients from 100rpm to 0rpm to -100 rpm:

To examine the sensorless performance of the stator current-based schemes at regeneration, this test is performed at 12.5% load. The performance of CM and NN based schemes is shown in Fig. 7.21. Stator current MRAS-CM scheme shows instability in the regenerating mode of operation. On the other hand, stator current MRAS-NN scheme shows stable operation as well as better speed response compared to that of the conventional rotor flux MRAS scheme shown in Fig. 6.22(a). Stable rotor flux estimation is obtained from NN at regeneration compared to that of the CM as shown in Fig. 7.22. However, the performance of the NN-based rotor flux MRAS scheme shown in Fig. 6.22 (b) is the most satisfactory among the different schemes with less steady state error in the whole speed region.

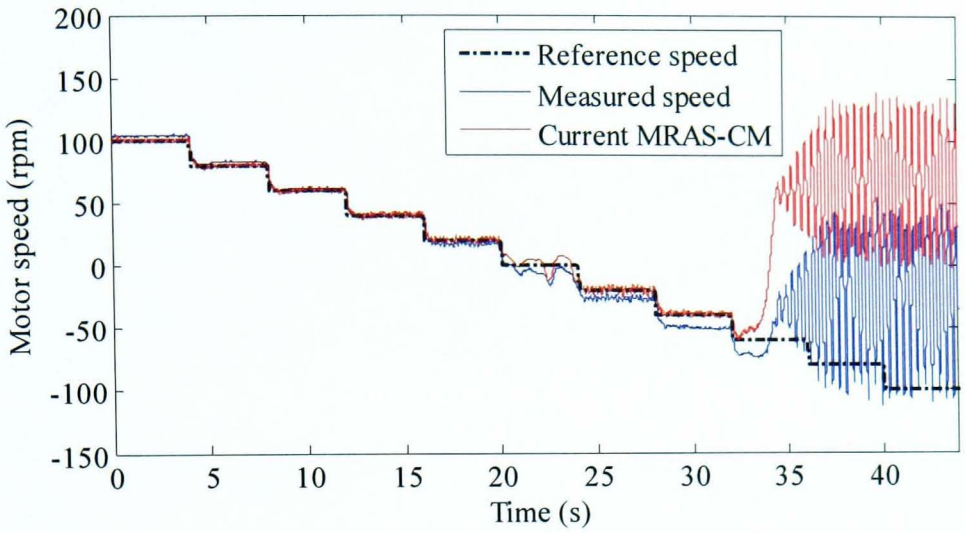

(a)

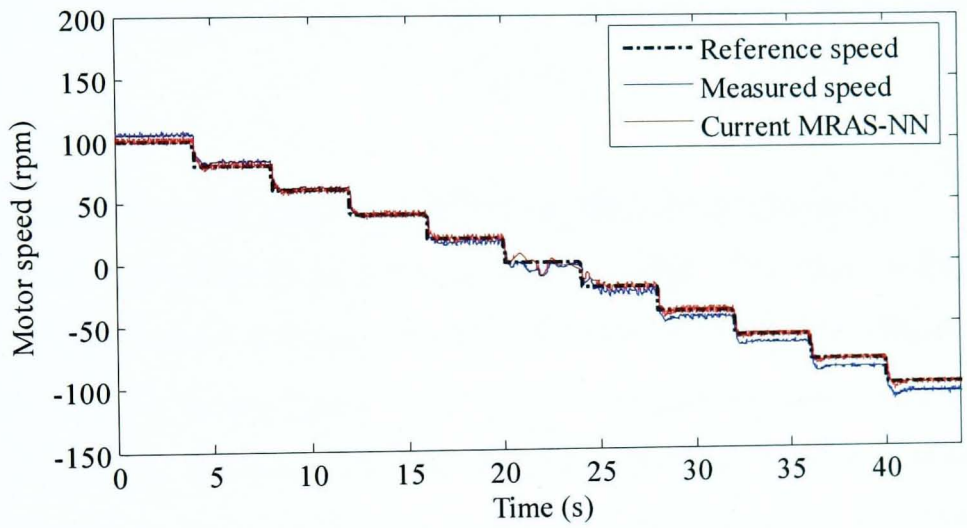

(b)

Fig. 7.21 Sensorless performance for test 2, 12.5% load. Speed response: (a) Stator current MRAS-CM (b) Stator current MRAS-NN

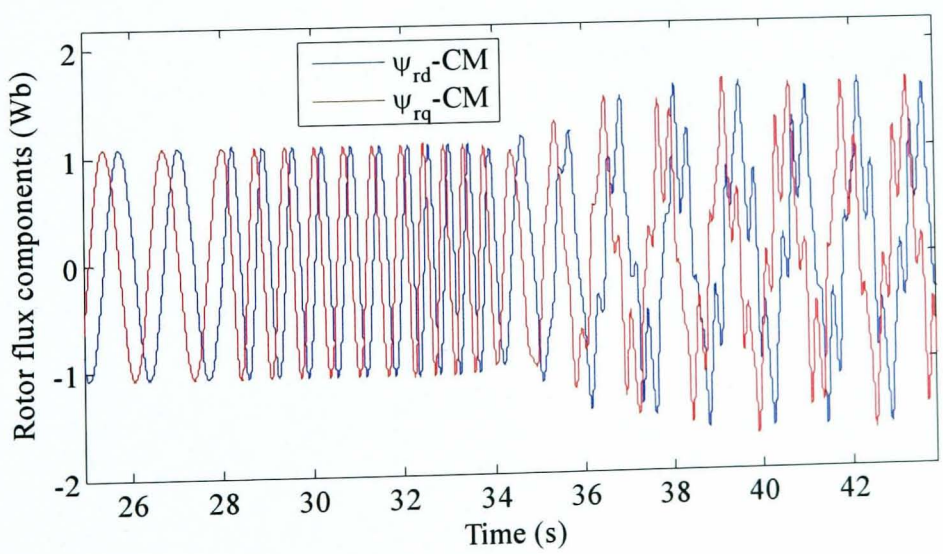

(a)

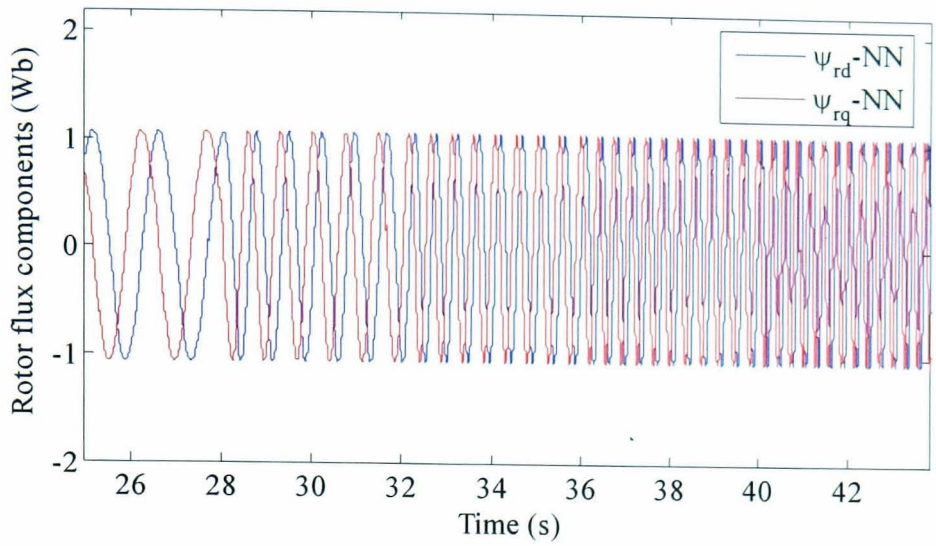

(b)

Fig. 7.22 Sensorless rotor flux estimation at regeneration for test 2, 12.5% load (a) CM (b) NN

Test 3: Take off from zero speed to 100 rpm after 30 sec at zero:

The results of this test at no load are shown in Fig. 7.23. Both schemes show better zero speed performance compared to the conventional rotor flux MRAS scheme. Stator current MRAS-NN shows better zero speed performance compared to stator current MRAS-CM scheme. However, in contrast to the NN-based rotor flux MRAS scheme, the stator current-based scheme can not completely hold zero speed at no load. This can be explained based on the fact that the rotor speed information in the stator current signal is lost at zero speed. Both schemes succeed in taking off to 100 rpm after 30s at zero speed.

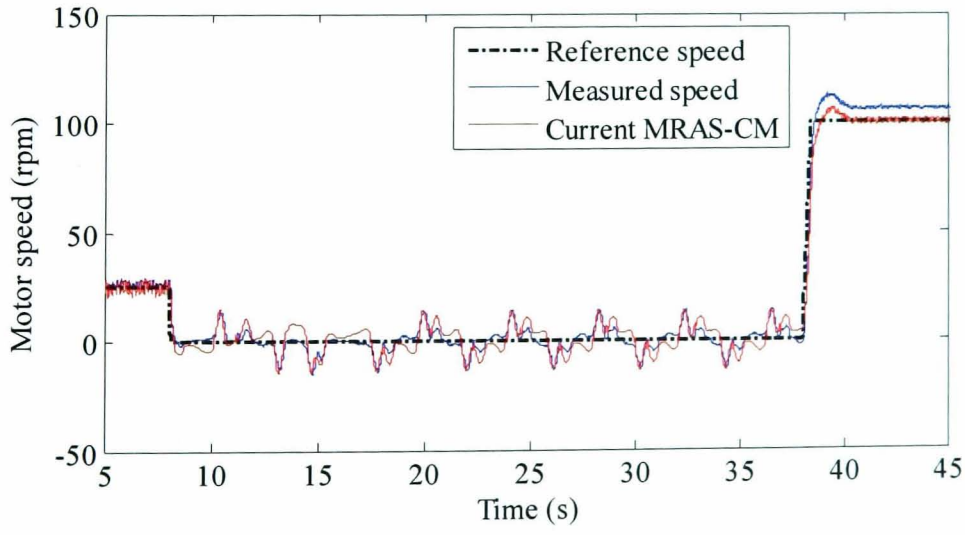

(a)

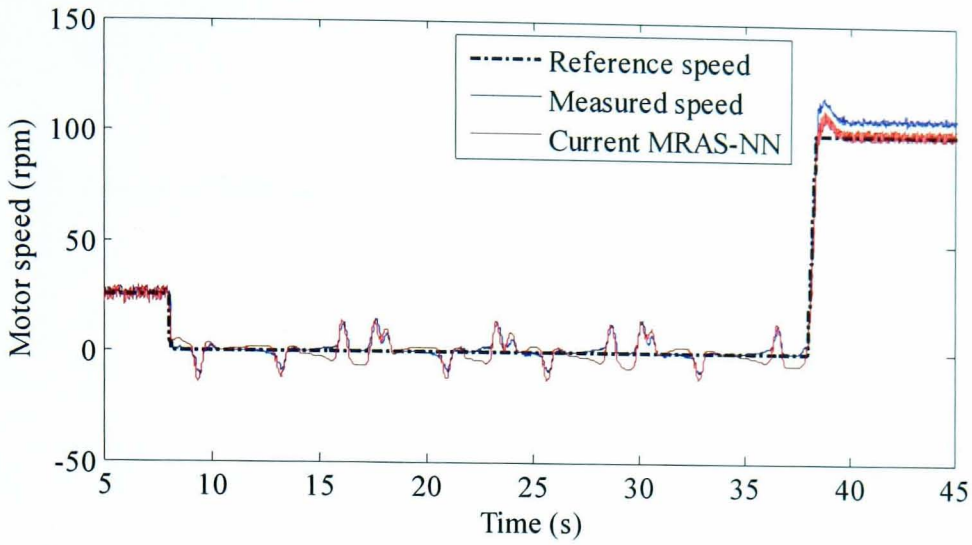

(b)

Fig. 7.23 Sensorless performance for test 3, no load (a) Stator current MRAS-CM (b) Stator current MRAS-NN

Test 4: Speed step down from 20 rpm to 0 rpm in three steps each of 10 rpm:

The results of this test at 10% load are shown in Fig. 7.24 (a)-(b) where stator current-based MRAS schemes show superior performance compared to that of the conventional rotor flux MRAS shown in Fig. 6.25 (a). Better zero speed performance is obtained from the stator current MRAS-NN scheme compared to the CM-based scheme. Rotor flux estimation performance of CM and NN observers is shown in Fig. 7.24 (c)-(d).

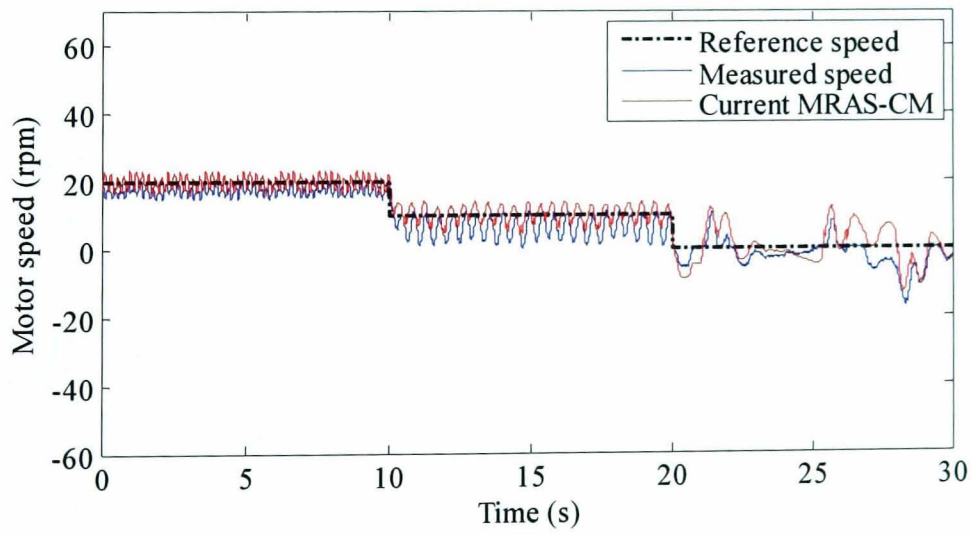

(a)

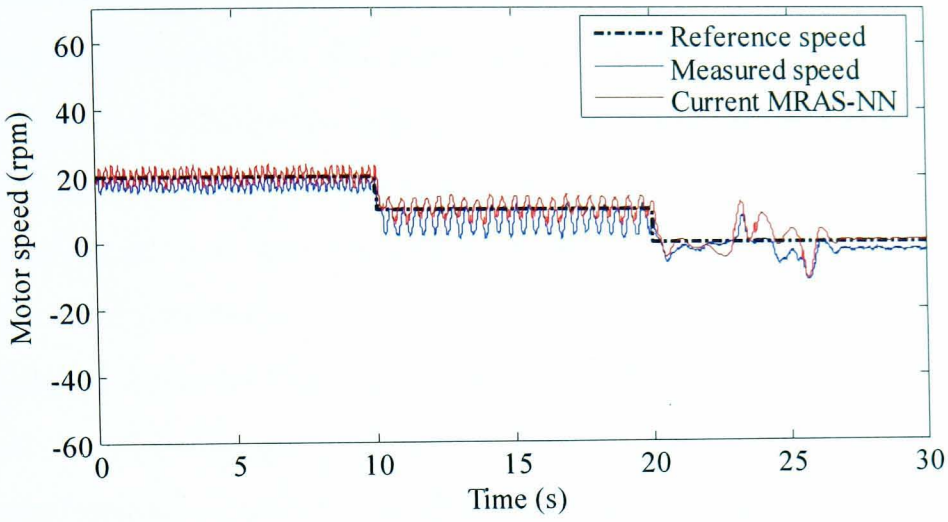

(b)

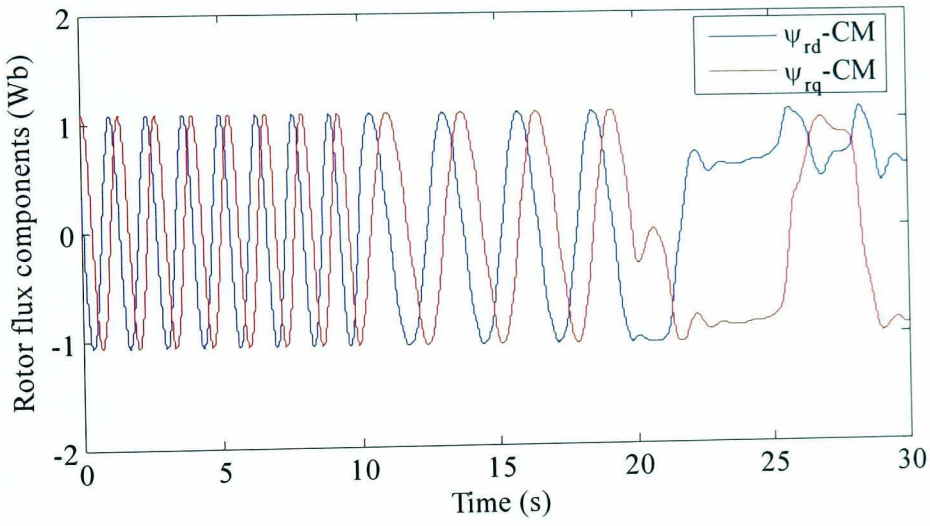

(c)

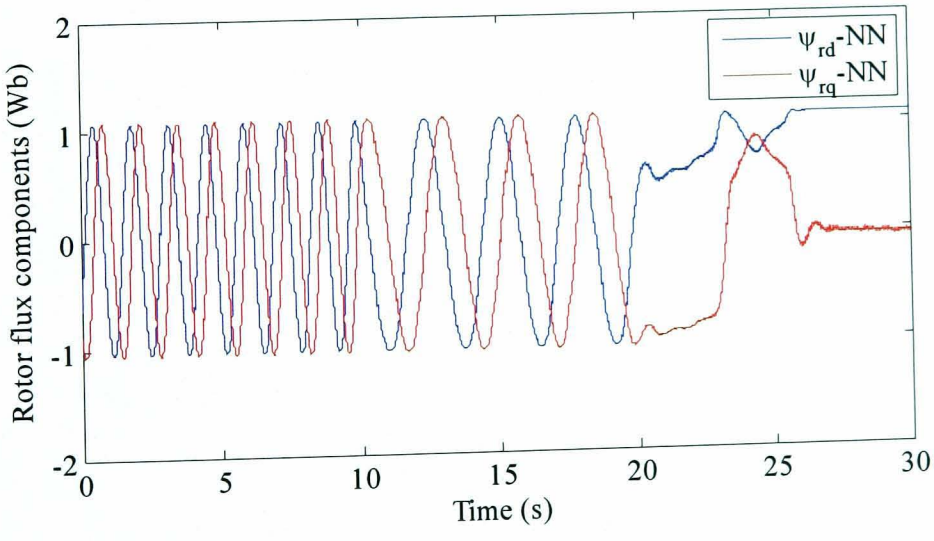

(d)

Fig. 7.24 Sensorless performance for test 4, 10% load. Speed (a) Stator current MRAS-CM (b) Stator current MRAS-NN. Rotor flux (c) CM (d) NN

Test 5: Sensorless load torque disturbance rejection:

Sensorless performance of the stator current-based schemes for 20% load torque disturbance rejection at 50 rpm is shown in Fig. 7.25 with better performance compared to that of the conventional rotor flux MRAS shown in Fig. 6.27 (a). To examine the sensorless performance in regeneration, both stator current-based MRAS schemes are subjected to a 20% load torque application at -50 rpm. Results shown in Fig. 7.26 reveal that the instability obtained from the stator current MRAS-CM in the regenerating mode is completely removed by using the NN flux observer. Fig. 7.27 shows the rotor flux estimation performance of the CM and NN observers at regeneration.

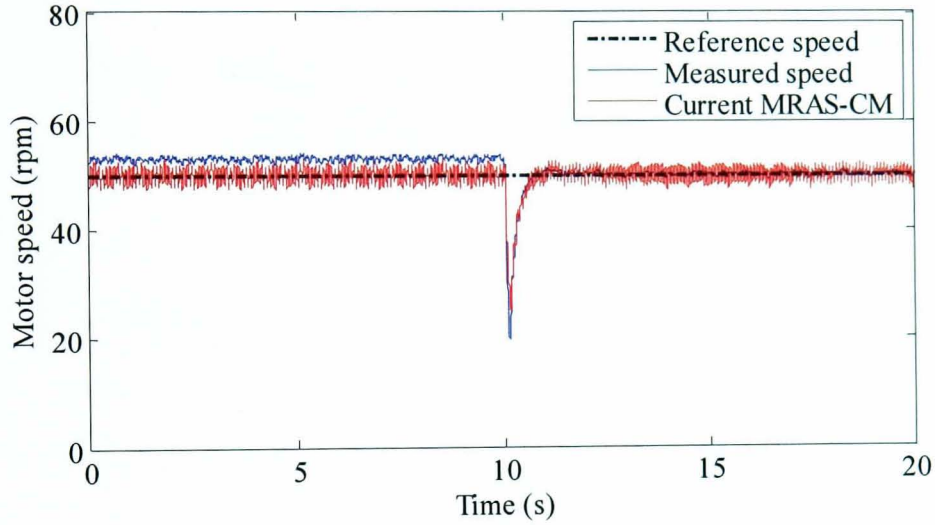

(a)

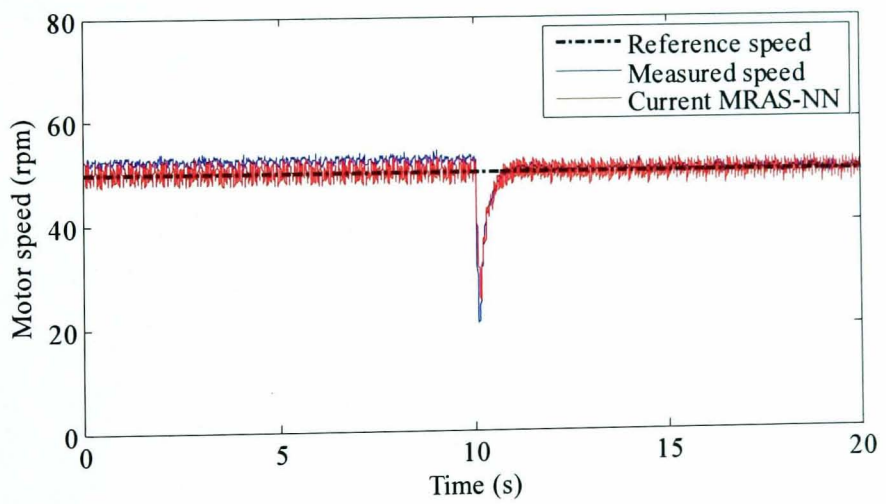

(b)

Fig. 7.25 Sensorless performance for test 5, 20% load at 50rpm (a) Stator current MRAS-CM (b) Stator current MRAS-NN

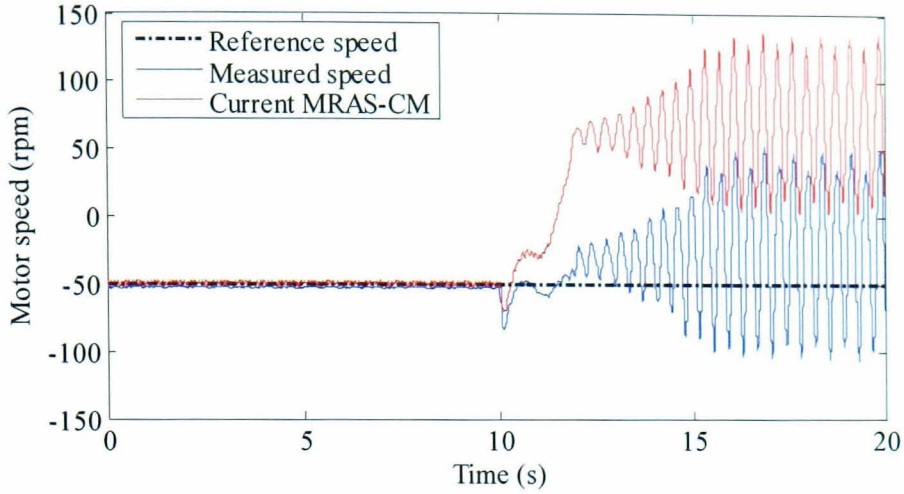

(a)

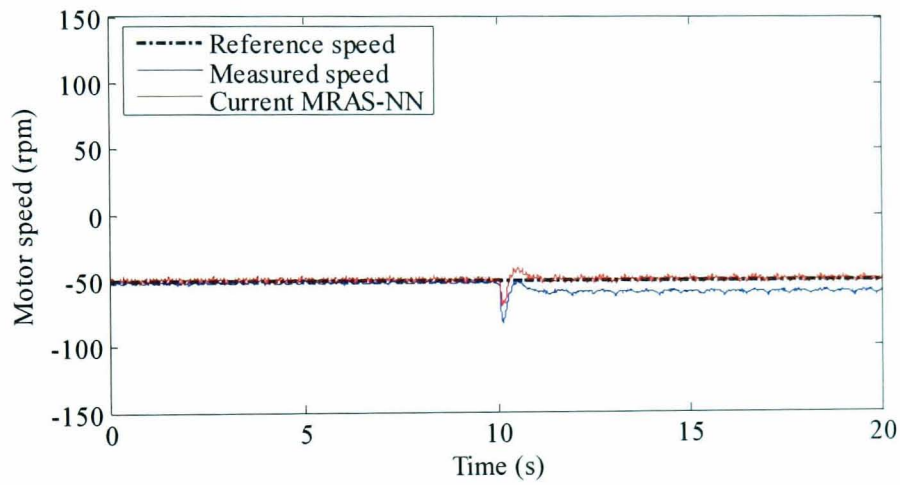

(b)

Fig. 7.26 Sensorless performance for test 5, 20% load at -50rpm (a) Stator current MRAS-CM (b) Stator current MRAS-NN

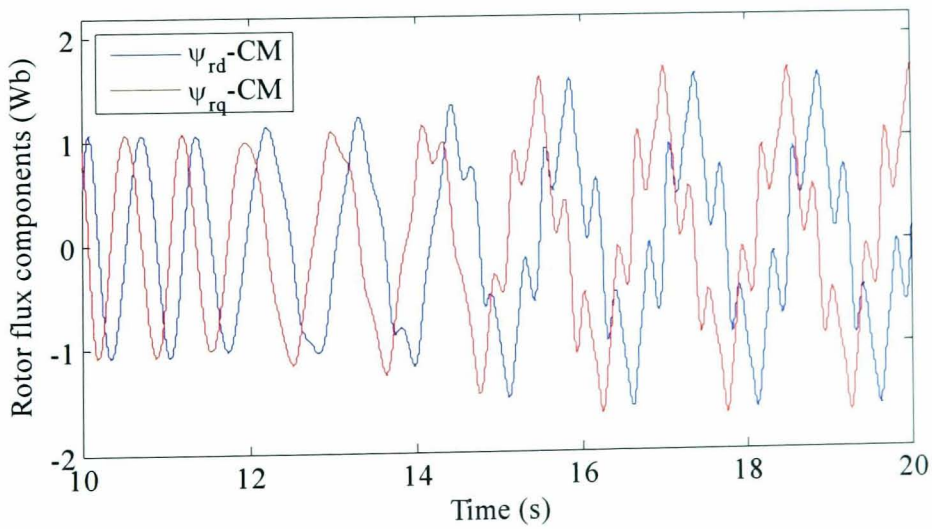

(a)

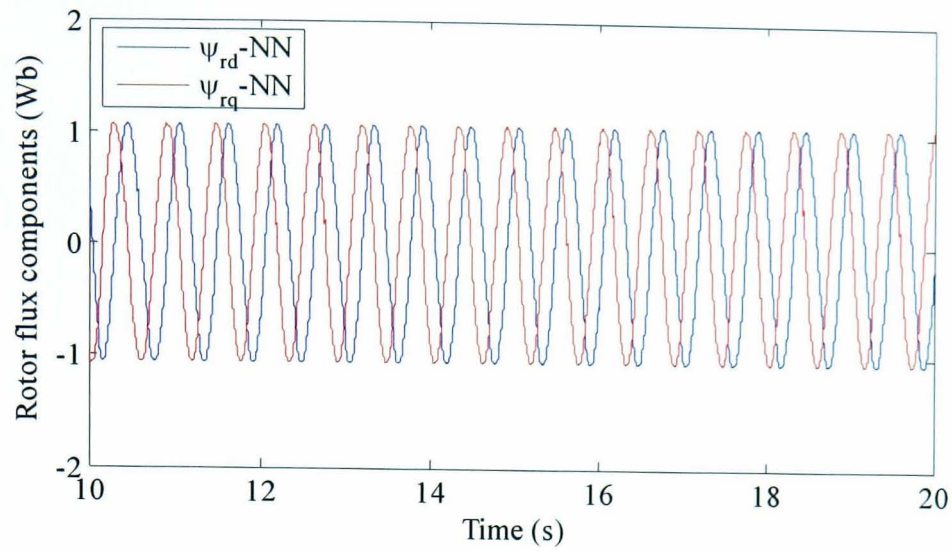

(b)

Fig. 7.27 Rotor flux estimation performance at regeneration (a) CM (b) NN

Test 6: Sensorless speed reversal at load:

Results for a sensorless ±25 rpm speed reversal demand at 10% load are shown in Fig. 7.28. Stator current MRAS observers show better performance compared to that of the conventional rotor flux MRAS shown in Fig. 6.29 (a).

When the test is performed at 25% load, unstable performance is obtained from the CM-based scheme compared to a stable performance for the NN-based scheme as shown in Fig. 7.29. CM and NN flux estimation performance is shown in Fig. 7.30. Moreover, stator current MRAS-NN shows better performance compared to that obtained from the conventional rotor flux MRAS shown in Fig. 6.30 (a). However, this performance for regeneration is inferior to that of the NN-based rotor flux MRAS shown in Fig. 6.30 (b).

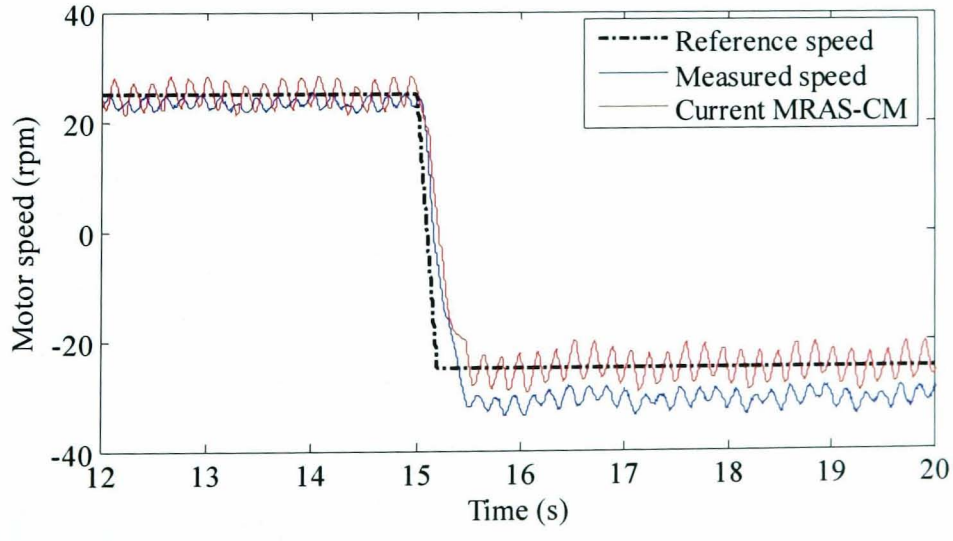

(a)

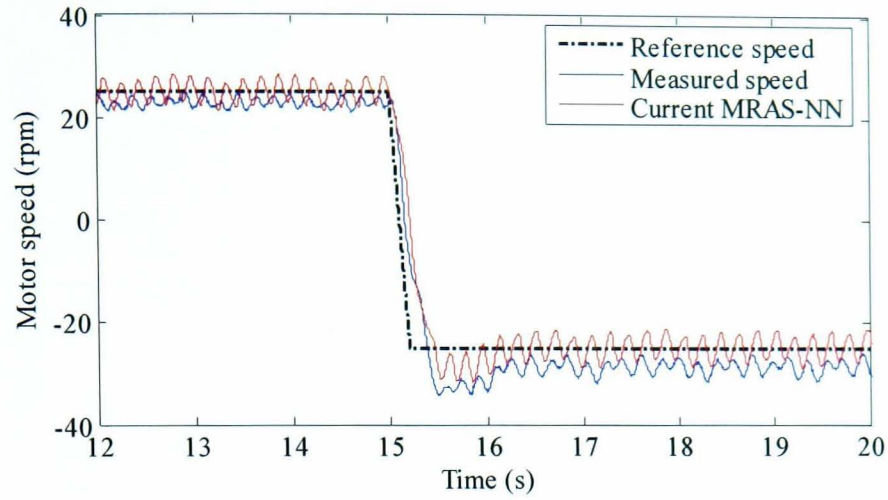

(b)

Fig. 7.28 Sensorless performance for test 6, ±25 rpm reversal, 10% load (a) Stator current MRAS-CM (b) Stator current MRAS-NN

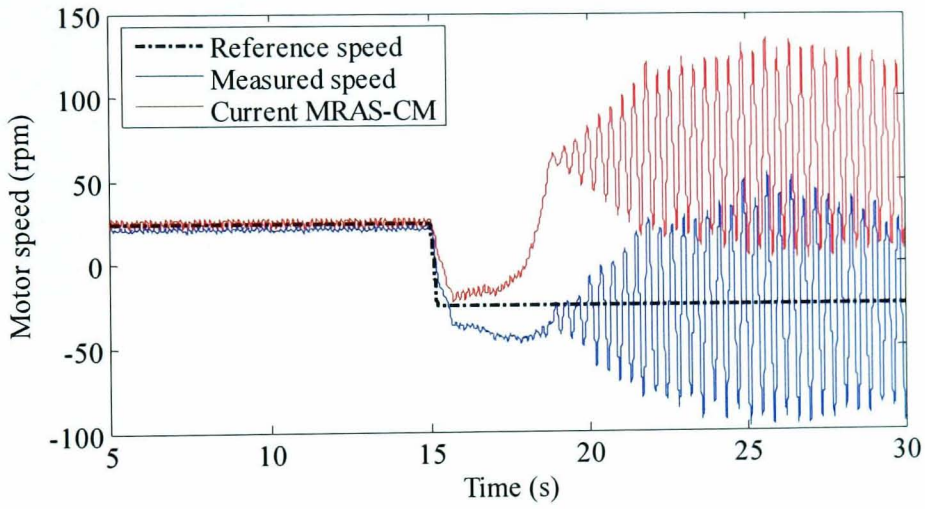

(a)

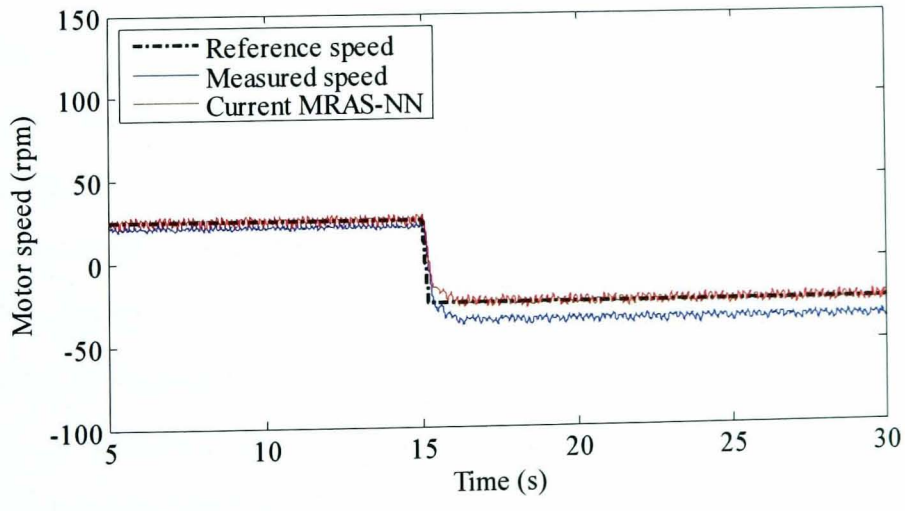

(b)

Fig. 7.29 Sensorless performance for test 6, ±25 rpm reversal, 25% load (a) Stator current MRAS-CM (b) Stator current MRAS-NN

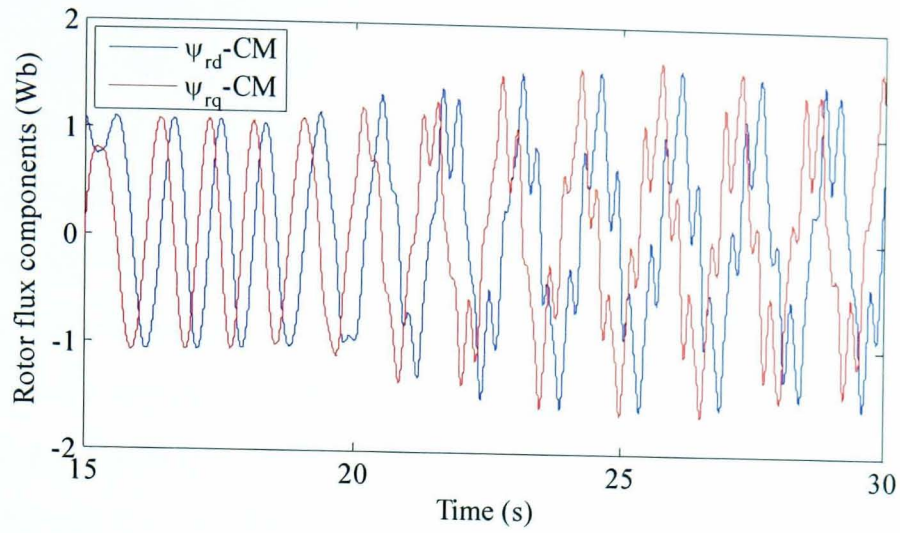

(a)

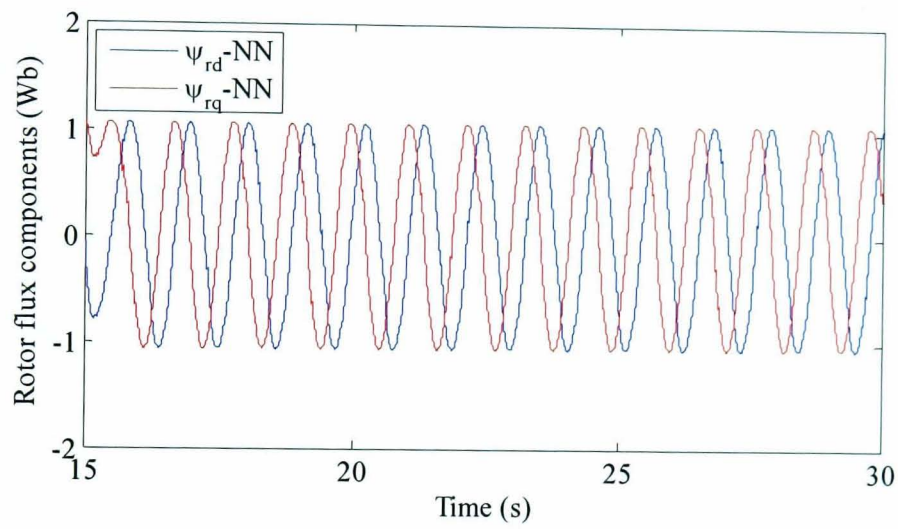

(b)

Fig. 7.30 Rotor flux estimation performance at regeneration (a) CM (b) NN

7.6 Conclusion

This chapter has presented a novel NN-based stator current MRAS observer for speed sensorless IM drives. A stator current observer is formulated based on machine equations and is represented by a two layer linear NN. Rotor flux estimation is required for the MRAS speed observer. Using a VM for rotor flux estimation causes problems at low speed due to stator resistance sensitivity and the pure integration for flux. A CM can be used instead to estimate the rotor flux from the measured stator currents and the estimated speed, which shows less sensitivity to stator resistance variation. However, the stator current MRAS scheme using the CM flux observer shows instability in the regenerating mode of operation. A multilayer feedforward NN is proposed to overcome

this problem for rotor flux estimation from present and past samples of the stator voltage and current. Using the NN flux observer gives less sensitivity to stator resistance variations compared to the VM and since the flux estimation is independent of the rotor speed; stable operation has been obtained for regeneration.

The stator current MRAS schemes have been validated by simulations and experimentally in open loop and sensorless modes of operation. Results show the improvement in the sensorless performance using the stator current MRAS-NN scheme. However, the performance of the NN-based rotor flux MRAS scheme described in chapter 6 is still superior to that obtained from the stator current MRAS-NN, especially at zero speed.

CHAPTER 8

CONCLUSIONS AND FUTURE WORK

8.1 Introduction

The research developed in this thesis has focused on the application of AI techniques for speed sensorless vector control IM drives. The main objective was to investigate different strategies using AI to improve the performance of sensorless drives which are based on MRAS observers. Particular focus was given to the critical low and zero speed regions of operation. Various AI-based schemes have been developed and tested as suitable means of producing a satisfactory performance at and around zero speed. The aim of this chapter is to summarise the investigations and findings of this research, present conclusions and recommend various possibilities for future studies.

8.2 Discussion and Conclusions

As described in chapter 1, the presence of a speed sensor in an IM drive may affect the reliability and the cost of the drive system. Therefore sensorless control methods are shown to offer great advantages. These techniques can be generally grouped into fundamental excitation and signal injection methods. Attention was given to fundamental model-based strategies where stator voltages and currents are used to estimate the flux linkage and the motor speed. However, these techniques usually fail at or around zero

speed. AI has been presented as a powerful strategy that can overcome classical control problems. These techniques consist mainly of neural networks, fuzzy logic and genetic algorithms.

Particular attention was given to MRAS speed observers due to their simple structure and low computational effort. The main problems associated with such observers are parameter sensitivity, pure integration problems and inverter nonlinearity. Various methods presented in the literature to solve these problems have been reviewed in chapter 2. A survey of different applications of AI techniques in sensorless IM drives was also discussed.

Mathematical modelling for the machine, controller and observer was presented in chapter 3. A state space representation of the IM in the stator reference frame, with the stator currents and the rotor flux linkages components as state variables, has been developed based on the *d-q* axes theory. Principles of vector control were also illustrated based on the motor model expressed in the synchronous reference frame. The machine dynamic equations have been used to formulate the conventional rotor flux-based MRAS observer originally developed by Schauder [53]. This scheme is the most common MRAS strategy extensively employed for sensorless control. An appropriate adaptation mechanism for rotor speed estimation was derived based on Popov's hyperstability theory. This derivation reveals that a PI controller can be used to generate an estimate of the rotor speed by minimizing a speed tuning signal. The experimental platform employed to test the proposed schemes in real time was described in chapter 4. This system is based on a 7.5 kW induction machine, a DC load machine and a dSPACE DS1103 controller board.

A classical fixed-gain PI controller is conventionally used in rotor flux based-MRAS speed observers. Not much concern has been given to study alternative mechanisms for speed tuning signal minimization. Therefore the purpose of chapter 5 was to fill this gap by proposing two novel adaptation mechanisms based on SM and FL strategies. For the SM scheme, a new speed estimation adaptation law was derived based on Lyapunov theory to ensure estimation stability and fast error dynamics. On the other hand, a Mamdani PI-Type FLC was proposed for speed tuning signal minimization to produce an estimate of the rotor speed. Hence two new rotor flux-based MRAS observers were described, MRAS-SM and MRAS-FL schemes.

Simulations were carried out to test the proposed schemes using a standard indirect vector control IM drive. An ideal environment was assumed during simulation stage which included an idealised inverter and PWM and ideal integration for flux. Simulation results in open and closed loop showed that better transient performance was obtained from both novel schemes compared to the conventional PI controller. The SM adaptation mechanism showed the smallest speed tuning signal. However, its performance is characterised by large chattering due to the need for a sign function in the adaptation law. Faster response was obtained from the FL scheme compared to the PI controller due to an optimal speed tuning signal during transients.

Experimental tests were conducted to examine the new adaptation mechanisms in real time with particular interest devoted to low speed operation. Flux pure integration problems were avoided by using a HPF at the outputs of the VM. Compensated reference voltages were used to avoid the need to measure the real stator voltages. PI and FL gain tuning was performed in such a way as to obtain similar steady state performance. A LPF was used at the output of the MRAS-SM to reduce the chattering in the estimated speed. Parameters of the SM scheme were obtained by trial and error to ensure optimal performance. Results obtained showed the improvement in the transient performance of the rotor flux-based MRAS observer at low speed. Both new schemes demonstrated better transient performance as well as better load torque disturbance rejection in both open loop and closed loop sensorless modes of operation. The need for a LPF in the MRAS-SM introduced delay in the estimated speed allowing better performance for MRAS-FL. However, the application of the novel schemes did not produce any modifications in the steady state performance of the estimator because a conventional VM is used. Improving the MRAS estimator steady state performance was raised and treated in chapter 6 using NN.

The main problems associated with the conventional VM are stator resistance sensitivity, the stator voltage acquisition problem, and flux open loop integration which may cause dc drift and initial condition problems. Using a conventional VM in rotor flux-based MRAS limits the performance of the observer at low and zero speed. NNs have been well-established as universal nonlinear function approximators. Multilayer feedforward NNs have shown a great capability to model complex nonlinear dynamic systems. Therefore a multilayer feedforward NN has been proposed for rotor flux

estimation from present and past samples of terminal voltages and currents. Training data for the NN was obtained from experimental measurements to take account of all the drive nonlinearities. Outputs from the CM, instead of search coils, were used as target values for the NN to provide harmonic-free signals and accurate outputs at low speed. A NN suitable for general purpose IM drives applications was developed. In some types of such applications, such as fans and centrifugal pumps, rated load is not required at low speed. The training of the NN was performed off-line with Matlab-Simulink using the Levenberg-Marquardt training algorithm. Extensive simulation and experimental tests have been carried out to test the performance of the NN observer. Compared to a VM flux observer, the NN avoids using either a pure integrator or a low pass filter which eliminates integrator drift and initial condition problems giving less sensitivity to motor parameter variations. Therefore a great improvement in the flux estimation performance at low speed was achieved using a NN.

The off-line trained NN was used as a reference model, instead of the VM, for the rotor flux MRAS observer to form a new NN MRAS scheme. This represents a completely different way of applying NNs to MRAS schemes. Numerous experimental tests were carried out to investigate the performance of the proposed scheme in both open loop and sensorless modes of operation. Results obtained from open loop tests showed the significant improvement in the transient and the steady state performance of the MRAS estimator at low speed. Another NN suitable for low speed rated load applications, such as elevators and conveyors, was also developed and tested in open loop. Results showed the improved low speed performance obtained from the NN MRAS scheme up to rated load. Sensorless performance of the NN MRAS scheme developed for general purpose applications was examined based on a systematic set of benchmark experimental tests. A detailed comparison between the performance of the proposed NN MRAS and the conventional rotor flux MRAS schemes has been conducted using an indirect vector control drive. Tests were carried out at different operating conditions at low speed including speed change, load disturbance rejection and speed reversal with load. One of the most substantial achievements of this study was that zero speed no-load sensorless operation has been successfully accomplished. Moreover, speed oscillations and instability at very low and zero speed, with and without load, obtained from the

conventional MRAS scheme have been completely removed using NN MRAS. This great improvement in the performance was achieved without using any voltage sensors.

The application of the proposed NN MRAS scheme for both integrated drive and mass-production purposes was also discussed. The scheme can be applied to integrated drive applications where the machine and inverter form one unit. In this case the NN observer is trained on the actual machine-inverter combination and it should be able to handle manufacturer's tolerance within the production line.

However, for a mass-production environment the application of this scheme is more difficult since a training phase is needed during commissioning for each inverter-machine combination. A possible solution to this problem is to use a number of pre-trained networks where the suitable one can be selected according to the machine rating.

Finally, a MRAS speed observer based on stator current was presented in chapter 7. This scheme avoids problems associated with the VM by using measured stator currents as reference model for the MRAS estimator. This makes the reference model, which is represented by the machine itself, free of pure integration problems and insensitive to motor parameter variations. A two layer linear NN stator current observer was derived and used as an adaptive model for the MRAS observer where the rotor speed is expressed as one of its weights. At each sampling period the error between the measured and estimated currents is minimized using backpropagation algorithm to update the value of the rotor speed online.

The NN-based stator current observer requires rotor flux estimation. The use of a VM causes problems at low speed due to stator resistance sensitivity and the need for pure integration for flux. A CM can be also used for rotor flux estimation from measured stator currents and estimated speed. However, the MRAS scheme employing the CM for flux estimation showed instability in the regenerating mode of operation. To overcome these problems, the multilayer feedforward NN developed in chapter 6 was proposed for flux estimation. Using the NN flux observer gives less sensitivity to stator resistance variation compared to the VM and since the flux estimation is independent of the rotor speed, stable operation was obtained for regeneration.

Simulations were carried out to test the stator current MRAS estimator performance for sensitivity to stator resistance variation and for stability at regeneration. Speed estimation performance with a 25% increase in the motor stator resistance was

investigated for the scheme using VM, CM and NN flux observers. All three schemes were affected by this variation due to the presence of R_s in the stator current observer equations. However, the MRAS scheme employing VM was found to be the most affected with oscillations in the estimated speed. This is due to the existence of R_s in the flux observer equation. Using the NN flux observer showed less sensitivity to R_s variation compared to the VM and consequently better speed estimation performance was obtained. Operation with regeneration was investigated for the stator current MRAS estimator using a ±40 rpm speed reversal at 25% load at nominal machine parameters. Unstable performance for regeneration was obtained using the CM. This is due to the need for the estimated speed for flux estimation and hence any deterioration in the speed estimation is fed back to the flux observer causing instability. By contrast, using a NN flux observer gives stable operation since flux estimation is independent of the estimated speed.

Experimental tests were conducted to validate the proposed stator current MRAS scheme when compared to the conventional rotor flux-MRAS. The two structures of the new scheme have been compared: Current MRAS-CM using CM flux observer and Current MRAS-NN using NN rotor flux observer. Both stator current-based schemes showed better transient and steady state open loop speed estimation performance at low speed. This is mainly due to the use of an improved reference model free of pure integration and insensitive to parameter variation in addition to accurate flux estimation obtained from the CM and NN observers. Stability problems have been illustrated experimentally for the current MRAS-CM scheme in regeneration which were avoided using the NN for flux estimation.

Sensorless tests demonstrated the improvement in the low speed performance using stator current MRAS estimator compared to the conventional rotor flux scheme. Better zero speed operation was given but which is still not as good as that obtained from the NN-based rotor flux MRAS. The stator current-based schemes can not completely hold zero speed at no load. Current MRAS-NN demonstrated better zero speed performance compared to the current MRAS-CM due to better flux estimation obtained from the NN at zero speed. Instability in regeneration was demonstrated for sensorless operation using the current MRAS-CM. The NN flux observer showed stable estimation performance leading to stable operation at regeneration.

In conclusion, neural networks have shown great capabilities to significantly improve the performance of sensorless IM drives which are based on MRAS observers in the critical low and zero speed region. A multilayer feedforward NN has been developed for rotor flux estimation from present and past samples of the stator voltage and current. This NN was proposed as a reference model for rotor flux-based MRAS and for rotor flux estimation in a stator current-based MRAS. Both schemes have been experimentally implemented and tested in both open loop and sensorless modes of operation. Experimental tests have focused on the operation at low and zero speed which represent a challenging region of operation for sensorless drives. A considerable enhancement in the performance was demonstrated using the proposed NN-based schemes compared to the conventional rotor flux-MRAS. However, the performance of the NN-based rotor flux MRAS scheme described in chapter 6 was found to be superior to that obtained from the stator current MRAS-NN introduced in chapter 7.

8.3 Recommendations for Future Work

The work developed in this thesis has shown completely new applications of AI techniques applied to speed sensorless IM vector control drives. Different adaptation mechanisms have been proposed to replace the classical PI controller. The tuning of different parameters has been carried out online by trial and error. A systematic method could be considered for parameter tuning such as use of a GA or SA. Moreover, other optimization algorithms may be considered for minimizing the speed tuning signal.

One of the major contributions of this work was to improve the performance of the sensorless drive, which is based on MRAS observer, at very low and zero speed. This has been achieved by replacing the conventional VM with a multilayer NN. Computational burden required by NN compared to a simple mathematical equation of the VM may impose a drawback of the proposed strategy. Therefore, it will be interesting if an investigation is carried out to study other NN structures and topologies to replace the VM. Furthermore, other AI-based strategies that require less computational effort can be also investigated and compared with the NN developed in this work.

REFERENCES

[1] J. W. Finch and D. Giaouris, "Controlled AC Electrical Drives," *IEEE Transactions on Industrial Electronics*, vol. 55, no. 1, pp. 1-11, February 2008.

[2] P. Vas, *Sensorless Vector and Direct torque control.* New York: Oxford University Press, 1998.

[3] J. Holtz, "Sensorless control of induction motor drives," *Proc. of the IEEE*, vol. 90, no. 8, pp. 1359-1394, August 2002.

[4] J. R. Heredia, F. Perez Hidalgo, and J. L. Duran Paz, "Sensorless control of induction motors by artificial neural networks," *IEEE Transactions on Industrial Electronics*, vol. 48, no. 5, pp. 1038-1040, October 2001.

[5] J. Holtz and J. Quan, "Drift and parameter compensated flux estimator for persistent zero stator frequency operation of sensorless controlled induction motors," *IEEE Transactions on Industry Applications*, vol. 39, no. 4, pp. 1052-1060, July/August 2003.

[6] K. D. Hurst, T. G. Habetler, G. Griva, and F. Profumo, "Zero-speed tacholess IM torque control: simply a matter of stator voltage integration," *IEEE Transactions on Industry Applications*, vol. 34, no. 4, pp. 790-795, July/August 1998.

[7] M. Rashed and A. F. Stronach, "A stable back-EMF MRAS-based sensorless low speed induction motor drive insensitive to stator resistance variation," *IEE Proceedings Electric Power Applications*, vol. 151, no. 6, pp. 685-693, November 2004.

[8] H. Rehman, A. Derdiyok, M. K. Guven, and L. Xu, "A new current model flux observer for wide speed range sensorless control of an induction machine," *IEEE Transactions on Power Electronics*, vol. 17, no. 6, pp. 1041-1048, November 2002.

[9] J. Holtz, "Sensorless Control of Induction Machines-With or Without Signal Injection?," *IEEE Transactions on Industrial Electronics*, vol. 53, no. 1, pp. 7-30, February 2006.

[10] P. Vas, *Artificial-Intelligence-Based Electrical Machines and Drives-Application of Fuzzy, Neural, Fuzzy-Neural and Genetic Algorithm Based Techniques.* New York: Oxford University Press, 1999.

[11] B. K. Bose, "Neural Network Applications in Power Electronics and Motor Drives—An Introduction and Perspective," *IEEE Transactions on Industrial Electronics*, vol. 54, no. 1, pp. 14-33, February 2007.

[12] T. Dillon and D. Niebur, *Neural Networks Applications in Power Systems.* London: CRL Publishing, 1996.

[13] K. Warwick, A. Ekwue, and R. Aggarwal, *Artificial intelligence techniques in power systems.* London: Institution of Electrical Engineers, 1997.

[14] M. Cirstea, A. Dinu, J. Khor, and M. McCormick, *Neural and Fuzzy Logic Control of Drives and Power Systems.* Oxford, Boston: Newnes, 2002.

[15] S. M. Gadoue, D. Giaouris, and J. W. Finch, "Tuning of PI speed controller in DTC of induction motor based on genetic algorithms and fuzzy logic schemes," in *Proc. 5th International Conference on Technology and Automation*, Thessaloniki, Greece, 2005, pp. 85-90.

[16] S. M. Gadoue, D. Giaouris, and J. W. Finch, "Genetic Algorithm Optimized PI and Fuzzy Sliding Mode Speed Control for DTC Drives," in *Proc. World Congress on Engineering*, London, UK, 2007, pp. 475-480.

[17] S. M. Gadoue, D. Giaouris, and J. W. Finch, "Artificial intelligence-based speed control of DTC induction motor drives-A comparative study," *Electric Power Systems Research*, vol. 79, no. 1, pp. 210-219, January 2009.

[18] M. Wlas, Z. Krzeminski, and H. A. Toliyat, "Neural-Network-Based Parameter Estimations of Induction Motors," *IEEE Transactions on Industrial Electronics*, vol. 55, no. 4, pp. 1783-1794, April 2008.

[19] M. N. Uddin and H. Wen, "Development of a Self-Tuned Neuro-Fuzzy Controller for Induction Motor Drives," *IEEE Transactions on Industry Applications*, vol. 43, no. 4, pp. 1108-1116, July/August 2007.

[20] Z. Ibrahim and E. Levi, "A comparative analysis of fuzzy logic and PI speed control in high-performance AC drives using experimental approach," *IEEE Transactions on Industry Applications*, vol. 38, no. 5, pp. 1210-1218, September/October 2002.

[21] M. N. Uddin, T. S. Radwan, and M. A. Rahman, "Performances of fuzzy-logic-based indirect vector control for induction motor drive," *IEEE Transactions on Industry Applications*, vol. 38, no. 5, pp. 1219-1225, September/October 2002.

[22] W. Oh, Y. Kim, C. Kim, T. Kwon, and H. Kim, "Speed control of induction motor using genetic algorithm based fuzzy controller," in *Proc. The 25th Annual Conference of the IEEE Industrial Electronics Society*, 1999, pp. 625-629 vol.2.

[23] F. Lin, H. Shieh, K. Shyu, and P. Huang, "On-line gain-tuning IP controller using real-coded genetic algorithm," *Electric Power Systems Research*, vol. 72, no. 2, pp. 157-169, 2004.

[24] O. Barambones, A. Garrido, and F. Maseda, "Integral sliding-mode controller for induction motor based on field-oriented control theory," *IET Proceedings Control Theory & Applications*, vol. 1, no. 3, pp. 786-794, 2007.

[25] F.-J. Lin, W.-D. Chou, and P.-K. Huang, "Adaptive sliding-mode controller based on real-time genetic algorithm for induction motor servo drive," *IEE Proceedings Electric Power Applications*, vol. 150, no. 1, pp. 1-13, January 2003.

[26] M. G. Simoes and B. K. Bose, "Neural network based estimation of feedback signals for a vector controlled induction motor drive," *IEEE Transactions on Industry Applications*, vol. 31, no. 3, pp. 620-629, May/June 1995.

[27] A. Ba-Razzouk, A. Cheriti, G. Olivier, and P. Sicard, "Field oriented control of Induction Motors using Neural Network decouplers," *IEEE Transactions on Power Electronics*, vol. 12, no. 4, pp. 752-763, July 1997.

[28] L. Ben-Brahim, S. Tadakuma, and A. Akdag, "Speed control of induction motor without rotational transducers," *IEEE Transactions on Industry Applications*, vol. 35, no. 4, pp. 844-850, July/August 1999.

[29] Y. Yusof and A. H. Yatim, "Simulation and modelling of stator flux estimator for induction motor using artificial neural network technique," in *Proc. National Power and Energy Conference*, 2003, pp. 11-15.

[30] B. Karanayil, M. Rahman, and C. Grantham, "Stator and rotor resistance observers for induction motor drive using fuzzy logic and artificial neural networks," *IEEE Transactions on Energy Conversion*, vol. 20, no. 4, pp. 771-780, December 2005.

[31] F. Filippetti, G. Franceschini, C. Tassoni, and P. Vas, "Recent developments of induction motor drives fault diagnosis using AI techniques," *IEEE Transactions on Industrial Electronics*, vol. 47, no. 5, pp. 994-1004, October 2000.

[32] D. Souza, W. Filho, and G. Sousa, "Adaptive Fuzzy Controller for Efficiency Optimization of Induction Motors," *IEEE Transactions on Industrial Electronics*, vol. 54, no. 4, pp. 2157-2164, August 2007.

[33] G. F. Uler, O. A. Mohammed, and C. Koh, "Design optimization of electrical machines using genetic algorithms," *IEEE Transactions on Magnetics*, vol. 31, no. 3, pp. 2008-2011, May 1995.

[34] B. Mirzaeian, M. Moallem, V. Tahani, and C. Lucas, "Multiobjective optimization method based on a genetic algorithm for switched reluctance motor design," *IEEE Transactions on Magnetics*, vol. 38, no. 3, pp. 1524-1527, May 2002.

[35] S. M. Gadoue, D. Giaouris, and J. W. Finch, "Performance Evaluation of a Sensorless Induction Motor Drive at Very Low and Zero Speed Using a MRAS Speed Observer," in *Proc. The third IEEE International Conference on Industrial and Information Systems*, India, 2008.

[36] S. M. Gadoue, D. Giaouris, and J. W. Finch, "A new fuzzy logic based adaptation mechanism for MRAS sensorless vector control induction motor drives," in *Proc. 4th IET Conference on Power Electronics, Machines and Drives*, York, UK, 2008, pp. 179-183.

[37] S. M. Gadoue, D. Giaouris, and J. W. Finch, "Sensorless Control of Induction Motor Drives at Very Low and Zero Speed Using Neural Network Flux Observers," *IEEE Transactions on Industrial Electronics*, Submitted.

[38] S. M. Gadoue, D. Giaouris, and J. W. Finch, "Low speed operation improvement of MRAS sensorless vector control induction motor drive using neural network flux observers," in *Proc. 32nd Annual Conference on IEEE Industrial Electronics*, Paris, France, 2006, pp. 1212-1217.

[39] S. M. Gadoue, D. Giaouris, and J. W. Finch, "A Neural Network Based Stator Current MRAS Observer for Speed Sensorless Induction Motor Drives," in *Proc. IEEE International Symposium on Industrial Electronics*, Cambridge, UK, 2008, pp. 650-655.

[40] J. C. Lopez, L. Romeral, A. Arias, and E. Aldabas, "Novel Fuzzy Adaptive Sensorless Induction Motor Drive," *IEEE Transactions on Industrial Electronics*, vol. 53, no. 4, pp. 1170-1178, August 2006.

[41] H. Kubota, K. Matsuse, and T. Nakano, "DSP-based speed adaptive flux observer of induction motor," *IEEE Transactions on Industry Applications*, vol. 29, no. 2, pp. 344-348, March/April 1993.

[42] T. Du, P. Vas, and F. Stronach, "Design and application of extended observers for joint state and parameter estimation in high-performance AC drives," *IEE Proceedings Electric Power Applications*, vol. 142, no. 2, pp. 71-78, March 1995.

[43] M. Barut, S. Bogosyan, and M. Gokasan, "Speed-Sensorless Estimation for Induction Motors Using Extended Kalman Filters," *IEEE Transactions on Industrial Electronics*, vol. 54, no. 1, pp. 272-280, February 2007.

[44] Y. Kim, S. Sul, and M. Park, "Speed sensorless vector control of induction motor using extended Kalman filter," *IEEE Transactions on Industry Applications*, vol. 30, no. 5, pp. 1225-1233, September/October 1994.

[45] K. L. Shi, T. F. Chan, Y. K. Wong, and S. L. Ho, "Speed estimation of an induction motor drive using an optimized extended Kalman filter," *IEEE Transactions on Industrial Electronics*, vol. 49, no. 1, pp. 124-133, February 2002.

[46] S. Buyamin and J. W. Finch, "Tuning Extended Kalman Filter for Induction Motor Drives using Simulated Annealing," in *Proc. 26th International Conference on Modelling, Identification, and Control*, 2007.

[47] B. Akin, U. Orguner, A. Ersak, and M. Ehsani, "Simple Derivative-Free Nonlinear State Observer for Sensorless AC Drives," *IEEE/ASME Transactions on Mechatronics*, vol. 11, no. 5, pp. 634-643, October 2006.

[48] Z. Yan, C. Jin, and V. Utkin, "Sensorless sliding-mode control of induction motors," *IEEE Transactions on Industrial Electronics*, vol. 47, no. 6, pp. 1286-1297, December 2000.

[49] V. Utkin, "Sliding mode control design principles and applications to electric drives," *IEEE Transactions on Industrial Electronics*, vol. 40, no. 1, pp. 23-36, February 1993.

[50] A. Derdiyok, M. K. Guven, H. Rehman, N. Inanc, and L. Xu, "Design and implementation of a new sliding-mode observer for speed-sensorless control of induction machine," *IEEE Transactions on Industrial Electronics*, vol. 49, no. 5, pp. 1177-1182, October 2002.

[51] M. Comanescu and L. Xu, "Sliding mode MRAS speed estimators for sensorless vector control of induction machine," *IEEE Transactions on Industrial Electronics*, vol. 53, no. 1, pp. 146-153, February 2006.

[52] M. Cirrincione and M. Pucci, "An MRAS-based sensorless high-performance induction motor drive with a predictive adaptive model," *IEEE Transactions on Industrial Electronics*, vol. 52, no. 2, pp. 532- 551, April 2005.

[53] C. Schauder, "Adaptive speed identification for vector control of induction motors without rotational transducers," *IEEE Transactions on Industry Applications*, vol. 28, no. 5, pp. 1054-1061, September/October 1992.

[54] F. Peng and T. Fukao, "Robust speed identification for speed-sensorless vector control of induction motors," *IEEE Transactions on Industry Applications*, vol. 30, no. 5, pp. 1234-1240, September/October 1994.

[55] R. Blasco-Gimenez, G. M. Asher, M. Sumner, and K. J. Bradley, "Dynamic performance limitations for MRAS based sensorless induction motor drives. Part

1: Stability analysis for the closed loop drive," *IEE Proceedings Electric Power Applications*, vol. 143, no. 2, pp. 113-122, March 1996.

[56] G. J. Armstrong, D. J. Atkinson, and P. P. Acarnley, "A comparison of estimation techniques for sensorless vector controlled induction motor drives," in *Proc. International Conference on Power Electronics and Drive Systems*, 1997, pp. 110-116 vol.1.

[57] K. J. Astrom and B. Wittenmark, *Adaptive control.* Second ed., Reading, Mass.: Addison-Wesley, 1995.

[58] Z. Wu, D. Zhi, and J. Ying, "Research on speed estimation algorithm for induction motor drive," in *Proc. The 4th International Power Electronics and Motion Control Conference*, 2004, pp. 1387-1392 vol.3.

[59] M. Tsuji, S. Chen, K. Izumi, and E. Yamada, "A sensorless vector control system for induction motors using q-axis flux with stator resistance identification," *IEEE Transactions on Industrial Electronics*, vol. 48, no. 1, pp. 185-194, February 2001.

[60] J. Campbell and M. Sumner, "Practical sensorless induction motor drive employing an artificial neural network for online parameter adaptation," *IEE Proceedings Electric Power Applications*, vol. 149, no. 4, pp. 255 - 260, July 2002.

[61] R. Blasco-Gimenez, G. M. Asher, M. Sumner, and K. J. Bradley, "Dynamic performance limitations for MRAS based sensorless induction motor drives. Part 2: Online parameter tuning and dynamic performance studies," *IEE Proceedings Electric Power Applications*, vol. 143, no. 2, pp. 123-134, March 1996.

[62] V. Vasic, S. N. Vukosavic, and E. Levi, "A stator resistance estimation scheme for speed sensorless rotor flux oriented induction motor drives," *IEEE Transactions on Energy Conversion*, vol. 18, no. 4, pp. 476-483, December 2003.

[63] L. Zhen and L. Xu, "Sensorless field orientation control of induction machines based on a mutual MRAS scheme," *IEEE Transactions on Industrial Electronics*, vol. 45, no. 5, pp. 824-831, October 1998.

[64] V. Vasic and S. Vukosavic, "Robust MRAS-Based algorithm for stator resistance and rotor speed identification," *IEEE Power Engineering Review*, vol. 21, no. 11, pp. 39-41, November 2001.

[65] Y. A. Kwon and D. W. Jin, "A novel MRAS based speed sensorless control of induction motor," in *Proc. the 25th Annual Conference of the IEEE Industrial Electronics Society*, 1999, pp. 933-938.

[66] B. Karanayil, M. F. Rahman, and C. Grantham, "An implementation of a programmable cascaded low-pass filter for a rotor flux synthesizer for an

induction motor drive," *IEEE Transactions on Power Electronics*, vol. 19, no. 2, pp. 257-263, March 2004.

[67] M. Hinkkanen and J. Luomi, "Modified integrator for voltage model flux estimation of induction motors," *IEEE Transactions on Industrial Electronics*, vol. 50, no. 4, pp. 818-820, August 2003.

[68] Q. Gao, C. S. Staines, G. M. Asher, and M. Sumner, "Sensorless speed operation of cage induction motor using zero drift feedback integration with MRAS observer," in *Proc. European Conference on Power Electronics and Applications*, 2005.

[69] C. Lascu, I. Boldea, and F. Blaabjerg, "A modified direct torque control for induction motor sensorless drive," *IEEE Transactions on Industry Applications*, vol. 36, no. 1, pp. 122-130, January/February 2000.

[70] I. Kumara, "Speed sensorless field oriented control for induction motor drive," Ph.D Thesis, Newcastle University, Newcastle upon Tyne, UK, 2006.

[71] J. Holtz and J. Quan, "Sensorless vector control of induction motors at very low speed using a nonlinear inverter model and parameter identification," *IEEE Transactions on Industry Applications*, vol. 38, no. 4, pp. 1087-1095, July/August 2002.

[72] M. Cirrincione, M. Pucci, G. Cirrincione, and G. A. Capolino, "Sensorless Control of Induction Machines by a New Neural Algorithm: The TLS EXIN Neuron," *IEEE Transactions on Industrial Electronics*, vol. 54, no. 1, pp. 127 - 149, February 2007.

[73] L. Ben-Brahim, "Motor speed identification via neural networks," *IEEE Industry Applications Magazine*, vol. 1, no. 1, pp. 28-32, January/February 1995.

[74] Y. Kim and Y. Kook, "Neural network based speed sensorless induction motor drives with Kalman filter approach," in *Proc. The 24th Annual Conference of the IEEE Industrial Electronics Society*, 1998, pp. 997-1001.

[75] S. Kim, T. Park, J. Yoo, and G. Park, "Speed-sensorless vector control of an induction motor using neural network speed estimation," *IEEE Transactions on Industrial Electronics*, vol. 48, no. 3, pp. 609-614, June 2001.

[76] B. Karanayil, M. F. Rahman, and C. Grantham, "Online Stator and rotor resistance estimation scheme using artificial neural networks for vector controlled speed sensorless induction motor drives," *IEEE Transactions on Industrial Electronics*, vol. 54, no. 1, pp. 167-176, February 2007.

[77] M. Cirrincione, M. Pucci, G. Cirrincione, and G. Capolino, "A new adaptive integration methodology for estimating flux in induction machine drives," *IEEE Transactions on Power Electronics*, vol. 19, no. 1, pp. 25-34, January 2004.

[78] C. Cao, M. Lu, and X. Wang, "Speed estimation and stimulation of DTC system based on wavelet neural network," in *Proc. International Conference on Machine Learning and Cybernetics*, 2003, pp. 755-759.

[79] C. Chen and T. Chen, "Speed Sensorless of an Induction Motor Using Self-tuning Fuzzy Identification," in *Proc. Second International Conference on Innovative Computing, Information and Control*, 2007, pp. 398.

[80] K. Lian and C. Hung, "Sensorless Control for Induction Motors via Fuzzy Observer Design," in *Proc. IEEE International Symposium on Industrial Electronics*, 2006, pp. 2140-2145.

[81] P. L. Jansen and R. D. Lorenz, "A physically insightful approach to the design and accuracy assessment of flux observers for field oriented induction machine drives," *IEEE Transactions on Industry Applications*, vol. 30, no. 1, pp. 101-110, January/February 1994.

[82] S. Maiti, C. Chakraborty, Y. Hori, and M. C. Ta, "Model Reference Adaptive Controller-Based Rotor Resistance and Speed Estimation Techniques for Vector Controlled Induction Motor Drive Utilizing Reactive Power," *IEEE Transactions on Industrial Electronics*, vol. 55, no. 2, pp. 594-601, February 2008.

[83] Y. D. Landau, *Adaptive Control The Model Reference Approach.* New York: Marcel Dekker, 1979.

[84] A. Smith, "Sensorless control of induction motors," Eng.D. Stage two report, Newcastle University, Newcastle upon Tyne, UK, 2004.

[85] "IEEE Standard Test Procedure for Polyphase Induction Motors and Generators," in *IEEE Std 112-2004 (Revision of IEEE Std 112-1996)*, 2004, pp. 0_1-79.

[86] dSPACE, "Solutions for Control," Available at: http://www.dspaceinc.com/ww/en/inc/home/products/hw/singbord/ppcconbo.cfm Retrieved: January 2007.

[87] L. Ben-Brahim, "On the compensation of Dead Time and Zero-Current crossing for a PWM-Inverter-controlled AC servo drive," *IEEE Transactions on Industrial Electronics*, vol. 51, no. 5, pp. 1113-1117, October 2004.

[88] J. Seung-Gi and P. Min-Ho, "The analysis and compensation of dead-time effects in PWM inverters," *IEEE Transactions on Industrial Electronics*, vol. 38, no. 2, pp. 108-114, April 1991.

[89] S. H. Kim, T. S. Park, J. Y. Yoo, G. T. Park, and N. J. Kim, "Dead time compensation in a vector-controlled induction machine," in *Proc. Power Electronics Specialists Conference*, 1998, pp. 1011-1016.

[90] F. Barrero, A. Gonzalez, A. Torralba, E. Galvan, and L. Franquelo, "Speed control of induction motors using a novel fuzzy sliding-mode structure," *IEEE Transactions on Fuzzy systems*, vol. 10, no. 3, pp. 375-383, June 2002.

[91] W. S. Levine, *The control handbook.* Boca Raton, FL: CRC Press, 1996.

[92] J. Lo and Y. Kuo, "Decoupled fuzzy sliding-mode control," *IEEE Transactions on Fuzzy systems*, vol. 6, no. 3, pp. 426-435, August 1998.

[93] K. Shyu and H. Shieh, "A new switching surface sliding-mode speed control for induction motor drive systems," *IEEE Transactions on Power Electronics*, vol. 11, no. 4, pp. 660-667, July 1996.

[94] "The MathWorks Fuzzy Logic Toolbox User's Guide," Available at: http://www.mathworks.com/access/helpdesk/help/pdf_doc/fuzzy/fuzzy.pdf Retrieved: July 2008.

[95] L. Zadeh, "Fuzzy sets," *Information and Control*, vol. 8, pp. 338-353, 1965.

[96] F. Zidani, M. Nait-Said, M. Benbouzid, D. Diallo, and R. Abdessemed, "A Fuzzy Rotor Resistance Updating Scheme for an IFOC Induction Motor Drive," *IEEE Power Engineering Review*, vol. 21, no. 11, pp. 47-50, November 2001.

[97] E. Bim, "Fuzzy optimization for rotor constant identification of an indirect FOC induction motor drive," *IEEE Transactions on Industrial Electronics*, vol. 48, no. 6, pp. 1293-1295, December 2001.

[98] M. Ta-Cao and H. Le-Huy, "Rotor resistance estimation using fuzzy logic for high performance induction motor drives," in *Proc. The 24th Annual Conference of the IEEE Industrial Electronics Society*, 1998, pp. 303 - 308.

[99] Y. Miloud and A. Draou, "Fuzzy logic based rotor resistance estimator of an indirect vector controlled induction motor drive," in *Proc. IEEE 28th Annual Conference of the Industrial Electronics Society*, 2002, pp. 961 - 966.

[100] S. Mir, M. E. Elbuluk, and D. S. Zinger, "PI and fuzzy estimators for tuning the stator resistance in direct torque control of induction machines," *IEEE Transactions on Power Electronics*, vol. 13, no. 2, pp. 279-287, March 1998.

[101] B. Karanayil, M. F. Rahman, and C. Grantham, "PI and fuzzy estimators for on-line tracking of rotor resistance of indirect vector controlled induction motor drive," in *Proc. IEEE International Electric Machines and Drives Conference*, 2001, pp. 820-825.

[102] Y. Lai and J. Lin, "New hybrid fuzzy controller for direct torque control induction motor drives," *IEEE Transactions on Power Electronics*, vol. 18, no. 5, pp. 1211-1219, September 2003.

[103] M. A. Denai and S. A. Attia, "Intelligent control of an induction motor," *Electric Power Components and Systems*, vol. 30, no. 4, pp. 409-427, April 2002.

[104] K. Ogata, *Modern Control Engineering.* Fourth ed., London: Prentice Hall, 2001.

[105] W. Leonhard, *Control of Electrical Drives.* Third ed., New York: Springer. 2001.

[106] L. M. Grzesiak and B. Ufnalski, "Neural stator flux estimator with dynamical signal preprocessing," in *Proc. The IEEE AFRICON*, 2004, pp. 1137-1142.

[107] M. Wlas, Z. Krzeminski, J. Guzinski, H. Abu-Rub, and H. A. Toliyat, "Artificial-Neural-Network-Based Sensorless Nonlinear Control of Induction Motors," *IEEE Transactions on Energy Conversion*, vol. 20, no. 3, pp. 520-528, September 2005.

[108] D. W. Patterson, *Artificial Neural Networks: Theory and Applications.* Singapore, New York: Prentice-Hall, 1995.

[109] K. Mehrotra, C. Mohan, and S. Ranka, *Elements of Artificial Neural Networks.* Cambridge, Mass.: MIT Press, 1997.

[110] T. El-balluq, "Adaptive speed control of electric drives using neural networks," Ph.D Thesis, Newcastle University, Newcastle upon Tyne, UK, 2003.

[111] "The Mathworks Neural Network toolbox User's guide," Available at: http://www.mathworks.com/access/helpdesk/help/pdf_doc/nnet/nnet.pdf Retrieved: August 2008.

[112] K. Ohyama, G. M. Asher, and M. Sumner, "Comparative experimental assessment for high-performance sensorless induction motor drives," in *Proc. IEEE International Symposium on Industrial Electronics*, 1999, pp. 386 - 391 vol.1.

[113] K. Ohyama, G. M. Asher, and M. Sumner, "Comparative analysis of experimental performance and stability of sensorless induction motor drives," *IEEE Transactions on Industrial Electronics*, vol. 53, no. 1, pp. 178 - 186, February 2006.

APPENDIX A

DYNAMIC MODELLING OF INDUCTION MACHINE

A.1 Space Vector Representation of Induction Machine

In a three phase induction machine, the space vectors of the stator current, voltage and flux in the stationary reference frame fixed to stator can be defined as:

$$\begin{aligned}\bar{i}_s &= \frac{2}{3}(i_{sA} + a i_{sB} + a^2 i_{sC}) \\ &= i_{sD} + j i_{sQ}\end{aligned} \tag{A.1}$$

$$\begin{aligned}\bar{v}_s &= \frac{2}{3}(v_{sA} + a v_{sB} + a^2 v_{sC}) \\ &= v_{sD} + j v_{sQ}\end{aligned} \tag{A.2}$$

$$\begin{aligned}\bar{\psi}_s &= \frac{2}{3}(\psi_{sA} + a \psi_{sB} + a^2 \psi_{sC}) \\ &= \psi_{sD} + j \psi_{sQ}\end{aligned} \tag{A.3}$$

where:

$$\begin{aligned}a &= e^{j\frac{2\pi}{3}} = -\frac{1}{2} + j\frac{\sqrt{3}}{2} \\ a^2 &= e^{j\frac{4\pi}{3}} = -\frac{1}{2} - j\frac{\sqrt{3}}{2}\end{aligned} \tag{A.4}$$

Using Faraday's and Kirchoff's laws the stator voltage equation of the three phase machine can be written as:

$$v_{sA} = R_s i_{sA} + \frac{d\psi_{sA}}{dt} \tag{A.5}$$

$$v_{sB} = R_s i_{sB} + \frac{d\psi_{sB}}{dt} \tag{A.6}$$

$$v_{sC} = R_s i_{sC} + \frac{d\psi_{sC}}{dt} \tag{A.7}$$

Substituting equations (A.5), (A.6) and (A.7) into (A.2) yields the stator voltage equation in the stator reference frame:

$$\bar{v}_s = \frac{2}{3}\left((R_s i_{sA} + \frac{d\psi_{sA}}{dt}) + a(R_s i_{sB} + \frac{d\psi_{sB}}{dt}) + a^2(R_s i_{sC} + \frac{d\psi_{sC}}{dt}) \right) \tag{A.8}$$

$$\bar{v}_s = \frac{2}{3}\left(R_s(i_{sA} + a i_{sB} + a^2 i_{sC}) + (\frac{d\psi_{sA}}{dt} + a\frac{d\psi_{sB}}{dt} + a^2\frac{d\psi_{sC}}{dt}) \right) \tag{A.9}$$

Recalling (A.1) and (A.3), Equation (A.9) yields the stator voltage equation in the stator reference frame using space vector notation which can be written as:

$$\bar{v}_s^s = R_s \bar{i}_s^s + \frac{d\bar{\psi}_s^s}{dt} \tag{A.10}$$

The superscript s and the subscript s stand for the stator reference frame and the stator quantities respectively.

Similar to the definition of the space vectors of the stator quantities in the stator reference frame, the space vectors of the rotor quantities in a reference frame fixed to rotor can be expressed as:

$$\bar{i}_r = \frac{2}{3}(i_{ra} + a i_{rb} + a^2 i_{rc}) \tag{A.11}$$

$$\bar{v}_r = \frac{2}{3}(v_{ra} + a v_{rb} + a^2 v_{rc}) \tag{A.12}$$

$$\bar{\psi}_r = \frac{2}{3}(\psi_{ra} + a\psi_{rb} + a^2\psi_{rc}) \tag{A.13}$$

The rotor voltage equations of the three phase machine can be written as:

$$v_{ra} = R_r i_{ra} + \frac{d\psi_{ra}}{dt} \tag{A.14}$$

$$v_{rb} = R_r i_{rb} + \frac{d\psi_{rb}}{dt} \tag{A.15}$$

$$v_{rc} = R_r i_{rc} + \frac{d\psi_{rc}}{dt} \tag{A.16}$$

Substituting equations (A.14), (A.15) and (A.16) into (A.12) yields the rotor voltage equation in the rotor reference frame:

$$\bar{v}_r = \frac{2}{3}\left((R_r i_{ra} + \frac{d\psi_{ra}}{dt}) + a(R_r i_{rb} + \frac{d\psi_{rb}}{dt}) + a^2(R_r i_{rc} + \frac{d\psi_{rc}}{dt})\right) \tag{A.17}$$

$$\bar{v}_r = \frac{2}{3}\left(R_r(i_{ra} + a i_{rb} + a^2 i_{rc}) + (\frac{d\psi_{ra}}{dt} + a\frac{d\psi_{rb}}{dt} + a^2\frac{d\psi_{rc}}{dt})\right) \tag{A.18}$$

Recalling (A.11) and (A.13), Equation (A.18) yields the rotor voltage equation in the rotor reference frame using space vector notation which can be written as:

$$\bar{v}_r^r = R_r \bar{i}_r^r + \frac{d\bar{\psi}_r^r}{dt} \tag{A.19}$$

The superscript r and the subscript r stand for the rotor reference frame and the rotor quantities respectively.

For mathematical modelling and control of the induction machine it is required to write down the machine equation in the same reference frame. Therefore the transformation between stator reference frame (D-Q) and another (d-q) frame is considered as shown in Fig. A.1.

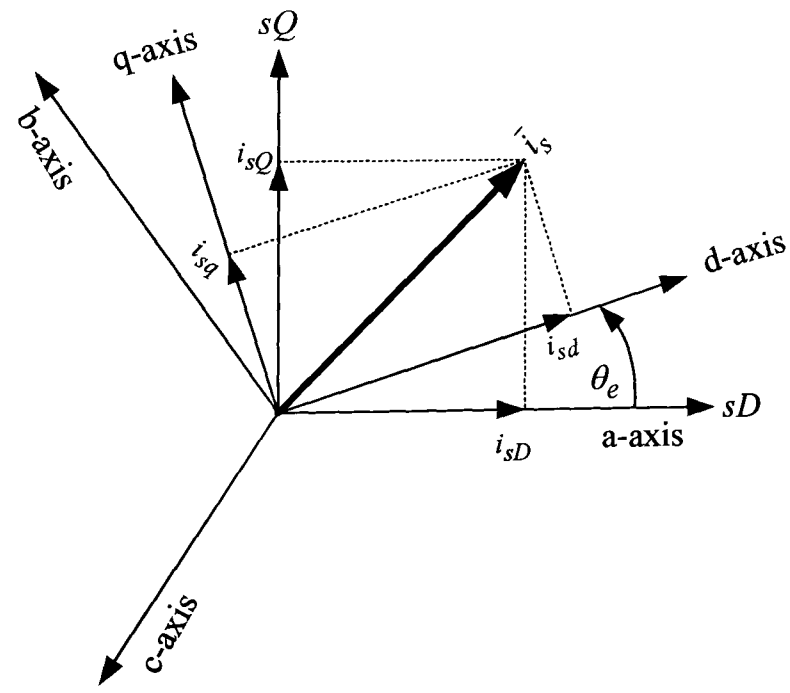

Fig. A.1 Transformation between D-Q and d-q reference frames

Resolving i_{sd} and i_{sq} on the *D*-*Q* axis yields:

$$\begin{aligned} i_{sD} &= i_{sd}\cos\theta_e - i_{sq}\sin\theta_e \\ i_{sQ} &= i_{sd}\sin\theta_e + i_{sq}\cos\theta_e \end{aligned} \tag{A.20}$$

This transformation can be written as:

$$\bar{i}_s^s = i_{sD} + j\, i_{sQ} = \bar{i}_s^e\, e^{j\theta_e} = (i_{sd} + j\, i_{sq})\, e^{j\theta_e} \tag{A.21}$$

where the superscript *e* stands for the *d*-*q* reference frame, which will be defined later as the synchronous frame.

(A.21) can be written in matrix form as:

$$\begin{bmatrix} i_{sD} \\ i_{sQ} \end{bmatrix} = \begin{bmatrix} \cos\theta_e & -\sin\theta_e \\ \sin\theta_e & \cos\theta_e \end{bmatrix} \begin{bmatrix} i_{sd} \\ i_{sq} \end{bmatrix} \tag{A.22}$$

And vice versa the transformation from stationary to *d*-*q* reference frame is given by:

$$\bar{i}_s^e = i_{sd} + j\, i_{sq} = \bar{i}_s^s\, e^{-j\theta_e} = (i_{sD} + j\, i_{sQ})\, e^{-j\theta_e} \tag{A.23}$$

$$\begin{bmatrix} i_{sd} \\ i_{sq} \end{bmatrix} = \begin{bmatrix} \cos\theta_e & \sin\theta_e \\ -\sin\theta_e & \cos\theta_e \end{bmatrix} \begin{bmatrix} i_{sD} \\ i_{sQ} \end{bmatrix} \tag{A.24}$$

Similarly, stator quantities can be written in a reference frame fixed to rotor as:

$$\begin{aligned} \bar{i}_s^r &= \bar{i}_s^s\, e^{-j\theta_r} \\ \bar{v}_s^r &= \bar{v}_s^s\, e^{-j\theta_r} \\ \bar{\psi}_s^r &= \bar{\psi}_s^s\, e^{-j\theta_r} \end{aligned} \tag{A.25}$$

Rotor quantities can be written in a reference frame fixed to stator as:

$$\begin{aligned} \bar{i}_r^s &= \bar{i}_r^r\, e^{j\theta_r} \\ \bar{v}_r^s &= \bar{v}_r^r\, e^{j\theta_r} \\ \bar{\psi}_r^s &= \bar{\psi}_r^r\, e^{j\theta_r} \end{aligned} \tag{A.26}$$

The rotor voltage equation (A.19) can be written in the stator reference frame based on the described transformations as:

$$\bar{v}_r^s\, e^{-j\theta_r} = R_r \bar{i}_r^s e^{-j\theta_r} + \frac{d}{dt}\left(\bar{\psi}_r^s e^{-j\theta_r}\right) \tag{A.27}$$

Let $\frac{d\theta_r}{dt} = \omega_r$, which is the angular rotor speed, equation (A.27) can be written as:

$$\bar{v}_r^s\, e^{-j\theta_r} = R_r \bar{i}_r^s e^{-j\theta_r} + e^{-j\theta_r} \frac{d\bar{\psi}_r^s}{dt} - j\omega_r \bar{\psi}_r^s e^{-j\theta_r} \tag{A.28}$$

Eliminating the term $e^{-j\theta_r}$ from (A.28) yields the rotor voltage equation in the stator reference frame:

$$\bar{v}_r^s = R_r \bar{i}_r^s + \frac{d\bar{\psi}_r^s}{dt} - j\omega_r \bar{\psi}_r^s \tag{A.29}$$

Resolving (A.10) and (A.29) into their real and imaginary parts yields the induction motor mathematical model in *d-q* coordinates established in the stator reference frame:

$$\begin{aligned} v_{sD} &= R_s i_{sD} + \frac{d\psi_{sD}}{dt} \\ v_{sQ} &= R_s i_{sQ} + \frac{d\psi_{sQ}}{dt} \\ v_{rd} &= R_r i_{rd} + \frac{d\psi_{rd}}{dt} + \omega_r \psi_{rq} \\ v_{rq} &= R_r i_{rq} + \frac{d\psi_{rq}}{dt} - \omega_r \psi_{rd} \end{aligned} \tag{A.30}$$

The stator and rotor flux linkages are given by:

$$\begin{aligned} \bar{\psi}_s &= L_s \bar{i}_s + L_m \bar{i}_r \\ \bar{\psi}_r &= L_m \bar{i}_s + L_r \bar{i}_r \end{aligned} \tag{A.31}$$

$$\begin{aligned} L_s &= L_m + L_{ls} \\ L_r &= L_m + L_{lr} \end{aligned} \tag{A.32}$$

where L_s, L_r are the stator and rotor self inductances, L_m is the mutual inductance and L_{ls}, L_{lr} are the stator and rotor leakage inductances respectively.

Equation (A.31) can be written in *d-q* format in the stator reference frame as:

$$\begin{aligned} \psi_{sD} &= L_s i_{sD} + L_m i_{rd} \\ \psi_{sQ} &= L_s i_{sQ} + L_m i_{rq} \\ \psi_{rd} &= L_m i_{sD} + L_r i_{rd} \\ \psi_{rq} &= L_m i_{sQ} + L_r i_{rq} \end{aligned} \tag{A.33}$$

Substituting (A.31) into (A.10) and (A.29) yields the stator and rotor voltage equations in the stator reference frame in terms of stator and rotor currents:

$$\bar{v}_s^s = (R_s + L_s p)\bar{i}_s^s + L_m p \bar{i}_r^s \tag{A.34}$$

$$\bar{v}_r^s = (R_r + L_r p)\bar{i}_r^s + L_m p\bar{i}_s^s - j\omega_r\left(L_m\bar{i}_s^s + L_r\bar{i}_r^s\right) \tag{A.35}$$

where p is the differential operator.

These equations can be expressed in matrix form as:

$$\begin{bmatrix}\bar{v}_s^s \\ \bar{v}_r^s\end{bmatrix} = \begin{bmatrix} R_s + L_s p & L_m p \\ (p - j\omega_r)L_m & R_r + (p - j\omega_r)L_r\end{bmatrix}\begin{bmatrix}\bar{i}_s^s \\ \bar{i}_r^s\end{bmatrix} \tag{A.36}$$

Equations (A.34) and (A.35) can be written in the *d-q* reference frame fixed to stator as:

$$\begin{aligned} v_{sD} &= (R_s + L_s p)i_{sD} + L_m p i_{rd} \\ v_{sQ} &= (R_s + L_s p)i_{sQ} + L_m p i_{rq} \\ v_{rd} &= L_m p i_{sD} + \omega_r L_m i_{sQ} + (R_r + L_r p)i_{rd} + \omega_r L_r i_{rq} \\ v_{rq} &= -\omega_r L_m i_{sD} + L_m p i_{sQ} - \omega_r L_r i_{rd} + (R_r + L_r p)i_{rq} \end{aligned} \tag{A.37}$$

A.2 State Space Model of Induction Machine

In this section a state space model of the induction machine in the stator reference frame is developed. The rotor current can be expressed in terms of the rotor flux From (A.31) as:

$$\bar{i}_r = \frac{1}{L_r}\left(\bar{\psi}_r - L_m\bar{i}_s\right) \tag{A.38}$$

Substituting (A.38) into (A.34) yields the following in the stator reference frame:

$$\begin{aligned} \bar{v}_s &= (R_s + L_s p)\bar{i}_s + \frac{L_m}{L_r}p\left(\bar{\psi}_r - L_m\bar{i}_s\right) \\ \bar{v}_s &= R_s\bar{i}_s + (L_s - \frac{L_m^2}{L_r})p\bar{i}_s + \frac{L_m}{L_r}p\bar{\psi}_r \\ \bar{v}_s &= R_s\bar{i}_s + L_s(1 - \frac{L_m^2}{L_s L_r})p\bar{i}_s + \frac{L_m}{L_r}p\bar{\psi}_r \end{aligned} \tag{A.39}$$

Defining σ as the leakage coefficient given by:

$$\sigma = 1 - \frac{L_m^2}{L_s L_r} \tag{A.40}$$

Equation (A.39) can be written as:

$$\bar{v}_s = R_s\bar{i}_s + \sigma L_s p\bar{i}_s + \frac{L_m}{L_r}p\bar{\psi}_r \tag{A.41}$$

Equation (A.41) can be written in *d-q* form as:

$$v_{sD} = R_s i_{sD} + \sigma L_s p i_{sD} + \frac{L_m}{L_r} p\psi_{rd} \tag{A.42}$$

$$v_{sQ} = R_s i_{sQ} + \sigma L_s p i_{sQ} + \frac{L_m}{L_r} p\psi_{rq} \tag{A.43}$$

Substituting (A.38) into (A.29) and using zero rotor voltage for a squirrel-cage machine yields:

$$0 = \frac{1}{T_r}\left(\overline{\psi}_r - L_m \bar{i}_s\right) + \frac{d\overline{\psi}_r}{dt} - j\omega_r \overline{\psi}_r \tag{A.44}$$

where T_r is the rotor time constant given by:

$$T_r = \frac{L_r}{R_r} \tag{A.45}$$

Rearranging (A.44) gives:

$$p\overline{\psi}_r = \frac{L_m}{T_r}\bar{i}_s - \frac{1}{T_r}\overline{\psi}_r + j\omega_r \overline{\psi}_r \tag{A.46}$$

Equation (A.46) can be written in *d-q* form as:

$$p\psi_{rd} = \frac{L_m}{T_r} i_{sD} - \frac{1}{T_r}\psi_{rd} - \omega_r \psi_{rq} \tag{A.47}$$

$$p\psi_{rq} = \frac{L_m}{T_r} i_{sQ} - \frac{1}{T_r}\psi_{rq} + \omega_r \psi_{rd} \tag{A.48}$$

Substituting (A.47) into (A.42) yields:

$$v_{sD} = R_s i_{sD} + \sigma L_s p i_{sD} + \frac{L_m}{L_r}\left(\frac{L_m}{T_r} i_{sD} - \frac{1}{T_r}\psi_{rd} - \omega_r \psi_{rq}\right) \tag{A.49}$$

Separating pi_{sD} gives:

$$pi_{sD} = \frac{1}{\sigma L_s}\left[v_{sD} - \left(R_s + \frac{L_m^2}{L_r T_r}\right) i_{sD} + \frac{L_m}{L_r T_r}\psi_{rd} + \frac{L_m}{L_r}\omega_r \psi_{rq} \right] \tag{A.50}$$

Using the definition of σ in (A.40) equation (A.50) can be written as:

$$pi_{sD} = \frac{v_{sD}}{\sigma L_s} - \left(\frac{R_s}{\sigma L_s} + \frac{1-\sigma}{\sigma T_r}\right) i_{sD} + \frac{L_m}{\sigma L_s L_r T_r}\psi_{rd} + \frac{L_m}{\sigma L_s L_r}\omega_r \psi_{rq} \tag{A.51}$$

Similarly, substituting (A.48) into (A.43) and separating pi_{sq} gives:

$$pi_{sQ} = \frac{v_{sQ}}{\sigma L_s} - \left(\frac{R_s}{\sigma L_s} + \frac{1-\sigma}{\sigma T_r}\right) i_{sQ} + \frac{L_m}{\sigma L_s L_r T_r}\psi_{rq} - \frac{L_m}{\sigma L_s L_r}\omega_r \psi_{rd} \tag{A.52}$$

Equations (A.51), (A.52), (A.47) and (A.48) can be used to represent the induction machine model in state space form in *d-q* coordinates established in the stator reference frame as:

$$\begin{bmatrix} pi_{sD} \\ pi_{sQ} \\ p\psi_{rd} \\ p\psi_{rq} \end{bmatrix} = \begin{bmatrix} -a_1 & 0 & a_2 & a_3\omega_r \\ 0 & -a_1 & -a_3\omega_r & a_2 \\ \dfrac{L_m}{T_r} & 0 & -\dfrac{1}{T_r} & -\omega_r \\ 0 & \dfrac{L_m}{T_r} & \omega_r & -\dfrac{1}{T_r} \end{bmatrix} \begin{bmatrix} i_{sD} \\ i_{sQ} \\ \psi_{rd} \\ \psi_{rq} \end{bmatrix} + \begin{bmatrix} \dfrac{1}{\sigma L_s} & 0 \\ 0 & \dfrac{1}{\sigma L_s} \\ 0 & 0 \\ 0 & 0 \end{bmatrix} \begin{bmatrix} v_{sD} \\ v_{sQ} \end{bmatrix} \tag{A.53}$$

where:

$$\begin{aligned} a_1 &= \frac{R_s}{\sigma L_s} + \frac{1-\sigma}{\sigma T_r} \\ a_2 &= \frac{L_m}{\sigma L_s L_r T_r} \\ a_3 &= \frac{L_m}{\sigma L_s L_r} \end{aligned} \tag{A.54}$$

A.3 Space Vector Voltage Equations in the General Reference Frame

In a general reference frame which rotates with a general speed ω_g with direct and quadrature axes x, y, as shown in Fig. A.2 , the space vector of stator voltage, current and flux can be written as:

$$\begin{aligned} \bar{v}_s^g &= v_{sx} + jv_{sy} \\ \bar{i}_s^g &= i_{sx} + ji_{sy} \\ \bar{\psi}_s^g &= \psi_{sx} + j\psi_{sy} \end{aligned} \tag{A.55}$$

Using the frame transformation the stator quantities can be written as:

$$\begin{aligned} \bar{v}_s^s &= \bar{v}_s^g e^{j\theta_g} \\ \bar{i}_s^s &= \bar{i}_s^g e^{j\theta_g} \\ \bar{\psi}_s^s &= \bar{\psi}_s^g e^{j\theta_g} \end{aligned} \tag{A.56}$$

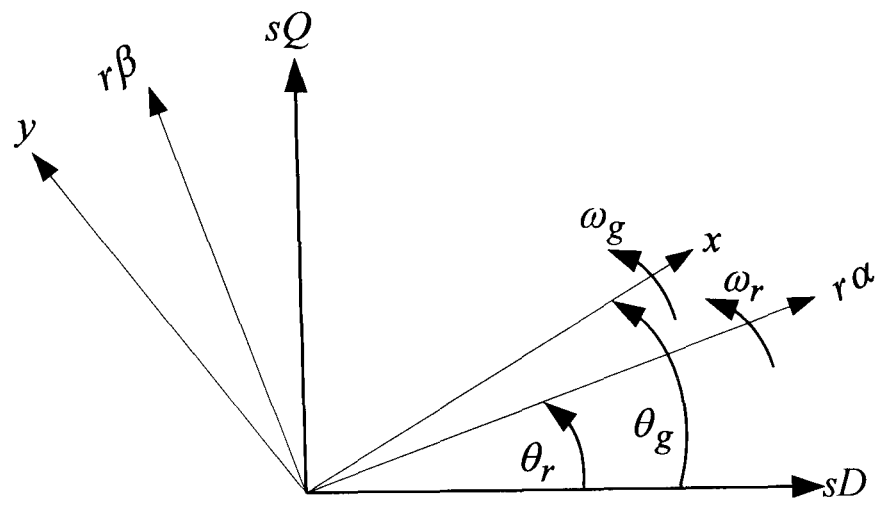

Fig. A.2 Application of the general reference frame

Substituting (A.56) into (A.10) gives the stator voltage equations in the general reference frame:

$$\bar{v}_s^g\, e^{j\theta_g} = R_s \bar{i}_s^g e^{j\theta_g} + \frac{d}{dt}\left(\bar{\psi}_s^g e^{j\theta_g}\right) \tag{A.57}$$

Let $\frac{d\theta_g}{dt} = \omega_g$ equation (A.57) can be written as:

$$\bar{v}_s^g\, e^{j\theta_g} = R_s \bar{i}_s^g e^{j\theta_g} + e^{j\theta_g} \frac{d\bar{\psi}_s^g}{dt} + j\omega_g \bar{\psi}_s^g e^{j\theta_g} \tag{A.58}$$

Eliminating $e^{j\theta_g}$ equation (A.58) can be written as:

$$\bar{v}_s^g = R_s \bar{i}_s^g + \frac{d\bar{\psi}_s^g}{dt} + j\omega_g \bar{\psi}_s^g \tag{A.59}$$

Similarly the rotor quantities in the general reference frame can be written as:

$$\begin{aligned} \bar{v}_r^g &= v_{rx} + jv_{ry} \\ \bar{i}_r^g &= i_{rx} + ji_{ry} \\ \bar{\psi}_r^g &= \psi_{rx} + j\psi_{ry} \end{aligned} \tag{A.60}$$

Using frame transformation the rotor quantities can be written as:

$$\begin{aligned} \bar{v}_r^r &= \bar{v}_r^g\, e^{j(\theta_g - \theta_r)} \\ \bar{i}_r^r &= \bar{i}_r^g\, e^{j(\theta_g - \theta_r)} \\ \bar{\psi}_r^r &= \bar{\psi}_r^g\, e^{j(\theta_g - \theta_r)} \end{aligned} \tag{A.61}$$

Substituting (A.61) into (A.19) yields the rotor voltage equations in the general reference frame:

$$\begin{aligned}\bar{v}_r^g e^{j(\theta_g-\theta_r)} &= R_r \bar{i}_r^g e^{j(\theta_g-\theta_r)} + \frac{d}{dt}\left(\bar{\psi}_r^g e^{j(\theta_g-\theta_r)}\right) \\ \bar{v}_r^g e^{j(\theta_g-\theta_r)} &= R_r \bar{i}_r^g e^{j(\theta_g-\theta_r)} + e^{j(\theta_g-\theta_r)}\frac{d\bar{\psi}_r^g}{dt} + j(\omega_g-\omega_r)\bar{\psi}_r^g e^{j(\theta_g-\theta_r)}\end{aligned} \tag{A.62}$$

Eliminating $e^{j(\theta_g-\theta_r)}$ equation (A.58) can be written as:

$$\bar{v}_r^g = R_r \bar{i}_r^g + \frac{d\bar{\psi}_r^g}{dt} + j(\omega_g-\omega_r)\bar{\psi}_r^g \tag{A.63}$$

The stator and rotor flux linkages in the general frame are given by:

$$\begin{aligned}\bar{\psi}_s^g &= L_s \bar{i}_s^g + L_m \bar{i}_r^g \\ \bar{\psi}_r^g &= L_m \bar{i}_s^g + L_r \bar{i}_r^g\end{aligned} \tag{A.64}$$

The stator and rotor voltage equations in the synchronous reference frame can be obtained by substituting $\omega_g = \omega_e$, which is the synchronous speed, and $\omega_g - \omega_r = \omega_{sl}$, which is the slip speed, into (A.59) and (A.63):

$$\bar{v}_s^e = R_s \bar{i}_s^e + \frac{d\bar{\psi}_s^e}{dt} + j\omega_e \bar{\psi}_s^e \tag{A.65}$$

$$\bar{v}_r^e = R_r \bar{i}_r^e + \frac{d\bar{\psi}_r^e}{dt} + j\omega_{sl} \bar{\psi}_r^e \tag{A.66}$$

Equations (A.65) and (A.66) can be written in *d-q* coordinates established in the synchronous reference frame as:

$$\begin{aligned}v_{sd} &= R_s i_{sd} + p\psi_{sd} - \omega_e \psi_{sq} \\ v_{sq} &= R_s i_{sq} + p\psi_{sq} + \omega_e \psi_{sd} \\ 0 &= R_r i_{rd} + p\psi_{rd} - \omega_{sl} \psi_{rq} \\ 0 &= R_r i_{rq} + p\psi_{rq} + \omega_{sl} \psi_{rd}\end{aligned} \tag{A.67}$$

The stator and rotor flux linkages in the synchronous reference frame can be written as:

$$\begin{aligned}\psi_{sd} &= L_s i_{sd} + L_m i_{rd} \\ \psi_{sq} &= L_s i_{sq} + L_m i_{rq} \\ \psi_{rd} &= L_m i_{sd} + L_r i_{rd} \\ \psi_{rq} &= L_m i_{sq} + L_r i_{rq}\end{aligned} \tag{A.68}$$

A.4 Power and Torque Relations using *d-q* Representation

The three phase input power to the induction machine can be written in terms of the three phase voltages and currents as:

$$P_i = v_{sA}i_{sA} + v_{sB}i_{sB} + v_{sC}i_{sC} \tag{A.69}$$

By expressing the three phase quantities by the equivalent two phase quantities. the expression for the input power can be written as:

$$\begin{aligned}
P_i &= v_{sD}i_{sD} + \left(-\frac{1}{2}v_{sD} + \frac{\sqrt{3}}{2}v_{sQ}\right)\left(-\frac{1}{2}i_{sD} + \frac{\sqrt{3}}{2}i_{sQ}\right) \\
&\quad + \left(-\frac{1}{2}v_{sD} - \frac{\sqrt{3}}{2}v_{sQ}\right)\left(-\frac{1}{2}i_{sD} - \frac{\sqrt{3}}{2}i_{sQ}\right) \\
P_i &= v_{sD}i_{sD} + \frac{1}{4}v_{sD}i_{sD} - \frac{\sqrt{3}}{4}v_{sD}i_{sQ} - \frac{\sqrt{3}}{4}v_{sQ}i_{sD} + \frac{3}{4}v_{sQ}i_{sQ} + \frac{1}{4}v_{sD}i_{sD} + \frac{\sqrt{3}}{4}v_{sD}i_{sQ} \\
&\quad + \frac{\sqrt{3}}{4}v_{sQ}i_{sD} + \frac{3}{4}v_{sQ}i_{sQ} \\
P_i &= \frac{3}{2}\left(v_{sD}i_{sD} + v_{sQ}i_{sQ}\right)
\end{aligned} \tag{A.70}$$

To prove the inverse transformation from three-phase to two-phase consider the input power expression in the *d-q* coordinates and substitute the three phase variables instead of the two phase quantities:

$$\begin{aligned}
P_i &= \frac{3}{2}\left(v_{sD}i_{sD} + v_{sQ}i_{sQ}\right) \\
&= \frac{3}{2}\left\{\begin{array}{l}\left(\frac{2}{3}v_{sA} - \frac{1}{3}v_{sB} - \frac{1}{3}v_{sC}\right)\left(\frac{2}{3}i_{sA} - \frac{1}{3}i_{sB} - \frac{1}{3}i_{sC}\right) \\ + \left(\frac{1}{\sqrt{3}}v_{sB} - \frac{1}{\sqrt{3}}v_{sC}\right)\left(\frac{1}{\sqrt{3}}i_{sB} - \frac{1}{\sqrt{3}}i_{sC}\right)\end{array}\right\} \\
&= v_{sA}i_{sA} + v_{sB}i_{sB} + v_{sC}i_{sC}
\end{aligned} \tag{A.71}$$

In general, the expression for active and reactive power of the induction machine using *d-q* representation can be written as:

$$\begin{aligned} S_i &= \frac{3}{2}\left(\bar{v}_s \bar{i}_s^{\Im}\right) \\ &= \frac{3}{2}\left\{\left(v_{sD} + jv_{sQ}\right)\left(i_{sD} - ji_{sQ}\right)\right\} \\ &= \frac{3}{2}\left\{\left(v_{sD}i_{sD} + v_{sQ}i_{sQ}\right) + j\left(v_{sQ}i_{sD} - v_{sD}i_{sQ}\right)\right\} \\ &= P_i + jQ_i \end{aligned} \tag{A.72}$$

where $\Im$ stands for the complex conjugate.

The expressions for input active and reactive power can be written as:

$$\begin{aligned} P_i &= \frac{3}{2}\left(v_{sD}i_{sD} + v_{sQ}i_{sQ}\right) \\ Q_i &= \frac{3}{2}\left(v_{sQ}i_{sD} - v_{sD}i_{sQ}\right) \end{aligned} \tag{A.73}$$

The mechanical power can be written as:

$$P_{mech} = \frac{3}{2}\left(e_{rd}i_{rd} + e_{rq}i_{rq}\right) \tag{A.74}$$

where $\bar{e}_r$ is the space vector of the rotor EMF induced in the rotor windings which can be expressed as:

$$\begin{aligned} \bar{e}_r &= e_{rd} + je_{rq} \\ \bar{e}_r &= -j\omega_r \bar{\psi}_r = -j\omega_r(\psi_{rd} + j\psi_{rq}) \\ \bar{e}_r &= \omega_r \psi_{rq} - j\omega_r \psi_{rd} \end{aligned} \tag{A.75}$$

Substituting (A.75) into the mechanical power equation yields:

$$P_{mech} = \frac{3}{2}\omega_r(\psi_{rq}i_{rd} - \psi_{rd}i_{rq}) \tag{A.76}$$

The electromagnetic torque, for a machine with P pole pairs, can be obtained by dividing the mechanical power by the mechanical rotor speed ω_{rm} as follow:

$$T_e = \frac{P_{mech}}{\omega_{rm}} = \frac{3}{2}P(\psi_{rq}i_{rd} - \psi_{rd}i_{rq}) = -\frac{3}{2}P\bar{\psi}_r \times \bar{i}_r \tag{A.77}$$

where the mechanical rotor speed is related to the electrical speed by:

$$\omega_{rm} = \frac{\omega_r}{P} \tag{A.78}$$

The torque expression obtained is similar in all reference frames. By using other machine variables, the electromagnetic torque can be also expressed as:

$$
\begin{aligned}
T_e &= -\frac{3}{2}P\bar{\psi}_r \times \bar{i}_r = \frac{3}{2}P(\psi_{rq} i_{rd} - \psi_{rd} i_{rq}) \\
T_e &= -\frac{3}{2}PL_m \bar{i}_s \times \bar{i}_r = \frac{3}{2}PL_m(i_{sq} i_{rd} - i_{sd} i_{rq}) \\
T_e &= -\frac{3}{2}P\bar{i}_s \times \bar{\psi}_s = \frac{3}{2}P(\psi_{sd} i_{sq} - \psi_{sq} i_{sd}) \\
T_e &= -\frac{3}{2}P\frac{L_m}{L_r}\bar{i}_s \times \bar{\psi}_r = \frac{3}{2}P\frac{L_m}{L_r}(\psi_{rd} i_{sq} - \psi_{rq} i_{sd})
\end{aligned}
\tag{A.79}
$$

APPENDIX B

FUZZY LOGIC CONTROL

B.1 Principles of Fuzzy Logic

The most frequently used FL system is the Mamdani-type which consists of three main parts: fuzzification, inference engine and defuzzification.

B.1.1 Fuzzification

Since FL is based on linguistic variables, the first step performed by FLC is to map all inputs to fuzzy sets and to assign membership values for each input to these different sets. This process is called *fuzzification* where each point from the input space (universe of discourse) is assigned a membership value μ (degree of membership) between 0 for no membership and 1 for full membership to a given fuzzy set. A common example is the set of hot temperatures where the universe of discourse consists of different temperatures between 15 degrees to 35 degrees as shown in Fig. B.1.

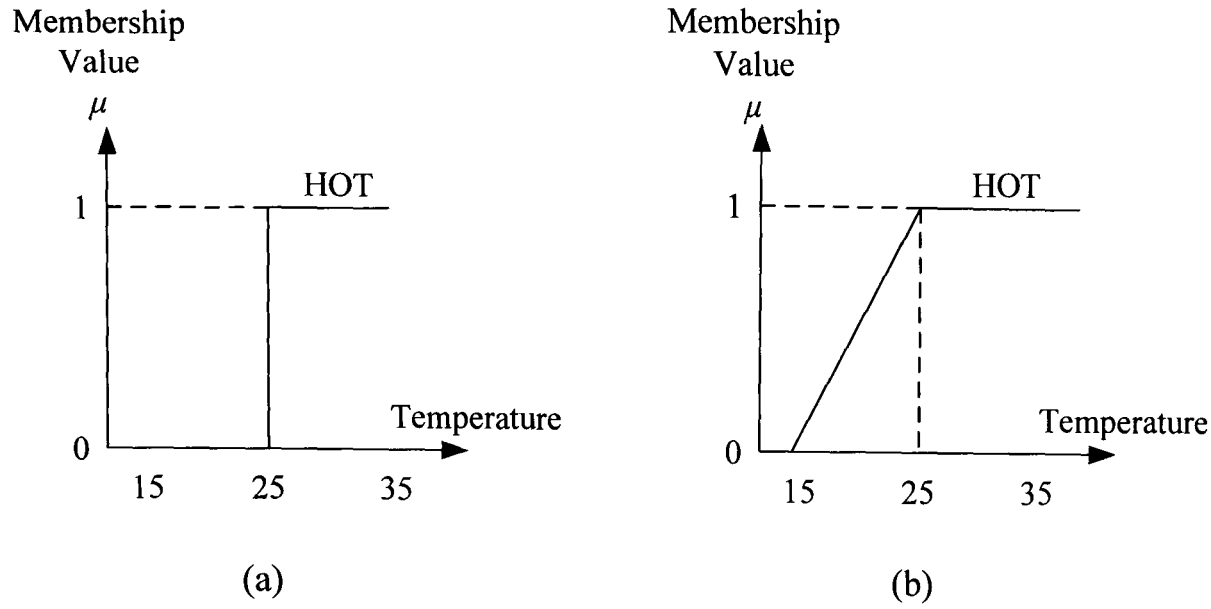

Fig. B.1 Hot temperature example representation (a) Classical crisp set (b) Fuzzy set

Using well-defined (crisp) approach a description of a hot temperature can be given to any temperature higher than 25 degrees. However it is unreasonable to define a temperature of 24 degrees to be not hot. This can be overcome by a fuzzy approach using a continuous curve, a membership function, passing from non-hot to hot to define how much a given temperature belongs to the HOT set. Hence 25 degrees has 100% membership to the Fuzzy set HOT where as 24 degrees and 16 degrees have 90% and 10% membership values respectively. This is different from Boolean logic where any point in the universe of discourse should be inside (full membership) or outside (no membership) the set.

There are many types of membership functions; some are smooth such as Gaussian and Sigmoid and others are non-smooth such as triangular and trapezoidal as shown in Fig. B.2. The choice of suitable membership function is not unique. However, simple membership functions such as triangular and trapezoidal are used in various applications due to their linear characteristics.

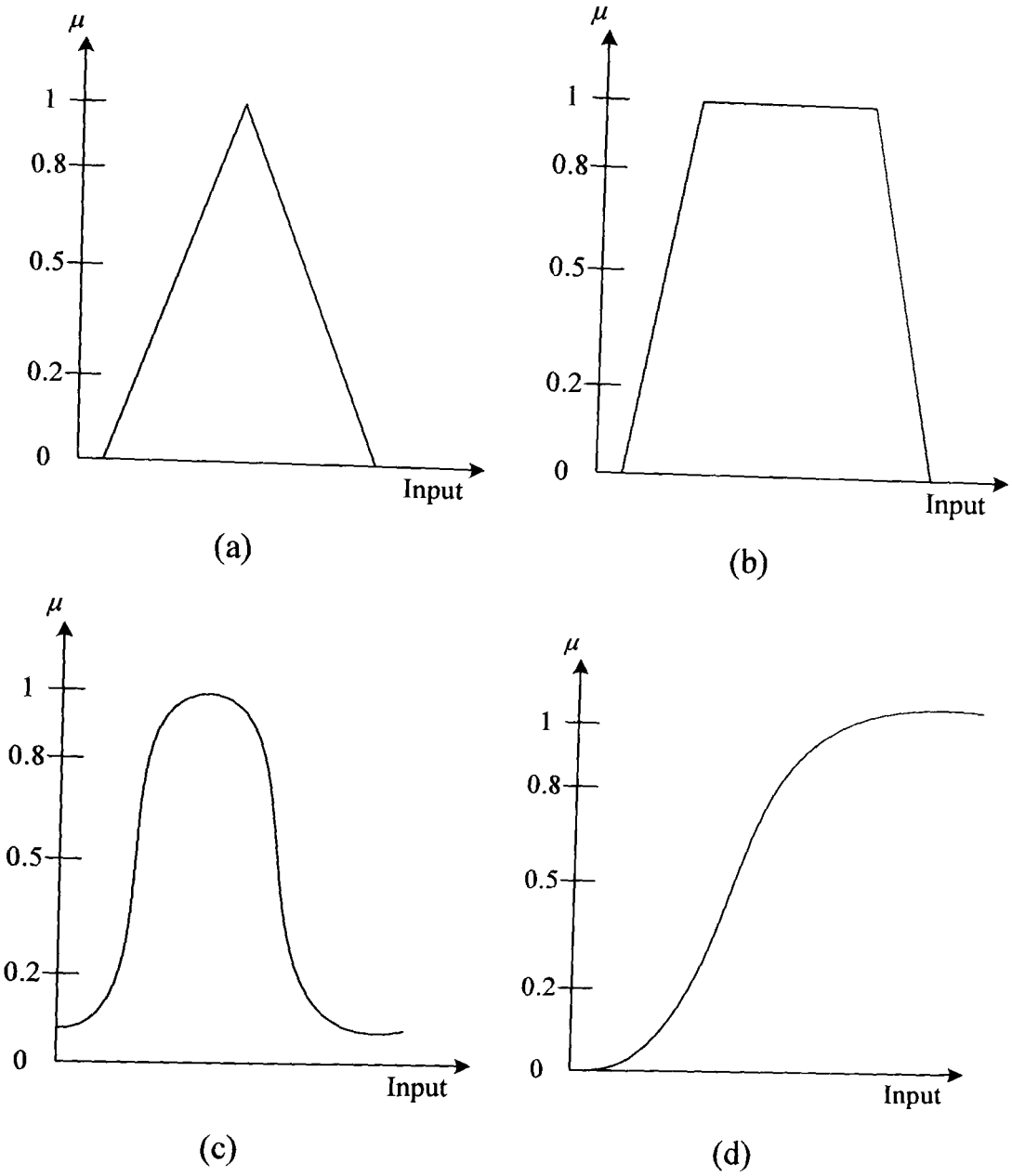

Fig. B.2 Fuzzy membership functions (a) Triangular (b) Trapezoidal (c) Gaussian (d) Sigmoid

B.1.2 Fuzzy Inference Engine

The fuzzy inference engine is used to generate the fuzzy outputs by connecting the fuzzified inputs to the output fuzzy sets based on linguistic rules. This mimics human reasoning which can be described by an *If-Then* expression: If x is A_i and/or y is B_i then z is C_i where x and y are the first and the second fuzzy inputs respectively and A_i and B_i are the membership functions for each input, z is the controller output C_i is the membership function of the output.

B.1.3 Defuzzification

The last step of the FLC is the *defuzzification* process where the output fuzzy set is transformed back to a real value. Different methods can be used for the defuzzification such as: maximum, mean of maxima, centre of area and centre of gravity.

Usually scaling factors are used in the input and the output of the FLC to normalize the value of the controller input and to de-normalize the controller output. More often the tuning of these parameters is performed off-line using any optimization technique such as GAs. After the tuning process these parameters remain constant during the normal operation of the controller. To improve the controller performance and robustness these parameters can be alerted online. If such an on-line tuning of scaling factors, fuzzy rules or membership functions is performed the controller becomes an adaptive fuzzy controller.

B.2 Fuzzy Logic Modelling

FLC can be modelled using the Matlab Fuzzy Logic Toolbox graphical user interface GUI as shown in Fig. B.3 (a). This allows an easy way to build the FLC graphically. Five primary GUI tools are provided to help building and editing the FLC: Fuzzy Inference System (FIS) editor, membership function editor, rule editor, rule viewer and surface viewer. These GUI tools are dynamically linked so that any change in one will affect the others. The FIS editor is used to determine number and names of inputs and outputs, membership function editor defines shapes of different membership functions and inputs-outputs range, rule editor is used for editing the FL rules. Rule viewer and surface viewer are read-only tools and are used to look at the FIS characteristics. Modelling of FLC described in chapter 5 in Simulink is shown in Fig. B.3(b).

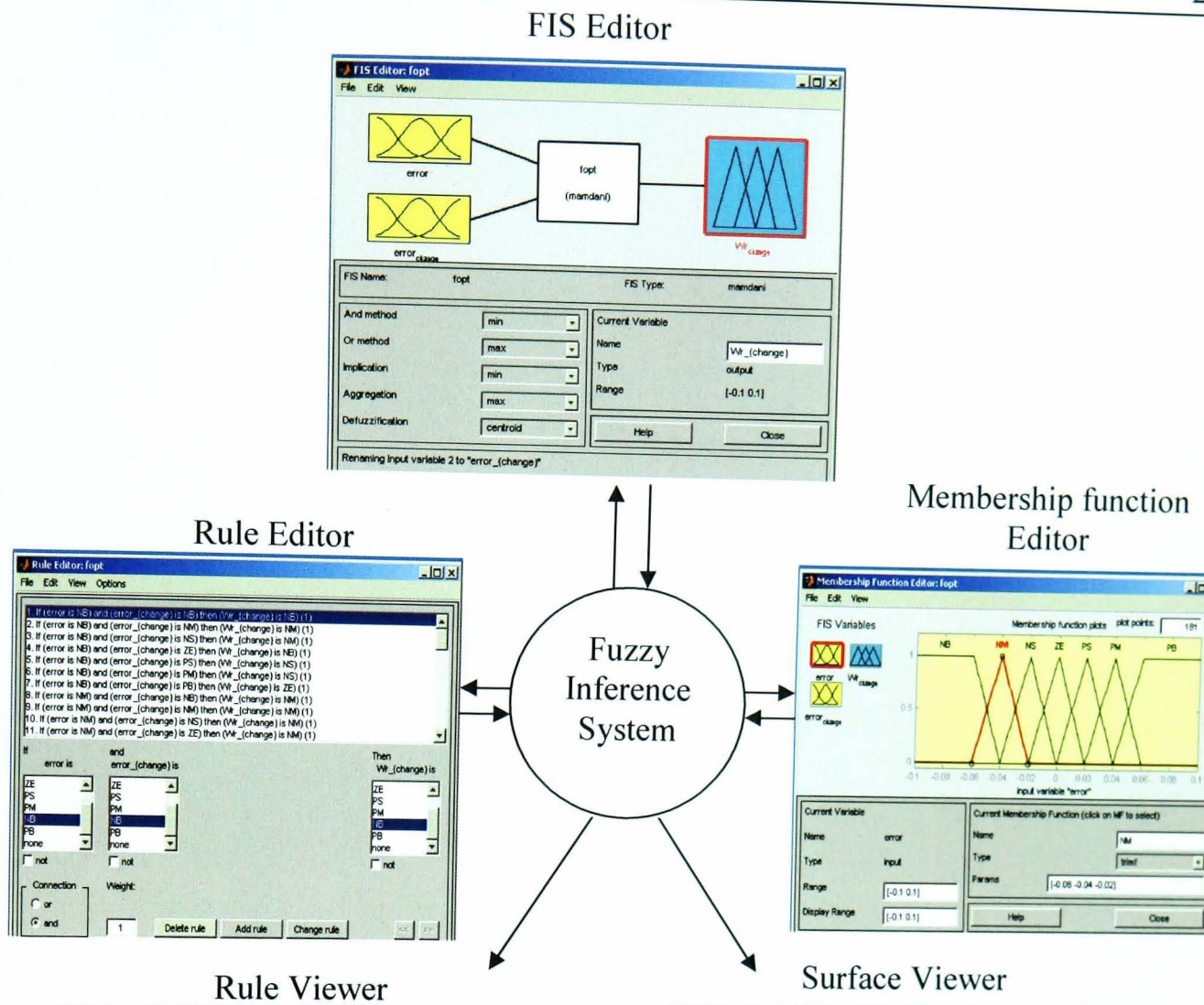

(a)

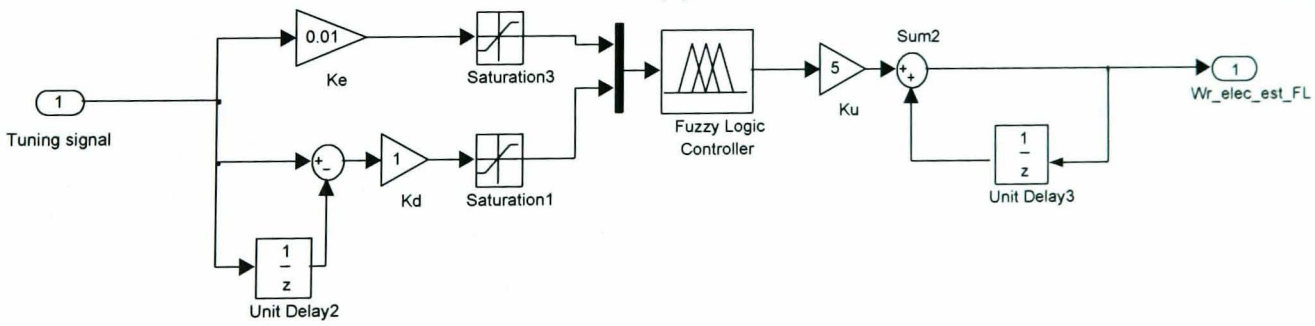

(b)

Fig. B.3 Fuzzy logic modelling using Matlab (a) Building model with Fuzzy logic toolbox (b) Simulink model